ERDC/CERL TR-23-7

Construction Engineering Research Laboratory

US Army Corps of Engineers®
Engineer Research and Development Center

ERDC
ENGINEER RESEARCH & DEVELOPMENT CENTER

4D Printing Structures for Extreme Temperatures Using Metakaolin Based Geopolymers

Ghassan Al-Chaar, Allison Brandvold, Andrij Kozych, and William Mendoza

April 2023

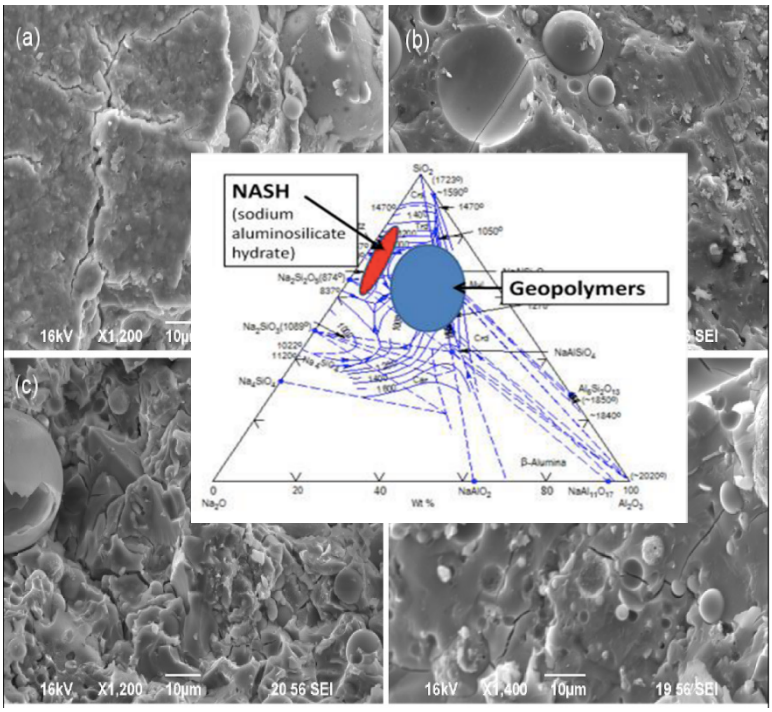

Distribution Statement A. Approved for public release: distribution is unlimited.

The US Army Engineer Research and Development Center (ERDC) solves the nation's toughest engineering and environmental challenges. ERDC develops innovative solutions in civil and military engineering, geospatial sciences, water resources, and environmental sciences for the Army, the Department of Defense, civilian agencies, and our nation's public good. Find out more at www.ERDC.usace.army.mil.

To search for other technical reports published by ERDC, visit the ERDC online library at https://ERDClibrary.on.worldcat.org/discovery.

ERDC/CERL TR-23-7
April 2023

4D Printing Structures for Extreme Temperatures Using Metakaolin Based Geopolymers

Ghassan Al-Chaar, Allison Brandvold, Andrij Kozych, and William Mendoza

US Army Engineer Research and Development Center (ERDC)
Construction Engineering Research Laboratory (CERL)
2902 Newmark Drive
Champaign, IL 61822

Final Report

Distribution Statement A. Approved for public release: distribution is unlimited.

Prepared for The Army Futures Command
701 Brazos St.
Austin, Texas 78701

and

Office of Senator Dick Durbin
711 Hart Building
Washington, DC 20510

Under "Robotic 4D Printing of Geopolymer Composites for Extreme Environments"
Program element 0603119A

Abstract

Geopolymers (GPs) are a class of amorphous, aluminosilicate-based ceramics that cure at room temperature. GPs are formed by mixing an aluminosilicate source, which is metakaolin in this case, with an alkali activator solution, which can be either sodium or potassium water glass. GPs have attracted interest for use in structural applications over the past few decades because they have superior mechanical properties to ordinary Portland cement (OPC). Additionally, they can tolerate much higher temperatures and produce a fraction of the CO_2 compared to OPC. This project aims to develop geopolymer composites for 4D printing (the fourth dimension being time) and test their mechanical properties. Rheology and the effects of curing in ambient conditions will be evaluated for fresh geopolymer. Freeze-thaw resistance will be evaluated on potentially printable composites for extreme temperature resistance, etc.

DISCLAIMER: The contents of this project are not to be used for advertising, publication, or promotional purposes. Citation of trade names does not constitute an official endorsement or approval of the use of such commercial products. All product names and trademarks cited are the property of their respective owners. The findings of this project are not to be construed as an official Department of the Army position unless so designated by other authorized documents.
DESTROY THIS PROJECT WHEN NO LONGER NEEDED. DO NOT RETURN IT TO THE ORIGINATOR.

Contents

Abstract ii

Figures and Tables vi

Preface xii

1 Introduction 1

1.1 Background: Geopolymer (GP) synthesis and precursors 1

1.1.1 Alkali-activated cements versus GPs 1

1.1.2 Kaolin and metakaolin 2

1.1.3 GP reaction 3

1.2 Processing and curing under ambient conditions 3

1.2.1 Curing under nonambient conditions 4

1.2.2 Temperature and humidity 5

1.3 Rheology 6

1.3.1 Shear thinning fluids 6

1.3.2 Yield stress 7

1.3.3 Principles of thixotropy 7

1.3.4 Oscillatory rheology 8

1.3.5 Vane geometry 9

1.3.6 Squeeze flow 9

1.4 Ultrasonic wave reflectometry (UWR) 10

1.5 4D printing 12

1.5.1 Introduction 12

1.5.2 Previous work in 3D printing 13

1.5.3 Mix design or fresh state properties 15

1.5.4 Printing parameters 16

1.6 Extreme temperature resistance 17

1.6.1 Introduction and problem 17

1.6.2 Forest fire characteristics 18

1.6.3 Physical and chemical behavior of concrete at high temperatures 19

1.6.4 Physical behavior of GP at high temperatures 19

1.6.5 GP at high temperatures 20

1.7 Mechanical properties of ordinary Portland cement (OPC) composites versus GP composites 21

1.8 Freeze-thaw (FT) of GPs and concrete 22

1.9 Objectives 25

1.10 Approach 25

2 Results and Discussion 26

2.1 Methods and materials 26

2.1.1 GP synthesis and materials sources 26

2.1.2 Fine aggregate characterization. 26

2.1.3 Metakaolin properties 28

2.1.4 Water glass composition *30*
2.2 Water retention and mechanical properties 30
2.2.1 Measuring water loss *30*
2.2.2 Methods and flexure properties of 1 × 1 × 10 cm (0.4 x 0.4 x 3.9 in.) samples *33*
2.2.3 Methods and flexure properties of 1 × 1 × 6 in. (2.54 × 2.54 × 15.24 cm) samples *37*
2.2.4 Water retention *55*
2.2.5 Scanning electron microscope (SEM) and pictures of samples *58*
2.2.6 SEM discussion *61*
2.3 Thermal properties and considerations 62
2.3.1 Effect of aggregate *62*
2.3.2 Effect of Si/Al ratio, water content, temperature on mechanical properties *64*
2.3.3 Difference between flexure and compression *67*
2.3.4 Optimizing sand and glass content for maximum high temperature strength *70*
2.3.5 Flexure strength evolution as function of temperature *72*
2.3.6 Flexure strength of GPC after simulated fire conditions *75*
2.3.7 The simulated fire testing *76*
2.4 Rheology 81
2.4.1 Methods and materials *81*
2.4.2 Experimental matrix *86*
2.4.3 Rheological results and discussion *87*
2.5 Ultrasonic wave reflectometry 116
2.5.1 Methods and materials *116*
2.5.2 Data-processing parameters *117*
2.5.3 Ultrasonic wave reflectometry results *118*
2.6 Mechanical properties of OPC composites versus GP composites (GPC) 119
2.6.1 Curing regime *119*
2.6.2 Materials *119*
2.6.3 Methods *119*
2.6.4 Test matrix *120*
2.6.5 Samples and weights *121*
2.6.6 Compressive strength results *121*
2.6.7 Flexural strength results *126*
2.6.8 Weight loss from drying *129*
2.7 FT characteristics 133
2.8 Corrosivity measurements 139
2.9 Portland cement versus GPs 142

3 Conclusions 150
3.1 Rheological conclusions 150
3.2 Mechanical properties of composites 151
3.3 Water retention and mechanical properties 152
3.4 Thermal considerations 152

4 Future Work 154
4.1 Rheology 154
4.2 Mechanical properties of composites 154

4.3 Thermal, mechanical, and FT properties of composites 155

References **157**

Abbreviations **169**

Appendix A: Water Retention and Mechanical Properties **171**

Appendix B: Rheology Values **177**

Report Documentation Page (SF 298) **188**

Figures and Tables

Figures

1. Experimental set up for ultrasonic wave reflectometry. 10
2. Gradation curve for various particulate reinforcements. 27
3. Pictures of aggregate used in Sections 2.2 and 2.3: (*1*) Cs, (*2*) gravel, (*3*) q, (*4*) fs, (*5*) wollastonite, (*6*) uroboros glass powder, and (*7*) basalt fiber. 28
4. Particle diameter distribution of the various types of metakaolin. 30
5. Four-point flexure results on 1 × 1 × 10 cm bars. 35
6. Image of the freezer/fridge samples (*left*) and the three-point 9 d fridge sample (*right*). 36
7. Black 1×1×10 cm bars (silica fume) and white bars (calcined silica fume). 37
8. Various 7-day-old flexure bars and pucks for water retention being cured in the humidity chamber (*left*). Flexure testing setup with a SG50 RH sample after failure (*right*). 38
9. Flexure strength for various temperatures and humidities (All data from Tables 10 through 13). 41
10. 20°C conditions separated out based on GP alkali type (Na versus K). 42
11. Picture of all the SG50 series samples taken at least a month after testing. One sample from each batch was chosen to represent a given temperature (10°C, 20°C, and 40°C), humidity, and time (3 d, 28 d). There are two bars in each group; *top* bar is SG50.Na and *bottom* bar is SG50. The 28 d/10°C condition was kept at 80 RH. 43
12. Densities of a few composites cured at 20°C/50 RH. 44
13. A composition containing silica fume, sand, and gravel (sg50sf1) that was heated with a torch. 45
14. XRD spectra of the two forms of silica fume calcined for 900°C for 12 hours. 45
15. An SF25 specimen that had been tested at 7 d after curing at 21°C/50 RH. 46
16. A piece of SG50SF2 submerged in DI water for 30 hours (*right*). Specimen before submerging (*left*). 47
17. Flexure strengths of GP composites, with varying water glass age times and temperatures, and "control," which is GP made from unaged water glass. 50
18. Flexure strengths of GP composites cured under different conditions. 51
19. The high shear mixing setup. 52
20. Flexure strengths of bars with variable mixing speed. All speeds and times tested (*left*), 2,000 rpm series (*right*). 53
21. SEM images of fracture surfaces with identifiable unreacted metakaolin *circled*. 55
22. Discoloration due to water loss in flexure samples. 56
23. Examples of the 3 in. puck samples. From *left* to *right*, S55.Na, sf15, and s55.Argical. 57
24. Mass retention of the pucks after approximately 350 hours. 57
25. Schematic showing different fracture surfaces to be analyzed. 59

26. Heat-treated GP samples. 63
27. Two samples of sample 6 with the visibly shrunken aggregates. 64
28. An example of heat deflection in sample FS30MG30.1:2:11.1100 °C on the *right* and sample FS40MG20.1:2:11.1100 °C on the *left*. All samples were heat treated on a flat piece of ceramic dusted with alumina powder. 67
29. Mechanical properties of heat treated and nontreated bars. Six specimens were tested for each bar. 68
30. Heat-treated and nontreated flexure samples (*left*). Fracture surfaces of heat-treated samples (*right*). Some surfaces have divots that were cut out for SEM imaging: *1*, FS40MG20; *2*, FS30MG30; *3*, FS30MG30.1:2:9; *4*, FS30MG30.1:1.5:9; *5*, FS30MG30.1:1:9; and *6*, FS30MG30.Na. 70
31. Optimizing for compressive strength samples with varying amounts of sand and glass. 71
32. Optimizing flexure strength of varying amounts of sand and glass GPC. 71
33. Fracture surfaces of the flexure bars of all the compositions and all the temperatures tested 73
34. Strength evolution with temperature of various composites. 74
35. Chunks of sf15 composite heated to (from *left* to *right*) 400 °C, 600 °C, 800 °C, and 1,000 °C with pH paper measurements of the resulting solution after 24 hours. 75
36. Simulated fire experimental set up. The chamber measures 25.4 cm long. The thermocouples are enclosed in 5 mm alumina tubes. The *left* picture shows a "low" temperature empty chamber flame 77
37. "Low" temperature flame test on SG50 (*left*). High temperature flame on SG50.Na (*right*). Note the glowing *left* thermocouple in the high temperature test. 77
38. Combined graph of flexure strength for sodium and potassium GP at low and high temperature. 79
39. (*a*), Na versus K-based composite at low temperature; (*b*), Na versus K-based composite at high temperature; (*c*), K-based composite at low and high temperature; (*d*), Na-based composite at low and high temperature. 79
40. Representative pictures of SG50 composite surfaces exposed to heat. Samples are 2.54 cm wide. 80
41. Representative pictures of SG50.Na composite surfaces exposed to heat 80
42. An image of the vane geometry used with the DHR2 83
43. The gray cylindrical cup used for testing (*left*) and the generic cup holder in the rheometer with a sample of KGP (*right*). 83
44. Image of the squeeze flow experimental set up for a sample of KGP reinforced with 60 wt% Quikrete sand and 3 wt%, 1/2 in. basalt fibers. 85
45. A visual of the shear sweep experiment as a function of time. 88
46. Shear sweep data for the various pastes tested. 89
47. A viscosity and stress versus shear rate plot of a plain KGP paste. 91
48. Stress ramp yield stress and HB model yield stresses of various metakaolin KGPs. 92
49. A stress versus shear rate graph for a stress ramp of a plain KGP paste. 93
50. Yield stress values for KGP composites and various sand. 95

51. Yield stress values for OPC composites and various sand. 95
52. A viscosity versus time curve for OPC held at a constant shear. 97
53. Initial viscosity versus time curve for KGP. 97
54. Further investigation for constant shear KGP. 99
55. The LVER of an OPC sample. 100
56. KGP paste oscillatory measurement results at 0.01 strain % and 1 Hz frequency. 101
57. A visual depiction of the viscosity recovery experimental procedure. 102
58. Viscosity versus time curves for viscosity recovery of a KGP paste at 5 minutes (*left*), 10 minutes (*middle*), and 15 minutes (*right*). 103
59. Cone used for qualitative shape retention testing of GP composites. 104
60. Shape retention cone for a GP composite with coarse sand and basalt fiber. 105
61. KGP with 60 wt% QS and 3 wt% 1/8 in. (3 mm) BF (*left*) and KGP with 60 wt% QS and 3 wt% 1/2 in. BF (*right*). 106
62. Three samples of KGP with 62 wt% Quikrete medium sand and 2 wt%, 1/2 in. BF (*top*), 3wt%, 1/2 in. BF (*middle*), and 4wt%, 1/2 in. BF (*bottom*). 107
63. KGP samples of varying Quikrete medium sand and gravel composition. 108
64. A basalt minirod treated with a sand coating. 109
65. A basalt minibar used for KGP reinforcement. 109
66. KGP samples containing various percentages of sand, basalt fiber, and basalt minirods. 110
67. KGP samples containing various percentages of sand, basalt fiber, and basalt minibars. 111
68. KGP paste sample after the squeeze flow test with 60 wt% Quikrete medium sand and 3 wt%, 1/2 in. basalt fibers. 111
69. Squeeze flow trendlines at 0.1 mm/s of KGP with 60 wt% sand and various basalt fiber sizes and percentages. 113
70. Squeeze flow trendlines at 0.1 mm/s of KGP with varying sand percentages and 3 wt% basalt fiber with either 1/2 in. or 1/8 in. at 0.1 mm/s. 114
71. Squeeze flow trendlines with varying sand percentage for both squeeze flow rates and 3 wt%, 1/2 in. basalt fiber. 115
72. Squeeze flow trendlines with varying sand percentage for both squeeze flow rates and 3 wt%, 1/8 in. basalt fiber. 116
73. A UWR run of a Metamax EF potassium GP. 117
74. Compressive strength of KGP versus OPC. 122
75. Average compressive strength of KGP versus OPC. 122
76. Failure of GP and OPC paste. 123
77. Failure of OPC (*top*) and GP composites with fine sand (*bottom*). 124
78. Failure of OPC (*top*) and GP composites with coarse sand (*bottom*). 125
79. Failure of OPC (*top*) and GP composites with fine sand and gravel (*bottom*). 126
80. Flexure strength of KGP versus OPC. 127
81. Average flexure strength of KGP versus OPC. 127
82. Cross section of failed KGP paste and fine sand mortar bars. 128

83. Cross section of failed OPC paste and fine sand mortar bars. 128
84. Cross section of failed KGP coarse sand mortar and concrete bars. 129
85. Cross section of failed OPC coarse sand mortar and concrete bars. 129
86. Water weight loss of pure cement cylinders and fine sand mortar cylinders. 130
87. Water weight loss of coarse sand mortar cylinders and concrete cylinders. 130
88. Water weight loss of pure cement bars. 131
89. Water weight loss of fine sand mortar bars. 131
90. Water weight loss of coarse sand mortar bars. 131
91. Water weight loss of concrete bars. 132
92. Surface cracks in KGP and OPC paste cylinders. 132
93. Freeze-thaw data for 16 out of 18 compositions created. 135
94. Representative close-ups of characteristic damage for all the samples after testing had completed. 137
95. Correlation statistics for dynamic modulus and the flexural load. 139
96. Representative pictures of the chief failure modes of the specimens. From *left* to *right*: Brittle failure (sample 7), a more ductile failure (sample 11), basalt fiber failure (sample 14). 139
97. Example of the two specimens after 12 days in the oven. 142
A-1. Pictures of discs of pure KGP with their respective coatings: (*a*) paper; (*b*) cornstarch; (*c*) sand; (*d*) talc; (*e*) silicone mold release spray; and (*f*) 55 wt% sand (<425 µm) composite after 9 days of drying at ambient conditions. 171
A-2. Percent mass retention of pure KGP with various coatings, dried under ambient conditions (20 °C, 50%±10 RH) for 206 hours, a control specimen dried under 95% RH, and a 55 wt% sand composite. 172
A-3. Mass retention of the S55 control sample with no coating and the two coatings. 173
A-4. Raw curve and peak fitting and identification for silica fume. 173
A-5. Sodium water glass after 7 d in freezer (*left*). Potassium water glass after 7 d in freezer (*right*). 174
A-6. Lateral views of the tested water glass age and control samples. A single representative bar was chosen. Bars were grouped by water glass age time and control type. The two bars in each group—(*a*), (*b*), etc.—are sodium (*top*) and potassium (*bottom*) GPs. The groups are (*a*) freezer, (*b*) 7 d age, (*c*) 14 d age, (*d*) control, and (*e*) control.9d. 174
A-7. Lateral views of control.2d samples: (*a*) SG50, (*b*) SG50.Na. 175
A-8. Images of the torched surfaces after testing. SG50 samples in the *left* picture and SG50.Na samples in the *right*. Samples heated at the same temperature are in columns, and samples heated for the same time periods are in rows. 175
A-9. Flexure testing setup for the flame test samples. Pictured is the SG50.Na, 2 minute, 676 °C sample after failure has occurred. 176

Tables

1. Sample extreme temperature and humidity values (temperature in Celsius/Relative humidity [Specific humidity (SH)]). 6
2. Relevant work results in 3D printing. 14
3. Materials used for testing. 26
4. X-ray florescence spectroscopy (XFS) of various commercial metakaolins (Sankar, Sutrisno, et al. 2018). 29
5. Additional characteristics of the relevant types of metakaolin. 29
6. Chemical makeup of KASOLV 16 and other potassium silicates. 30
7. Geometrical calculations for various structures and samples. 32
8. Three point bending tests for several compositions cast and cured for 24 hr at 21°C/95% RH and 24 hr 50°C/95% RH (in *grey*). The strengths are listed as follows: strength [95% two-sided confidence interval (CI)] 34
9. Four-point flexure tests with a load span of 2 cm and a support span of 6 cm. Remaining % composition is GP. All bars had nominal dimensions of 1 × 1 × 10 cm. The above tests were repeated for four-point testing, which gave markedly lower, albeit more accurate, results. 34
10. Seven-day flexure strength data for 1 × 1 × 6 in. specimens of various compositions cured at 21°C and 50% RH. 38
11. Flexure when cured at 21°C (versus time).* 40
12. Flexure when cured at 10°C (versus time). 40
13. Flexure when cured at 40°C (versus time versus humidity). 41
14. Other curing conditions in *pink*, water glass aging in *white*. 49
15. Results of mixing at different speeds for different times. 53
16. Compositions and results of water loss. 56
17. SEM images of fracture surfaces. 59
18. Compositions of aggregates for heat treatment. 62
19. Strength of GPC cured at RT. 65
20. Strength of GPC treated at 1,100°C at one hour. 66
21. Images of compression samples and SEM images of the flexural samples. 68
22. Heat-treated (1,100°C, one hour) samples' flexure strength. 70
23. Flexure strength of samples heated to varying temperatures for 1 hour. 72
24. Range of temperatures (°C) at each setting for thermocouples TC1 (*left*) and TC2 (*right*). 78
25. Flexure versus duration at approximately 676°C (intermediate temperature). 78
27. List of measured or calculated constants for the vane geometry. 82
28. A matrix of possible rheological experiments and an explanation of goal and variables. 86
29. Yield stresses measured with the Hershel-Bulkley Model. 90
30. Power law indexes of various metakaolin systems. 90
31. The yield stresses of various pastes found by stress ramp experiments. 92
32. Yield stress values from stress ramp testing and Herschel-Bulkley model. 94

33. Recovery time data for plain KGP pastes. 103
34. Various composites tested for shape retention. 105
35. UWR data from various GP systems. 118
36. Test matrix for OPC–GP comparison. The proposed test matrix of samples with their respective sample numbers. 120
37. OPC sample measurements. All weights are in grams. 121
38. GP sample measurements. 121
39. Compositions of varying beams tested. 133
40. Loads of all the samples. 138
41. Corrosivity results. 140
B-1. Compiled list of calculated values from the power law model. 177
B-2. Compiled list of values calculated from the Hershel Bulkley model. 182

Preface

This study was conducted for a Congressional Mandate Increase CERL Focus Area: FY21 Program Increase for Program Element (PE) 0603119A, Ground Advanced Technology, Line 55, Research on Construction Materials project entitled "Robotic 4D Printing of Geopolymer Composites for Extreme Environments," dated 15 December 2021.

The work was performed by the Materials and Structures Branch of the Infrastructure Science and Engineering Division, US Army Engineer Research and Development Center, Construction Engineering Research Laboratory (ERDC-CERL). At the time of publication, Mr. Sean Wallace was the branch chief of the Materials and Structures; Mr. Tim Shelton was division chief; and Dr. Justin Berman was the technical director for Infrastructure, Science, and Engineering. The deputy director of ERDC-CERL was Michelle Hanson, and the Director was Dr. Andrew J. Nelson.

ERDC-CERL would like to thank Prof. Waltraud Kriven at UIUC for her advisement.

COL Christian Patterson was commander of ERDC, and Dr. David W. Pittman was the director.

1 Introduction

1.1 Background: Geopolymer (GP) synthesis and precursors

1.1.1 Alkali-activated cements versus GPs

The synthesis of geopolymers (GPs) generally involves mixing an aluminosilicate source with an alkali activator solution. Aluminosilicate sources, such as slag and fly ash, create alkali-activated cements (AACs), which should not be confused with GPs as AACs contain irreproducible impurities of various metal oxides (Komljenović et al. 2010) and are not composed with 1:1:4:11 M_2O:SiO_2:H_2O geopolymer stoichiometry (Kriven 2018), where M is sodium or potassium.* The general polymerization reaction of AACs and subsequent mechanical properties are influenced by several factors, including but not limited to composition (Li et al. 2017; Alonso et al. 2001), aluminosilicate particle size, set time, and curing conditions (Shi et al. 2003; Duxson, Fernández-Jiménez, et al. 2007; Peijiang 2005; Provis and Deventer 2007a; Singh 2018). This makes obtaining consistent, reproducible results difficult (Komljenović et al. 2010). For example, alkali-activated slag produces different products and properties than Class F fly ash (Li et al. 2017). Nevertheless, AACs are an attractive structural material due to their use of waste products (fly ash, blast furnace slag, etc.), lower CO_2 footprint, higher mechanical properties, increased fire resistance (Sarker et al. 2014; Okoye 2016), and increased resistance to freeze thaw (Kukko and Mannonen 1982) and corrosion (Bakharev 2005) compared to ordinary Portland cement (OPC) (Komljenović et al. 2010; S. D. Wang et al. 1995; A. Wang et al. 2020; Roy 1999). The science of geopolymer systems has been mostly settled. One of the barriers that remains to the introduction of GPs into the construction industry is the lack of standardization and, more importantly, the lack of data on long-term GP durability (A. Wang et al. 2020).

* For a full list of the spelled-out forms of the chemical elements used in this document, please refer to *US Government Publishing Office Style Manual*, 31st ed. (Washington, DC: US Government Publishing Office, 2016), 265, https://www.govinfo.gov/content/pkg/GPO-STYLEMANUAL-2016/pdf/GPO-STYLEMANUAL-2016.pdf.

1.1.2 Kaolin and metakaolin

To eliminate the inhomogeneities and excess variables associated with AACs, metakaolin, a relatively pure aluminosilicate source, is used to fabricate structures with similar desirable properties as AACs. Metakaolin is derived from kaolinite. Kaolin is an off-white, soft, and nonabrasive mineral, which is composed of alternating sheets of silica tetrahedra and aluminum octahedra, giving a theoretical composition of 46.54% SiO_2, 39.5% Al_2O_3, and 13.96% H_20 by mass. Being a raw mineral, kaolin is often contaminated with other trace minerals, such as quartz, iron oxides, muscovite, feldspar, siderite, etc., which lend to its off-white color (Prasad et al. 1991; Grimshaw 1971). There are a variety of physical and chemical methods to purify kaolin, including but not limited to, magnetic separation, leaching with organic acids, and simple sieving (Saikia et al. 2003). Global sources of kaolin should be identified and evaluated if geopolymer technology for structural applications is to remain feasible. The world's commercial kaolin deposits include Georgia (US), Brazil, the Czech Republic, Slovakia , England, and Ukraine (Prasad et al. 1991). Millions of tons of raw kaolin are mined globally every year.

When kaolinite is heated, it undergoes a dihydroxylation reaction and loses water, forming an amorphous aluminosilicate where some of the octahedrally coordinated aluminum Al(VI) transforms into a strained, reactive five-fold aluminum (Al[V]) (Kriven 2018). The temperatures that this occurs at have been reported to be 450°C–600°C* and as high as 850°C by Sanz et al. (1988), who used the relative intensities of peaks in Al nuclear magnetic resonance (NMR) (H. Wang et al. 2011; Grim 1962). However, several studies found that the ideal calcination temperature is 750°C based on compressive strengths of metakaolin added to cement (Huat 2006; Potgieter-Vermaak and Potgieter 2006). Metakaolin's reactivity and pozzolanic properties, therefore, stem from the calcination temperature, which determines particle size, surface area, and Al(V) content (Davidovits 2015; Gordon et al. 2005; Sankar, Sutrisno, et al. 2018; Samuel et al. 2020) as well as mineral impurities from the raw kaolin (Zibouche et al. 2009; Duxson, Fernández-Jiménez, et al. 2007). Sankar, Sutrisno, et al. (2018) and Samuel et al. (2020) investigated the

* For a full list of the spelled-out forms of the units of measure used in this document, please refer to *US Government Publishing Office Style Manual*, 31st ed. (Washington, DC: US Government Publishing Office, 2016), 248–52, https://www.govinfo.gov/content/pkg/GPO-STYLEMANUAL-2016/pdf/GPO-STYLEMANUAL-2016.pdf.

mechanical property effects that variables related to calcination temperature had on geopolymers synthesized with various types of commercial metakaolin (MK): Argical 1,200S, Powerpozz, Metamax HRM, and a few others.

The varying reactivities of these types of commercial MK could be used to tailor the setting time of 4D-printed geopolymer composite (GPC). Set time will be investigated for some of these MKs to be used as a fast-setting coating for water retention as well as mechanical properties testing for future potential prints.

1.1.3 GP reaction

The geopolymerization reaction involves mixing metakaolin with an alkali silicate activator solution and takes place in three distinct steps—dissolution of the metakaolin, gel formation, and condensation/polymerization (Duxson, Mallicoat, et al. 2007; Davidovits 1994a; Provis and Deventer 2007a).

The resultant structure is amorphous and consists of alternating units of AlO_4 and SiO_4 tetrahedra. The reaction rate and subsequent mechanical properties are dependent on processing conditions, curing conditions, concentration of alkali and metakaolin quality (Rahier et al. 1997; Alonso et al. 2001; H. Wang et al. 2005). The synthesis of geopolymers is a variable that will be held constant in this study. A potassium-based geopolymer will be synthesized with the following molar ratio: 1 K_2O:1 Al_2O_3:4 SiO_2:11 H_2O, and the effects of curing conditions and various quantities of reinforcement will be varied instead.

1.2 Processing and curing under ambient conditions

The geopolymerization reaction is normally carried out at room temperature (RT) (21°C) in contrast to most ceramics, which rely on energy intensive high temperatures and pressures to drive sintering and densification. In GPs, water plays a critical role in the geopolymer formation process where it serves as a medium for the metakaolin/water glass polymerization reaction to take place, allowing for the reaction to be done at RTs as opposed to the high-temp, solid-state processes needed to form most ceramics. Potassium-based geopolymer (KGP) exposed to low humidity, ambient conditions has the potential to dry out prematurely, which leads to cracking (Kuenzel et al. 2012). GP shrinkage and cracking is

thought to occur due to strong capillary forces between wet and dry areas in the micropores of the material, which initiate crack propagation. Kuenzel et al. (2012) also reported other variables to have an effect on shrinkage, such as initial water content, Si/Al ratio, and the alkali ion used in the water glass (Na^+ versus K^+). To minimize shrinkage and cracking GPs should be dried out as slowly as possible and have significant reinforcements added.

Most research with geopolymers is conducted on pure geopolymer that is typically sealed in a mold and cured at RT, a high temperature of up to 80°C, or some combination of the two at a high humidity level (Alonso et al. 2001; H. Wang et al. 2005; Kuenzel et al. 2012; Heah et al. 2011; Rovnaník 2010). The GP is typically sealed in a mold for the curing step and is then taken out and allowed to dry at the general lab environment (21°C, 50±10% relative humidity [RH]). In this step, the residual water evaporates until equilibrium is reached as the water is not incorporated into the GP structure (Kuenzel et al. 2012).

1.2.1 Curing under nonambient conditions

However, large-scale additive manufacturing of geopolymers is expected to be done under a variety of conditions: hot and cold, wet and dry. Therefore, it is expedient to test several compositions at several conditions, which will be controlled with a climate/humidity chamber to ascertain the effects of these curing conditions on the final mechanical properties. Some work has been done on ambient curing that researched various mechanical properties of open-air-cured, alkali-activated concrete using Na alkali and Fly ash/granulated blast furnace slag (GBFS) as a starting material (Manjunatha et al. 2014). However, the concrete was cured in a mold for the initial 24 hours, and the ambient-curing humidity conditions were not specified. D.S. Perera et al. (2007) studied porosity, compressive strength, and other values for pure Na/metakaolin-based geopolymers at various temperatures and RH values from 30%–70% and found that samples cured at a high initial temperature/humidity level (40°C/70% RH/48 h) did not crack when exposed to lower humidity values (30% RH) after initial curing. Therefore, care must be taken to ensure minimal water loss at the onset of setting and curing. Rovnaník evaluated the effect of temperature on a Na alkali/metakaolin-based GP composite and found that specimens cured at lower temperatures (10°C) for the initial 4 hours achieved equal or higher mechanical strengths than those cured at higher temperatures from 20°C to 80°C (Rovnaník 2010).

Water loss will be evaluated qualitatively and quantitatively according to the following equation:

$$\%\ Mass\ Retention\ = \frac{final\ mass\ of\ pure\ GP}{(Initial\ mass\ of\ pure\ GP)} \quad (1)$$

Note: Even samples cured in ideal conditions are expected to lose approximately 10 percent by weight (wt%) water when fully cured as the moisture content in the geopolymer reaches equilibrium with the surroundings. Final mass is the mass after equilibrium has been achieved and there is no appreciable mass loss. Finally, Yousefi Oderji et al. (2019) investigated the effects of relative humidity on a sodium-alkali-fly-ash-based cement and found that components achieved the highest compressive and flexural strength at 70% RH from a range of 30–90%.

1.2.2 Temperature and humidity

Temperature and humidity will be two of the variables altered in the following report. Generally, geopolymers achieve higher flexure strengths with longer curing times and higher environmental humidity. Low humidity increases water evaporation, which leads to early hardening and a premature end to the geopolymerization reaction, which is predicted to decrease strength due to surface crack formation. This effect must be known and quantified if geopolymer composites are to substitute concrete in outdoor applications.

Relative humidity (RH) is the dominant form of calculating humidity and is used in meteorology, research, and most sensors. However, it does not give a good indication of the absolute amount of water vapor in the air because it is dependent on temperature. For example, a unit of air at 30°C holds almost five times as much water as the same unit at 5°C with the same RH. Because of this, specific humidity (SH) will be calculated and displayed where applicable.

To simulate real-world conditions, example extreme temperatures and humidities were gathered from around the world. Average humidity was taken from weather-and-climate.com, and the corresponding monthly average minimum and maximum temperatures were taken and are displayed in the table below (Table 1) (World Wide Travel Organization, n.d.).

Table 1. Sample extreme temperature and humidity values (temperature in Celsius/Relative humidity [Specific humidity (SH)]).

	Hot environment	Cold environment
High humidity	Chennai, India (May) 37 °C/61% [0.024]	Anchorage, Alaska (May) 3 °C/62% [0.003]
Low humidity	Giles, Australia (January) 37 °C/23% [0.0089]	—

Colder air is inherently drier. Alaska is relatively humid compared to other states but has almost three times less water per unit of air compared to Giles, Australia. A low specific humidity in a cold environment rarely occurs, and that box in Table 1 was left empty. Table 1 will be used to inform experimental design. Samples will be cured at several static conditions to imitate deployment of 4D-printing GP outside the lab environment.

1.3 Rheology

To understand the optimal way to successfully print geopolymers, the rheological properties of GP and OPC pastes needed to be investigated in terms of fluid properties, yield stresses, effects of thixotropy, time limitations, and overall flow mechanisms.

1.3.1 Shear thinning fluids

It is important to consider the rheological properties of cementitious paste when designing an optimal 4D printing system. Rheology is the study of "deformation and the flow of matter" (Morrison 2001). Some of the common challenges associated with 4D printing are shape retention, workability, ease of flow, and overcoming yield stress to extrude the paste out of the 4D printer. Geopolymers and cement are categorized as non-Newtonian fluids, meaning their viscosity is dependent on the shear or stress rate that is being applied to the system. This specific phenomenon is called shear thinning when the viscosity decreases with an increase in shear rate or stress. Other common examples of shear thinning materials include inks and varnishes (Żołek-Tryznowska 2016). Shear thinning properties arise from the alignment of particles upon greater stress or shear, which reduces the resistance to flow or viscosity.

1.3.2 Yield stress

Geopolymer and OPC are also Bingham fluids that need to overcome a yield stress to initiate flow as well. There is much controversy surrounding the relevance of yield stress measurements, as each different method used to determine this property can produce a different result (Barnes 1999). Factors such as experiment type, rheometer geometry, choice of dependent variable, and material system all play a role in influencing the measurement of yield stress for a fluid (Moller et al. 2006). Despite the large variance in testing methods and results, yield stress values of fluids have been found useful as approximate parameters for flow in practical application. When considering the process of 4D printing, yield stress is most applicable to the stress required for extrusion out of the printer head to occur. For flow to occur, the 4D printer must provide sufficient stress on the geopolymer or OPC paste to overcome the yield stress, allowing extrusion to take place. Nguyen and Boger introduce the concept of indirect and direct measurements of yield stress (Nguyen and Boger 1992). Indirect measurements are those that are extrapolated from data or those that consider zero shear viscosity. Direct measurements of yield stress involved an experimental start and stop of flow to determine the point at which the fluid yields. For the usage of yield stresses in this project, both an indirect and direct method of calculating yield stresses are used and will be introduced later in the report.

1.3.3 Principles of thixotropy

In addition to their shear thinning capabilities, cement and geopolymers are also thought to be thixotropic. Thixotropy is a rheological phenomenon associated with a decrease in viscosity as a constant stress or shear is applied for a certain period of time. Thixotropy has been an active area of rheological research for several years, but there is still some disagreement about its definition, and the mechanisms that cause thixotropy are not well understood. Mewis and Wagner (2009) define three essential parameters for thixotropy: it is based on viscosity, it is a time-dependent decrease of viscosity, and the effect of thixotropy is reversible when the stress or shear is ceased. Investigating the extent of thixotropy varies based on experiment type, material, and parameters such as shear rate and stress. One of the common methods of assessing thixotropy is through a hysteresis loop of shear rate and stress. The amount of stress required for flow decreases from the ramping segment to the down segment of the experiment. This is due to the mechanical breakdown of the structure on

initial increase in stress or shear rate that happens in such a time frame that the material has not yet recovered on start and completion of the down segment (Mewis and Wagner 2009). Measuring thixotropy with materials that undergo a setting process also presents several obstacles, particularly the competing mechanisms of the physical setting and hardening of the material and thixotropic restructuring of the material while in the fluid state.

While both thixotropy and shear thinning behaviors reflect a drop in viscosity, they are two distinct rheological phenomena. While these two fluid properties are commonly found together, the important distinction between the two revolves around the cause of the drop in viscosity and subsequent recovery. Thixotropy as defined above is time dependent, while shear thinning is shear rate or stress dependent. On the cessation of flow of a shear thinning fluid, the viscosity will instantaneously revert back to its preflow state, whereas a thixotropic material needs an additional amount of elapsed time for full structural recovery. Knowing the shear history of a material is imperative to understanding its thixotropic features, which is why most rheology experiments, not just those pertaining to thixotropy, often start with a preshear. The addition of a preshear step ensures each sample starts with identical shear history.

1.3.4 Oscillatory rheology

In addition to flow rheological testing, oscillatory rheology is essential to understanding the solid- and liquid-like behavior of cementitious materials at different strain percentages and frequencies. Oscillatory-motion-focused experiments measure primarily the storage and loss modulus of a paste as a function of frequency, strain percentage, or time. The storage modulus is representative of stored elastic energy (solid like behavior), and the loss modulus is representative of the dissipation of energy. The tan delta is also calculated, which is the ratio of loss to storage modulus and is also reflective of solid- or liquid-like behavior (Larson and Larson 1999). To design valid oscillatory measurements, the linear viscoelastic region (LVER) and critical strain parameters must be determined. The LVER is an important parameter because it is the range at which damage inflicted on the internal structure of the paste is elastic, whereas outside this range, the deformation on the system is plastic and can vastly change the values of storage and loss moduli (Anton Paar, “Amplitude Sweeps,” n.d.). Once the critical strain is determined, further oscillatory measurements can be conducted below the LVER range to

ensure all deformation is elastic and recoverable, eliminating strain percentage as a variable of storage and loss modulus.

1.3.5 Vane geometry

Measuring the rheological characteristics of cementitious materials is often difficult due to high variability of viscosity and the addition of high weight percentages of reinforcements, such as sand, chamotte, or gravel. Typical rheometer geometries such as the Peltier plate system, cone and plate system, or the concentric cylinder geometry have limited potential to measure rheological properties of plain geopolymer or OPC pastes but are incapable of measuring cementitious material with large reinforcements. A few attempts in the early stages of this project were made to use the Peltier plate system to measure but were unsuccessful due to bad contact with the top plate and the effects of viscoelasticity with some composites. The best recommended geometry for bulk measurements of this type is the vane geometry, which is a four paneled spindle (Barnes and Carnali 1990). The vane geometry is also commonly used for applications in food technology, colloidal dispersions, bioengineering, miscellaneous dispersion, and also with foams (Barnes and Nguyen 2001).

The adaptation of the vane geometry allows for the bulk measurements of systems with high viscosity and high weight percentage of reinforcement and limits the effects of wall slip. Pertaining to the measurement of thixotropic materials, the loading of the vane geometry into the sample introduces less shear, which leads to much less deformation that could affect the overall measurement of thixotropic properties (Owens et al. 2020). The stress and shear rate on the paste decays exponentially as measured further from the center of the vane as is typical with this type of geometry. For all these reasons, the vane geometry was chosen for the rheological testing of geopolymer and OPC paste.

1.3.6 Squeeze flow

While the rheological testing of cementitious pastes gives valuable insight into their fluid properties, highly reinforced systems cause issues with rheometer system limits. Highly reinforced systems with extremely high viscosities and yield stresses typically surpass the maximum torque and stress limits on commercially made rheometers and viscometers, either requiring a custom piece of equipment for testing or an alternative method for assessing fluid properties of the composite. For the purpose of

assessing the fluid properties of highly reinforced systems, this study has adapted the squeeze flow test, based off the work of Grandes et al. (2018) and Toutou et al. (2005). Highly reinforced cementitious materials also have unique internal friction due to the variety of shapes and materials used as reinforcement. The application of a controlled strain rate allows for the influence of frictional components to be assessed at various locations of compression.

As reinforcements are compressed together and frictional components are forced to interact, the resistance to compression can increase to resist further deformation. The results of this type of experimentation can help assess shape retentive qualities of composites and their ability to hold up the weight of sequential layers. The squeeze flow method also gives insight to the phase separation of the fluid material if any occurs (Grandes et al. 2021).

1.4 Ultrasonic wave reflectometry (UWR)

Ultrasonic wave reflectometry (UWR) is an effective, nondestructive way to measure the set time of a cementitious material. During ultrasonic testing, a shear wave is generated from a transducer attached to a buffer material, which contains the testing material. During testing, the shear wave propagates through the buffer material until it hits the sample material, which either transmits or reflects the wave back to the transducer based on the current state of setting of the material. It is well known and documented that shear waves effectively propagate through a solid and will reflect when met with a liquid. A visual of the experimental set up is shown in Figure 1.

Figure 1. Experimental set up for ultrasonic wave reflectometry.

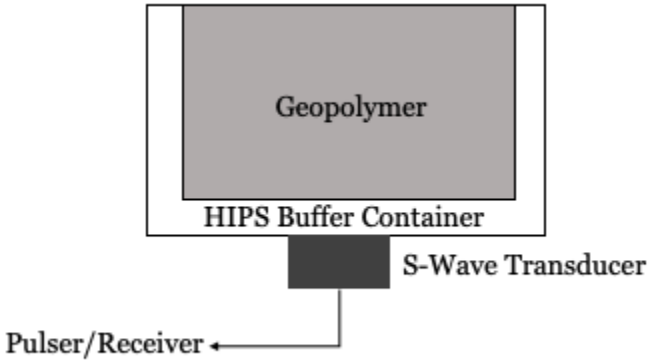

The set time of the material is determined by assessing the change in the reflection coefficient over time. The reflection coefficient is derived from the impedances of the buffer material and the test material, which are further defined in Equation (2). A further explanation of UWR is given by Subramaniam and Lee (2007).

$$Reflection\ Coefficient\ = \left| \frac{Z_2 - Z_1}{Z_2 + Z_1} \right|, \tag{2}$$

where

Z = the impedance of the buffer material, and
Z_2 = the impedance of the test material.

The impedance of a material can also be defined through Equation (3).

$$Z\ = \sqrt{\rho G}, \tag{3}$$

where

ρ = density, and
G = shear modulus.

As the material starts to set, the density starts to increase, which also causes the impedance value to increase for the cementitious material. As the Z_2 value gets closer in magnitude to Z_1, the numerator of the reflection coefficient equation decreases until it reaches zero, at which point the impedance value of the test material surpasses that of the buffer material. As the material continues to set and densify, the reflection coefficient starts to increase.

UWR is used as an alternative to standard penetration tests such as ASTM C403. The penetration tests are able to determine when a certain amount of resistance is supplied by the material after setting when met with a force exerted by a penetrative device such as a Vicat needle (ASTM C191). While these types of experiments can be useful in determining when a cementitious material can resist a certain force and support a weight, they give little insight into the formation of the solid network of the material below the externally exposed surface. The comparison between these two types of set time assessments is further elaborated in a study done by Sankar, Stynoski, et al. (2018).

1.5 4D printing

1.5.1 Introduction

3D printing of cementitious materials was championed by researchers such as Pegna (1997), who used a method similar to selective laser sintering (SLS) to fabricate table-top-sized structures out of OPC. This method is called binder jet printing (BJP) and is the more limited application due to multiple constraints, such as powder flowability tolerances and over-pressing of the powder bed (Rehman and Sglavo 2020; Nematollahi et al. 2018).

The second, more widespread method relies on an extrusion of a prepared paste to build the final component layer by layer and will be the route taken in this project. This is typically done by pumping the concrete mixture through a hose or tube and out an extrusion nozzle that is mounted to the 3D printer.

Khoshnevis et al. (2004) introduced the concept of contour crafting, a method of fully automated building construction. While full automation is still mostly conceptual, this is being developed with the current focus on the automatic incorporation of reinforcements into the print (Marchment and Sanjayan 2020). For example, Bos et al. (2018) modified a printing head to deposit and reinforce concrete with a steel cable. This technology has since been the subject of numerous papers, with the hopes of being deployed to reduce labor costs, material waste, and workplace injury and greatly speed up construction time (Lim et al. 2012; Wangler et al. 2016).

4D printing refers to the fourth dimension, time, which will be incorporated as an influencing factor that induces shear thinning in the geopolymer composite, making it easier to extrude.

The three main types of cementitious material that have been 3D printed by extrusion successfully are

- Cement based
- AAC based
- GP based

1.5.2 Previous work in 3D printing

Lim et al. (2012) and Bos et al. (2018) both printed meter-scale structures using concrete made from a proprietary cement and sand mortar. T. T. Le et al. (2012) used cement with fly ash and silica fume to make concrete prints of varying sizes. Nematollahi et al. (2018) 3D printed 2.5 × 3 cm cross section bars with a Na alkali/fly-ash-based cement that used sand and polypropylene fibers as reinforcements. Bong et al. (2019) 3D printed cm scale bars using fly ash/GBFS/Na and K alkali-based cement and tested mechanical properties of the cured composite. Archez et al. (2021) printed cm scale beams and hollow cylinders from a K alkali/MK-based GP reinforced with sand, kaolin, wollastonite, and others. Archez et al. (2021) also investigated the slump behavior of different mixes and the effect curing at varying temperatures and relative humidities has on the microstructure with a scanning electron microscope (SEM). The paper by Archez et al. is the closest to the focus of this project, which intends to develop a K alkali/MK-based GP composite that has acceptable fresh state properties and can withstand setting and maintaining strength in hostile climates and to print with the composite in m scale. This hasn't been done before to the extent of our knowledge, previous researchers have cured their 3D prints at RT and high humidity (Nematollahi et al. 2018; Bong et al. 2019). Relevant work results in 3D printing are summarized below in Table 2.

Table 2. Relevant work results in 3D printing.

				Relevant mechanical properties		
Literature source	GP/AAC source	Additives	Rheology tested	Flexure strength (maximum, MPa)	Interlayer debonding strength	Curing conditions
Archez (2021)	K alkali/MK	Glass fibers, wollastonite, sand, kaolinite	Slump based on layer height	approximately 15 MPa	—	Not specified, likely room temp and ambient humidity
Bong (2019)	Na and K alkali/slag and fly ash	Fine and coarse sand	Slump based on bottom layer width	7.1 (Na based)	2.7	Sealed in a container
Panda (2018)	K alkali/slag and fly ash	Silica fume, sand	Rheometer w/vane apparatus	—	approximately 1.4	Room temp and ambient humidity
Nematollahi (2018)	Na alkali/fly ash	CMC (sodium carboxymethyl cellulose), sand, Polypropylene (PP) fibers	Slump Test ASTM C1437	approximately 7.2	approximately 3.1 (with PP fibers)	Sealed and placed in an oven at 60 °C for 24 hr
Sun (2020)	Na alkali/slag	$CaCO_3$, CMS (sodium carboxymethyl starch)	Rheometer	approximately 13 MPa (0% CMS)	—	Not specified, likely room temp and ambient humidity

This is not an exhaustive list of relevant research. It should be noted that there is no standard for measuring slump of a 3D-printed wall section, which depends on layer height, wall thickness, and buildup rate. Therefore, caution should be exercised in comparing values across different literature works.

3D-printed components of any type have anisotropic mechanical properties that arise from the multiple interfaces that form as a result of 3D printing. Interface weakness is regarded to stem from deposition time between layers and will be explained in Section 1.5.4 below. Therefore, samples 3D printed in this study will be tested in a minimum of two different loading directions, following the methodology described in the previous papers mentioned above.

Different studies on 3D-printed cement had differing results on the relative flexure strengths of the varying axis. F*x*, in this case, is the direction normal to a cross section of layers, F*y* is the direction that compressed layers atop one another, and F*z* is the direction parallel to the printed layers. As summarized by Xiao et al. (2021), six out of seven researchers found F*z* to be the strongest loading direction with no clear

answer on F*y* versus F*x*. Five out of seven researchers found F*x* to be strongest in compression, and four out of those five found F*z* to be the second strongest. Xiao et al. (2021) reports that a reduction in compressive strength is due to interface shear failure and subsequent slip between the layers when the loading direction is normal to the interface. Therefore, F*x* shows the highest relative strength, because loading in the *x* direction is not normal to either deposition or translation interface, so slip type failure does not occur.

Successful 3D printing depends on a few variables, which will be described in Sections 1.5.3 and 1.5.4 below:

1. Mix design (fresh state properties)
2. Printer parameters

1.5.3 Mix design or fresh state properties

Compositions have been modified to achieve a balance of the desired characteristics, which have been identified below (Lim et al. 2012; Le et al. 2012).

1. Extrudability—the materials' ease of getting moved through the delivery system and out the nozzle
2. Workability—the ability of the material to retain its shape once extruded; a material's shear stress
3. Open time—the time where the material's extrudability and workability are within acceptable tolerances

Extrudability and workability (also called buildability [Le et al. 2012]) both vary with time, and their effects are inversely proportional. As the cementitious material starts to react and set, extrudability decreases and workability increases. Therefore, it is necessary to quantitatively measure these variables. Some researchers have used the slump cone test (ASTM C1437) to measure slump at different time intervals to measure workability and estimate a reasonable open time window (Alhozaimy 2009). This test is simple to carry out, but it does not give a scientific rheological parameter, so Le et al. (2012) and Austin et al. (1999) both used a shear vane apparatus to measure the shear stress of their respective mixes. Extrudability was qualitatively evaluated by Le et al. (2012) by printing a single filament 9 mm wide × 300 mm long and checking for tears. Le et al. (2012) found that a mixture having shear stress 0.55 kPa to

have both good extrudability and workability. Mixtures of lower and higher shear stresses, 0.3 and 0.9 kPa respectively, either deformed considerably after a few layers or experienced tears in the filament. Set time can be approximated with the workability tests and also with ASTM C191-19 and UWR (see Section 1.5.1). The methods used to evaluate workability in this study are rheometry and UWR.

Cement-based prints are more commonly studied in literature due to the low cost of the starting materials and reproducibility of mechanical properties. The materials commonly added to form a printable mix are fly ash, silica fume, superplasticizers (sodium carboxymethyl cellulose [CMC]), set accelerators (aluminum salt, diethanolamine), decelerators (formaldehyde, citric acid, etc.), and other additives (PVA) (Lim et al. 2012; Bong et al. 2019; Le et al. 2012; Gibbons et al. 2010). These additives are used to create desirable rheological properties of the print and to tailor the set time. Therefore, the additives used in this study will be inert materials: sand, fine silica sand, and gravel. Silica fume (crystallized, densified) will also be used as a noninert foaming agent for potential niche applications.

1.5.4 Printing parameters

Printing parameters refers to the user-dependent variables that can be varied before and during printing, such as nozzle diameter, nozzle thickness, printing speed, layer height, and buildup time.

All of these play a role in the amount of slump in the fresh GP as well as subsequent mechanical properties. Generally, fast buildup results in increased slump due to the bottom layer not having sufficient shear strength to bear the load. Slow buildup reduces slump but also reduces interlayer bond strength in both cement-based and alkali-material-based prints due to decreasing surface moisture (Sanjayan et al. 2018; Nerella et al. 2019; Panda et al. 2018). Panda et al. (2018) also found that interlayer bond strength increases with decreasing nozzle stand-off difference and decreasing nozzle speed (best results at 7 cm/sec). Nozzle stand-off refers to the distance between the nozzle and the printed layer beneath it. Roussel (2006) defined a relationship between structuration rate, A_{thix}, and shear stress, which is described in Equation (4):

$$\tau_0(t) = \tau_{0,0} + A_{thix}t\,, \tag{4}$$

where

$\tau_{0,0}$ = initial shear stress of the fresh state material (Pa), and
A_{thix} = setting rate (Pa/s).

In cement-based prints, shear stress increases linearly for up to 60 mins and then increases exponentially afterwards (Perrot et al. 2015; Lootens et al. 2009). Yuan et al. (2019) developed a more relevant equation:

$$t_{int} = \frac{k\rho gh - \tau_{0,0}}{A_{thix}}, \quad (5)$$

where

ρ = density,
g = gravitational constant,
h = single layer thickness,
K = dimensionless critical yield stress value in the range of 0.5–0.66 (Roussel and Coussot 2005), and
t_{int} = time interval between layers.

A_{thix} and t_{int} can be plotted as y versus x, and the resultant graph used to set a minimum t_{int} to avoid wall slump and buckling.

1.6 Extreme temperature resistance

One of the objectives of the project is to develop a composition that, once set and fully cured, is capable of resisting extreme heat and cold while maintaining its strength. GP composites are projected to withstand more extreme temperatures than concrete and are therefore ideal for construction in hostile environments.

1.6.1 Introduction and problem

GPs were first investigated by Davidovits in the 1970s as a potential fire proofing material after a series of fires in France (Davidovits 2015). Recently, extreme heat spells likely caused by climate change are spurring more fires (X. Wang et al. 2017; Kirchmeier-Young et al. 2019; Goss et al. 2020; Boer et al. 2020). Research done by a collaboration of scientists from Idaho State University and NASA analyzed documented wildfires in the western United States from 1950 to 2017 and found that wildfires are continuing to burn with increasing frequency and increasing size (Weber et al., n.d.). The discrepancy between mean and median as well as the large variation in the mean can be attributed to individual megafires. Eleven

western states were examined for that study. Other studies have linked this increase to anthropogenic climate change. As the air becomes warmer and drier, fuel flammability increases (Turco et al. 2017). Turco et al. (2017) modeled burn area changes in the Mediterranean area given global warming scenarios of 1.5°C, 2°C, and 3°C, while Barbero et al. (2015) looked at the increased potential for large fires in the United States. Both Barbero et al. (2015) and Turco et al. (2017) found that fire rates in fire prone areas will continue to follow the current trend and keep increasing based on climate modeling.

Wildfires cost billions of dollars in damages each year in the US and are projected to cause more damage and casualties as the population grows. Therefore, a relatively inexpensive and nontoxic coating or building material should be developed and implemented to protect critical infrastructure and commercial and private residences against further damage.

GPs are a promising high-temperature, relatively low-cost application of wildfire protection. There are a few values that have to be taken into consideration when developing a high-temperature mixture, including forest fire temperature profile, the phase change temperatures for geopolymer composites, aggregate stability, and resistance to cyclic extreme heat and thermal shock.

1.6.2 Forest fire characteristics

Santín et al. (2016) measured the temperature profiles of a Canadian, 1.7 ha pine forest fire at the forest floor and found temperatures to range from 550°C to 976°C, averaging at 745°C. The average heat duration was 176 seconds and ranged from 65 to 364 seconds. The fire intensity was recorded as approximately 8,000 kW m^{-1}. Ndalila et al. (2018) found that fire intensity varied due to variables such as relative humidity and slope and calculated a maximum fire intensity of 68,571 kW m^{-1} using Byram's fire-line intensity equation as an estimate.

Other nonacademic sources claimed fires that exceeded 10,000 kW m^{-1} and exceeded temperatures of 1,200°C. While the paper by Santín et al. (2016) seems to suggest the temperature duration is short, these temperatures are more than enough to damage or destroy critical communications and energy infrastructure, such as constructions using steel trusses. Alexis et al. (2010) used thermally sensitive paints to

determine the maximum temperature of an oak/scrub ecosystem ground fire and found the temperature to vary between 370°C and 760°C, averaging at 490°C.

1.6.3 Physical and chemical behavior of concrete at high temperatures

Normal OPC concrete loses 63% of its flexural strength and 47% of its compressive strength when heated to 800°C (Husem 2006). High-performance OPC with added superplasticizer performs better, but the strengths of both concretes decrease rapidly after 600°C (Husem 2006). Hager (2013) found a compressive strength reduction of 80% for concrete cooled from 600°C. This reduction is because hydrated Portland cement contains a significant amount of calcium hydroxide, which decomposes at 400°C–450°C into CaO. Wetting or exposure to moisture in postfire concrete results in higher levels of damage due to the rehydration of residual CaO and increase in accompanying volume as a result of hydration, which adds additional stresses (Akoz et al. 1995; Duxson et al. 2006). Hager explored the effect aggregates had on concrete and evaluated their thermal stability. Cracking in concrete occurs due to a mismatch in thermal strains of the aggregate and OPC. At lower temperatures, the OPC shrinks due to dehydration, and the aggregate expands. At higher temperatures, various aggregates change phases or undergo reactions: limestone and dolomite decompose around 700°C, quartz aggregates and sands undergo a β to α inversion, which is accompanied by a volumetric increase. Hager also conducted a color change analysis for concrete and noted that a cross section of the concrete surface with exposed aggregate turns red with increasing temperature up to 1,000°C and attributed this to siliceous riverbed aggregates containing iron (Hager 2013).

1.6.4 Physical behavior of GP at high temperatures

GP is purported to be stabler at higher temperatures than cement. GP stability at extreme temperatures depends on a large number of variables: the alkali cation (Na^+ versus K^+), ratios of cation to Al and Si, aluminosilicate source, aggregate type and size, and heating rate and duration (an external variable). Most GPs have similar microstructure evolution when heated to high temperatures. The first dehydration and shrinkage happen due to loss of free water between 100°C and 300°C. Between 300°C and 600°C, further deformation is caused by dihydroxylation and condensation of the OH groups in the GP (Duxson et al. 2006). Between 550°C and 900°C, more shrinkage occurs due to GP

densification and sintering (Rickard et al. 2010). Finally, the last amount of shrinkage occurs when the GP crystallizes, which is accompanied by a negative volume change. Potassium-based GP of the stoichiometry 1:1:4 K:Al:Si (the same as used throughout this study) transforms to crystalline leucite around 1,000°C, while sodium GP transforms to nepheline and a glass phase (He et al. 2020).

Lahoti et al. (2018) found the amount of shrinkage in fly-ash-activated GPs depended on alkali cation. The aluminosilicate source also plays a role in shrinkage. Kong et al. (2007) found that metakaolin-based GPs sustained more microstructure damage when heated to 800°C than fly ash GPs due to the increased amount of water needed in metakaolin GP to retain fresh state workability and the lower interconnectivity of the pores, which would create water vapor pressure buildup and cracking.

Multiple papers have focused on thermal properties of stoichiometries that vary away from the common 1:1:4:11 ratio. Changing the chemical makeup of GPs has an effect on the as-cured microstructure, which then affects the microstructure and mechanical properties of GPs at high temperatures. Rickard et. al (2010) found that a high (≥5) Si/Al ratio in fly ash showed increased compressive strengths in sodium-activated GPs heated to 1,000°C. However, these ratios gave relatively worse results in unfired specimens. Sodium-silicate-activated GP was found to be denser and had more GP gel but experienced swelling of the silicate rich phase at increased temperature, which stressed and cracked the microstructure. Because of this, sodium silicate performed better at RT and worse after heating to 1,000°C compared to sodium-aluminate-activated GP. Duxson et al. (2006) found that increasing the Si/Al ratio from 1.5 to 2.15 increased the amount of shrinkage that occurred in both sodium and potassium alkali, metakaolin-based GP.

Therefore, the microstructure, thermal shrinkage, and mechanical properties of GPs at high temperatures depend on the alkali activator source composition, the metakaolin source composition, and the type and amount of additive.

1.6.5 GP at high temperatures

Thermal shrinkage and cracking in GPs can be handled by adding a significant volume fraction (>50%) of inert mineral reinforcement. A few papers have focused on developing GPs for high-temperature applications.

Temuujin et al. (2010) tested the fireproofing ability of fly-ash-based sodium GP coating on mild steel plate and found a 1.5 mm thick coating exposed to a standard fire curve took 9 minutes to reach a 180°C difference on the unexposed side. Masi et al. (2015) found flexural properties to almost double from 600°C to 1,000°C for porous, fly ash GP reinforced with 1% volume basalt fiber. Keane et al. (2021) developed a self-healing KGP composite with basalt fiber and glass powder that "activated" the self-healing after 900°C, when the glass starts to flow and seal up the cracks caused by shrinkage. This resulted in an increase in flexure after 900°C.

1.7 Mechanical properties of ordinary Portland cement (OPC) composites versus GP composites

Ordinary Portland cement is one of the cheapest and most commonly used building materials (Garside 2021). In 2010, 3.3 billion metric tons of OPC were produced globally, which has increased to over 4 billion every year since 2014. In the past decade, the United States' production has grown from 67 million metric tons to 90 million (Lehne and Preston 2018). OPC composites in the form of mortar and concrete create structures such as sidewalks, foundations, floors, and columns, and the desired strengths for each application has been varied and optimized over time (Bentz et al. 2017; Vu et al. 2020). GP composites have been regarded highly in the literature due to high mechanical properties, namely compressive and flexural strength, and the relatively low-emission production of metakaolin is desirable in using GP composites as an alternative to concrete (Ramujee and PothaRaju 2017). However, there is a scarcity of studies comparing GP composites directly to concrete with similar compositions.

Compressive strength is defined as the maximum compressive stress that a solid material can undergo without fracture under gradually applied load. The equation for compressive strength is given by $\sigma = F/A$, where F is load and A is the sample's area.

Flexural strength is also known as the modulus of rupture and is similar to compressive strength, where it is the maximum stress that a solid material can undergo without fracture under gradually applied load. The load is applied in a three-point flexural strength test and results in the equation $\sigma = 3/2\ FL/bd^2$, where F is load, L is the length of the specimen, b is the width at the fracture, and d is the depth of the specimen at the fracture.

The compressive and flexural strength of concrete depends on the water and cement ratio, degree of compaction, cement and aggregate ratio, and the shape, size, and strength of the aggregate. A high water and cement ratio is detrimental to the strength of the concrete because too much water leads to a saturated mixture and the reaction within the concrete will be inhibited (Ramujee and PothaRaju 2017). Despite this, enough water must be mixed in the concrete to make it workable. A low cement and aggregate ratio, such as a mixture with too much sand, also lowers the mechanical strength of concrete and results in a grainy texture that will be unable to bind together. The shape, size, and strength of the aggregates used are important, especially when making concrete with sand and coarse aggregates such as gravel (Bentz et al. 2017; Vu et al. 2020; Abdullahi 2012; The Engineering ToolBox 2009).

The compressive and flexural strength of GP composites depends on the GP and aggregate ratio and shape, size, and strength of the aggregate. It has been shown that the addition of fillers has an appreciable effect on GP composite mechanical strength, but too much filler decreases the workability. The amount of water is fixed in the GP reaction, or else the stoichiometry of the product will not be correct. However, care must be taken when curing and drying GP composites because GPs are susceptible to cracking from drying, which causes a decrease in mechanical strength (Ramujee and PothaRaju 2017; Carpinteri et al. 1997; Wright and Garwood 1952; Korniejenko et al. 2016; Center for Geopolymer Research and Applications, n.d.).

This project will compare basic OPC and GP composites as well as OPC paste and GP paste. Four types of OPC and GP composites will be made with the following additives: fine sand, coarse sand, and 3/16 in. (4.75 mm) gravel.

1.8 Freeze-thaw (FT) of GPs and concrete

Freeze thaw has the biggest effect on concrete deterioration in cold climate regions (Tanesi and Meininger 2007). The causes of freeze thawing on concrete as well as GP will be investigated.

Concrete is generally poor in freeze-thaw resistance because of its open pore structure, which allows water to ingress in and then expand when frozen, placing the material under stress and promoting crack nucleation

and growth. Concrete damage can be characterized by long cracks in the bulk of the structure or as spalling on the surface.

Freeze-thaw damage of rock and cementitious material occurs when water is absorbed into the material and expands when frozen, stressing the microstructure and initiating microcracks. Repeating the freezing cycle causes crack growth and spalling damage.

In concrete, air voids occur as gel pores (0.5–2.5 nm), capillary pores (10–50 nm), entrained air (0.01–1 mm), and entrapped air, which is larger, nonhomogenous, and occurs from mixing. Water in capillary pores cannot freeze above -78°C due to the small size (Powers and Helmuth 1953).

Damage to concrete can be explained by a few theories. The critical saturation theory by T. C. Powers stated damage only occurs when the capillaries in cement exceed more than 91.7% volume of water, due to water's expansion of about 9% (Powers 1954). Powers also proposed a damage mechanism caused by frozen water pushing unfrozen water through capillaries, creating a hydraulic pressure buildup inside the capillaries (Powers 1954). Powers and Helmuth proposed a third theory to explain inconsistencies between the second theory and experimental results. Here, water flows to the capillaries from the gel pores because the melting temperature of water in the larger capillaries is higher than -78°C and more thermodynamically favorable. This flow of water exacts pressure on the capillaries. The formation of ice in the capillaries leaves behind a more concentrated solution of various ions, which pulls more water in via osmosis and further increases the pressure (Powers and Helmuth 1953).

The purpose of air entrainment is to incorporate well-distributed, tiny bubbles in the fresh mixture that act as capillary pressure relief sites. Entrainment is accomplished with the use of ionic and anionic surfactant additives (Tanesi and Meininger 2007).

GPs also contain nanometer scale pores and capillaries and are also vulnerable to freeze-thaw damage (Kriven 2018). In this study, damage to GP specimens will be measured by nondestructive modal testing according to ASTM C666. Microcracks reduce and dampen the vibrational frequency, which is then used to calculate the relative dynamic modulus (RDM), which is expressed as a percentage. The formula for this is

$$RDM = \frac{n_{c^2}}{n^2} \times 100, \quad (6)$$

where

n_c = the resonant frequency after c cycles, and
n = the original resonant frequency.

Numerous work has recently been conducted on the freeze-thaw resistance of GP composites.

Zhao et al. (2019) focused on how curing conditions changed physical and chemical parameters in a red mud slurry, fly-ash-based, sodium-activated paste after up to 50 freeze-thaw cycles (ASTM C666), finding that samples cured at RT were more brittle and lost weight after freeze-thaw conditioning, whereas samples cured at 50°C–80°C increased in mass and were more ductile.

Aygormez et al. (2020) performed freeze-thaw tests on metakaolin-based, sodium-alkali-activated GP composites reinforced with polypropylene fibers, silica fume and colemanite waste material as well as other tests. No significant reduction was found between flexure, compression, and ultrasonic pulse testing between the control samples and the 56-cycle samples across all compositions. A slight decrease in values was found to occur for all compositions at 300 cycles of freeze thaw. The addition of polypropylene fibers raised the flexure strength of the composite slightly.

Mermerdaş et al. (2021) tested fly-ash-based GPCs made with basalt, glass, and steel fibers and found the flexure strengths to decrease slightly from 0 to 300 cycles across all the compositions.

Azarsa and Gupta (2020) tested freeze-thaw characteristics of potassium-based ash composites with fly ash and bottom ash as the silicate source and found that bottom ash samples performed much better compared to fly ash. These samples lost less mass (0.7%–4%) and had a much better relative dynamic modulus (80%–45%) at 300 cycles.

Yan et. al (2020) tested the freeze-thaw resistance of sodium alkali, metakaolin-based GP pastes with different ratios of Si/Al and Na/Al. These ratios were found to influence the capillary and gel pore parameters in the GP paste, which determined freeze-thaw resistance results. Increasing the ratios of both was generally found to shift the pore size

distribution and create larger pores while simultaneously reducing the total pore volume. A Na/Al ratio of 1.26 was found to have the lowest pore volume, the best compressive strength, and the best FT resistance. GP with larger pore channels and fewer pores produced better freeze-thaw resistance because hydraulic pressure relaxation is inversely proportional to the water permeability through the capillary pores. Larger capillary pores had increased water permeability and reduced the amount of time it took for the pressure to fall to the same value compared to a thin pore system, which alleviated the pressure on the pore walls and slowed crack nucleation and growth (Yan et al. 2020).

1.9 Objectives

The objectives are to

1. Develop a potassium alkali, metakaolin-based GP composition for 4D printing that has both good workability and extrudability using UWR and rheology,
2. Test the effect different static curing environments and different compositions of sand/silica powder/gravel have on final mechanical properties,
3. Evaluate the effect extreme hot and cold temperatures have on Na- and K-based GPCs, and
4. Give a direct comparison of OPC cement, mortar, and concrete with appropriate GP paste and composites.

1.10 Approach

The approach to this project is to build a systematic understanding where possible. This includes the characterization of all aggregates and fillers, OPC, and geopolymer precursors; the role of water in geopolymer synthesis; and the effects of time on the rheology of geopolymers. With the results of each experiment, formulations can be predicted and prepared for printing. Overall, the goal of this approach is to create small-scale and large-scale structures.

2 Results and Discussion

2.1 Methods and materials

2.1.1 GP synthesis and materials sources

GP was synthesized with water glass made from amorphous silica fume (Cabot), Potassium hydroxide 87% (Fisher Scientific), and deionized (DI) water. The metakaolin used was Metamax HRM . The aluminosilicate source and alkali activator were mixed with an IKA 200 high-shear impeller at 2,000 rpm for 10 minutes. The GP was then mixed with the aggregate of choice by hand, then vibrated for 1 minute to degas. Other water glasses were made from Metsobead-2048 and KASOLV-16, a sodium and potassium silicate respectively (PQ corp). These two products will be used for the bulk of the project. The final molar ratios of water glasses used will be held constant for the experiment and are 1 K_2O:1 Al_2O_3:4 SiO_2:11 H_2O and 1 Na_2O:1 Al_2O_3:4 SiO_2:13 H_2O. All materials are summarized in Table 3 below.

Table 3. Materials used for testing.

Product	Source	Abbreviation
Quikrete Medium Sand	Lowes	Q
Fine Sand	Prairie Material (Champaign, IL)	FS
Coarse Sand	Prairie Material (Champaign, IL)	CS
Gravel	Prairie Material (Champaign, IL)	Gravel
Silica Fume (grey, densified, crystalline)	US Silica Company	SF
Fumed Silica (white, amorphous)	Cabot Corp	-
Potassium Hydroxide	Acros Organics approximately 85%	KOH
	Duda Diesel 90%	
Basalt Fibers ½ in. long, 16 µm diameter	Imerys	BF
Glass Powder	Recycling Waste, Uroboros Co.	G
Wollastonite Tailings	Imerys	W

2.1.2 Fine aggregate characterization.

All reinforcements in Figure 2 below except for coarse sand (CS) and wollastonite tailings (W) were determined using a Horiba laser particle size analyzer model: LA-950V2. The coarse sand and wollastonite were too large for the particle analyzer and were characterized using a set of ASTM sieves. The coarse sand size average was 490 µm, and the fine sand was

850 µm, which seems counterintuitive; however, the coarse sand was termed coarse because it contained a significant portion of larger, 1–4 mm sized sand particles and had a nonnormal size distribution, while the "fine" sand had a very narrow distribution of sub-mm sized grains. These designations given by the manufacturer "fine" and "coarse" are nonstandard. These materials were dried and used as delivered by the ton from the supplier.

Figure 2. Gradation curve for various particulate reinforcements.

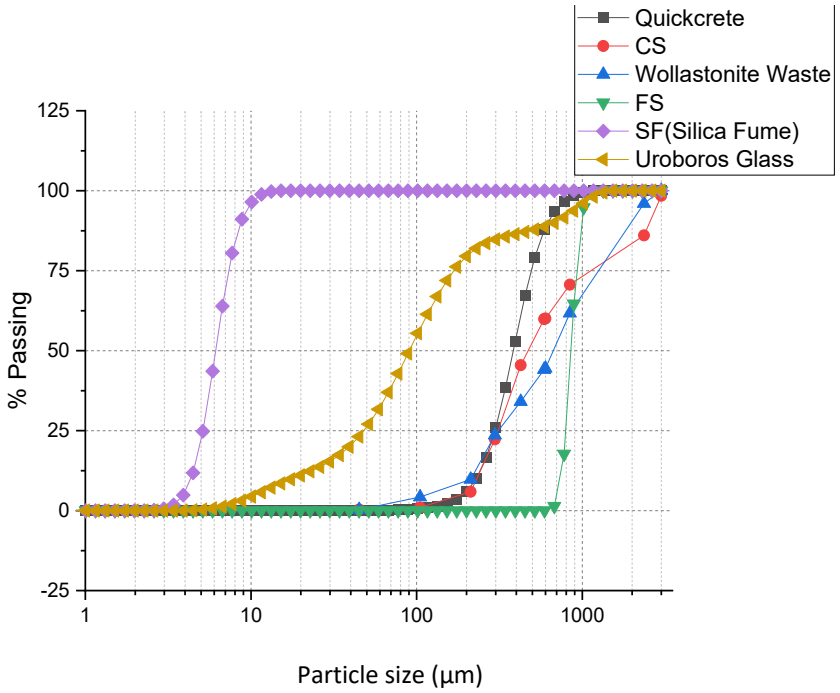

The wollastonite could be characterized as calcium metasilicate needles, and the other minerals as sand-like particulates.

Figure 3. Pictures of aggregate used in Sections 2.2 and 2.3: (*1*) Cs, (*2*) gravel, (*3*) q, (*4*) fs, (*5*) wollastonite, (*6*) uroboros glass powder, and (*7*) basalt fiber.

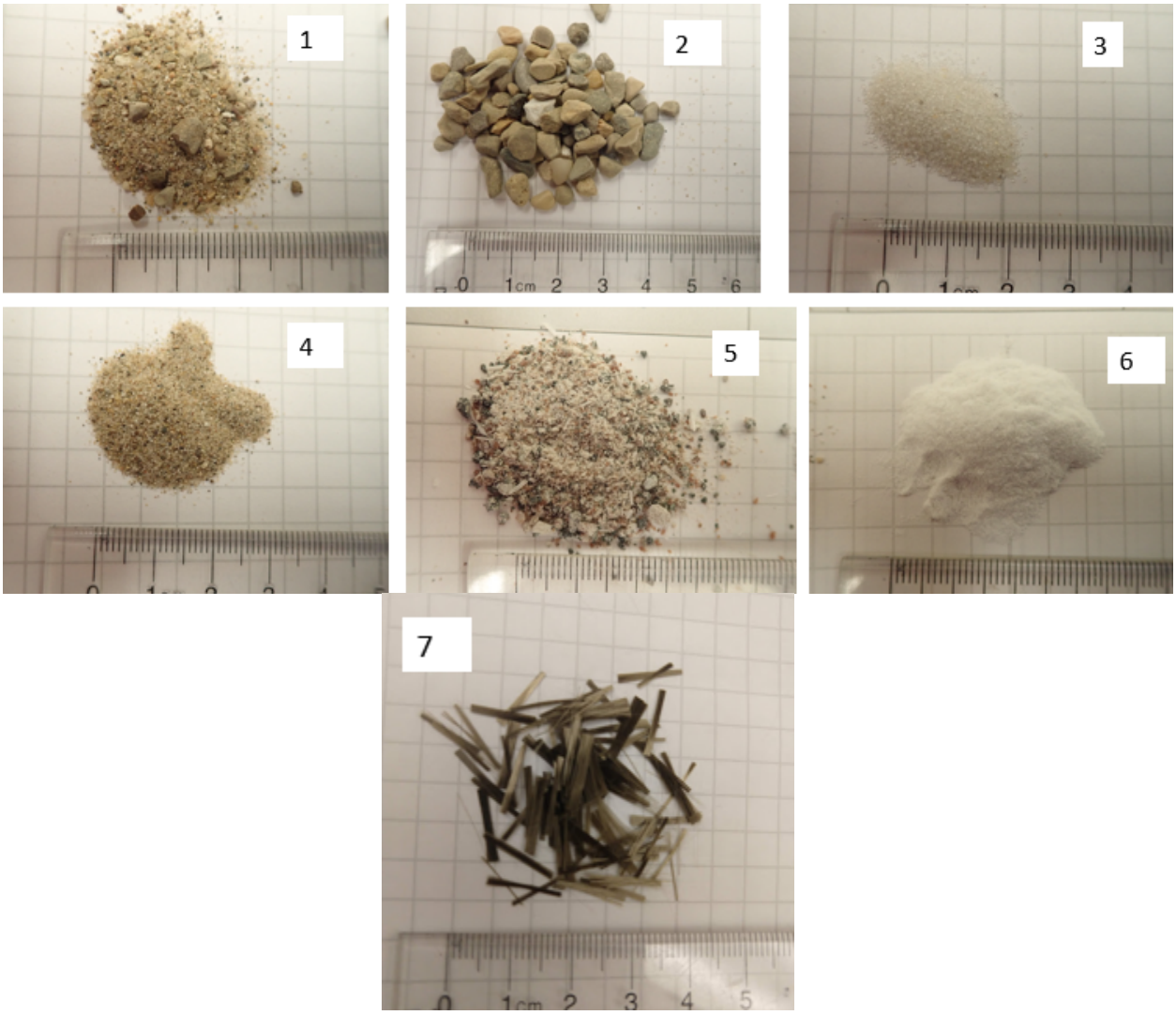

2.1.3 Metakaolin properties

Table 4 below shows compositions of the various metakaolins used in this project study. Metamax will be used for the majority of the mechanical testing.

Table 4. X-ray florescence spectroscopy (XFS) of various commercial metakaolins (Sankar, Sutrisno, et al. 2018).

Oxide	Argical M1200S Metakaolin	Metastar 501 HP	Metastar 501	Powerpozz Metakaolin	BASF Metamax Metakaolin
	Result wt (%)	Result wt (%)	Result wt (%)	Result wt (%)	Result wt (%)
Al_2O_3	43.03	47.22	46.98	43.67	46.52
SiO_2	53.42	51.24	51.29	53.49	50.15
SO_3	0.07	0.04	0.03	0.06	0.05
K_2O	0.74	0.14	0.11	0.19	0.12
TiO_2	1.33	0.57	0.76	0.98	1.24
Cr_2O_3	0.02	0.02	0.02	0.02	0.00
MnO	0.01	0.01	0.00	0.00	0.00
Fe_2O_3	1.33	0.38	0.40	1.24	0.32
CuO	0.01	0.01	0.01	0.01	0.00
ZnO	0.01	0.00	0.00	0.01	0.00
Ga_2O_3	0.01	0.01	0.01	0.01	0.00
SrO	0.00	0.00	0.00	0.01	0.01
ZrO_2	0.03	0.01	0.01	0.02	0.00
P_2O_5	0.00	0.02	0.02	0.14	0.00
CaO	0.00	0.02	0.01	0.03	0.00
V_2O_5	0.00	0.09	0.11	0.15	0.00
MgO	—	0.24	0.24	—	—

Particle size analysis was conducted on each metakaolin using the Horiba Partica particle size analyzer. The results are tabulated in Table 5 along with aluminum atomic percent data from Sankar, Sutrisno, et al. (2018). A visual of the distribution of particle diameters is shown in Figure 4. All aluminum values are from Sankar, Sutrisno, et al. (2018).

Table 5. Additional characteristics of the relevant types of metakaolin.

Metakaolin	Mean particle size (μm) [SD]	Amount Al (IV) (at %)	Amount Al (V) (at %)	Amount Al (VI) (at %)
Metamax HRM	4.669 [+/- 2.9]	36	52	12
Metamax EF	2.695 [+/- 1.9]	-	-	52
Powerpozz	12.528 [+/- 12.1]	24	71	5
Argical 1,200S	6.785 [+/- 3.2]	33	40	26
Metastar 501 HP	3.576 [+/- 1.5]	32	58	9

Figure 4. Particle diameter distribution of the various types of metakaolin.

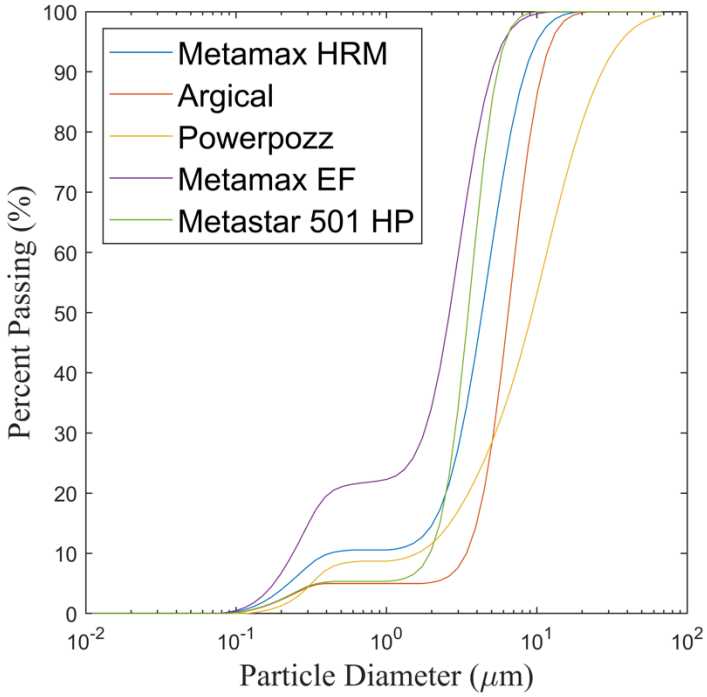

2.1.4 Water glass composition

The chemical makeup of the commercially produced potassium silicate source, KASOLV 16, is shown in Table 6.

Table 6. Chemical makeup of KASOLV 16 and other potassium silicates.

PQ Product Name	Wt Ratio SiO_2:K_2O ±0.01	Wt % K_2O ±0.8	Wt % SiO_2 ±0.9	Wt % H_2O ±3.0	Density		Particle Size, Tyler
					lb/ft^3	g/cm^3	
KASIL® 2.5 Flake Glass	2.50	28.4	71.0	0	77	1.24	1" x 1/6" plates
KASOLV® 16	1.60	32.5	52.8	14.5	43	-	99% thru 40 mesh
KASIL® SS Pwd	2.50	28.4	71.0	0	51	-	48% thru 200 mesh

The chemical composition of Metsobead 2048 is given as 100% 1 Na_2O:1 SiO_2, anhydrous sodium metasilicate. PQD, the silica provided by PQ Corp, was calculated to have a molar composition of 1 Na_2O:1 SiO_2:12 H_2O.

2.2 Water retention and mechanical properties

2.2.1 Measuring water loss

Since water is not chemically bound to the GP structure, it will start to evaporate once the GP paste or mortar is exposed to air. The overall

specimen will continue to lose water until it equilibrates with the outside environment. As stated above, water should be retained as long as possible to produce a GP of high quality. This section will focus on-quantifying water loss and finding a solution for retarding it.

There are two methods that can be used for evaluating the efficacy of a coating or bulk GP composite at retaining water: plotting mass loss of the GP component of the composite as a function of time and rating retention efficacy using the slope, and calculating % mass loss after a given period of time or until no further mass loss occurs according to Equation 1 above.

The first method is only accurate when the samples have the same geometry and a similar amount of pure GP in each sample. Water loss in thinner specimens (5 mm) is also more logarithmic with time, whereas thicker specimens experience a more linear mass loss. Water loss is also dependent on geometry, so two geometry factors were identified for a few sample sizes.

$$\% \text{ Exposed surface area} = SA_1/SA_{tot}, \tag{7}$$

where

SA_1 = area exposed to air, and

SA_{tot} = total surface area (some part of the area is touching the ground).

$$SA/V \text{ ratio} = SA_1/\text{part volume} \tag{8}$$

It can be seen in Table 7 that a free standing 4D-printed wall would be most affected by whatever effect ambient drying has on the surface. The puck geometry was used to evaluate different coatings.

Table 7. Geometrical calculations for various structures and samples.

Geometry	% Exposed surface area	Exposed SA/V ratio
30 × 7.5 × 0.3 ft free standing wall	98%	6.21
Blue weigh boat (approximately 3 in.) molded pucks	approximately 50%	2.22
3 in. PVC pucks	40%	2
1 × 1 × 10 cm flexure samples (in mold with one face exposed)	24%	1

There are a few methods which can be employed to slow down water evaporation which are listed below:

A. A non-KGP-based coating, such as saran wrap or polyurethane foam
B. Fast-setting MK KGP coating
C. High wt% particulate reinforcement in the bulk GPC
D. A fast-setting MK in the bulk GPC
E. Combinations C+B and C+A

Powder coatings such as fine sand and talc powder were picked because of the ease of application but were found not to be effective at slowing water loss in pure GP. Plastic wrap provided the best protection against evaporation, but using it would prove difficult for several reasons. The plastic must adhere well to the GP and form a “seal” for it to be effective, and adhesion decreases with increasing particulate reinforcement. For example, compositions above 60 wt% sand do not stick to nitrile gloves and can be easily molded into different shapes. This method also generates plastic waste as the wrap would be impractical to reuse. Other promising coatings not attempted are Vaseline, paraffin wax, and a commercial oil-based paint. Another option would be to use a blow-up tent around the structure to be built where the climate can be controlled, but this is not feasible for larger structures. Other possible solutions are using a rapid-setting metakaolin in the bulk of the print or to use metakaolin in the coating.

2.2.2 Methods and flexure properties of 1 × 1 × 10 cm (0.4 x 0.4 x 3.9 in.) samples

Several specimens were made using different water glasses and compositions and cured in the traditional method for the sake of comparison: 24 hr at RT, 95% RH followed by 24 hr at 50°C, 95% RH. The samples were then demolded and kept in a sealed plastic bag for 2–3 days, then laid out on a shelf at ambient lab conditions (21°C) to dry for another 4–5 days, then tested on an Instron with a 2 kN load cell and a rate of 0.01 mm/min. The samples made with the traditional method were labeled "Control." This curing regime was employed because it produces high early age strength.

All the composite samples were made by casting the GPC into molds with one face (area = 10 cm) exposed to air, then placed in the fridge for the given time duration. This was done to test the effect of temperature and of having one face open to ambient air. These specimens are summarized below in Table 8. The sand used for these tests was Quikrete Medium Sand (Q). "Traditional" water glass was made from potassium hydroxide, silica fume, and water. "KASOLV"-based potassium alkali water glass was made from KASOLV 16 (PQ corp) and adjusted with potassium hydroxide (Duda diesel 95%) to give the same K/Si ratio as the traditional water glass. KASOLV 16 was picked because it eliminates the use of silica fume, which is difficult to work with due to its low density and ability to easily disperse in air.

The fridge samples were kept in a commercial fridge that had a constant temperature of 10±1°C and 22%±5 RH. A freezer was also used that had a temperature of approximately -1°C. Table 8 shows the flexural strengths achieved by each composition and curing conditions.

Table 8. Three point bending tests for several compositions cast and cured for 24 hr at 21°C/95% RH and 24 hr 50°C/95% RH (in *grey*). The strengths are listed as follows: strength [95% two-sided confidence interval (CI)].

ID:	Composition	Water glass type	# of specimens	Flexure strength MPa [95% CI]
Q55.KASOLV.Control	55% sand rem. GP	KASOLV	9	8.07[0.48]
Q0.KASOLV.Control	100% GP	KASOLV	8	9.93[3.02]
Q55.Trad.Control	55% sand/rem GP	Traditional	10	7.59[0.26]
SF15.Control	15% silica fume	KASOLV	6	17.20[1.58]
Q0.Beads.Control	100% GP	Metsobeads	7	13.79 [1.81]
Q55.PQD.Control	55% sand/rem GP	PQD	12	10.08[0.66]
Q55.KASOLV.9d.Fridge	55% sand/rem GP	KASOLV	6	2.15[0.39]
Q55.KASOLV.15d.Fridge	55% sand/rem GP	KASOLV	7	9.21[0.95]
Q55.KASOLV.28d.Fridge	55% sand/rem GP	KASOLV	6	17.0[1.02]

Table 9. Four-point flexure tests with a load span of 2 cm and a support span of 6 cm. Remaining % composition is GP. All bars had nominal dimensions of 1 × 1 × 10 cm. The above tests were repeated for four-point testing, which gave markedly lower, albeit more accurate, results.

ID:	Composition	Water glass type	# of samples	Flexure strength (MPa) [CI]
Q0.KASOLV.Control	100% GP	KASOLV	7	10.43[2.74]
Q55.Trad.Control	55% sand	Traditional	9	5.32[0.39]
SF15.Control	15% silica	KASOLV	8	6.24[0.62]
Q55.Beads.Control	55% sand/rem GP	Metsobeads	8	8.46[0.40]
Q0.PQD.Control	55% sand/rem GP	PQD	7	8.87[1.74]
SF15.Control.1	15% calcined silica	KASOLV	-	-
Q43.S15.Control (1:1:0.35)	42.5% sand, 15% silica	KASOLV	9	11.35[1.14]
Q55.KASOLV.9d.Fridge	55% sand/rem GP	KASOLV	3	0.62[0.054]
Q55.KASOLV.15d.Fridge	55% sand/rem GP	KASOLV	9	5.27[0.64]
Q55.KASOLV.30d.Fridge	55% sand/rem GP	KASOLV	8	8.32[1.38]
Q55.KASOLV.22d.Freezer/15d.Fridge	55% sand/rem GP	KASOLV	10	6.78[0.36]

The results from Table 9 are summarized in Figure 5 below.

Figure 5. Four-point flexure results on 1 × 1 × 10 cm bars.

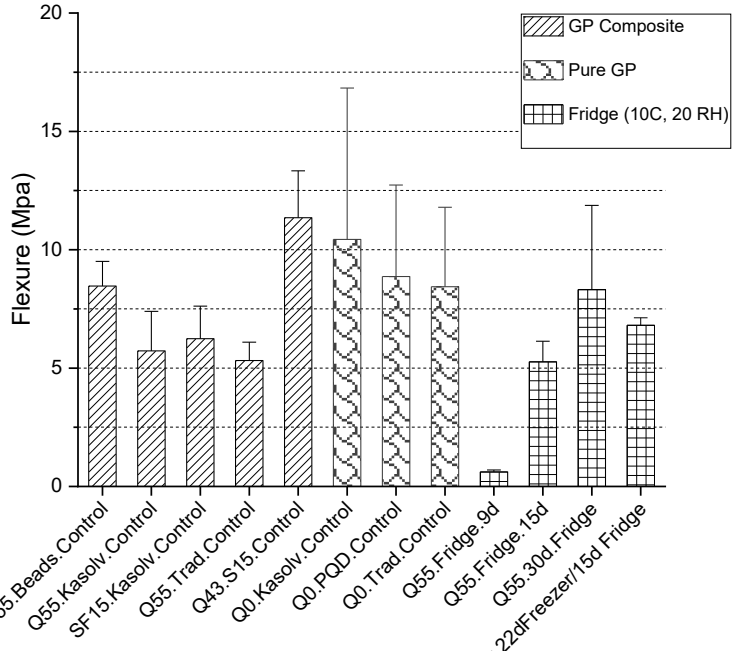

KASOLV-based water glass yielded the strongest pure GP. There was no statistical significance (p = 0.743, α = 0.05) when comparing K-based water glass made traditionally and PQD (Q0.PQD.Control).

Generally, the composites had lower strengths than the pure samples, likely due to surface effects stemming from the specimen preparation method. The composite specimens were cast with one of the rectangular faces exposed to air since the mix was too thick to pour through one of the ends. The surface exposed to air was relatively uneven and could have functioned as a crack nucleation point, thus lowering the strength. The surface effect was pronounced for the 10°C fridge and freezer samples due to the formation of large voids at the edges. Despite this, the 15 d and 30 d samples performed similar or better than the control samples. The flexure strength of the freezer (-20°C) samples indicate that fresh, K-based GP mixes are stable at temperatures below freezing but need exposure to an above zero temperature to fully cure. It can be inferred that some curing occurs at -20°C because the 22 d freezer/15 d fridge sample is significantly stronger than the 15 d fridge sample. However, larger 1 × 1× 6 in. samples cured at the same temperature and higher humidity show very little curing at 10°C and likely no curing at lower temperatures. Curing speeds for a variety of low temperatures and the identification of a critical temperature

beyond which no curing occurs can be the subject of a future study if this printing technology is to be deployed in cold conditions. The incorporation of reinforcement reduces the variation in flexure strength when comparing the “pure GP” group to the “GP composite” group, which allows for more predictable properties.

Note the lesions at the edges in Figure 6. The cause for this is unclear. These did not occur with the larger 1 × 1 × 6 in. (2.54 × 2.54 × 15.24 cm) fridge specimens and is predicted to not be an issue in a free-standing printed wall due to no interface.

Figure 6. Image of the freezer/fridge samples (*left*) and the three-point 9 d fridge sample (*right*).

The silica fume samples, shown in Figure 7, had puffed up, likely due to the silicon impurity reacting with the alkali hydroxide to produce hydrogen gas, which acts as a foaming agent. When these samples were demolded, they were warped slightly but were still able to be tested. GP samples made with 15 wt% silica fume that was calcined at 900°C for 10 hours warped significantly after demolding and were not able to be tested.

Figure 7. Black 1×1×10 cm bars (silica fume) and white bars (calcined silica fume).

2.2.3 Methods and flexure properties of 1 × 1 × 6 in. (2.54 × 2.54 × 15.24 cm) samples

Next, 1 × 1 × 6 in. (2.54 × 2.54 × 15.24 cm) specimens were prepared in molds with one face uncovered and placed into a Test Equity model 1007H humidity chamber. One face was left uncovered to see what effect temperature and humidity have on the GP in a given constant environment. Ideally, it would be best to demold the samples as soon as possible so that the effect ambient conditions have on mechanical properties can be better ascertained since more of the sample would be exposed to the ambient conditions. Removing samples too early would lead to warping and inconsistent mechanical properties, so all samples were instead demolded after 7 days. Six samples were broken for each test. The tests were done on an Instron with a 50 kN load cell and a load rate of 0.01 mm/min (Figure 8). The load span was 1 in. (2.54 cm) apart, while the support span was 3 in. (7.72 mm) apart. Table 10 shows the strength data for the various compositions.

Figure 8. Various 7-day-old flexure bars and pucks for water retention being cured in the humidity chamber (*left*). Flexure testing setup with a SG50 RH sample after failure (*right*).

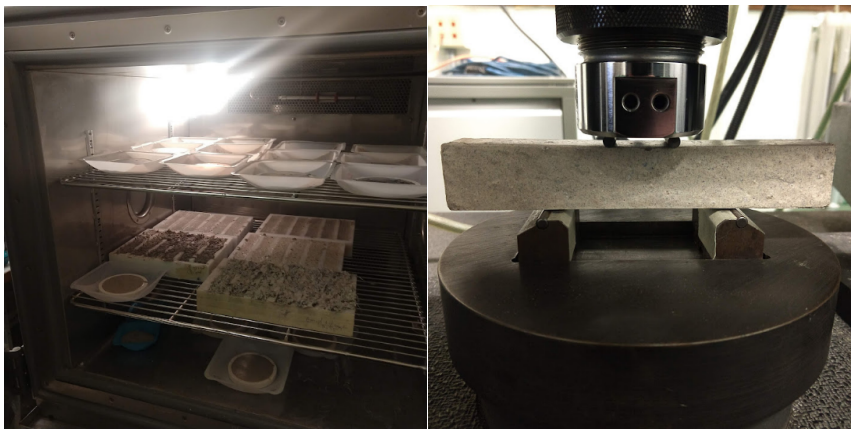

Table 10. Seven-day flexure strength data for 1 × 1 × 6 in. specimens of various compositions cured at 21°C and 50% RH.

	Composition (parts, by weight)						
Sample ID	FS	CS	Other	GP	Gravel (<3/16 in.)	Flexure (MPa)	% Mass Retention GP (50% RH)
SG50	1	1	—	2	2	4.78	93.0
SG60	1.5	1.5	—	2	5	5.67	94.1
SG60G	1.5	1.5	—	2	3	5.97	—
SG66	1	1	—	1	1.85	5.83	—
SG50.Na	1	1	—	2	2	5.08	95.7
SG50SF2	1	1	0.6*	2	2.3	4.53	95.7
SG50SF1	1	1	0.34	2	2	2.98	—
CS50	-	1	—	1	—	3.69	93.2
FS50	1	—	—	1	—	4.30	93.9
SF25	—	—	0.25*	0.75	—	1.50	95
SF15	—	—	0.15*	0.85		1.20	94.1
S40	0.2	0.2	—	0.6	—	3.16	92.3
S50	.225	.225	—	0.5	—	4.44	93.4
S60	0.3	0.3	—	0.4	—	5.65	91.3
S70	0.35	0.35	—	0.3	—	6.22	93.1
S30G7.5	0.5	0.5	0.233†	2.1	1.66	3.63	96.4
W60	—	—	3‡	2	2.5	7.14	94.6
W30S30	0.75	0.75	1.5‡	2	—	6.17	94.5
SG50BF	1	1	0.14§	2	2	8.11	95.1
SG9G37	0.087	0.087	0.7**	1	0.875	6.05	94.2
G25BF	—	—	0.05§ 0.34**	1	1	7.66	92.2

* Silica Fume (SF)

† Waste Glass Powder (coarse glass, mean size = 636 µm, SD = 507 µm)

‡ Wollastonite Waste Tailings (W)(Imerys)

§ Chopped Basalt Fiber 1/2 in. (1.77 cm) long, 16 µm diameter)

** Ouroboros Glass Powder (mean size = 198 µm, SD = 289.6 µm)

It should be noted that the standard deviations for the samples in Table 9 varied from 0.19 to 0.77, creating predictable mechanical strengths. Adding sand continuously increases the strength up to 70 wt%, the maximum amount that could be added. The addition of gravel added no significant difference in mechanical strength (S50 versus SG50) $\alpha = 0.05$, $p = 0.132$). Any reinforcement added in a significant volume amount greatly improves mechanical properties by mitigating drying shrinkage and providing a mechanism for crack deflection under load; pure potassium GP cured for 9 days at RT/95% RH and then slowly dried produced a strength of only 1.25±0.7 MPa. This is almost 10 times lower than the strength of the 1 × 1 × 10 cm GP composition because of Weibull effects. Larger ceramics have a greater amount of critical flaws simply due to their size and a lower survivability because of this. Fine sand composites were found to be stronger than coarse sand composites, likely because fine sand acts as a pore breaker and reduces pore size. This effect is immediately obvious in the SG50SF2 sample, where the addition of sand reduces the pore size considerably; pores that form after mixing likely get broken up into smaller, irregularly shaped pores by getting pushed through the grains of sand. The wollastonite waste is a stronger reinforcement than sand and gives a 20% greater (approximately 1.5 MPa more) flexure strength (comparing S60 to W60). The composites involving basalt fiber were expected to be higher according to basalt fiber GP composites tested by Kriven (2021). Basalt fiber length, weight % added, manufacturing technique, and surface coating have significant effects on mechanical properties of the composites. Because of the sand and gravel already mixed in, thoroughly mixing in additional fibers where the fibers separate from one another is difficult and is likely responsible for the lower strength here and variation in research values (Keane et al. 2021). Keane et al. (2021) also used superplasticizer which allowed more basalt fibers to be added and a better fiber dispersion achieved. Table 11, Table 12, and Table 13 show the flexure strength test results for curing temperatures of 21°C, 10°C, and 40°C, respectively.

Table 11. Flexure when cured at 21°C (versus time).*

	Composition					1 d	3 d			7 d			28 d		
ID	FS	CS	SF	GP	Gravel	50% RH	22% RH	50% RH	80% RH	22% RH	50% RH	80% RH	22% RH	50% RH	80% RH
SG50.Na	1	1	-	2	2	-	1.51	1.49	1.12	6.67	5.08	5.73	4.83	5.41	5.59
SG50	1	1	-	2	2	-	1.70	1.47	2.0	6.63	4.6	5.10	4.25	3.96	4.93
SG50SF1	1	1	0.34	2	2.17	0.82	NT	1.82	NT	NT	3.18	NT	NT	10.68	NT

*NT means not tested. Dash "-" means could not be tested.

Table 12. Flexure when cured at 10°C (versus time).

					Flexure Strength (MPa)	
	Composition				28 d	35 d
ID	FS	CS	GP	Gravel	80% RH	28 d, 10°C + 7 d, 20°C, 50% RH
SG50.Na	1	1	2	2	0.24	2.04
SG50	1	1	2	2	1.20	5.66

Neither 10°C sample had solidified enough at 7 d to be able to test. At 11 days, the SG50 sample was hard enough where it could not be penetrated with a steel pick. The SG50.Na sample was still pliable at this point and could be dented easily. The SG50 sample was demolded at 11 days, and the SG50.Na samples were demolded after 21 days and deformed significantly during the demolding process due to their still being plastic.

The strengths of samples at 10°C and 28 d were low for both sodium and potassium GP due to the lack of full curing (Table 12). This is exemplified by the relatively large strain values at failure of 0.099 and 0.05 mm/mm for SG50 and SG50.Na GPs, respectively. The 7 d/50% RH specimens had strains at failure that averaged around 0.002 mm/mm as a comparison. Some samples were not tested at 28 d but were instead transferred to a climate oven and kept at 20°C/50% RH for seven more days and then tested immediately after. This produced markedly stronger GP (compared to 20°C, 50% RH, 28 d strength) for the potassium GP. This falls in line with the 1 × 1 × 10 cm fridge tests, which showed higher quality GP is produced through low temperature, slow curing. The disadvantage to a strong final age GP is the long set and cure time, which rules out applications in cold regions where high early age strength is needed for projects such as additive manufacturing, roads, and others that are time sensitive. There are other ways of decreasing the set time, such as reducing the silica content in the water glass and experimenting with other types of

metakaolin. The sodium GP was weaker than expected at 35 d due to large surface defects caused during demolding.

Table 13. Flexure when cured at 40°C (versus time versus humidity).

					Flexure Strength (MPa)							
	Composition				1 d		3 d		7 d		28 d	
ID	FS	CS	GP	Gravel	20% RH	80% RH	20% RH	80% RH	20% RH	80% RH	20% RH	80% RH
SG50.Na	1	1	2	2	5.39	0.31	5.81	1.63	5.38	3.31	4.65	6.51
SG50	1	1	2	2	4.78	1.26	6.86	2.97	5.17	4.08	5.28	6.27

Relative humidity played a large effect on GP set time and the 28 d strength at 40°C. Samples exposed to high humidity were observed to set slower but produce the strongest GP out of all the conditions at about approximately 6.4 MPa for both Na and K (Figure 9). High temperature and high humidity are the optimal conditions for both water retention and curing because of the relatively large amount of water in the air. At a low humidity, the samples achieved a high early age strength that then peaked at 3 d and deteriorated slightly till 28 d.

Figure 9. Flexure strength for various temperatures and humidities (All data from Tables 10 through 13).

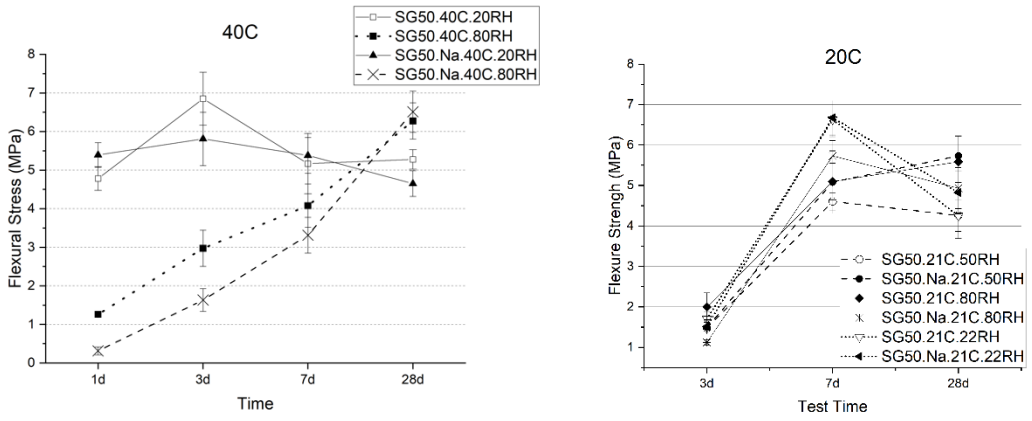

This peak was also seen for all 20°C, 22% RH samples at 7 d (Figure 10). This was likely due to slow crack nucleation and propagation between 7 and 28 d due to drying shrinkage, which resulted in significantly lower mechanical properties at 28 d.

Figure 10. 20°C conditions separated out based on GP alkali type (Na versus K).

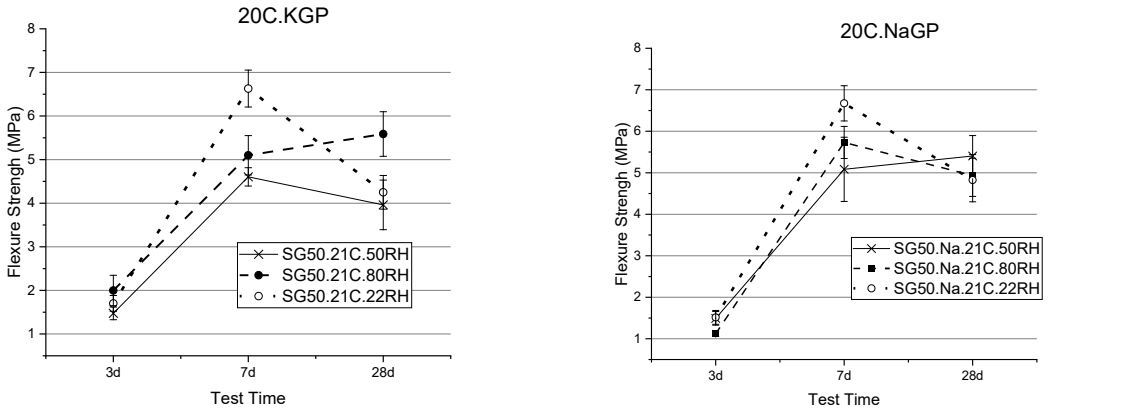

Potassium GP produced the best strength at high humidity and 40°C, supporting earlier work done that found the best strength in seal-cured GPs at 40°C–80°C (Heah et al. 2011; Rovnaník 2010; Manjunatha et al. 2014). There was no difference between intermediate and low humidity strengths at 28 d.

Conversely, sodium GP had a significantly higher 28 d strength at 50% RH than 22% or 80% RH (p = 0.013 and 0.021, respectively), which supports work done by Yousefi Oderji et al. (2019). They found sodium, fly-ash-based GP to have the best compressive and flexural properties at 70% RH when testing humidities at 30%–90% RH. NaGP was more tolerant of extreme humidities than KGP since the 28 d averages of the 20°C, NaGP samples coincided more with one another. KGP and NaGP, cured under their own ideal conditions, produced statistically identical strengths at 28 d (p = 0.627).

Most of the flexure bar surfaces that were exposed to air were found to take on a beige color and formed a darker layer several mm thick (Figure 11). All samples exposed to air at 20°C and 50% RH formed this layer, indicating the cause to be excessive evaporation. This layer only forms when the GP is air dried before it has set and cured, which takes a minimum of 3 d for both Na and KGP at ambient conditions. This was found because 20°C samples demolded and tested at 3 d had developed a uniform beige layer on all sides. All the 40°C samples only had a beige layer at the top surface rather than all the sides after demolding, indicating setting and curing had already taken place.

Figure 11. Picture of all the SG50 series samples taken at least a month after testing. One sample from each batch was chosen to represent a given temperature (10°C, 20°C, and 40°C), humidity, and time (3 d, 28 d). There are two bars in each group; *top* bar is SG50.Na and *bottom* bar is SG50. The 28 d/10°C condition was kept at 80 RH.

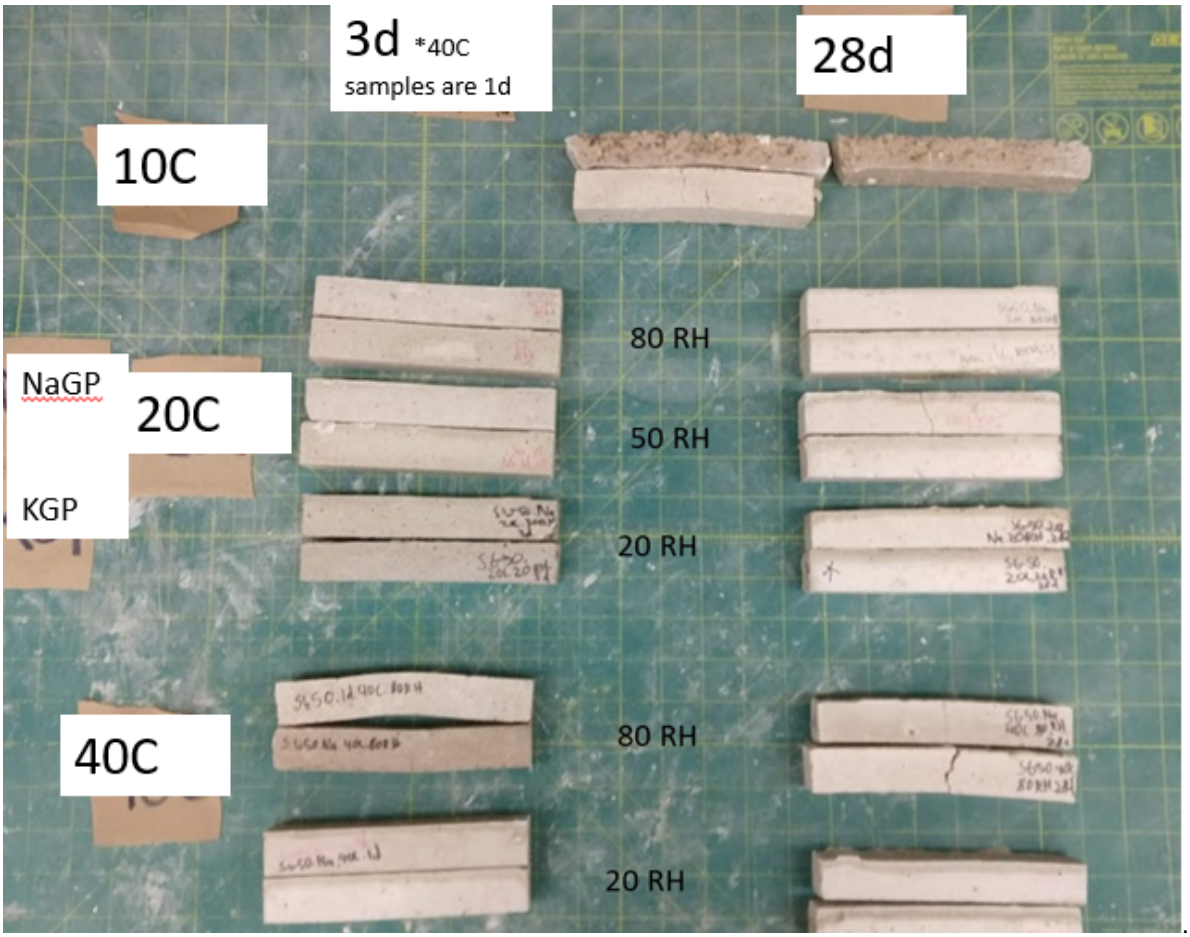

This color change may be due to the extent of geopolymerization and will be analyzed further in Section 3.1. All the 3 d samples and the 40°C/20% RH/1 d sample had the same color. The 40°C/20% RH samples had cured enough at the higher temperature where any additional water loss did not cause a color change on the surfaces not immediately exposed to air. The 28 d samples were demolded after 7 d and only showed a distinct beige layer on the top surface due to initial water evaporation.

All the 28 d samples had a beige layer except for SG50.Na cured at 40°C, 80% RH, 28 d and the 10°C samples. The potassium sample cured at 40°C/80% RH had a very faint beige layer. This is due to a high amount of moisture at 40°C and the low water evaporation rate at 10°C, which prevents the beige layer from forming by slowing down water leaving the sample.

The samples were prepared by fragmenting the cured GPC into pieces a few mms in diameter. The density was measured with a Micromeritics AccuPyc II 1340 V1.05 helium pycnometer (Figure 12). Increasing the amount of sand from 40 to 70 wt% linearly increased the density as expected. The porous silica fume samples had reduced density relative to the other samples tested and the wollastonite tailings samples had the greatest density. The tested samples of SG50 and SG50.Na may vary more than indicated in Figure 12 because of the inhomogeneities of the sample arising from the addition of coarse aggregate.

Figure 12. Densities of a few composites cured at 20°C/50 RH.

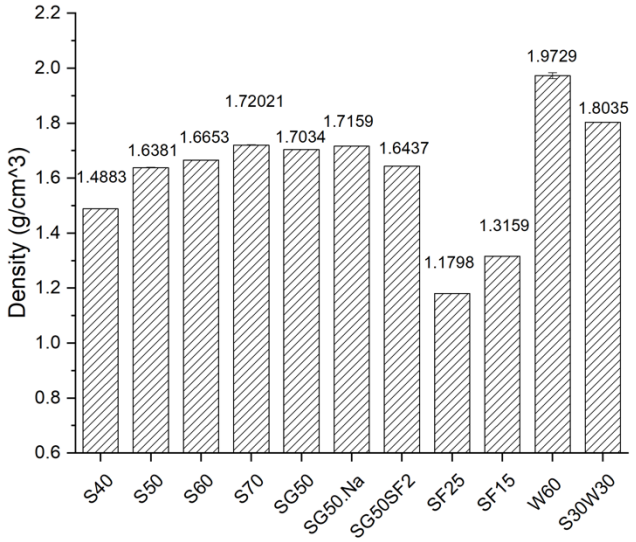

2.2.3.1 Silica fume: a more in-depth look

The addition of silica fume creates an initially sticky and hard to clean mix and results in a final product that is light and porous yet very strong in flexure once properly dried. Silica fume also reduces the set time. Firing or blow torching a composite made with silica fume or calcined silica fume causes a glassy phase to appear as can be seen in

In Figure 26, the *left* picture has 1,000°C samples freshly removed from the oven next to untreated 1,100°C samples. The *right* picture is the samples after 10 days of resting on the lab bench.

Figure 26 in the next section or in Figure 13 below.

Figure 13. A composition containing silica fume, sand, and gravel (sg50sf1) that was heated with a torch.

X-ray diffraction spectroscopy (XRD) was done on calcined and noncalcined silica fume powders on a Bruker D8 advance XRD with a Cu-Kα source at the Illinois Materials Research Laboratory (MRL). The background was subtracted, and the peaks matched with MDI Jade, v. 2021 (Figure 14).

Figure 14. XRD spectra of the two forms of silica fume calcined for 900°C for 12 hours.

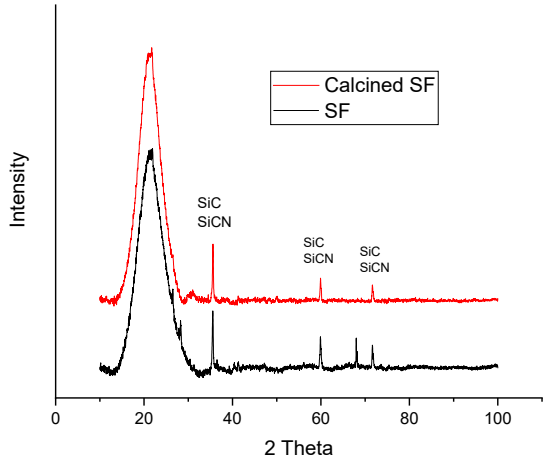

Originally, the research team thought that the grey color of the silica fume was due to a silicon impurity reacting with the alkali hydroxide to form hydrogen gas and an alkali silicate. However, no silicon could be detected,

and so the cause of the bubble formation and the porosity remains unknown. The only other reaction expected to happen besides the geopolymerization is the dissolution of the amorphous silica fume by the excess alkali to form an alkali silicate, which does not generate gas. The grey color could be attributed to a carbon impurity, which would not manifest itself on XRD due to its light atomic mass. The broad peak at 21 (2θ) could not be identified but is likely amorphous SiO_2, which would explain the glazing behavior at high temperature. The SiC and SiCN peaks are likely due to trace impurities of those compounds. Last, there is an unresolved impurity at 68 (2θ), which gets burnt off during calcination.

This thin-walled porous network may partially explain the plastic behavior and weak mechanical strength seen at 7 days. Silica fume samples of 1 × 1 × 10 cm that had dried for a week experienced no plastic behavior and failed in a brittle manner (Figure 15). Samples tested after only a day of drying after demolding showed significant plastic deformation. Previous samples with identical compositions showed indentations after drying on toothpicks, indicating viscous behavior on the timescale of multiple days.

Figure 15. An SF25 specimen that had been tested at 7 d after curing at 21°C/50 RH.

Samples that had lower amounts of silica fume and ample drying time gave exceptionally high strengths. However, all the silica fume composites made were found to disintegrate in water leaving behind a highly basic, liquid suspension of silica particles and a fine silty layer on the bottom of the container (Figure 16).

Figure 16. A piece of SG50SF2 submerged in DI water for 30 hours (*right*). Specimen before submerging (*left*).

This limits the use of silica fume to structures in arid environments that experience little to no precipitation or for niche uses in ceramics processing, as a dissolvable formwork for example. The disintegration of samples was regarded to occur due to capillary forces exerting pressure on the thin walls of the μm sized pores of the composite and breaking them up. However, GP composite made with 15 wt% silica fume that was previously calcined at 900°C for 1 hour also disintegrated despite having no porous structure. Dissolution may occur due to a significant portion of unreacted material created because the alkali component reacted with the silicon in the silica fume instead of dissolving the metakaolin and aiding in the geopolymerization reaction.

Interestingly, a 25 wt% silica fume composite heat treated to 1,000°C for one hour at 10°C ramp rate and then submerged in water after cooling to RT did not disintegrate. This may be due to the enlargement of the nano-scale pores, which would result in decreased pressure acting on the matrix according to the Young-Laplace equation.

$$\Delta p = y/R \,, \tag{9}$$

where

Δp = the pressure,
y = the surface tension (water), and
R = the radius of the sphere formed by the meniscus of a fluid moving up a tunnel.

Larger pores and tunnels caused by thermal shrinkage would lessen the pressure on the matrix and could explain the little to no disintegration observed in high temperature samples. It is worth noting that glazing did not occur at this temperature and that some other microstructural change, such as silica sintering, may be responsible for the lack of dissolution.

2.2.3.2 Other curing conditions and water glass aging

Other curing conditions investigated were the Control, Control.9d, and Control.2d conditions. The Control was 24 hours at RT in a saturated water vapor environment followed by 24 hours at 50°C in a high humidity environment (same as the "control" conditions described in Section 2.2.2). This was followed by demolding and drying slowly over an 8–9-day period until the sample's water mass loss was negligible. The Control.9d condition consisted of 9 days at RT and high humidity followed by demolding and slow shelf drying for 9 days at 21°C and 22% RH. The Control.2d specimens were cast into Delrin molds and cured at 21°C and 45% RH for two days, then demolded and cured for an additional 19 days. The flexure bars were made with the same compositions and cast in the same way as the samples in Tables 14 and 15, with one face of the mold open to air. The samples were tested according to the same method as described in Section 2.3.5.

A water glass aging experiment was devised and carried out to determine optimal storage conditions of potassium and sodium water glass prepared from KASOLV 16 and Metsobead 2048, respectively. Freshly prepared water glass was poured into an HDPE container, sealed, and then placed in two different conditions: 50°C for 7 d and 14 d, and -20°C for 7 d. The water glasses were given 15 minutes to come to RT, then used to make compositions SG50 and SG50.Na (1:1:1, fine and coarse sand: GP: gravel). These samples were cured using "control conditions." The results of both of these tests are summarized in Table 14. The term "freezer" relates to the

samples kept at -20°C for 7 d, while the other "wtgage" samples were kept in a 50°C oven.

The purpose of the aging experiment was to determine the temperature stability of water glass, which is a main precursor of GPs. The water glass was the only variable in the aging experiment; the compositions and curing conditions were kept the same. This information is useful since it pertains to storage of water glass when making GPs in the field. Metakaolin is an inert powder that can be stored in any condition provided it is kept dry.

Table 14. Other curing conditions in *pink*, water glass aging in *white*.

Composition ID	Sample age	Flexure (MPa) [SD]
SG50.Control	11 days	5.24 [0.17]
SG50.Na.Control		5.25 [0.45]
SG50.Control.9d	18 days	4.48 [0.24]
SG50.Na.Control.9d		5.33 [0.73]
SG50.Control.2d	21 days	4.30 [0.45]
SG50.Na.Control.2d		4.07 [0.58]
SG50.wtgage.7 d	11 days	5.71 [0.58]
SG50.Na.wtgage.7 d		6.03 [0.62]
SG50.wtgage.Freezer		4.94 [0.80]
SG50.Na.wtgage.Freezer		4.54 [0.48]
SG50.wtgage.14d		6.27 [0.75]
SG50.Na.wtgage.14d		5.66 [0.64]

No polymerization of water glass was evident. There was no observable difference in the viscosity of the fresh GP paste prepared from frozen and

heated water glass. The sodium water glass (NaWG) had frozen completely, while the potassium water glass (KWG) formed a heterogenous, two-phase mixture of ice and liquid. The difference can be attributed to NaWG having 13 moles of water per mol of water glass versus KWG's 11 moles. The cured samples all had a moisture-affected zone except for the Control.9d samples (see Section A.2).

A one-way analysis of variance was conducted, and there was no significant difference found between the untreated sodium and potassium water glass samples (SG50.Control) and the 7 d and 14 d heat-treated water glass samples ($\alpha = 0.05$, $p = 0.0710$), indicating water glass can be kept at higher ambient temperatures for relatively short time increments and can be kept at RT (Figure 17). There was also no significant difference between SG50.Control and SG50.wtgage.Freezer ($p = 0.083$). However, there was a significant difference between the sodium water glass control and freezer ($p = 0.046$).

Figure 17. Flexure strengths of GP composites, with varying water glass age times and temperatures, and "control," which is GP made from unaged water glass.

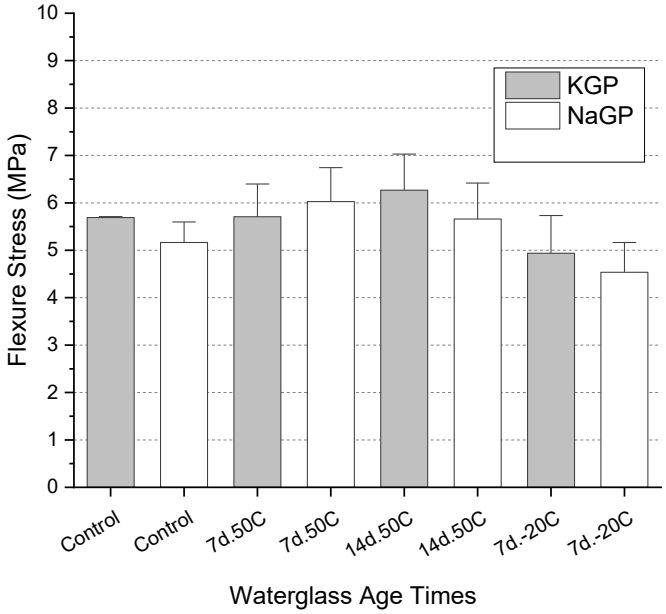

The act of completely freezing sodium water glass has a damaging effect on the final GP composite and should be avoided. Increased temperature/time has no effect on the strength.

Another analysis of variance was conducted on the control samples, which found no significant difference between the two "Control" Na and K samples and SG50.Na.Control.9d (p = 0.197) (Figure 18). There was also no difference between the two Control.2d samples and SG50.Control.9d (p = 0.405). The use of high temperature and high humidity is responsible for the high strengths of both "Control" samples, while high humidity and a longer curing time is responsible for the high strength of the sodium Control.9d sample.

Figure 18. Flexure strengths of GP composites cured under different conditions.

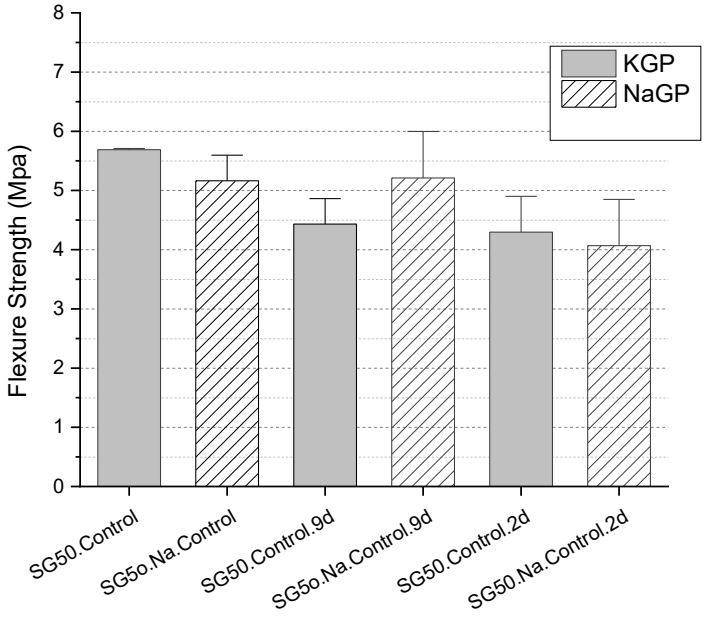

The weaker strength of the potassium-based Control.9d sample could be attributed to cracking on the edges of the sample due to weak GP formation stemming from the condensation of water vapor on the surface of the sample. Evaporation from the surface and the sides of the Control.2d samples contributed to drying shrinkage and a weakened GP matrix, which reduced strength. All samples except for both Control.9d samples showed a beige moisture-affected zone. Pictures of samples are shown in Figure A-8.

2.2.3.3 GP paste mixing conditions

Different GP mixing speeds and times are used to make flexural composite samples and SEM images of the pure paste.

The final strength of the GP composite is dependent on the completeness of the reaction (Table 15). Metakaolin is composed of micron-sized particles, which have repeating sheets of silica tetrahedra and alumina octahedra. To ensure full dissolution of the metakaolin by the alkali activator, these sheets must be sloughed off to increase the surface area, which necessitates high shear mixing. Mixing kinetics are dependent on

1. The mixing container
2. The batch size
3. The mixing blade
4. Blade speed
5. Mixing duration

1 and 3 are fixed variables; the blade should be proportional to the mixing container. The blade should be designed to have high shear and high flow capabilities in larger batches.

2.2.3.4 Methods

The blade used was a 4 in. diameter high shear blade with an 8 in. diameter plastic bucket (Figure 19).

Figure 19. The high shear mixing setup.

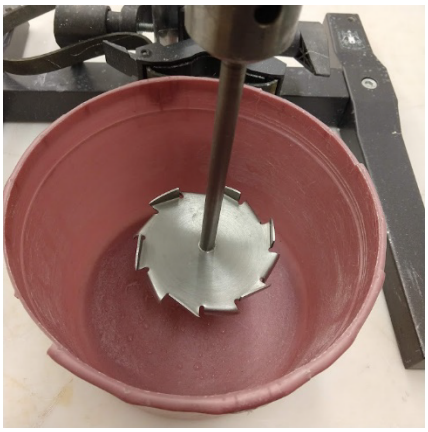

Table 15. Results of mixing at different speeds for different times.

Sample ID	Mixing speed (RPM)	Mixing time (mins)	Flexure strength [SD]
S60.2000.15	2,000	15	7.60 [0.65]
S60.2000.10	2,000	10	9.83 [1.60]
S60.2000.5	2,000	5	7.91 [0.96]
S60.1000.10	1,000	10	8.72 [1.21]
S60.1000.5	1,000	5	7.97 [0.89]

Metamax metakaolin and KASOLV 16-based water glass were used to form the paste. Two different speeds and two different mixing times were selected for a 4 × 4 matrix. Each batch was the same size, about 540 g of GP. Each batch was first mixed at 400 rpm for 30–40 seconds to incorporate the metakaolin into the water glass to avoid kicking metakaolin powder into the air at higher speeds. This was followed by the high-speed mixing protocol. The mixing was done at RT conditions of 21°C and RH held within 2%. The paste was then mixed by hand with 60 wt% fine sand and cast into 1 × 1 × 6 in. Delrin molds, which were then cured for 24 hours at 20°C/95% RH followed by 24 hours at 50°C/95% RH followed by an incremental drying procedure at 20°C. The samples were tested in four point bending 7 days after demolding (Figure 20).

Figure 20. Flexure strengths of bars with variable mixing speed. All speeds and times tested (*left*), 2,000 rpm series (*right*).

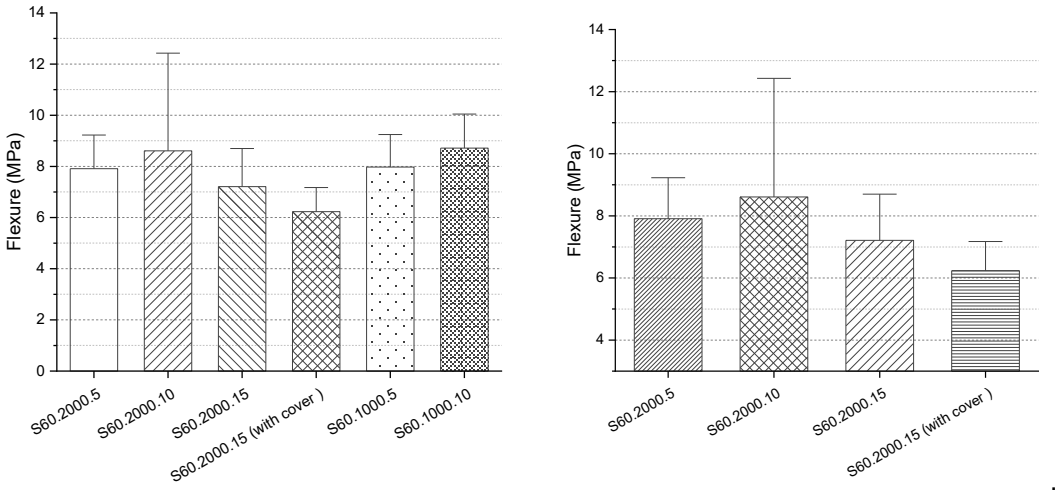

It was initially thought that the slight decrease in strength from a 10- to 15-minute mixing time at 2,000 rpm was due to water evaporation and a decrease in the geopolymerization reaction. Another test was performed where the plastic mixing bucket was covered with saran wrap with a small

hole for the mixing blade. This test was labeled S60.2000.15 (with cover). However, an analysis of variance study determined that the strength of this sample was significantly weaker than the other samples (p = 0.003). This difference was attributed to the covered sample because a separate analysis of variance, which excluded the covered sample, revealed no significant difference between any of the 1,000 rpm or 2,000 rpm samples (p = 0.08). A small amount of water evaporation may be desirable during mixing, likely because it reduces the pores created by aggregated water molecules in the set GP.

The overall data indicate that the mixing blade speed is not as crucial to producing high-quality GP as the mixing time. Reducing the time by half in the 2,000 rpm series reduced the strength by about 20%, while reducing the speed in both the 5 and 10 min series had no difference on the flexure strength.

These strengths are some of the highest that were obtained. The S60.2000.10 samples are 1.78 times stronger than SG50.Control from Figure 20 above. The only difference between the two samples was the composition. The SG50.Control sample contained fine sand, coarse sand, and gravel, whereas the stronger sample had fine sand as the reinforcement. The addition of gravel reduced the strength considerably in samples cured according to the "control" method. This is likely because the round river gravel used offers a smooth crack deflection path over the surface of the gravel, while the crack in the sand composite requires more energy to deflect around much more numerous grains of sand. Interestingly, the flexure strength was found to decrease from 10 to 15 min of mixing to the point where it was the same as the 5-minute mixing time. Additional mixing is thought to disrupt gel formation, which would result in less complete polymerization of the GP.

Mixing blade speed was kept from 1,000 to 2,000 rpm. Using larger blades would lower the minimum rpm speed needed because of increased tangential velocity resulting in higher shear.

SEM imaging was conducted using an accelerating voltage of 8 kV on fracture surfaces of pure GP paste that was sampled from the different mixing conditions (Figure 21). The fractured specimens were gold coated using a JEOL sputtering machine.

Figure 21. SEM images of fracture surfaces with identifiable unreacted metakaolin *circled*.

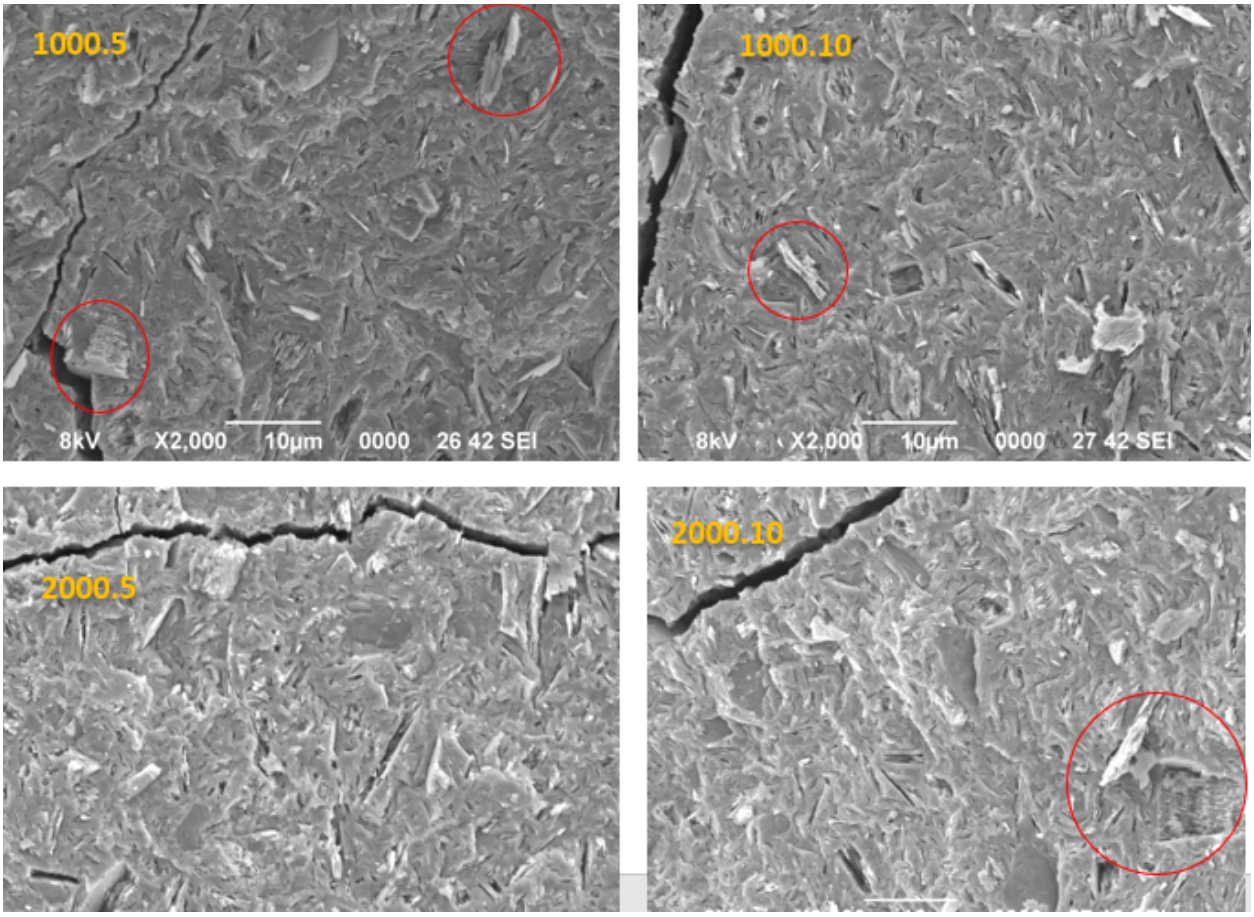

There was no clear trend in the amount of unreacted metakaolin as a function of mixing speed or mixing time for the 2,000 rpm speeds and 1,000 rpm, 10-minute speed. The 1,000 rpm, 5-minute sample had the most unreacted material as predicted. Mechanical properties are the best figure of merit for complete geopolymerization.

2.2.4 Water retention

Excessive water evaporation during the first few days of reaction and curing created a water-affected layer that ranged from 3 to 9 mm thick. The amount of sand aggregate does not have as much of an effect on the depth of the layer as the curing condition does. The layer in the Q55.Control sample was hard to distinguish due to the use of light quartz (Quikrete) sand, but it was significantly smaller, measuring 2 mm compared to approximately 7.5 mm in the S series. Figure 22 shows various flexure testing samples—from *top to bottom*: S40, S50, S60, S70,

Q55.Control. The 1 × 1 × 6 in. flexure samples that were previously tested with the beige layer.S series samples were cured at 20°C/50% RH for 7 d.

Figure 22. Discoloration due to water loss in flexure samples.

There was no significant trend or difference in mass loss of the GP in the S40–S70 series of samples (Table 16).

Table 16. Compositions and results of water loss.

ID	Metakaolin type	Water glass type	Additive	Average mass retention (%)	SD
S55	Metamax HRM	KASOLV	*	94.1	0.00305
S55.15 mm	Metamax HRM	KASOLV	*	94.9	0.00226
S55.Na	Metamax HRM	Metsobead	*	94.7	0.0137
S55.Argical	Argical 1,200S	KASOLV	*	94.5	0.00436
SF15	Metamax HRM	KASOLV	Silica fume 15 wt%	90.8	0.0124

To better quantify mass loss, an experiment was devised where different compositions were cast into 3 in. PVC pucks and the masses recorded until steady state was reached. The PVC was cut to the desired thickness (either 5, 10, or 15 mm) and then mounted to a large weigh boat with the use of hot glue (Figure 23). The water vapor loss through the sides of the PVC pipe, the hot glue layer, or the weigh boat bottom were assumed to be negligible.

Figure 23. Examples of the 3 in. puck samples. From *left* to *right*, S55.Na, sf15, and s55.Argical.

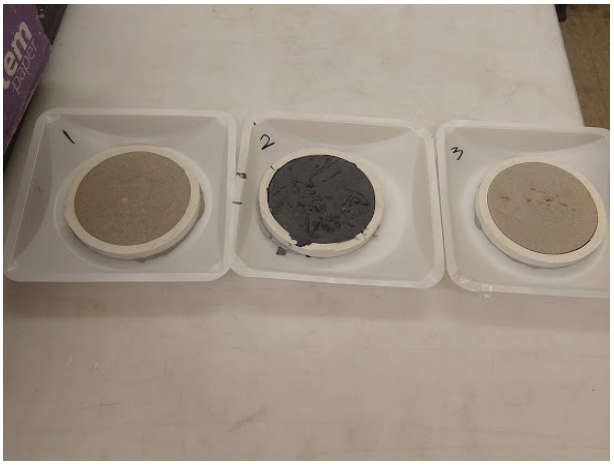

The mass retention was calculated by taking the absolute mass of the GP, which was done by subtracting the mass of the weigh boat and reinforcement from the final and initial masses, then dividing the two (Figure 24). Four samples were tested and averaged for the results.

$$\%\ Mass\ Retention\ = \frac{final\ geopolymer\ mass}{initial\ geoploymer\ mass} \quad (10)$$

Figure 24. Mass retention of the pucks after approximately 350 hours.

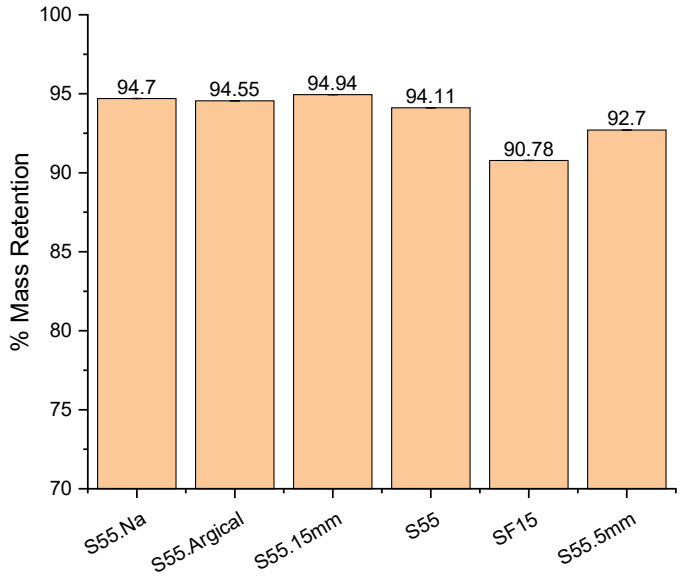

GP composites with an equal thickness differed by less than 1%. The exception to this was SF15 due to its open, porous structure and high

surface area, which leads to higher water loss. The 5 mm specimen performed similarly and lost more water because the evaporation of residual water in the bulk of the thicker pucks was limited by diffusion.

Making the puck thicker than 10 mm, using Argical metakaolin, and using sodium water glass resulted in a slight increase in water retention. The Argical metakaolin was found to set faster than the Metamax HRM and had fractionally higher water retention as a result of its increased reactivity. NaGP was found to dehydrate less because of Na ions' higher hydration energy (Duxson et al. 2006).

Coatings were tested on pure GP and on a 55 wt% sand composite. Powder coatings and silicone spray were found to be ineffective at preventing water loss. GLAD food plastic wrap was the best "coating" with a water retention of 96.7%. GP cured in ideal condition for 9 days and then allowed to dry normally had a retention of 89.4%. Comparing this to the sand samples in Figure 24, it is noted that dry aggregate helps retain water. Additional coatings were tested on a 55 wt% GP composite: a commercial concrete moisture retardant (Sikafilm, 5% vol solution) and a diluted Na water glass solution (1:3 wg:water by vol). These were also found to be ineffective and decreased mass retention slightly. These findings are summarized in Appendix A.

2.2.5 Scanning electron microscope (SEM) and pictures of samples

SEM imaging was conducted on samples taken from a few 1 × 1 × 6 in. specimens. Images were taken from the side and top of the sample to evaluate drying damage and from two fracture surfaces to evaluate the extent of geopolymerization via the amount of unreacted metakaolin (Table 17). The top fracture surface in Figure 25 (indicated by *f*) is the darker colored moisture-affected zone and the middle fracture surface is the larger, paler area.

Figure 25. Schematic showing different fracture surfaces to be analyzed.

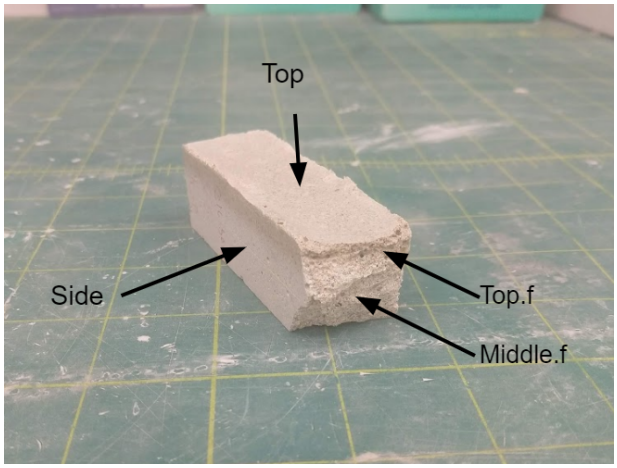

Table 17. SEM images of fracture surfaces.

Specimen ID	Side	Top	Top.f	Middle.f
S40. 20°C. 50% RH	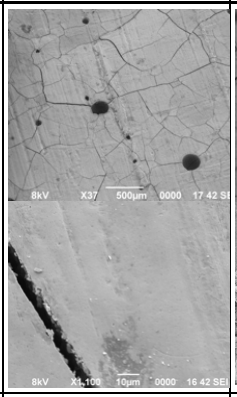	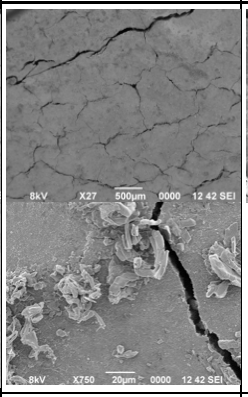	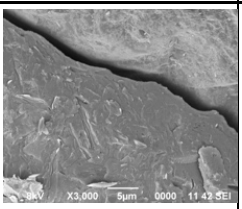	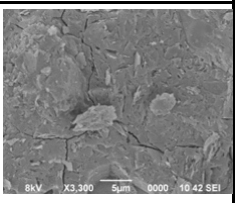
SG50 SF2. 20°C. 50% RH	NT	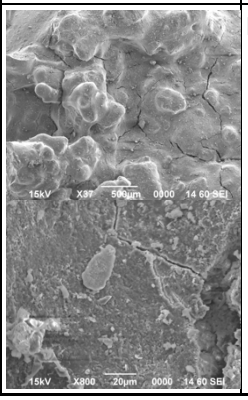	NT	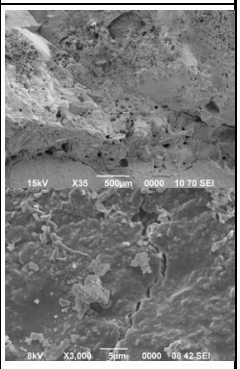

Specimen ID	Side	Top	Top.f	Middle.f
SF25. Control	NT	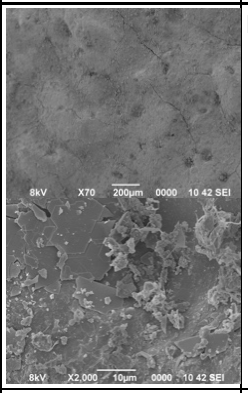	NT	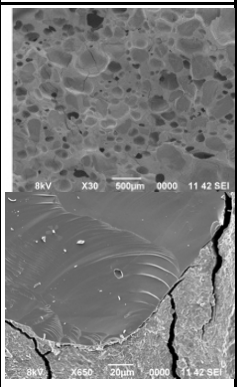
SF25. 20°C. 50% RH	NT	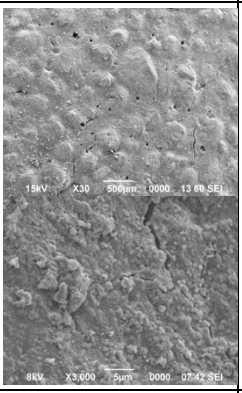	NT	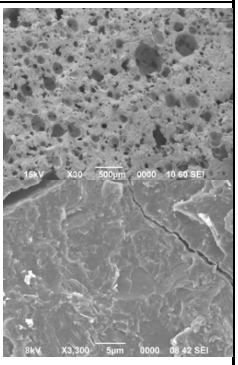
SF15. 20°C. 50% RH	NT	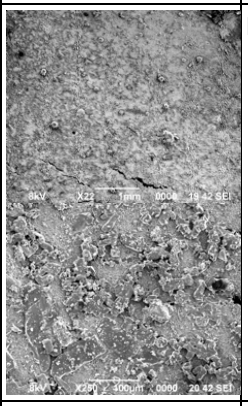	NT	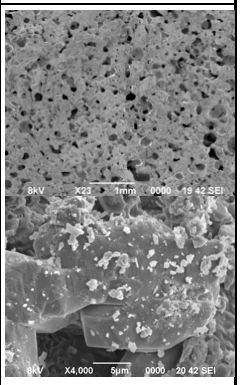
Calcined SF15	NT	NT	NT	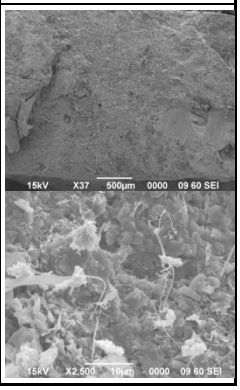

2.2.6 SEM discussion

All the sand samples had characteristic cracking on the surfaces. The side of the samples in contact with the mold all had similar amounts of sharp, interconnected, hairline cracks, which could be attributed to drying of set GP from capillary forces. The surface of the sand composites featured wavy cracks, which occur due to dehydration of the fresh paste. A significant difference in crack length and size between S40.20°C.50 RH and S70.20°C.50 RH can be observed, which occurred because there was a smaller volume fraction of GP to dehydrate and shrink. The reduction in surface flaws partially explains the continuous increase in strength from S40.20°C.50 RH to S70.20°C.50 RH. Images of the top and middle fracture surfaces were taken to look for unreacted metakaolin sheets. S70.20°C.50 RH was found to contain fully reacted GP for the two cross sectional points examined, while S40.20°C.50 RH contained little to no unreacted metakaolin in the top fracture surface and a discernible amount of the material in the bulk of the fracture surface. The reason for the light beige color in the GPC exposed to air could not be determined with the SEM.

The silica-fume-reinforced GP likewise showed fully reacted GP. Only a single type of fracture surface was taken for the silica fume because there was no moisture-affected zone. Not surprisingly, SF25.20°C.50 RH had larger and more pores than SF15.20°C.50 RH because of the greater amount of silica added and the more gas produced. Curing conditions appear to affect pore size, with the SF25.Control sample having larger, more numerous pores than SF25.20°C.50 RH. This can be attributed to the higher temperature accelerating the gas evolution reaction. Surface SEM images of these two samples revealed a few breakout pores on an otherwise intact surface. SF25.20°C.50 RH had a surface studded with evenly spaced, pronounced bumps 300–400 μm across, which were caused by underlying bubbles, while SF25.Control featured more gradual hills and pits. SF15.20°C.50 RH did not have any lumps on the surface and instead had a significant amount of surface debris caused by sawing the sample. Subsequent samples were formed by chiseling chips out of the 1 × 1 × 6 in. bar that had already been tested.

2.3 Thermal properties and considerations

2.3.1 Effect of aggregate

The effect coarse aggregate, fine aggregate, and glass powder had on postheat-treatment stability was investigated. A few compositions were prepared from KASOLV-based water glass and Metamax HRM metakaolin, cast into approximately 3 in. diameter weigh boats and cured at 21°C/50% RH. Samples 6 and 9 were heaped onto a flat surface and cast into a 1 × 1 × 6 in. mold. The sample geometry is not important in this experiment as long as the sample is large enough where the components are homogenously distributed. These samples were then broken in half with the left side of the sample heated to 1,000°C and the right side to 1,100°C. The compositions are listed in Table 18 below.

Table 18. Compositions of aggregates for heat treatment.

Additive								
ID	FS	Glass (Oroboros)	Gravel (3/16 in.>)	BF	Calcined SF	Gravel (3/8 in. >)	GP	Description
1	1	-	1	-	-	-	1	Sand + gravel
2	0.5	0.5	1	-	-	-	1	Sand + glass + gravel
3	-	-	-	-	0.15	-	0.85	Calcined SF
4	1	-		-	-	-	1	Sand
5	0.174	1.4	0.875	-	-	-	1	Sand+glass+gravel
6	0.64	0.44	-	-	-	1.04	1	Sand+glass+gravel
7	1	1	-	-	-	-	2	Sand + glass
8	2	-	2	0.14	-	-	2	Sand+gravel+basalt fiber
9		0.34	1	0.05	-	-	1	Glass+basalt+gravel

In Figure 26, the *left* picture has 1,000°C samples freshly removed from the oven next to untreated 1,100°C samples. The *right* picture is the samples after 10 days of resting on the lab bench.

Figure 26. Heat-treated GP samples.

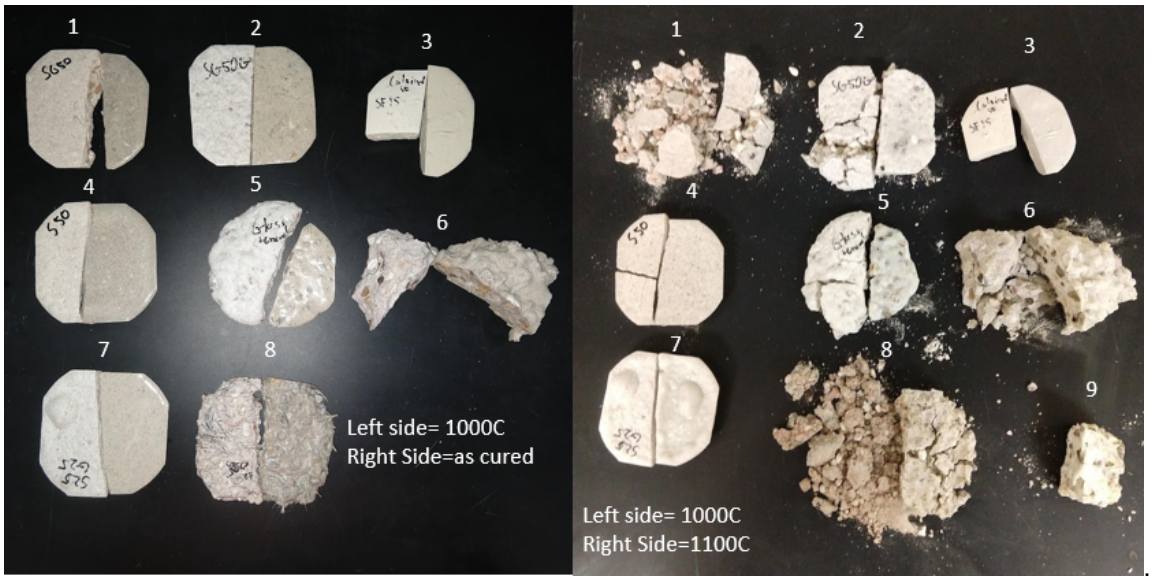

The sand composite (4) did not disintegrate and held its shape but was exceedingly brittle; the crack seen in sample *4* in the *left* piece was caused by the researchers and did not happen on its own. Interestingly, large air bubbles formed in sample 7 at both temperatures but not in sample 2. Bubble formation was likely due to self-glazing and sintering on the surface forming an impermeable barrier for the residual and dehydroxylated water vapor. The presence of gravel likely broke up any large bubbles that formed in sample 2.

All samples with gravel heated to 1,000°C disintegrated after 10 days. All samples which contained gravel and glass did not disintegrate, but only when heated to 1,100°C. As explained by Hager, the gravel undergoes many physical and chemical changes that weaken the structure (Hager 2013). Shrinkage is evident in some aggregates due to decomposition and gas formation, which stresses the adjacent GP and initiates slow growing cracks. Significant aggregate shrinkage was observed to occur between 1,000°C and 1,100°C, as shown in Figure 27 below. There are opposing factors for strength as a function of temperature; gravel lowers composite strength with increasing temperature, while the glass powder gets activated at a certain minimum temperature and time interval, 1,100°C in this case. As can be seen in the sample shown at the bottom of Figure 31, the self-healing effect of glass prevented the sample from disintegrating.

Figure 27. Two samples of sample 6 with the visibly shrunken aggregates.

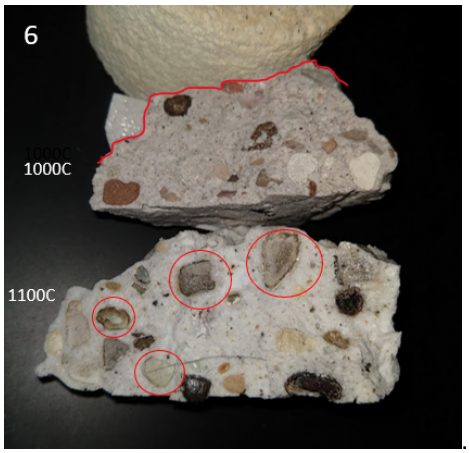

Like the results found by Keane et al. (2021), self-healing and strengthening only occurred once the glass melted and flowed into the cracks and pores formed by the dehydration of the GP (Keane et al. 2021). The sample containing glass and gravel (5) deformed and experienced some flow at both 1,000°C and 1,100°C in the absence of an inert reinforcement such as sand for shape retention. Therefore, composites containing mostly glass as the reinforcement should be avoided in applications that require load bearing and high, prolonged temperatures, such as a molten salt containment vessel. More quantitative research is needed to support this finding. Flexure and compressive strengths of heat-treated samples with differing amounts of glass powder will be discussed below.

2.3.2 Effect of Si/Al ratio, water content, temperature on mechanical properties

Flexure samples of 1 × 1 × 6 in. (2.54 × 2.54 × 15.24 cm) and compression samples of 2 × 2 × 2 in. (5.1 × 5.1 × 5.1 cm) were made with water glasses of different Si/Al ratios and different water contents. Samples were reinforced with sand and recycled glass powder (Vitro Minerals, medium glass [MG], mean size = 636 µm, SD = 507 µm), cast into molds, and cured like the other "control" specimens, then dried incrementally and tested on an Instron with a 50 kN load cell and load rate of 0.02 mm/min, and the cubes were tested on a Testmark compression tester at a load rate of 300 lb/sec (Table 19).

Some samples were heat treated in an oven (Carbolite) for 1 hour at 1,100°C with 10°C/min heat and cool rate. Samples were tested within 1–3 days after heat treating (Table 20).

This set of testing was done to determine the strength of composites that have completely changed phase and to optimize for the best water glass to use as well as the best composition. The results should not be used to predict mechanical strengths.

The abbreviations are FS = fine sand, MG = medium glass powder, and GP = geopolymer. The numbers in front of the letters constitute weight percent. The default water glass type used in the general report makes GP with a Si/Al molar ratio of 2 (1 Al_2O_3 :4 SiO_2). The water glass type is denoted as a molar ratio of K_2O:SiO_2:H_2O.

Reducing the silica content below a Si/Al ratio of 2 was found to reduce the set time and also completely eliminate the dark beige moisture-affected region seen when using 1.2.11-type water glass as in Section 2.2.

Table 19. Strength of GPC cured at RT.

Sample	FS:MG:GP	Water glass type	Si/Al ratio in the GP	Regular flexure strength [SD]	Regular compressive strength [SD]
FS40MG20.1:2:11	0.4:0.2:0.4	K 1:2:11	2	5.24 [0.98]	51.6 [17.09]
FS30MG30.1:2:11	0.3:0.3:0.4	K 1:2:11	2	4.81 [0.21]	49.8 [6.9]
FS30MG30.1:2:9	*	K 1:2:9	2	4.56 [0.32]	51.4 [7.4]
FS30MG30.1:1.5:9	*	K 1:1.5:9	1.75	3.90 [0.39]	54.4 [7.00]
FS30MG30.1:1:9	*	K 1:1:9	1.5	3.83 [0.69]	46.2 [3.9]
FS30MG30.Na.1:2:11	*	Na 1:2:11	2	5.20 [0.47]	42.6 [8.24]

Increasing the amount of sand and reducing glass was found to slightly increase the flexural strength of the composite and had no significant impact on the compressive strength. This is likely due to the smooth conchoidal fracture surfaces of the glass, which are difficult for the GP to stick to, allowing the cracks to propagate through the aggregate/GP interface. Reducing the water content in the 1:2:11 water glass to 1:2:9 and the 1:2:13 sodium water glass to 1:2:11 made the GP highly viscous and difficult to mix and resulted in a reduction in flexural properties due to surface defects stemming from the inability of the mixture to compact into molds well and to flow when vibrated. The compressive strength was not affected.

The sodium water glass with reduced water content (1:2:11.Na) performed slightly better than reduced water potassium in flexure (*t* test, $p = .03$) but 17% worse in compression. Reducing the water content in the 1.75 and 1.5 Si/Al ratio composites created highly workable pastes with similar viscosity to the 1:2:11 water glass. A one-way analysis of variance on all of the unheated compression samples showed no significant difference in the means ($n = 6$, $a = 0.05$, $p = 0.197$), indicating that reducing the silica or the water content had no significant effect. These findings are different from that of Duxson, Mallicoat, et al. (2007) who found that compressive strength of K- and Na-based GP paste increases from a Si/Al ratio of 1.15 to 1.9 and then decreases slightly at 2.15. This can be attributed to the addition of the high vol% of reinforcement in this study, which reduces the differences between the two GPs.

Varying the water content, composition, and alkali cation also had no difference on flexure strength ($p = 0.124$). Lowering the silica content reduced flexural properties when compared to 1.2.9 water glass ($p = 0.033$).

Table 20. Strength of GPC treated at 1,100°C at one hour.

Sample	FS:MG:GP	Waterglass Type	Si/Al Ratio in the GP	Oven Flexure Strength	Oven Compressive Strength
FS40MG20.1:2:11.1100C	0.4:0.2:0.4	K 1:2:11	2	5.06 [0.57]	28.4 [10.3]
FS30MG30.1:2:11.1100C	0.3:0.3:0.4	K 1:2:11	2	7.34 [0.57]	13.7 [5.2]
FS30MG30.1:2:9.1100C	*	K 1:2:9	2	4.18 [0.68]	10.4 [4.3]
FS30MG30.1:1.5:9.1100C	*	K 1:1.5:9	1.75	5.33 [0.68]	7.83 [2.91]
FS30MG30.1:1:9.1100C	*	K 1:1:9	1.5	4.92 [0.25]	11.3 [2.02]
FS30MG30.Na.1:2:11.1100C	*	Na 1:2:11	2	NT*	NT*

*NT–Means not tested. The sodium GP composite melted and ran all over the place.

Heat treating leaves the flexure strength largely unchanged because of the healing effect of the glass, which seals dehydration cracks at the surface and prevents stresses from concentrating at those cracks. Heated samples showed flexure strengths equal to or better than the unheated samples but far worse compressive strength.

2.3.3 Difference between flexure and compression

The microstructure is assumed to be the same in both compression and flexural samples from heating at 100°C for an hour, so the difference can be attributed to the sample geometry itself. The larger cube samples deform more than the flexure samples, though characteristic deformation was found to vary between sample groups, as can be seen in Table 21. Ultimate compressive strength is sensitive to surface flatness; a convex, irregular, or sloping surface such as those seen in FS30MG30.1:1:9.1100°C, FS30MG30.1:2:9.1100°C, and FS30MG30.1:2:11.1100°C, respectively, all serve to reduce the actual strength by creating uneven pressure concentrations, which results in premature failure at those points. Conversely, flexure samples don't deform as much because they are smaller and the glazing seals up microcracks and other surface defects that have a negative impact on flexure strength.

Increasing glass content from MG20 to MG30 (while reducing sand by the same amount) increases flexure strength significantly due to better glazing but reduces compressive strength due to sample deformation (Figure 28). The compressive strengths of all the heated specimens except FS40MG20.1:2:11.1100°C have statistically identical averages (p = 0.109), meaning the Si/Al ratio and water content have no difference here (Figure 29).

Figure 28. An example of heat deflection in sample FS30MG30.1:2:11.1100°C on the *right* and sample FS40MG20.1:2:11.1100°C on the *left*. All samples were heat treated on a flat piece of ceramic dusted with alumina powder.

Figure 29. Mechanical properties of heat treated and nontreated bars. Six specimens were tested for each bar.

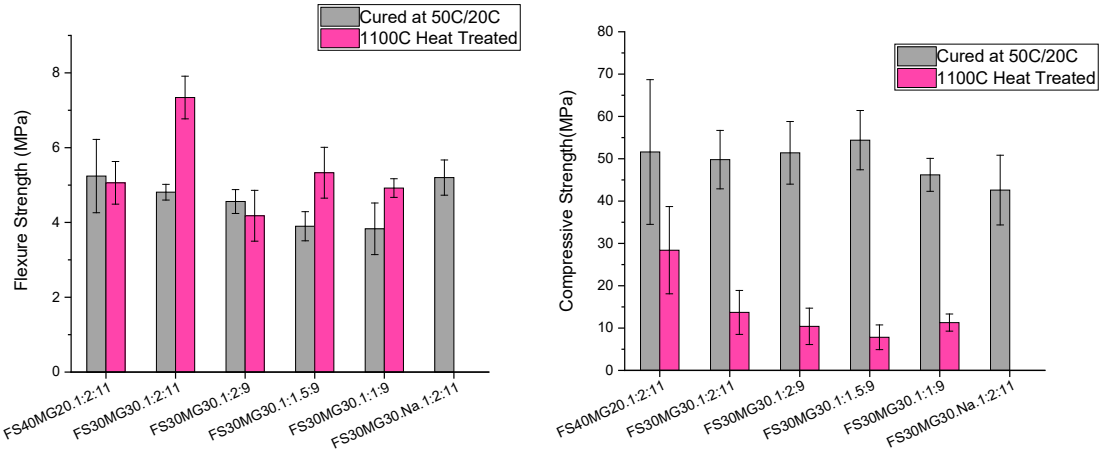

Table 21. Images of compression samples and SEM images of the flexural samples.

Sample	Before testing	After testing	SEM
FS40MG20.1:2:11.1100°C	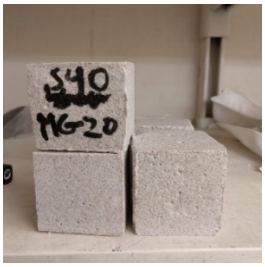	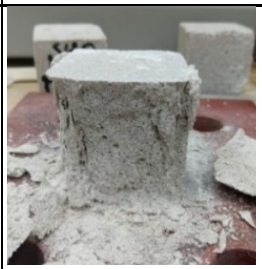	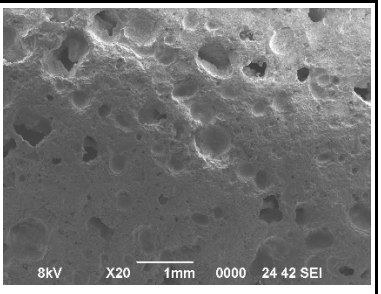
FS30MG30.1:2:11.1100°C			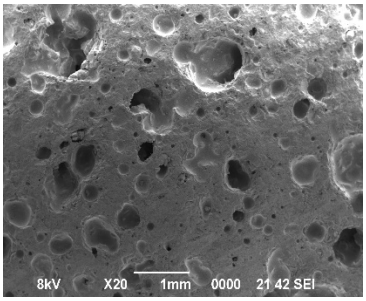
FS30MG30.1:2:9.1100°C			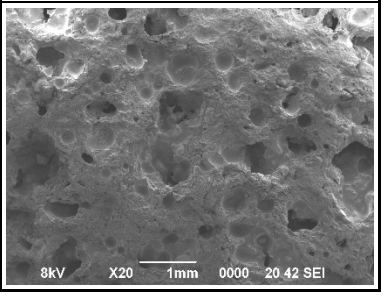

Sample	Before testing	After testing	SEM
FS30MG30.1:1.5:9.1100°C			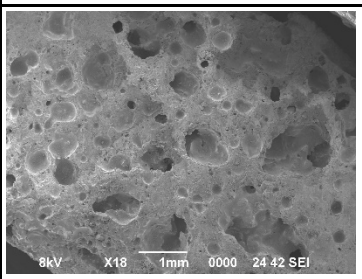
FS30MG30.1:1:9.1100°C	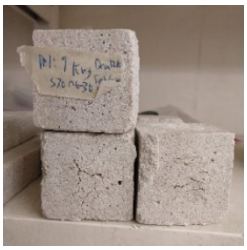		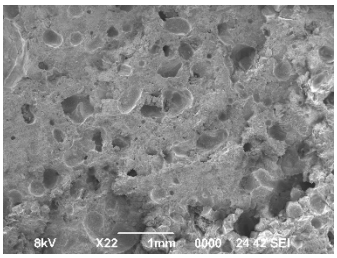
FS30MG30.Na.1:2:11.1100°C		NT	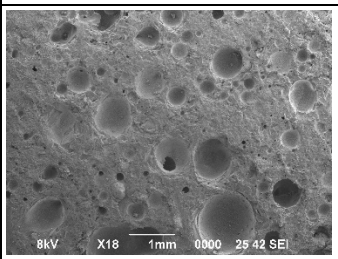

The sodium GP composite melted completely and was not tested. Reducing the initial water glass water creates a sample that doesn't glaze and deform as much as FS30MG30.1:2:11.1100°C but forms a rough, slightly convex surface with large cracks. The samples with differing Si/Al ratios formed similar cracks at the sides due to bulging of the sample under its own weight at high temperature.

It should be noted that failure for most of the heat-treated specimens, with the exception of FS40MG20.1:2:11.1100°C, failed by slow crushing and longitudinal crack development.

While there were a few statistically significant differences between the samples, there was no considerable difference between any of the RT compressive or flexure samples. At high temperature, FS40MG20.1:2:11 and FS30MG30.1:2:11 performed best in compression and flexure, respectively (Figure 30).

Figure 30. Heat-treated and nontreated flexure samples (*left*). Fracture surfaces of heat-treated samples (*right*). Some surfaces have divots that were cut out for SEM imaging: *1*, FS40MG20; *2*, FS30MG30; *3*, FS30MG30.1:2:9; *4*, FS30MG30.1:1.5:9; *5*, FS30MG30.1:1:9; and *6*, FS30MG30.Na.

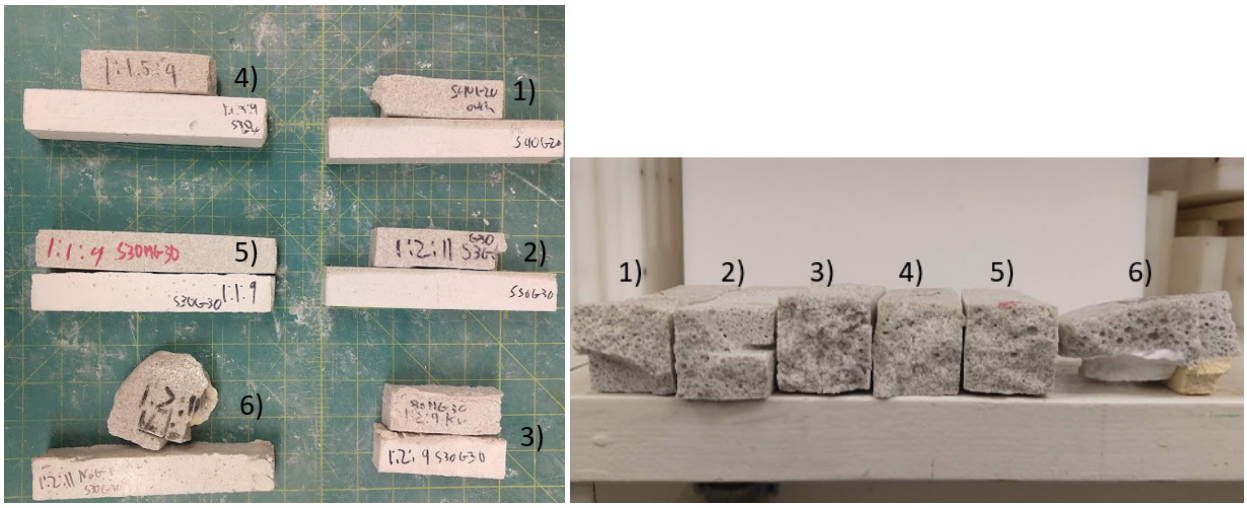

2.3.4 Optimizing sand and glass content for maximum high temperature strength

As mentioned above, increasing glass content benefits flexural strength but increases high temperature slump and reduces compressive strength. Samples were remade like in Section 2.3.4 above with differing compositions of recycled waste glass and fine sand to determine an optimal high strength at high temperature composition (Figure 31–Figure 32). Equal to or better strength was attained with a 1.2.11 mol water glass (Table 22).

Table 22. Heat-treated (1,100 °C, one hour) samples' flexure strength.

Sample	Flexural strength	Compressive strength
FS30MG30	7.34 [0.57]	13.7 [5.2]
FS40MG20	5.06 [0.57]	28.4 [10.3]
FS45MG15	5.54 [0.56]	33.3 [5.81]
FS50MG10	4.87 [0.29]	31.0 [3.77]
FS55MG5	3.38 [0.41]	20.2 [1.33]

Figure 31. Optimizing for compressive strength samples with varying amounts of sand and glass.

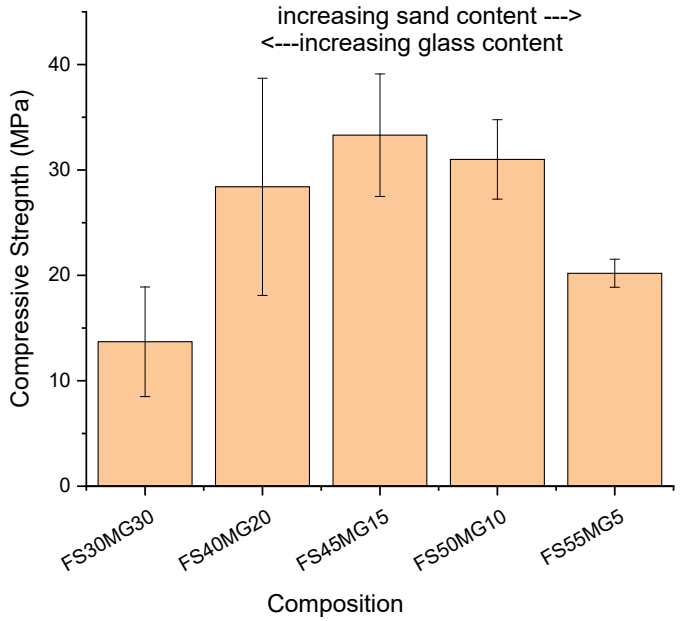

Figure 32. Optimizing flexure strength of varying amounts of sand and glass GPC.

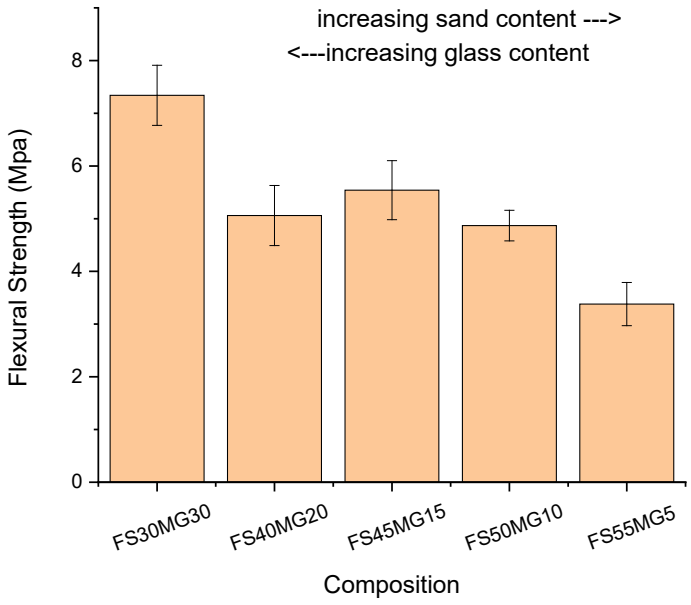

The limiting factor in the amount of glass to add for larger samples is the high temperature slump caused by the weight of the sample itself, as seen in Table 21. If an excess of sand is added, there is not enough glass to seal all the cracks that form under higher temperature and a reduction in

strength is observed. The optimum composition for shape retention for composites heated to higher temperatures is 45 wt% sand and 15 wt% glass. Flexure samples do not experience much heat deflection or deformation at this temperature, so more glass can be added, which increases the flexure strength.

Therefore, the optimal composition depends on the application and the geometry of the composite. For example, applications for samples standing more than an inch tall or with tight size tolerances should use more sand and less glass.

2.3.5 Flexure strength evolution as function of temperature

The research team evaluated the temperature at which self-healing occurs for the waste glass and the silica fume and the extent of coarse aggregate decomposition. The team then compared these two properties to those of sand.

Samples were made using 1:2:11 standard water glass and cured according to the "control" method stated above. Samples were also dried using the same methods. Samples were heated to the desired temperature for one hour, then taken out, allowed to age for 3–5 days, then tested in four-point flexure (Table 23 and Figure 33).

Table 23. Flexure strength of samples heated to varying temperatures for 1 hour.

Sample	SF	FS	Glass powder*	Gravel	GP	RT	400°C	600°C	800°C	1,000°C
SF15	0.15	-	-	-	0.85	2.62 [0.38]	7.78 [0.81]	7.089 [0.58]	7.27 [0.32]	5.78 [1.37]
MG30	—	—	0.3	—	0.7	2.38 [0.23]	0.62 [0.09]	1.53 [0.46]	5.95 [2.46]	6.62 [0.98]
S60	—	0.6	-	—	0.4	9.83 [1.60]	3.21 [0.86]	2.04 [0.19]	0.78 [0.31]	—
S60.Na	—	0.6	-	—	0.4	4.52 [1.61]	3.26 [0.16]	1.63 [0.20]	0.31 [0.05]	—
SG50	—	0.33	-	0.33	0.33	5.68 [0.43]	1.71 [0.18]	0.71 [0.16]	—	—

*Vitro Minerals waste glass (636 µm avg. particle size).

Figure 33. Fracture surfaces of the flexure bars of all the compositions and all the temperatures tested.

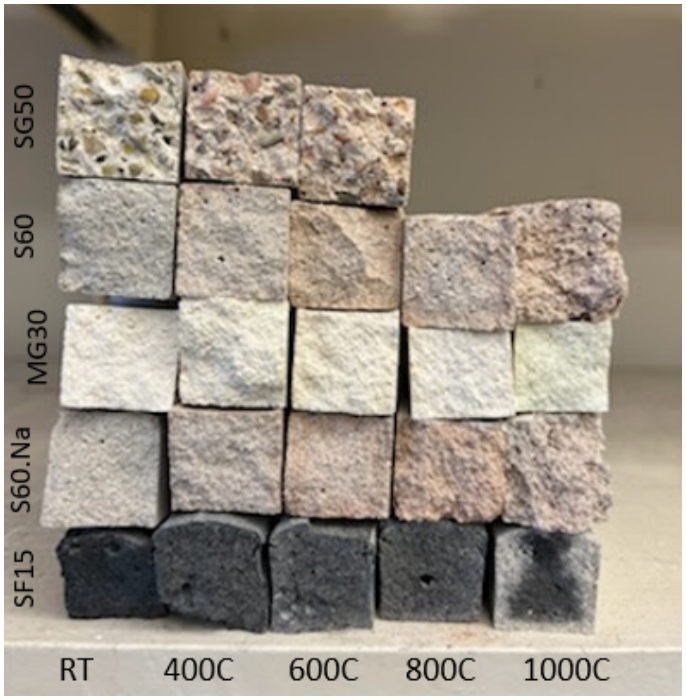

The reddish color of the sand composites is from trace iron containing mineral impurities in the fine sand. A partial transformation was observed in the 1,000°C silica fume sample, where the outsides of the bar turned white, likely due to the oxidation of the trace silicon metal to SiO_2. The partiality of the reaction can be explained by the proposed structure of the silica fume, where the silicon impurity is enclosed by a shell of SiO_2, making the reaction diffusion limited. The oxygen would need to diffuse through the shell to react with the underlying metal, which happens as a function of high temperature and time. The oxidation of silicon is thermodynamically favorable at 1,000°C and happens quickly. The partial reaction could also be explained by the composite's good insulation, as the color change happens from the outside inwards.

The RT flexure strength of the glass was weak relative to the other samples likely because the conchoidal fracture surface of the glass was atomically smooth and had poor adhesion to the GP. The flexure strength of pure glass was much higher than that of GP, so the crack likely propagated through the area of least resistance, which was the glass/GP interface. Self-healing by glazing started to occur at 800°C, which provided significant strengthening of the composite to the point where it was almost three times as strong as the RT sample.

The rapid decreases in strength in the sand and gravel samples from RT to 400°C can be attributed to shrinkage and cracking in the GP matrix due to dehydration and dihydroxylation (Duxson et al. 2006). There were no discernible differences in strength between the sodium and potassium GP samples from 400°C and higher. Sample strength continued to decrease from 400°C to 600°C due to continuing dehydration, the transformation of α-quartz to β-quartz at 570°C (Swamy et al. 1994), and from decomposition of gravel. Sand-containing samples heated to 1,000°C came out in one piece but then became extremely fragile and could be crushed to a powder in the palm of a hand. This was due to the continuing transformation of β-quartz to tridymite at 870°C as well as the crystallization of both sodium and potassium GPs. These phase changes caused heterogenous changes in volume, which stressed the microstructure and caused it to crack (Figure 34).

Figure 34. Strength evolution with temperature of various composites.

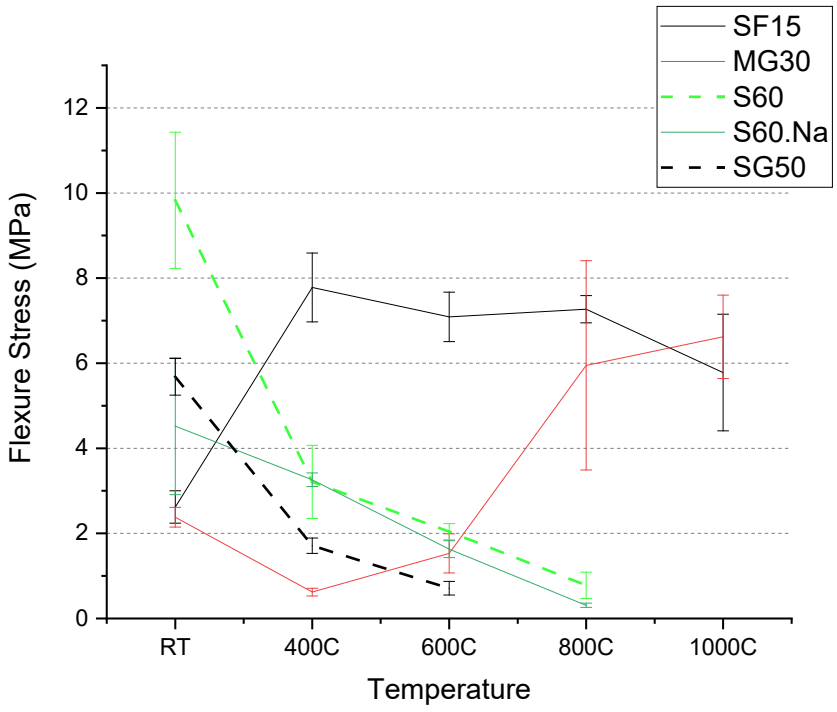

Interestingly, the porous silica fume sample gained strength after heating to 400°C and above, surprising for a foamy ceramic. This finding supports the theory that the RT SF15 composite dissolves in water because it contains a large portion of unreacted metakaolin and water glass, which fall apart in water (Figure 35). The higher temperatures allow the

solidified reactants to react more fully and gain strength. Also, silica fume samples heated above 400°C do not dissolve in DI water but make the solution slightly basic instead, which lends support to this theory.

Figure 35. Chunks of sf15 composite heated to (from *left* to *right*) 400°C, 600°C, 800°C, and 1,000°C with pH paper measurements of the resulting solution after 24 hours.

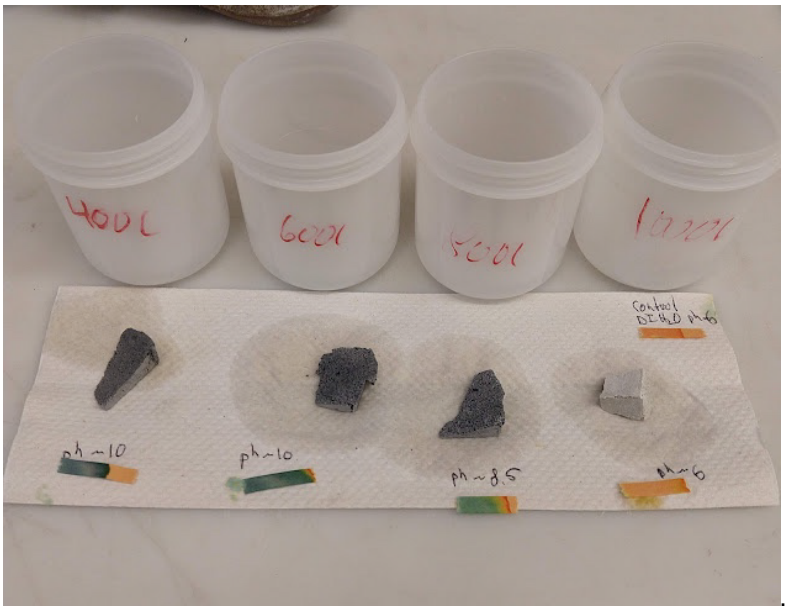

The test in Figure 35 above was done by chipping 1.5–2 g whole chunks from the tested samples in Table 23 and submerging them in 20 ml of DI water in a sealed polypropylene cup for 24 hours. All samples turned out to be completely intact, and no residue was found at the bottom of the cup. This should be contrasted with Figure 35 that shows a silica fume sample containing sand and gravel dissolved partially.

2.3.6 Flexure strength of GPC after simulated fire conditions

Bars measuring 1 × 1 × 6 in. were made using a traditional cement aggregate mix consisting of a 50/50 mix of fine and coarse sand and 3/16 in.> pea gravel, which was free of fines. KASOLV 16-based potassium water glass was used to make the potassium GP paste, and Metsobead 2048-based water glass was used to form the sodium paste. The paste was formed using high shear hand mixed with the aggregate and then cast into Delrin molds. The samples were demolded after 48 hours of curing at 20°C and 45%±3 RH and were cured for an additional 11 days. The samples were then heated in the propane forge furnace and then aged for an additional 9–10 days prior to flexure four-point testing at a speed of 0.01 mm/min. A control sample at zero seconds was made and tested at

the same time as the other samples in the batch. The final ages of all the samples were between 20 and 22 days. The samples were tested with the side exposed to fire facing down so that any surface damage would create a measurable decrease in the flexural strength by concentrating tensile forces at defects. See Figure A-9 for a picture of the setup.

2.3.7 The simulated fire testing

To stimulate a wildfire, a Cast Master CMF1000 propane furnace was chosen to deliver the flame source. This consisted of an oval steel container, which was lined with ceramic wool, closed at one end with a firebrick, and contained one burner port. Two thermocouple probes were inserted into alumina tubes, which were held in place by the firebrick and their tips positioned in the middle of the chamber and to the sides of the specimen to semiquantitively determine the temperature (Figure 36). The temperatures of the two thermocouples were averaged. Two sets of temperatures were tested: a "low" forest fire temperature setting of 600°C–700°C and a high temperature setting of 800°C–900°C. These settings were set by altering the amount of gas flow into the furnace. A low amount of flow created a yellow/blue flame with a lower temperature due to incomplete combustion of the propane, while increasing flow created a hot blue flame as seen in Figure 37 below.

Flame temperatures have large thermal gradients, which are dependent on gas flow and surrounding air currents making them difficult to measure accurately.

Figure 36. Simulated fire experimental set up. The chamber measures 25.4 cm long. The thermocouples are enclosed in 5 mm alumina tubes. The *left* picture shows a "low" temperature empty chamber flame.

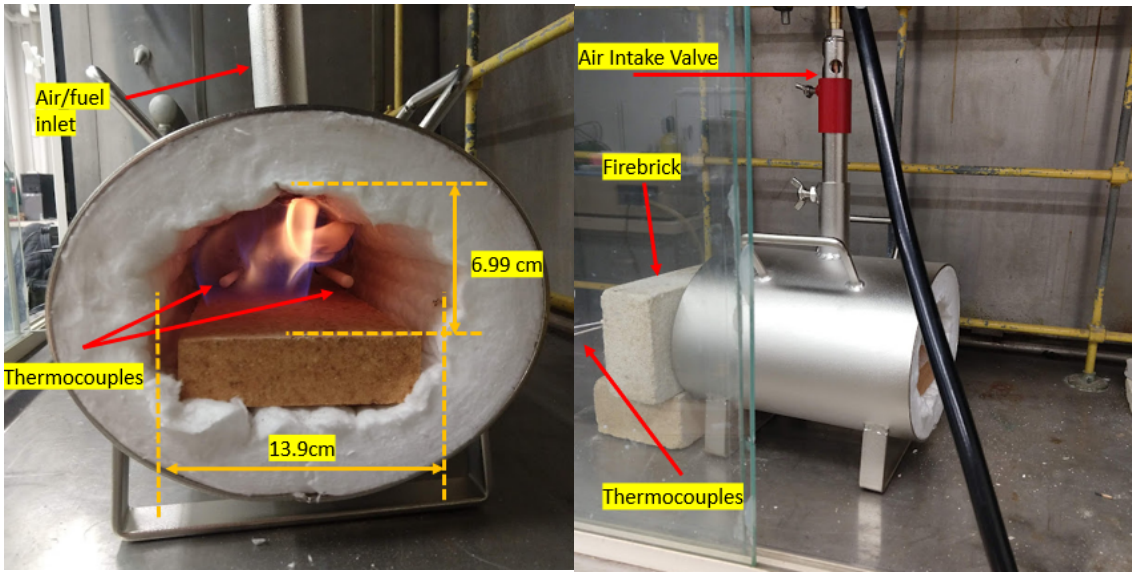

Figure 37. "Low" temperature flame test on SG50 (*left*). High temperature flame on SG50.Na (*right*). Note the glowing *left* thermocouple in the high temperature test.

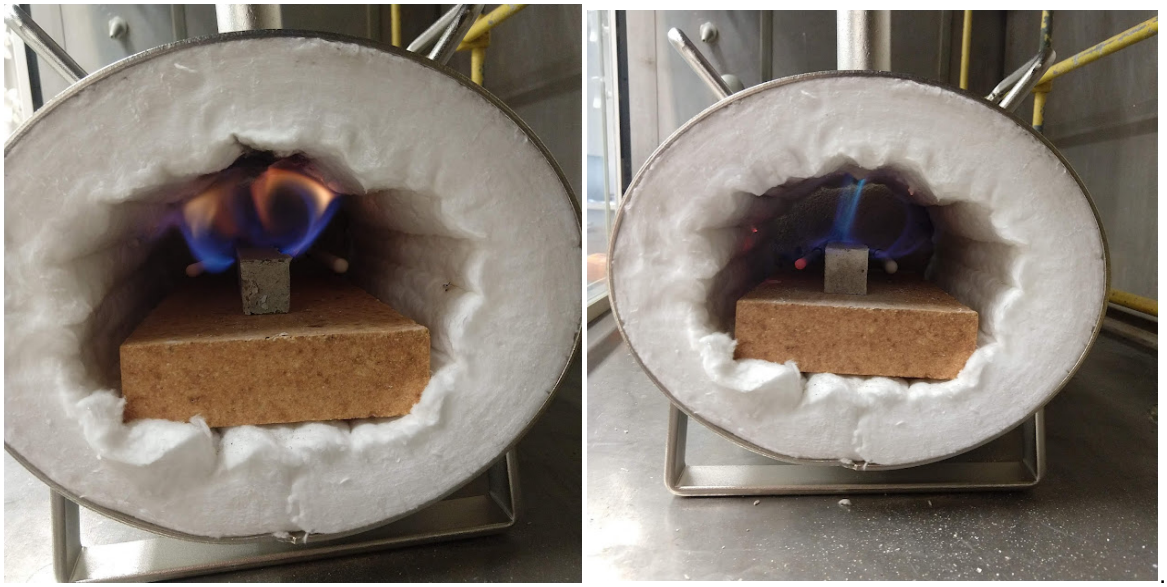

The presence of the specimens altered the flow of gas and caused a decrease in temperature of around 50°C to 100°C that was measured at the thermocouples. There was also a large temperature discrepancy between thermocouples due to the turbulent flow of the gas. See Table 24 below for more details.

Table 24. Range of temperatures (°C) at each setting for thermocouples TC1 (*left*) and TC2 (*right*).

	Empty chamber		Full chamber	
"High" setting	TC1: 795–850	TC2: 733–770	TC1: 712–740	TC2: 609–700
"Low" setting	TC1: 670–683	TC2: 328–402	TC1: 470–570	TC2: 320–350

The temperature of the flame can be approximated as 822°C for the high setting and 676°C for the low setting. This was done by averaging TC1 empty chamber thermocouple temperature ranges since the flame was directly in contact with this thermocouple.

The effect of the higher temperature led to a reduction in strength of about 0.5–1 MPa except for the 30 s SG50 sample, which saw no reduction in strength between the two temperatures tested (Table 25–Table 26 and Figure 38–Figure 39). KGP composite was slightly stronger than NaGP composite from 1 minute of torching onwards, which is expected since sodium GP undergoes more shrinkage and deformation compared to potassium after approximately 160°C (Lahoti et al. 2018). Shrinkage and cracking introduced flaws into the surface of the sample and caused it to fail at a lower load due to stress concentration and buildup. All the Na-based samples featured mm scale microcracks that occurred in the 0 s samples and grew in size after the heat treatments. The K-based samples were all free from visible microcracks, which explains the reduced strength in the Na-based samples.

Table 25. Flexure versus duration at approximately 676°C (intermediate temperature).

Sample	Sand	Gravel (<3/16 in.)	GP	0 s	30 s	1 min	2 min	5 min
SG50.Na	1	1	1	4.07 [0.58]	3.69 [0.32]	3.32 [0.72]	2.32 [0.20]	1.59 [0.47
SG50	1	1	1	4.29 [0.45]	3.77 [0.19]	3.96 [0.51]	3.12 [0.15]	2.53 [0.34]

Table 26. Flexure versus duration at approximately 822°C (high temperature).

Sample	Sand	Gravel (<3/16 in.)	GP	30 s	1 min	2 min	5 min
SG50.Na	1	1	1	3.03 [0.99]	2.59 [0.35]	1.76 [0.12]	0.97 [0.19]
SG50	1	1	1	3.69 [0.57]	3.42 [0.25]	2.03 [0.32]	1.45 [0.76]

Figure 38. Combined graph of flexure strength for sodium and potassium GP at low and high temperature.

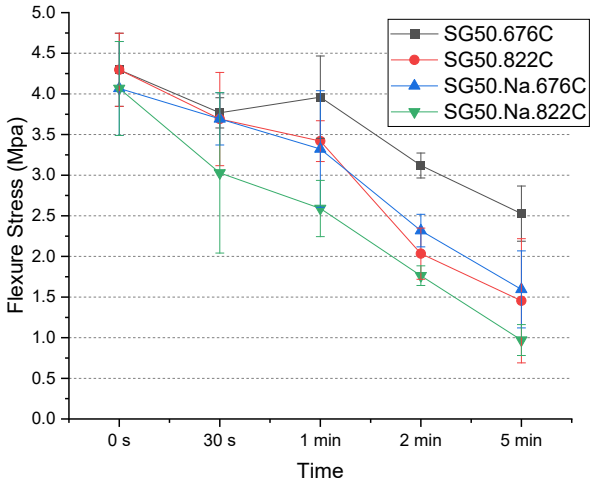

Figure 39. (*a*), Na versus K-based composite at low temperature; (*b*), Na versus K-based composite at high temperature; (*c*), K-based composite at low and high temperature; (*d*), Na-based composite at low and high temperature.

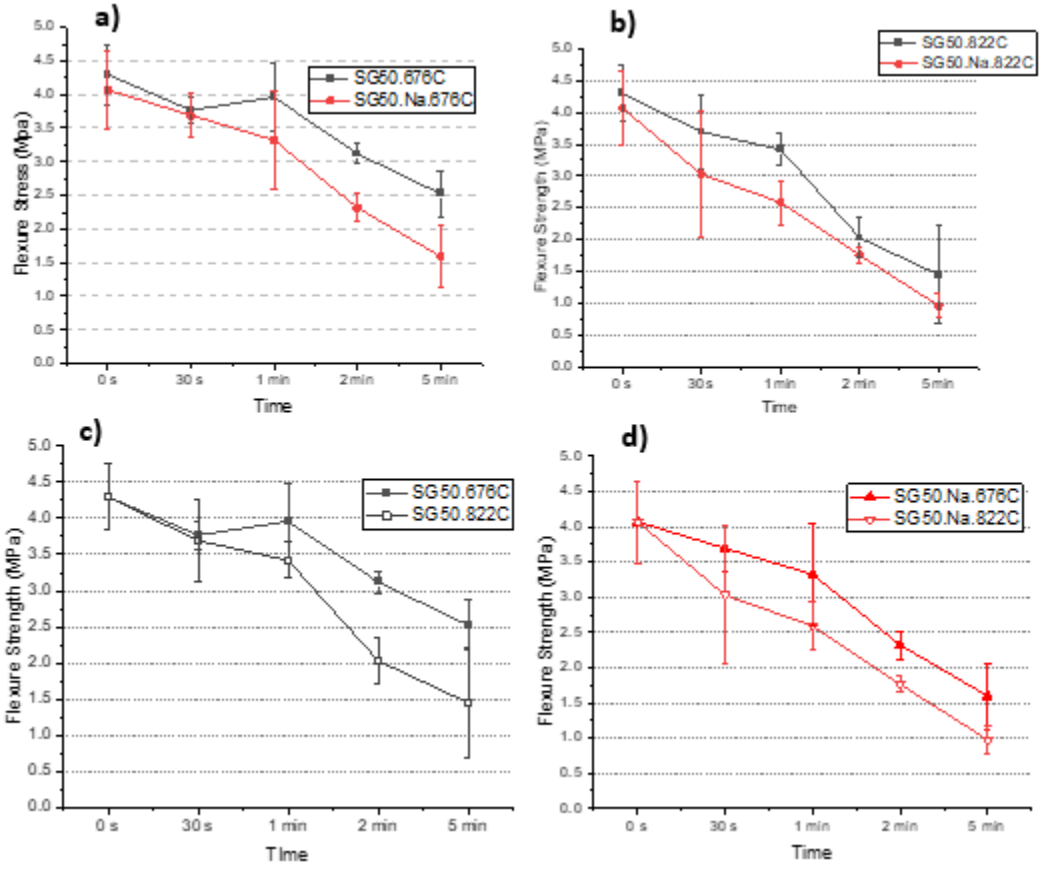

All samples steadily accumulated damage with time. After 5 minutes of heating, SG50 lost 41% and 66% of its strength at low and high temperature, respectively (Figure 40). SG50.Na lost 61% and 76% of its initial strength at low and high temperature, respectively (Figure 41). All the samples tested experienced brittle failure with a slow crack propagation that left the sample intact after failure.

Figure 40. Representative pictures of SG50 composite surfaces exposed to heat. Samples are 2.54 cm wide.

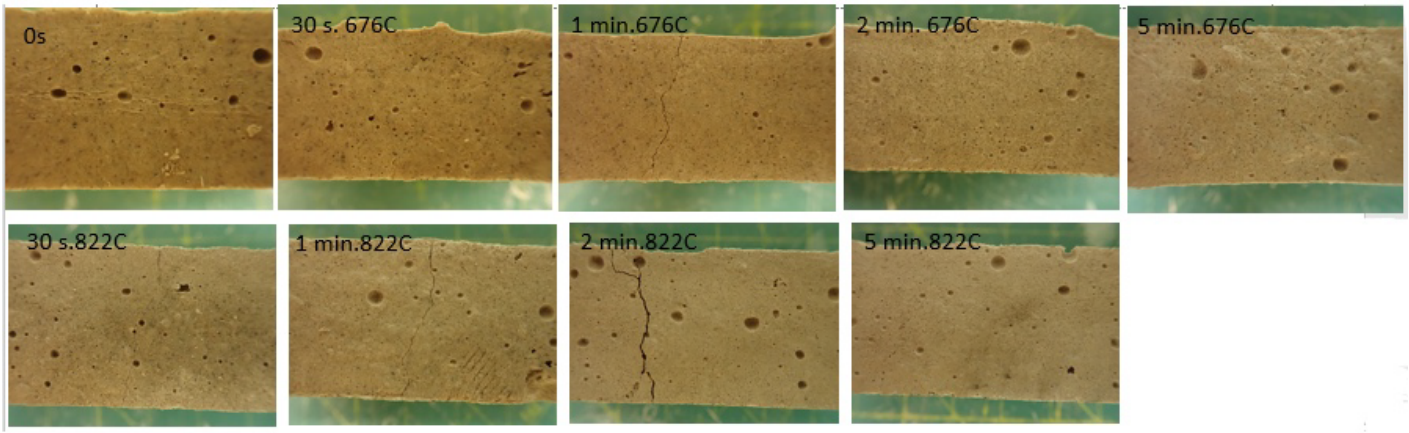

Figure 41. Representative pictures of SG50.Na composite surfaces exposed to heat.

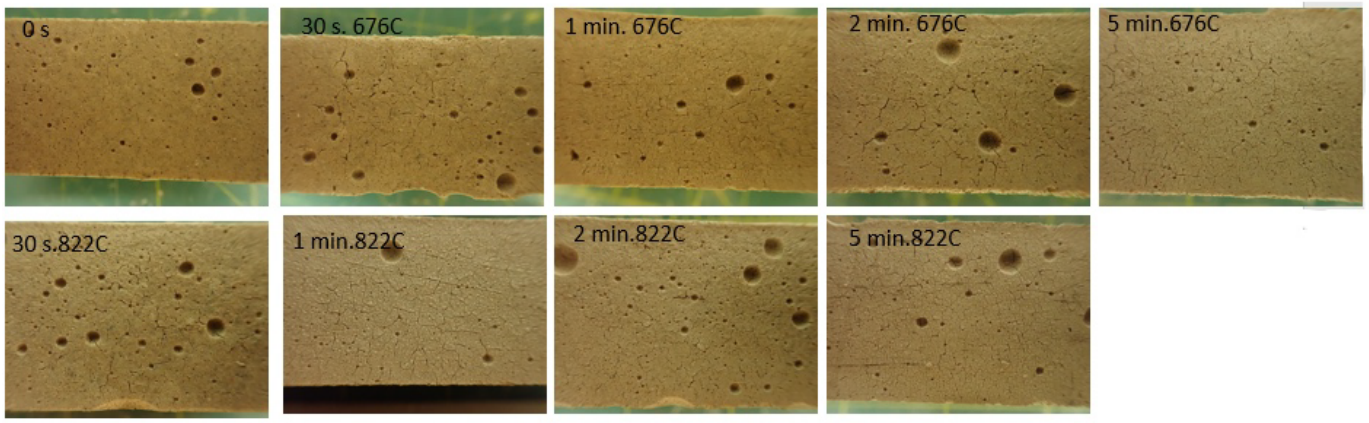

The unheated samples were beige in color due to dehydration of the fresh GP paste. GP cured under ideal conditions is white in color. Surfaces exposed to the torch became whiter in color, which likely occurred due to the dehydration of residual water. This color change is better depicted Figure A-8. The samples did not take on a reddish tinge or start to disintegrate as the SG50 samples seen in Figure 33, indicating that the decomposition and phase changes of the sand and gravel did not occur. Only one composition was tested here. It is feasible that increasing the

amount of sand and gravel or switching to a different aggregate would impact temperature resistance of the composite. In the case of increasing sand, the thermal conductivity would increase, which could have ranging effects depending on the fire conditions and structural geometry. A higher conductivity would increase the damage to the bulk of the sample in the case of a hot or long-lasting fire while avoiding surface damage in a low-intensity fire by diffusing concentrated heat away from surface thermal spots into the bulk of the material. Mix design for increased flame resistance could be the focus of future work.

2.4 Rheology

2.4.1 Methods and materials

The GP pastes used for the rheological testing were synthesized from water glass made with 85% pure potassium hydroxide flakes (ACROS Organic) or 93.5% pure potassium hydroxide flakes (Dudadiesel), amorphous silica fume (Cabot M-5 or Aerosil 200), and DI water. Most of the samples were created using Metamax HRM Metakaolin (referred to as Plain KGP) from BASF; however, other metakaolins used included Argical 1,200S, Powerpozz, Metamax EF, and Metastar 501 HP. The particle properties of the different type of metakaolins can be found in Table 5. The metakaolins and alkali silicate source were mixed in an identical manner as described in Section 2.1.1 . The ordinary Portland cement (OPC) mixture was QUIKRETE Type I/II Portland cement mix.

OPC samples were mixed with DI water and cement power at a ratio of 0.45 water/cement and sheared with a high shear impeller at 2,000 rpm for 5 minutes. All rheological experiments were run using the Discovery Hybrid 2 Rheometer (DHR2) from TA Instruments using a four-propeller vane rotor geometry and the “generic cup holder.” The vane rotor geometry is based on a concentric cylinder model, and the stress and strain constants had to specifically be calculated with the gray cylindrical cup used for testing. Figure 42 is an image of the four-propeller vane geometry that was used for rheological testing with the DHR2. Figure 43 shows the gray cylindrical cup used for testing and shows the generic cup holder, gray cup, vane rotor and rheometer set up for paste testing. The following equations were provided by TA Instruments for calibration purposes, and Table 27 shows the values measured and calculated for the constants. The accurate calculation of these constants is important, as they

are used when determining the stress put on the material system and determining properties, such as viscosity and torque on the system.

$$K_\gamma = \frac{(1+\delta^2)}{(\delta^2-1)}, \tag{11}$$

where

K_γ = strain constant ($\frac{1}{rad}$), and
δ = ratio of cup radius to vane radius.

$$K_\sigma = \frac{(1+\delta^2)}{(4\times\pi\times L\times {R_b}^2\times cL\times\delta^2)}, \tag{12}$$

where

K_σ = stress constant ($\frac{Pa}{N\times m}$),
δ = ratio of cup radius to vane radius,
R_b = radius of vane,
R_c = radius of cup, and
cL = 1.1 (given by TA Instruments).
L = length of vane in rotor

Table 27. List of measured or calculated constants for the vane geometry.

Variable	Value
R_b	0.014 m
R_c	0.02555 m
cL	1.1
d	1.825
L	0.042
K_γ	1.8581 ($\frac{1}{rad}$)
K_σ	11,426.598 ($\frac{Pa}{N\times m}$)

Figure 42. An image of the vane geometry used with the DHR2.

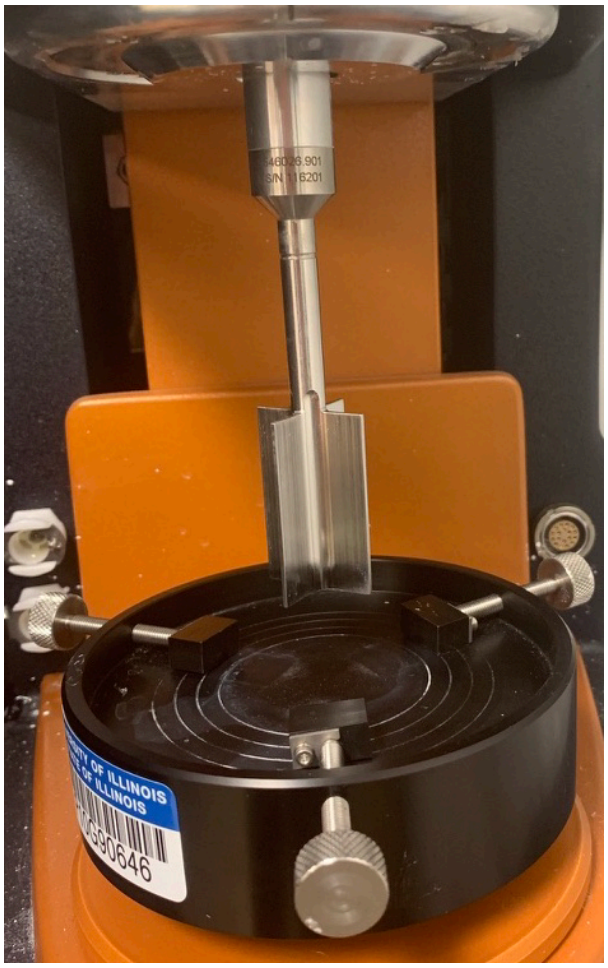

Figure 43. The gray cylindrical cup used for testing (*left*) and the generic cup holder in the rheometer with a sample of KGP (*right*).

All samples that were used for rheological testing endured a 60-second wait time, a 60-second 100 (1/s) preshear, followed by a 2-minute wait time before the start of any test to ensure each sample started with identical rheological history.

2.4.1.1 Power law model

One common way to assess the shear thinning capabilities of a material is to conduct a shear sweep and apply a power law model. This model can only be used for non-Newtonian fluids (viscosity varies with shear rate) and allows a numerical value to quantify the shear thinning capabilities of fluid. The power law equation is as follows:

$$\eta = m\dot{\Upsilon}^{n-1}, \tag{13}$$

where

η = viscosity in (Pa × s),
m = material constant known as consistency index (Pa × s²), and
n = power law index.

Shear thinning abilities are inversely proportional to the power law index. The closer the *n* value is to zero, the more a material is able to drop in viscosity when the shear rate is increased. For all shear thinning materials, the *n* values fall between numerical values of 0 and 1 (Berker 2002). While this model is useful for understanding the basic shear thinning properties of a paste, issues tend to arise with the addition of aggregates.

2.4.1.2 Herschel-Bulkley model

The Herschel-Bulkley (HB) model is a commonly applied model to calculate the yield stress of a fluid. While the yield stress of complex fluids (such as GP paste and OPC) is heavily dependent on the method of measurement, the HB model can be easily applied to a shear sweep experiment and compared to a stress ramp experiment to validate the yield stress values calculated with curve fitting. The HB model equation is as follows (Mullineux 2008):

$$\tau = K'\Upsilon^{n} + \tau_0, \quad (14)$$

where

τ = shear stress (Pa),
K = consistency index (Pa/s),
Υ = shear rate (1/s),
n = flow behavior index (HB Index), and
τ_0 = yield Stress (Pa).

In addition to the rotational rheometer, flow experiments were conducted using a squeeze flow test for highly reinforced compositions (Grandes et al. 2018). The squeeze flow samples were tested on an Instron machine with a flat cylindrical head (45.5 mm diameter) and a 50 kN load cell. Each paste sample was formed into a cylinder of approximately 46 mm diameter and 15 mm height for testing. An image of the experimental set up is shown in Figure 44.

Figure 44. Image of the squeeze flow experimental set up for a sample of KGP reinforced with 60 wt% Quikrete sand and 3 wt%, 1/2 in. basalt fibers.

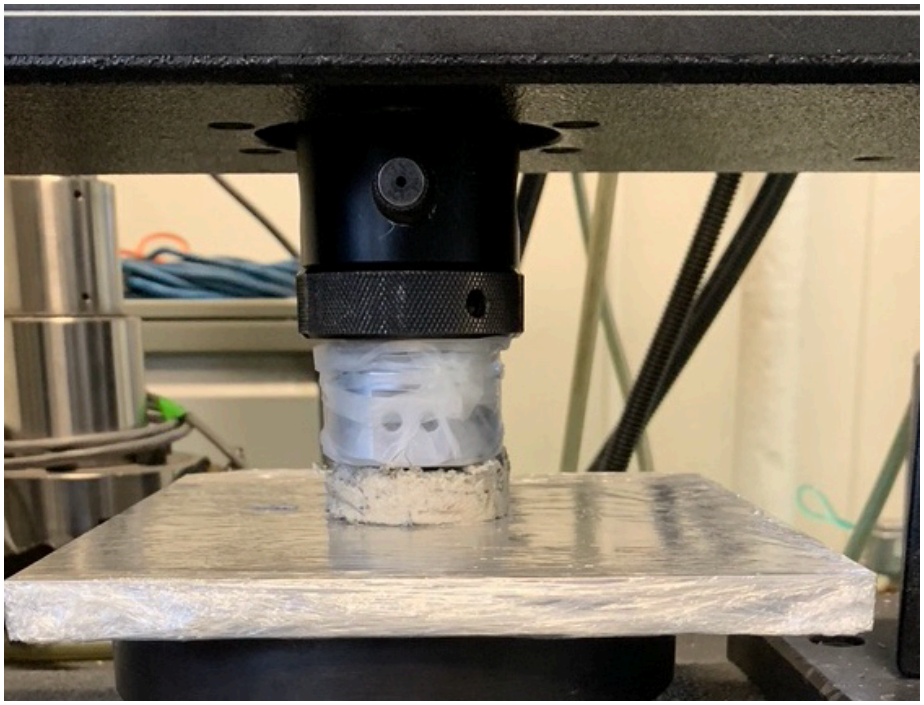

Each composition was tested five times consecutively to account for any inhomogeneous deformation and small variations in sample uniformity. After each squeeze flow trial was finished, the paste was removed from the

bottom metal plate and placed back in the paste container, firmly mixed by hand with a spatula for 15 seconds, and then reshaped into the squeeze flow test geometry. For a foundational understanding of the flow properties, the five trials were averaged into one line using a power law approximation. Squeeze flow rates of both 0.1 mm/s and 1.0 mm/s were tested for a variety of compositions.

The underlying goal of the squeeze flow test is to assess the amount of stress required for a certain amount of displacement for a composite, which is useful in determining the required strength for shape retention and printing. This also provides a quantitative measurement for how the weight of subsequential layers might affect the bottom layer of a printed structure.

2.4.2 Experimental matrix

Table 28 lists the various types of rheological experiments used for this study.

Table 28. A matrix of possible rheological experiments and an explanation of goal and variables.

Experiment name	Description	Goal	Independent variable	Dependent variables of interest	Constants
Shear Sweep	Increasing the shear rate at certain increments to understand non-Newtonian properties	Power law index measurement, proof of shear thinning, thickening, or Newtonian behavior. Also measures the yield stress with HB model	Shear Rate (1/s)	Viscosity, Stress	N/A
Stress Ramp	Increasing the stress from zero to a certain maximum	Find the yield stress of a material and prove thixotropy	Stress (Pa)	Shear Rate, Viscosity	N/A
Constant Shear	Hold material at a constant shear rate for a certain increment of time	Understand the effect of time on viscosity or stress —could find thixotropy, rheopexy, or Newtonian behavior	Time (s/min/hr)	Stress, Viscosity	Shear Rate (1/s)

Experiment name	Description	Goal	Independent variable	Dependent variables of interest	Constants
Constant Oscillatory Motion	Hold material at a constant frequency for a certain period of time	Understand the effect of time on liquid- and solid-like behavior of the fluid	Time (s/min/hr)	Storage and Loss Modulus, Tan Delta, Potentially Viscosity	Frequency (Hz)
Oscillatory Sweep	Increase the frequency at certain increments to understand the material response	Understand how solid- and liquid-like behavior changes at different oscillating frequencies	Frequency (Hz) or Angular Frequency (rad/s)	Storage and Loss Modulus, Tan Delta, Potentially Viscosity	N/A
Low, High, Low Shear Rate	Hold material at low shear rate for a segment of time, hold at higher shear rate for same time followed by another low shear rate segment identical to the first one	Understand material response and recovery time to a period of high shear (used for thixotropy)	Time (s/min/hr) and Strain Rate	Viscosity and Stress	N/A
Strain Oscillatory Sweep	Hold material at a constant frequency for a certain period of time but also simultaneously increase the strain percentage at which the material oscillates	Understand the effect of strain percentage on oscillatory data, determine the LVER	Time (s/min/hr) and Strain Percentage	Storage and Loss Modulus, Potentially Viscosity, Potentially Torque	Frequency (Hz)

2.4.3 Rheological results and discussion

The results of the rheological testing are separated into fiver topics: shear sweep, stress ramp, constant shear, oscillatory testing, and viscosity recovery that correlate to the experiment type.

2.4.3.1 Shear sweep

Shear sweep experiments consist of recording the viscosity and stress of a material as the shear rate is varied. For the research team's experimental purposes, a shear rate loop was used for understanding any possible hysteresis effects on either stress or viscosity for each sample. The shear rate was increased from 0.001 (1/s) to 150 (1/s), decreased from 150 (1/s) to 0.001 (1/s), and cycled through the ramping and down segment one more time. Five measurements were made per decade of shear rate, and

each data point was allowed to equilibrate for 10 second followed by a 20 second measurement segment. A visual of the shear rate versus time lapse for the shear sweep experiments is shown in Figure 45. From the shear sweep data, researchers were able to apply the power law model mentioned in Section 2.4.1.1 and the Herschel-Bulkley model that is mentioned in Section 2.4.1.2 .

Figure 45. A visual of the shear sweep experiment as a function of time.

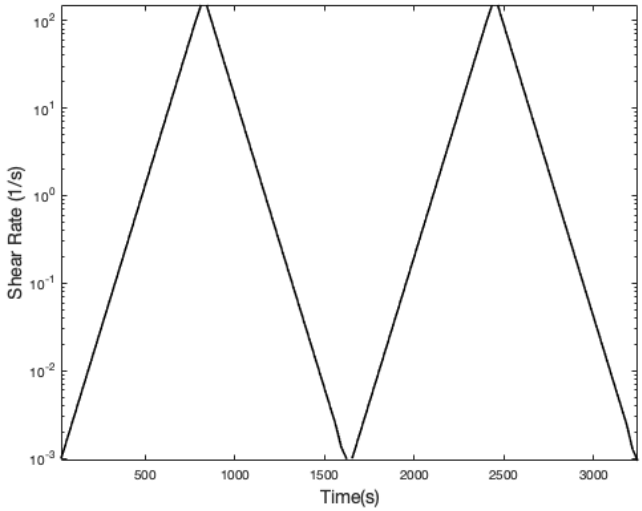

The goal of this type of experiment is to characterize the basic rheological properties of each KGP paste and compare the relative viscosities at different shear rates. A compilation of the various types of metakaolin pastes and the single OPC paste tested are shown in Figure 46, where each material has four lines, two of which being the ramp segments and two being the down segments of the shear sweep. All four lines are included to show consistency and general viscosity trends.

Figure 46. Shear sweep data for the various pastes tested.

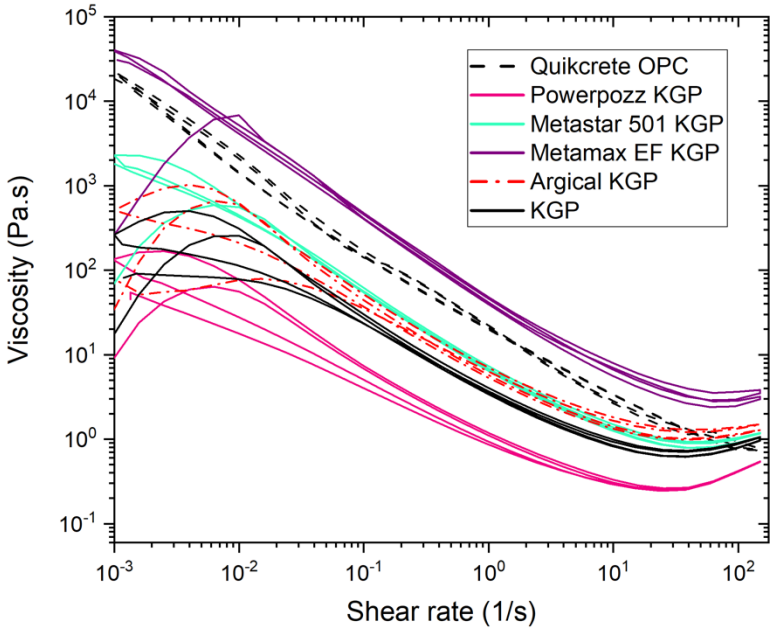

The decrease in viscosity with an increase in shear rate is proof of the KGP pastes and OPC pastes being non-Newtonian shear thinning fluids. There are, however, two areas of interest to note at the edges of the shear rate range. Between 10^{-3} and 10^{-2} 1/s shear rates, some of the viscosities underwent a slight increase before the typical shear thinning decrease in viscosity, and this was likely due to inertia effects or the rheometer still being below the yield stress. On reaching the yield stress, the material started to flow and exhibited a decrease in viscosity. The second area of interest pertains to the shear rates above 10^{1} 1/s. In samples such as the Powerpozz KGP, another increase in viscosity is displayed at the higher shear rates, and this was likely due to the onset of turbulent flow or some kind of secondary flow mechanism as a result of greater stress and shear applied to the system. For each of the four segments, the Herschel Bulkley model was applied and averaged, but the power law model was applied and averaged for all segments except ramp 1 to eliminate the influence of surpassing the yield stress for the first time. A compilation of the calculated yield stresses from the Hershel Bulkley model is displayed in Table 29 and the calculated power law indexes are shown in Table 30.

Table 29. Yield stresses measured with the Hershel-Bulkley Model.

System	YS by average of HB model (Pa)
Metamax KGP	2.777
Argical KGP	4.313
Powerpozz KGP	0.845
Metastar 501 HP KGP	5.7495
Metamax EF KGP	44.430
Quikrete OPC	17.900

As a general trend shown with the shear sweep curve and the approximated yield stresses interpolated by the HB model, larger particle sizes resulted in a lower viscosity and a lower yield stress. This was likely due to the decrease in particle surface area with an increase in particle size, resulting in less internal friction between each metakaolin particle.

Table 30. Power law indexes of various metakaolin systems.

System	Power law index (*n*)
Metamax KGP	0.650
Argical KGP	0.620
Powerpozz KGP	0.413
Metastar 501 HP KGP	0.371
Metamax EF	0.140
Quikrete OPC	N/A

As for the power law index, the research team hypothesizes that the index is greatly affected by the starting magnitude of viscosity and potentially particle size. This is best reflected by the Metamax EF data, which have the smallest particle size and also the smallest power law index; however, a more general trend needs to be investigated as this theory does not align with some of the other metakaolin samples. The OPC sample did not fit the power law model well and resulted in a negative power law index, which does not fit the limitations set by the equation. Appendix B lists all the shear sweep (power law and Hershel Bulkley model) values.

2.4.3.2 Stress ramp

For stress ramp experiments, a linearly increasing stress was applied to the material during a 60-second time interval. Similar to the shear sweep experiments, these also had alternating ramp and down segments for two total stress cycles, but the first cycle was used for measuring yield stress, and both segments together were used for observing thixotropy. The maximum stress applied varied for each material system, but the maximum stress was ensured to be above the yield stress of the testing material. An example of the first ramping segment of a plain KGP pastes is shown in Figure 47. The point at which the viscosity reaches a maximum and starts to decrease is where the yield stress is found. A *red-dotted line* represents where the maximum viscosity is found, and the intersection with the stress values is the yield stress. The measured yield stress values from stress ramp experiments are shown in Table 31.

Figure 47. A viscosity and stress versus shear rate plot of a plain KGP paste.

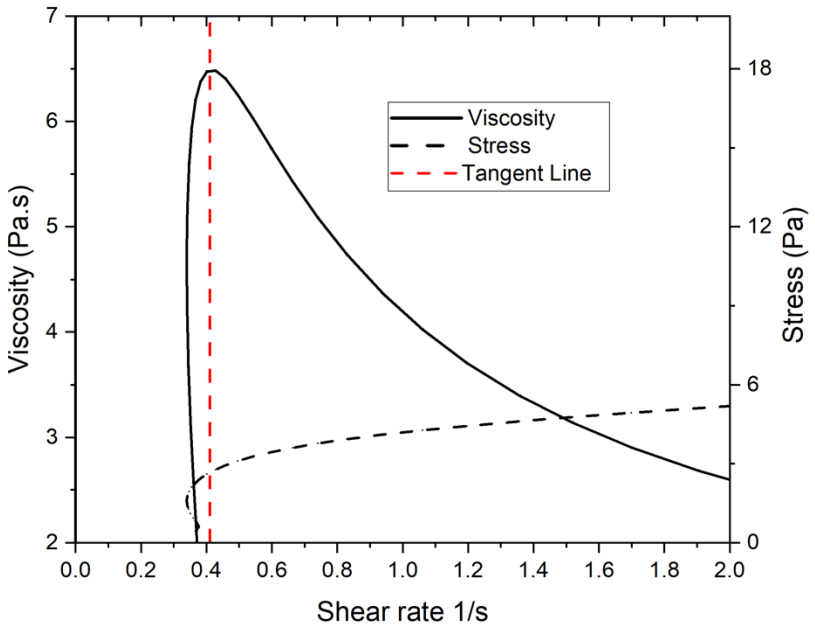

Table 31. The yield stresses of various pastes found by stress ramp experiments.

System	Yield stress (Pa)
Metamax KGP	2.884
Argical KGP	4.544
Powerpozz KGP	1.222
Metastar 501 HP KGP	7.537
Metamax EF KGP	57.67
Quikrete OPC	12.18

Similar to the HB model, the values measured with the stress ramp experiment also reflect that smaller particle sizes lead to greater yield stresses. When comparing the two models, they are relatively close at low stress and tend to differ more at higher applied stresses. This is likely due to the interpolation of the HB model versus the direct measuring of yielding with the stress ramp experiment. Figure 48 shows a direct comparison of the two models for each metakaolin used for a GP.

Figure 48. Stress ramp yield stress and HB model yield stresses of various metakaolin KGPs.

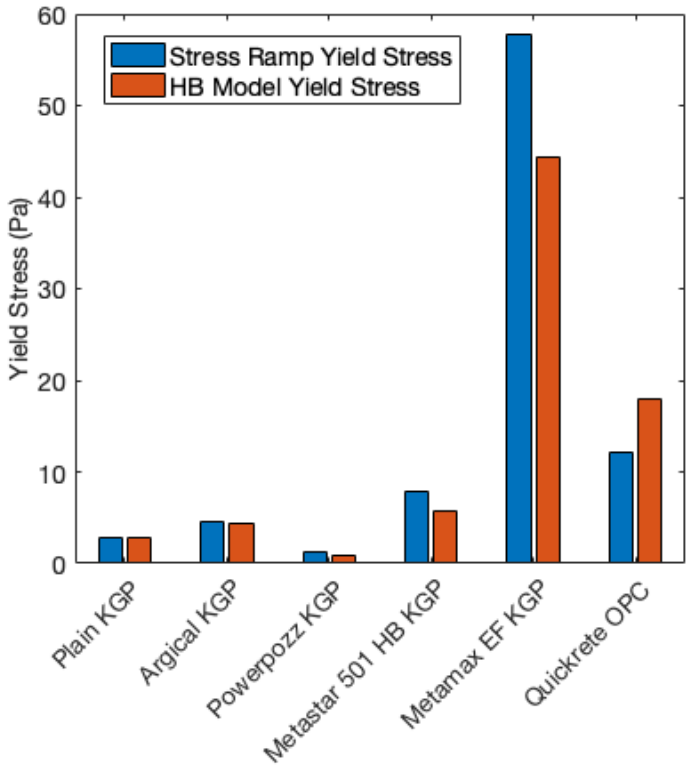

In addition to observing the yield stresses, stress ramp experiments are also able to assess thixotropy. The ramp and down segments of a plain KGP paste are shown in Figure 49. The area between the ramp and down

segment is thought to be known as the thixotropic index, or a value to determine the strength of the thixotropic properties. The greater the area between the ramp and down stress curve, the more the material exhibits thixotropy.

Figure 49. A stress versus shear rate graph for a stress ramp of a plain KGP paste.

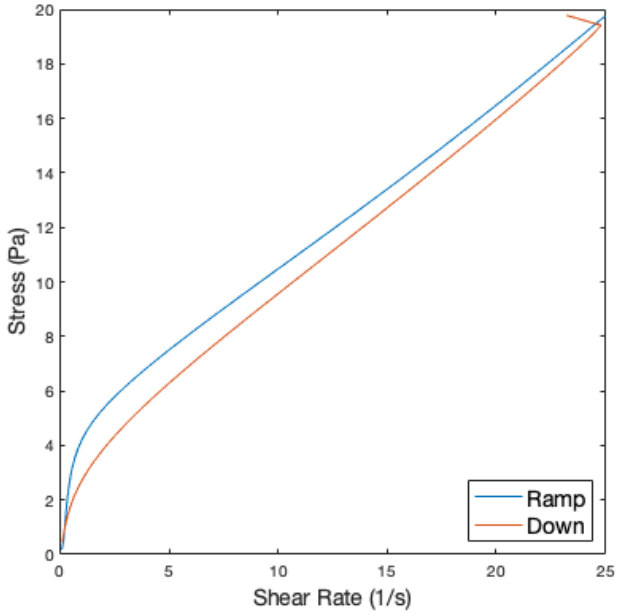

To gain an even better understanding of the differences between the two yield stress models, a sand study was conducted using Quikrete sand (Q) and coarse sand (CS) on both KGP and OPC. During this study, the stress ramp experiments and shear sweep experiments were conducted on OPC or KGP paste with increasing weight percentages of fine sand, coarse sand, or a mixture of the two. From these experiments, the yield stresses were measured or calculated and compared for an understanding of how to interpret the values received by both models. Table 32 is a compilation of the fine versus coarse sand study conducted in both KGP and OPC paste. All OPC pastes were made with a water to cement ratio of 0.45. Figure 50 and Figure 51 are a visual depiction of all the yield stress values for KGP and OPC with various weight percentages and types of sand.

Table 32. Yield stress values from stress ramp testing and Herschel-Bulkley model.

Material system	Yield stress (Pa)	Herschel-Bulkley yield stress (Pa)
Metamax KGP	2.88	2.78
KGP 10 wt% Q	11.53	7.02
KGP 20 wt% Q	9.31	8.44
KGP 30 wt% Q	9.31	8.49
KGP 40 wt% Q	9.721	10.686
KGP 50 wt% Q	10.54	11.190
KGP 60 wt% Q	17.2	19.370
KGP 10 wt% CS	8.82	7.44
KGP 20 wt% CS	10.32	9.07
KGP 30 wt% CS	9.83	9.20
KGP 40 wt% CS	9.721	11.081
KGP 50 wt% CS	12.18	17.830
KGP 60 wt% CS	19.66	34.730
KGP 10 wt% CS + 10 wt% Q	8.82	7.27
KGP 15 wt% CS + 15 wt% Q	9.30	8.76
Quikrete OPC	12.18	17.90
OPC 10 wt% Q	16.38	21.72
OPC 20 wt% Q	18.02	25.08
OPC 30 wt% Q	20.53	30.92
OPC 40 wt% Q	26.61	38.65
OPC 50 wt% Q	36.04	55.218
OPC 60 wt% Q	68.81	122.970
OPC 10 wt% CS	15.510	19.898
OPC 20 wt% CS	21.35	27.41
OPC 30 wt% CS	30.67	38.47
OPC 40 wt% CS	43.50	58.59
OPC 50 wt% CS	79.13	113.543
OPC 60 wt% CS	297.00	197.50
OPC 10 wt% CS + 10 wt% Q	14.04	25.840
OPC 10 wt% CS + 10 wt% Q	20.53	32.478

Figure 50. Yield stress values for KGP composites and various sand.

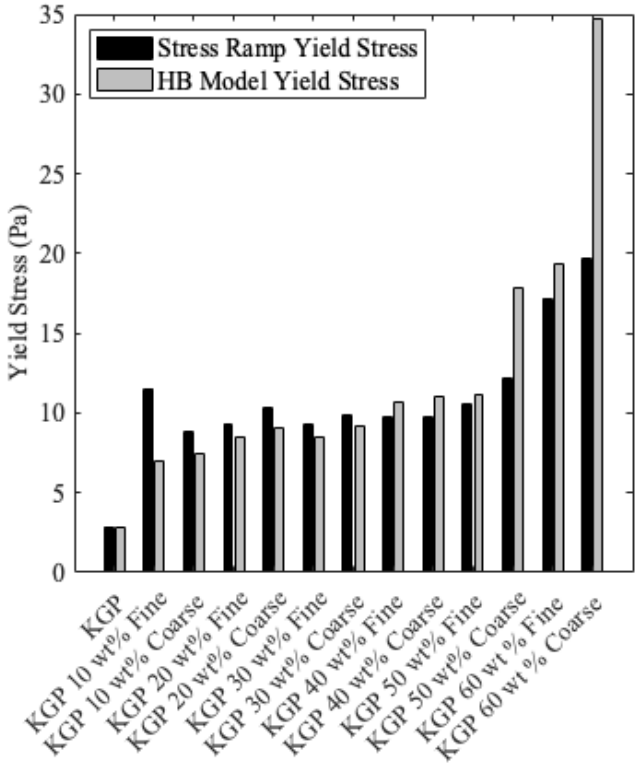

Figure 51. Yield stress values for OPC composites and various sand.

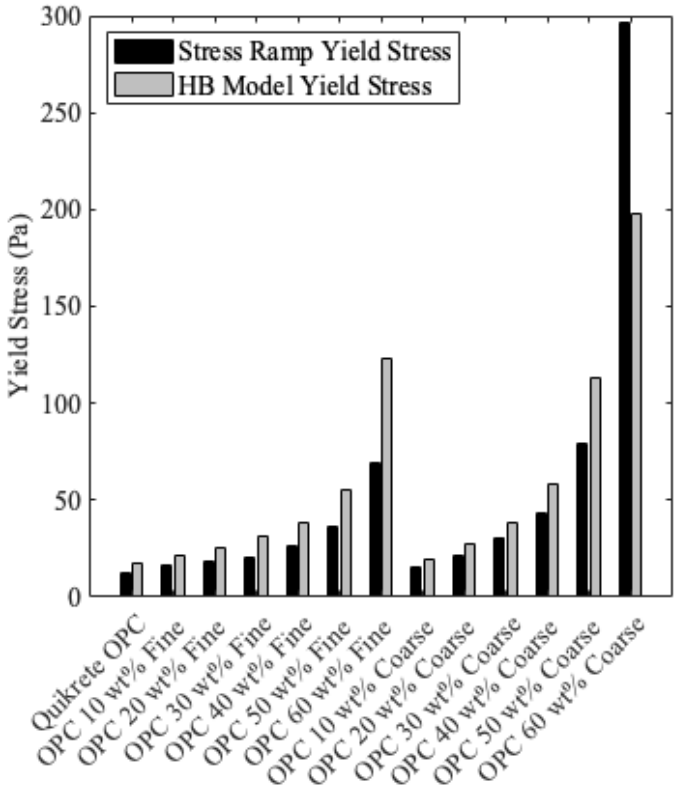

In a similar fashion to the plain metakaolin GP, the models started to vary at high stresses. In relevance to the addition of sand, the higher weight percentages of reinforcement (in this case sand) reflect even greater variance again from the models. This phenomenon was likely due to several reasons. The size of the sand particles varied slightly with each sample; however, the overall size distribution of the coarse sand was greater than the Quikrete medium sand. If one of the larger aggregates hit one of the four vane propellers during testing, it would likely drive up the yield stress. The Quikrete sand distribution was more homogeneous, reducing the possibility of hitting a larger sand particle that would drastically increase the yield stress. The variance in values between the two models could also result from the difference in testing methods, stress ramp being more direct and instantaneous and the Herschel-Bulkley model resulting from data interpolation that is over four different segments, which is more time intensive. Overall, the yield stress values for OPC were much higher than for KGP, and to attain good shape retention, much reinforcement must be added, and other reinforcement than sand must be added.

2.4.3.3 Constant shear

Constant shear rheological experiments hold a paste at a certain shear rate for an extended period, which allows researchers to investigate any change in rheological properties with respect to time. For a basic understanding of the constant shear properties of OPC and plain KGP, each material system was held at 10, 50, and 100 (1/s) for 100 minutes following the preshear and 2-minute wait time. Figure 52 shows the response of 0.45 w/c OPC to constant shear, and Figure 53 shows the rheological response of Metamax KGP (plain KGP) to the constant shear experiment.

Figure 52. A viscosity versus time curve for OPC held at a constant shear.

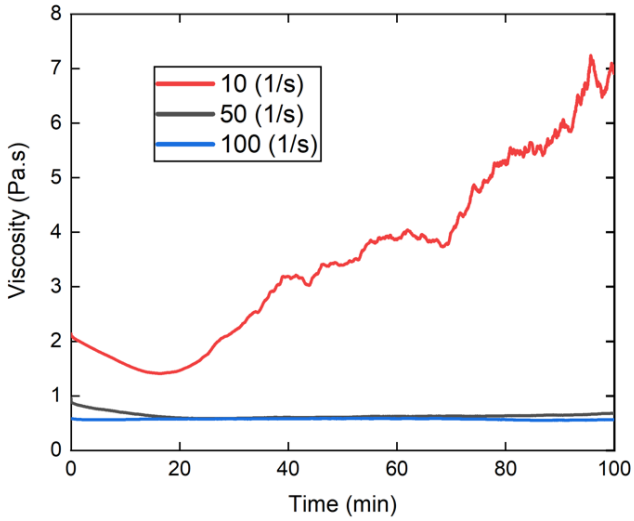

Figure 53. Initial viscosity versus time curve for KGP.

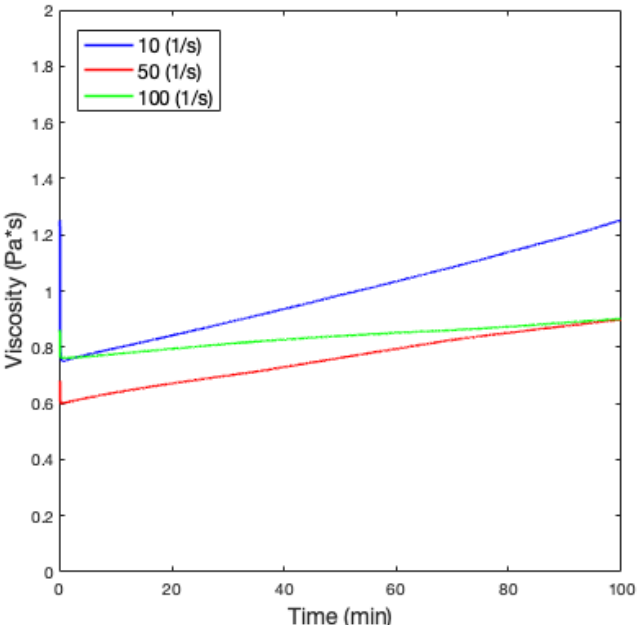

Difficulty interpreting constant shear data results from the competing mechanisms of thixotropy, setting, dissolution of ions, and polycondensation in either OPC or GP. In Figure 52, the 10 1/s sample of OPC exhibits a large drop in viscosity that hits a minimum around the 18–20-minute time mark. These data reflect a time-dependent decrease in viscosity as a result of constant shear, which falls under the basic characterization of thixotropic materials (Larson and Larson 1999). The 50 1/s sample also reflects a time-dependent decrease in viscosity with a minimum again around the 18–20-minute mark; however, the overall

drop in viscosity is not as significant as seen with the 10 1/s sample of OPC. The higher viscosity for the lower shear rate reflects the shear thinning properties of the OPC paste, but the magnitude of the viscosity drop cannot be fully explained without further investigation. It is possible that sedimentation or separation of cement and water powder was occurring, but that would likely lead to an increase in viscosity instead of a decrease. The 100 1/s OPC sample does not reflect any drop in viscosity with elapsed time, but this is likely due to the heightened shear rate, which is on the cusp of secondary fluid motion and around the onset of turbulent flow for OPC.

The GP samples in Figure 53 reflect a very small drop in viscosity right after the start of flow occurred, which was likely due to the breakage of an interconnected GP network that formed during the rest time after preshear. This drop can loosely be interpreted as evidence of thixotropy, but further exploration for differences in various shear rates was necessary for a better understanding. The current definitions of thixotropy define a time dependence but do not define the extent of time that must pass. The viscosity magnitudes followed the expected trend for shear thinning materials; at lower shear rates the viscosity was higher, and the reverse being true for low shear rates.

It was initially understood that thixotropy was evident in the very small drop that happened at the start of the experiment for the three shear rates tested and the increase in viscosity resulted from the chemical setting of the material. Further experimentation was necessary for a better understanding of the change in viscosity resulting from the constant shear. To further explore these properties, a second constant shear experiment test was conducted at shear rates of 10, 25, 50, 100, 150, 200, and 250 1/s for 60 minutes with a 15-minute wait time after preshear to allow for some amount of thixotropic restructuring to occur. The second set of constant shear experiments are shown in Figure 54.

Figure 54. Further investigation for constant shear KGP.

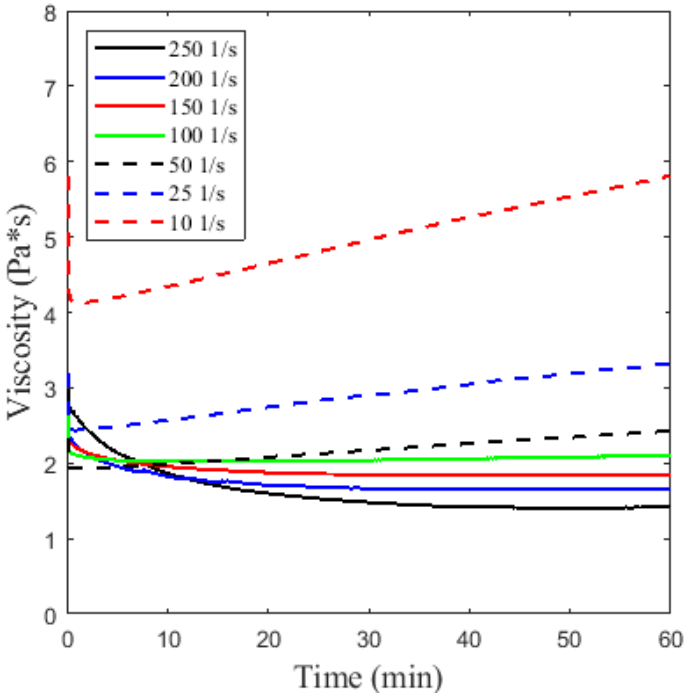

For the constant shear experiments, the research team could identify a critical shear rate of 100 1/s needed to disturb the fluid structure enough and cause breakdown, which contributed to the drop in viscosity. If the research team first examined the lower shear rates for the second trial (10, 25, and 50 1/s), the viscosity gradually increased as the test time progressed, as shown also in the initial rounds of constant shear data (validate repeatability). The shear rate that the GP paste was being subjected to was not great enough to disturb the fluid structure or halt the onset of the chemical reaction of setting GPs. At a shear rate of 150 1/s, a small, but notable, decrease in viscosity occurred during the first 30 minutes of shearing, indicating that the rate of shear undergone by the sample was great enough to disturb the fluid, breaking physical structures that formed or any polymerization that may have occurred during the 15-minute wait period after preshear. The slope of the 150 1/s line eventually goes to zero due to full disruption and no structure in the fluid remaining. The same result followed for the 200 1/s rate sample, with a greater overall drop in viscosity due to the greater amount of shear exerted on the sample. The 250 1/s rate sample follows suit with the trend; however, at this shear rate, the fluid had reached the point where it was influenced by turbulent or secondary flows, the effect of which is unknown.

2.4.3.4 Oscillatory testing

To determine the LVER and critical strain of GPs and OPC, amplitude sweeps were performed. Each amplitude sweep was conducted at a frequency of 1 Hz and consisted of two up and down ramps from strain percentages of 0.0001% strain to 10% strain. Like the shear sweep data collection parameters, five measurements were made per decade of strain percentage and each data point was allowed to equilibrate for 10 seconds followed by a 20-second measurement segment. Figure 55 shows the storage and low modulus for the first ramping segment of OPC. A strain sweep was tested on both the OPC and various GP pastes, and the limit of the LVER for OPC and KGP pastes was found to be 0.1 strain percentage. Measuring this value allows researchers to design further oscillatory experiments that eliminate magnitude of strain as a variable of storage and loss modulus.

Figure 55. The LVER of an OPC sample.

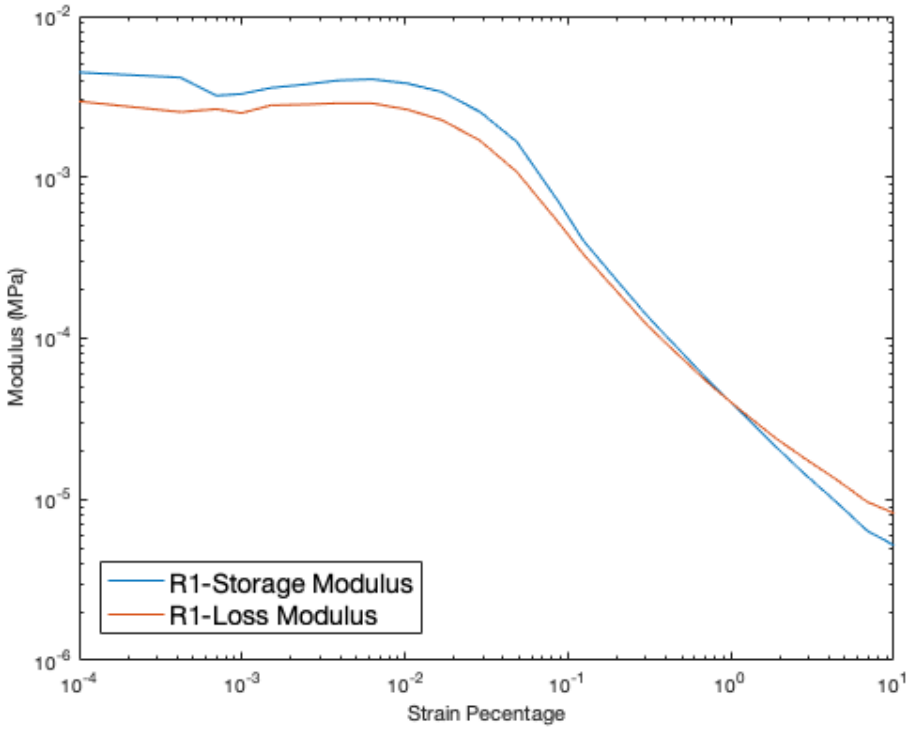

For determination of network formation features of KGP, a time sweep was conducted on fresh paste. This experiment consisted of the standard preshear with an immediate oscillatory experimentation period conducted at 0.01 strain percentage and 1 Hz frequency for 180 minutes. No wait time was included to ensure the restructuring behavior immediately after

shear could be observed. Figure 56 shows the results from the oscillatory time sweep experiment.

Figure 56. KGP paste oscillatory measurement results at 0.01 strain % and 1 Hz frequency.

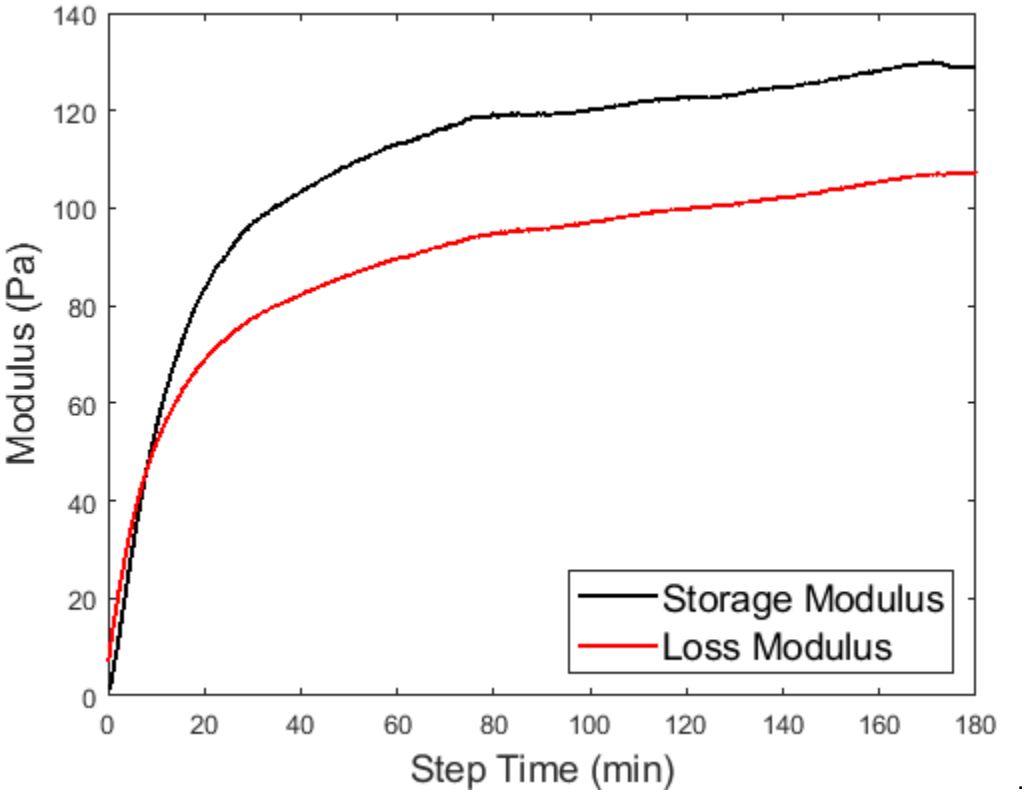

A crossover between the storage and loss modulus occurs around 8 minutes, indicating some sort of gelation or network restructure has occurred. The storage and loss modulus indicate the amount of energy stored (solid-like behavior) and dissipated energy (liquid-like behavior), respectively. The crossover further indicates that the GP has become more solid-like in nature, and the linear slope region from 0 to 20 minutes also indicates the increase in network structure occurring immediately after high shear. Another key feature is the decrease in slope around 30 minutes, which likely indicates the structure of the GP having formed and the start of the polymerization process.

2.4.3.5 Viscosity recovery

Viscosity recovery experiments were conducted by holding a sample at a low shear rate for a set period of time, followed by a much higher shear rate, followed by a third step that holds the material back at the original

low shear rate once again (Anton Paar, “Basics of Thixotropy, ”n.d.). A visual of the varying shear rate at certain time intervals is shown in Figure 57.

Figure 57. A visual depiction of the viscosity recovery experimental procedure.

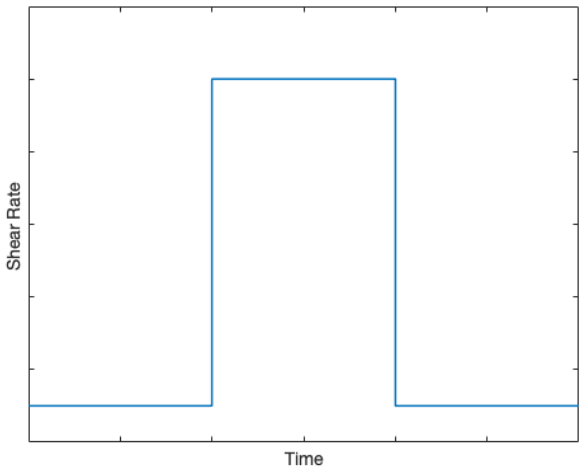

The underlying goal was to measure the recovery time of the paste when sheared for different lengths of time. Figure 58 shows a GP sample that was held at 5, 10, and 15 minutes for each of the three segments. The two low shear rate segments were at 1 1/s, and the high shear rate segment was held at 100 1/s. A tangent line was drawn on the second low shear rate segment to determine recovery time. Table 33 is a compiled list of the recovery time measured for various increments of time, only for plain KGP paste, to get a general idea of recovery time trends.

Figure 58. Viscosity versus time curves for viscosity recovery of a KGP paste at 5 minutes (*left*), 10 minutes (*middle*), and 15 minutes (*right*).

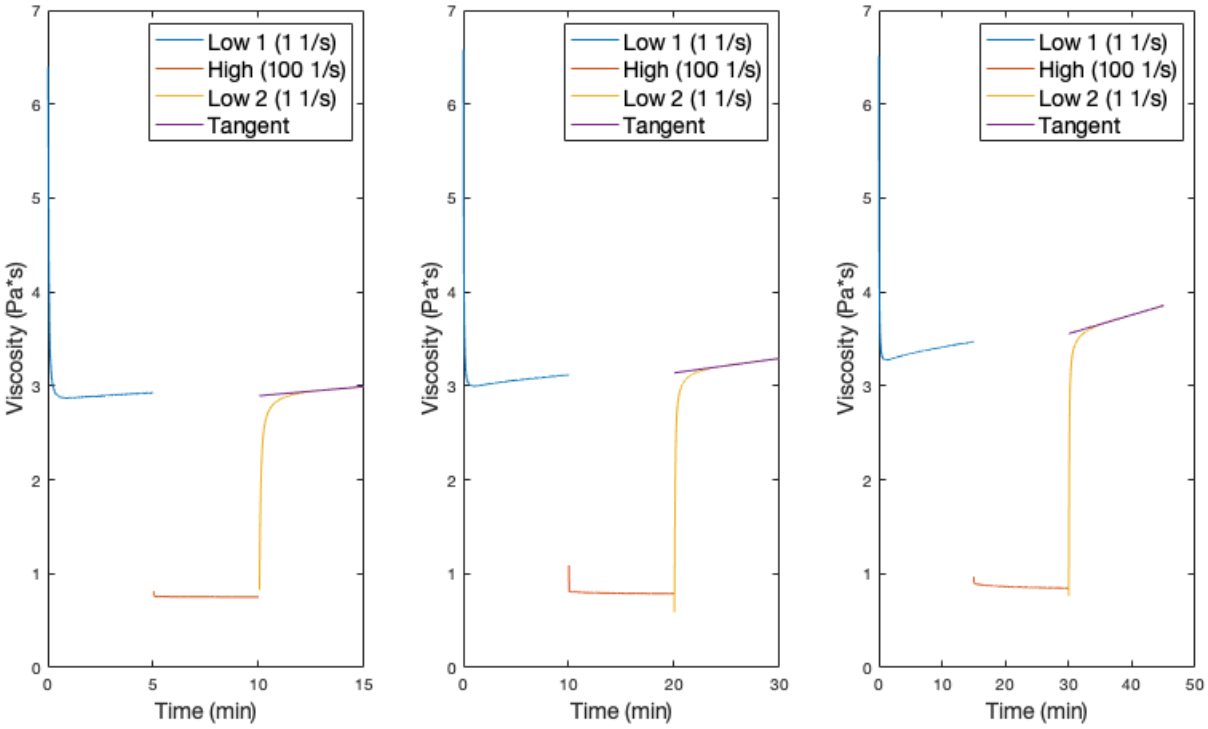

Table 33. Recovery time data for plain KGP pastes.

Constant shear time (mins)	Recovery time (s)	Recovery time (mins)	Recovery % of shear time (1 step)
1	34.02	0.567	57%
2	49.02	0.817	41%
5	118.2	1.97	39%
10	202.2	3.37	34%
15	243	4.05	27%
20	334.8	5.58	28%
25	439.8	7.33	29%
30	502.8	8.38	28%

Smaller constant shear times (such as 1, 2, and 5 minutes) took an overall longer percentage of time to recovery in terms of percentage of time sheared. However, at constant shear times above 10 minutes, the recovery time seemed to equilibrate around approximately 30% of the total high shear rate shear time. This was likely due to the amount of network destruction that occurred during the high shear rate segment of testing. The longer the paste was allowed to shear at the 100 1/s rate, the less able the GP was to start forming its 3D polymeric network. This information is

crucial for understanding the recovery time for GPs when at a high rate of shear to revert back to low shear rate viscosity.

2.4.3.6 Shape retention

Basic shape retention testing was conducted using a small 3D-printed polymeric cone with the dimensions of top radius being 25.28 mm, bottom radius being 33.98 mm, and the height being 6 cm. An image of the shape retention cone is shown in Figure 59. The cone was designed and 3D printed by Andrij Kozych.

Figure 59. Cone used for qualitative shape retention testing of GP composites.

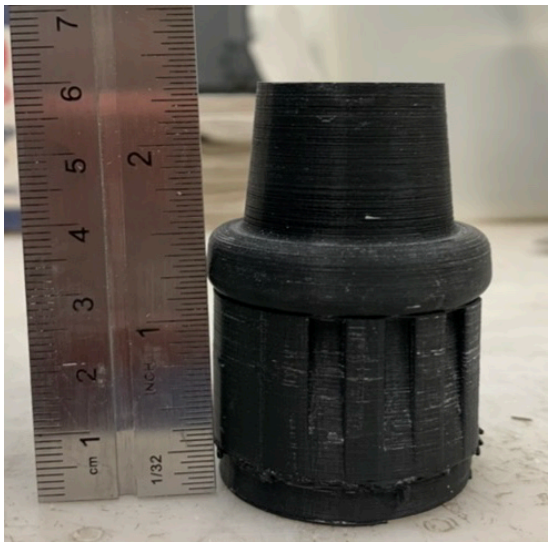

The primary goal of the qualitative shape retention testing was to gain a foundational understanding for how different particle sizes, components, and weight percentages impact the ability of the GP composite to hold a shape and have the potential to support not only its own weight but the weight of following layers. Components such as Quikrete sand; Prairie land coarse sand; basalt fiber, minibars, and minirods; and chamotte were incorporated in varying amounts. Figure 60 shows an example of a KGP composite with 62 wt% Prairie land coarse sand and 3 wt%, 1/8-inch (approximately 3 mm) basalt fibers. In addition, Table 34 shows the various compositions tested for qualitative shape retention. The various acronyms used in the table are as follows: QS–Quikrete medium sand, CS–Prairie land coarse sand, BF–basalt fiber, MR–basalt minirod, C–Chamotte, MB–basalt minibar. The number directly to the right of the acronym is the weight percentage for each component, and for basalt

fibers, the number after the underscore is the denominator of the length size (ex: BF3_8 is 3 wt% basalt fibers with a length of 1/8 inch).

Figure 60. Shape retention cone for a GP composite with coarse sand and basalt fiber.

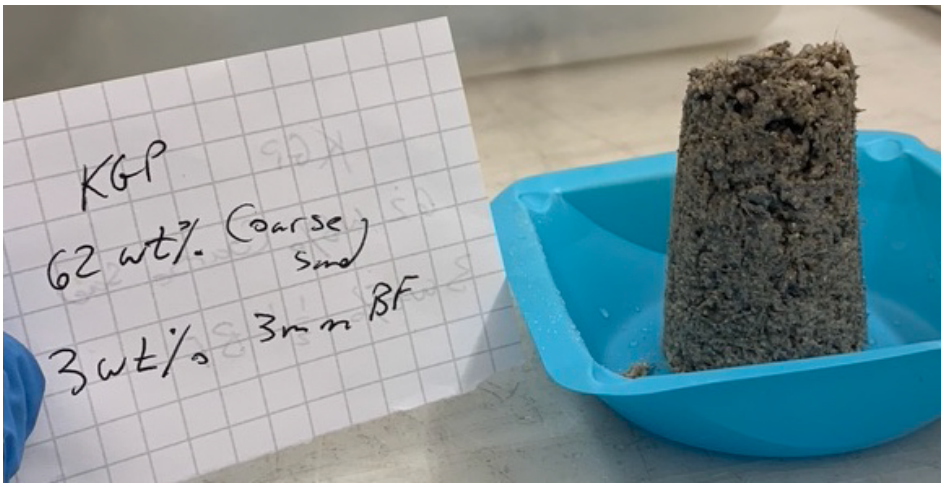

Table 34. Various composites tested for shape retention.

QS60	QS65BF3_2	QS55BF3_2C5	QS60BF3_2
QS62BF3_2	QS60BF3_8	QS50BF8_2	QS30G30BF3_2
QS10G50BF3_2	G60BF3_2	QS40G20BF2_2	QS20G40BF2_2
QS30G30BF3_8	CS62BF3_2	CS62BF3_8	CS30G30BF3_2
QS50SMR10BF3_2	QS40SMR20BF3_2	QS30SMR30BF3_2	QS50MB10BF3_2
QS40MB20BF3_2	QS55MR5BF3_2	QS55MB5BF3_2	QS55MB5BF3_8
QS62BF2_2	QS62BF4_2		

Several important properties were noted during the qualitative testing. The first important discovery was the impact of the size of the basalt fibers. This is best shown with Figure 61, which shows the difference in a KGP sample with 60 wt% Quikrete sand and either 1/8 in. (3 mm) or 1/2 in. basalt fibers.

Figure 61. KGP with 60 wt% QS and 3 wt% 1/8 in. (3 mm) BF (*left*) and KGP with 60 wt% QS and 3 wt% 1/2 in. BF (*right*).

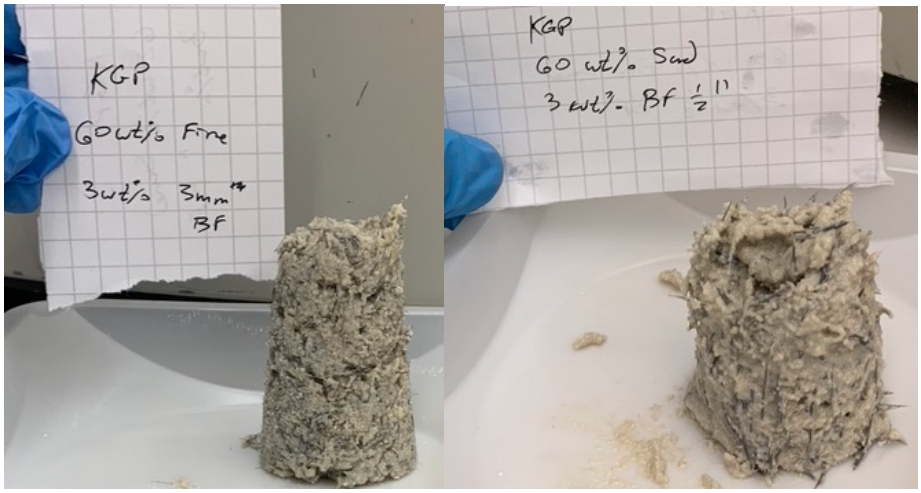

The smaller fiber size increased the amount of surface area of reinforcement, which increased the amount of internal friction between the GP and reinforcement material. This increased internal friction required more stress to disform, allowing the composite to hold its weight and shape to a sharper extent than with the 1/2 in. BFs. In addition, from an extruder head standpoint, the longer BFs had a greater likelihood of causing some sort of clog during extrusion and deposition, making the 1/8 in. fibers more favorable in terms of printability and workability.

The second important parameter discovered was the effect of the weight percentage of the basalt fibers, which is best shown in Figure 62.

Figure 62. Three samples of KGP with 62 wt% Quikrete medium sand and 2 wt%, 1/2 in. BF (*top*), 3wt%, 1/2 in. BF (*middle*), and 4wt%, 1/2 in. BF (*bottom*).

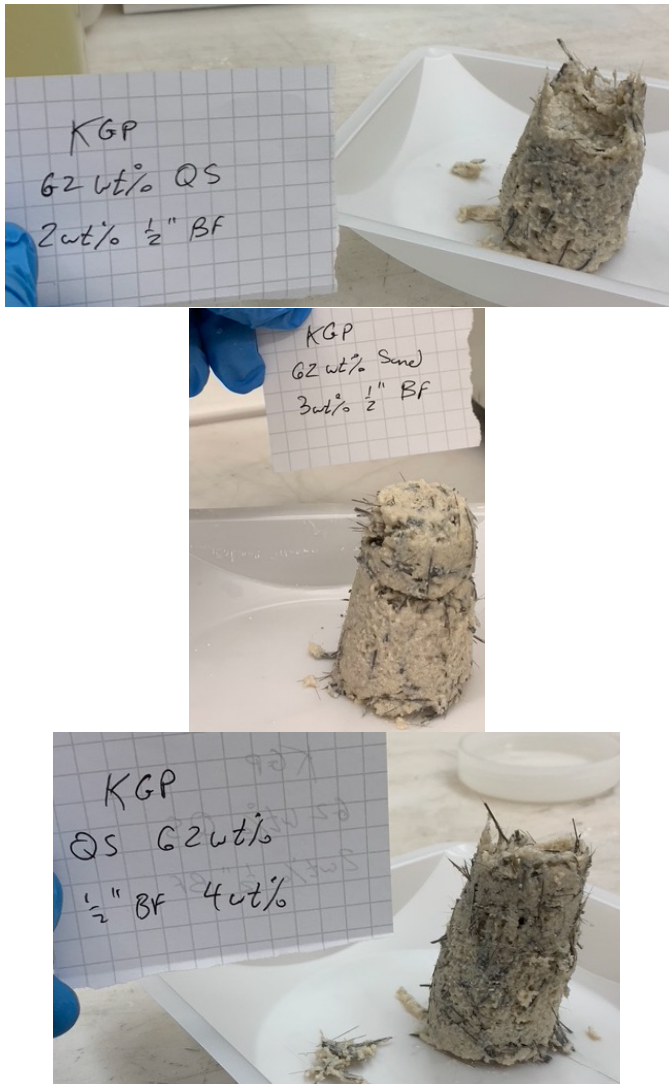

The 2 wt%, BF-reinforced composition had a certain stickiness that allowed it to adhere more to the surfaces of the mold and increased the difficulty of extrusion. However, the addition of this stickiness provided good cohesion of GP layers to one another on deposition. If the overall shape retention of the material is not significant beyond its need to hold its own weight, the 2 or 3 weight percentages of basalt fiber are excellent candidates for reinforcement of a printable composition. The 4 wt% basalt fiber was more on the dry scale due to the increased amount of reinforcement and surface area provided by the extra amounts of basalt fiber. If shape retention is specifically crucial, the 3 wt% of basalt fiber reinforcement is the most ideal.

In addition, the use of gravel is commonly used in the cement industry as a reinforcement in 3D printing. Gravel had an adverse effect on the shape retention, workability, and extrudability of GPs, as shown in Figure 63.

Figure 63. KGP samples of varying Quikrete medium sand and gravel composition.

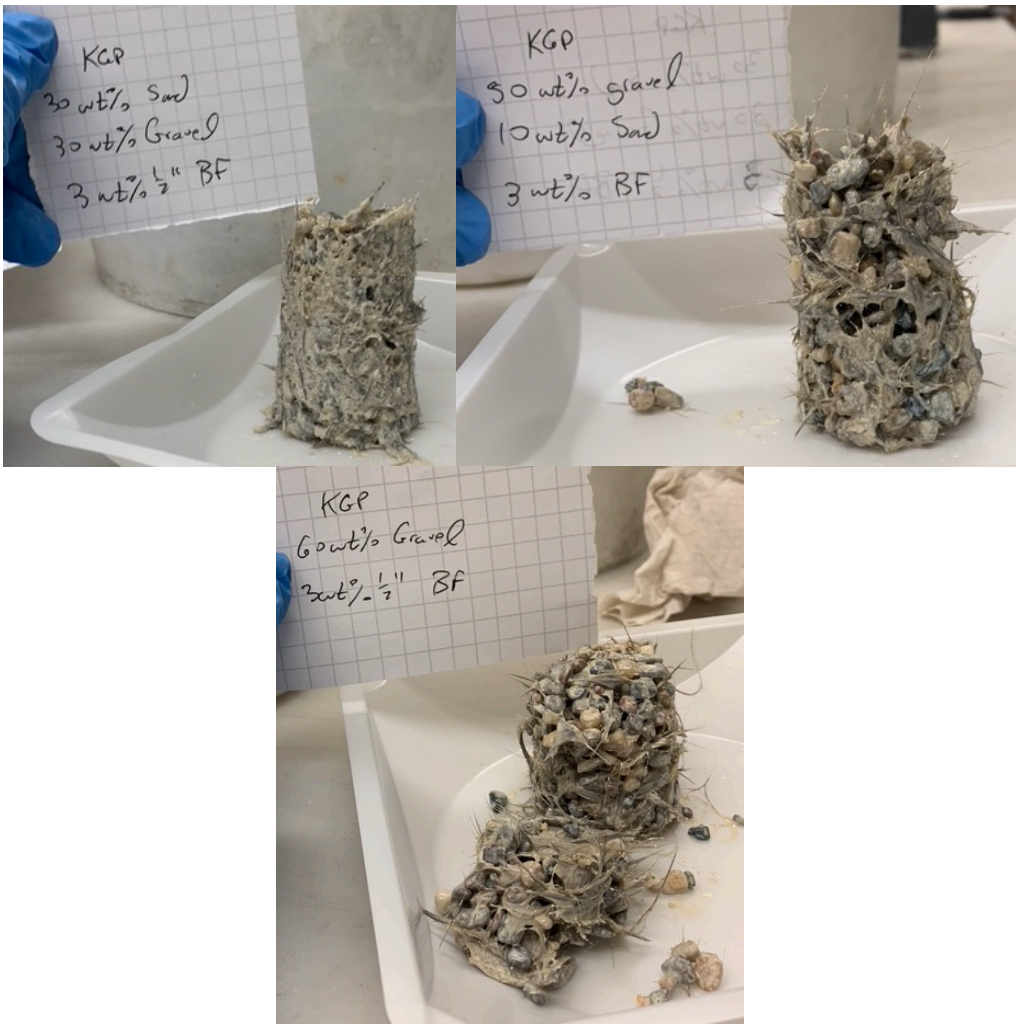

The increase in weight percentage of gravel increased the amount of void space in the GP matrix, which was seen in the large gaps in between gravel particles as gravel weight percentage increased. The last image in Figure 63 shows the lack of shape retention and strength brought about by an entirely basalt fiber and gravel GP matrix. If gravel is to be used as GP reinforcement for 3D printing, it is recommended to use 30 wt% or less in addition to sand and basalt fiber.

In addition, the use of basalt minibars and minirods were examined in relatively larger weight percentages. Figures 64 and 65 are images of a

basalt minirod and a minibar, respectively, used for shape retention testing of KGP composites.

Figure 64. A basalt minirod treated with a sand coating.

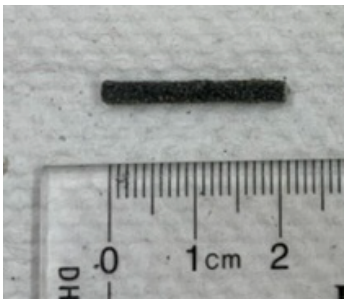

Figure 65. A basalt minibar used for KGP reinforcement.

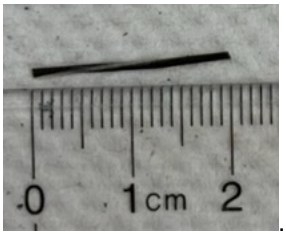

Figure 66 shows images of the cone shape with 5, 10, 20, and 30 wt% of basalt minirod with Quikrete medium sand and 1/2 in. basalt fiber for a total reinforcement percentage of 63%. Figure 66 shows images of the cone shape with 5, 10, and 20 wt% of basalt minibars with Quikrete medium sand and 1/2 in. basalt fiber, again with a total reinforcement percentage of 63%.

Figure 66. KGP samples containing various percentages of sand, basalt fiber, and basalt minirods.

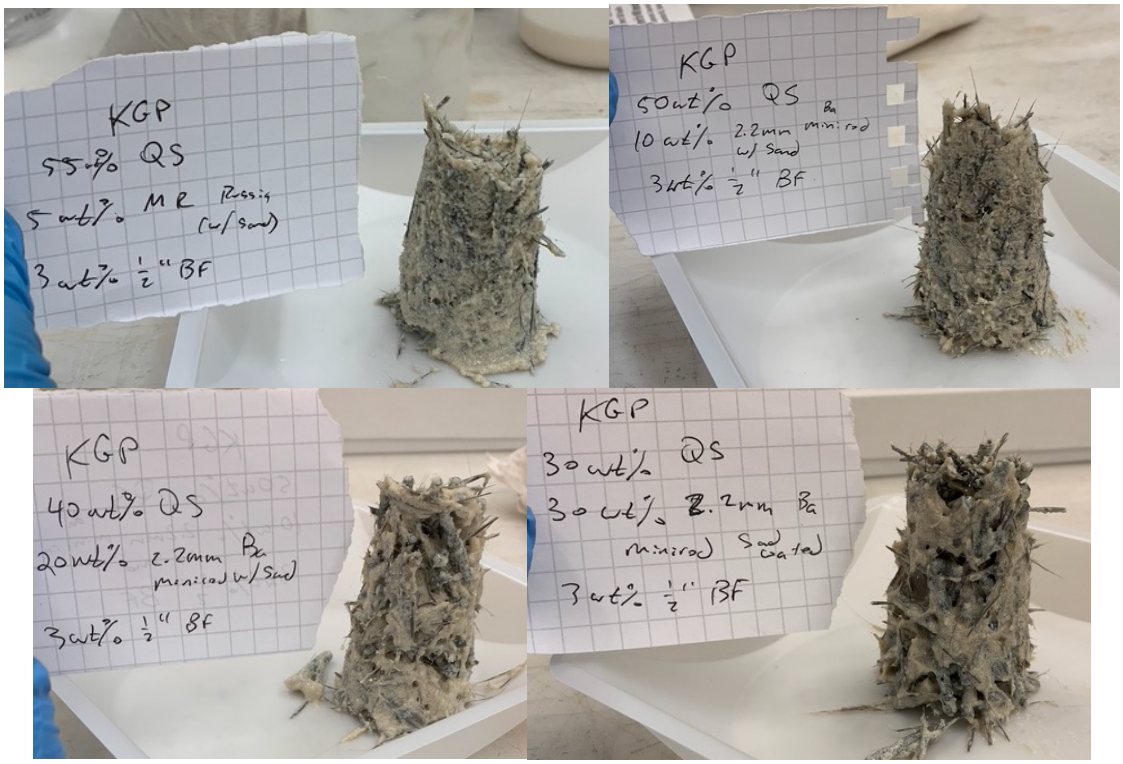

In similar fashion to the samples containing various percentages of gravel, the minirods provide relatively good shape retention at lower weight percentages. With an increase in the weight percentage of the minirods, the workability of the paste decreases as there is much void space due to the large minirod structures. In addition to issues with extrudability, an increase in the weight percentage of the basalt minibars has the potential to clog the extruder head due to their large shape relative to the sand and basalt fiber particles. The minibar samples, shown in Figure 67, decrease workability, extrudability, and shape retention with an increase in weight percentage to a greater extent than the gravel and the minirods. The longer length of the minibars allows them to interlock with one another during and after mixing, preventing easy workability of the GP paste. The longer length also has a highly likely probability to cause issues with the extruder head, more so than the minirods, which have a chance of aligning with flow to prevent clogging. Moreover, the addition of interlocking bars greatly increases void space, which causes weakness in the mechanical properties once the GP has cured. From the shape retention tests and images below, the basalt minibars were ruled out as a potential reinforcement.

Figure 67. KGP samples containing various percentages of sand, basalt fiber, and basalt minibars.

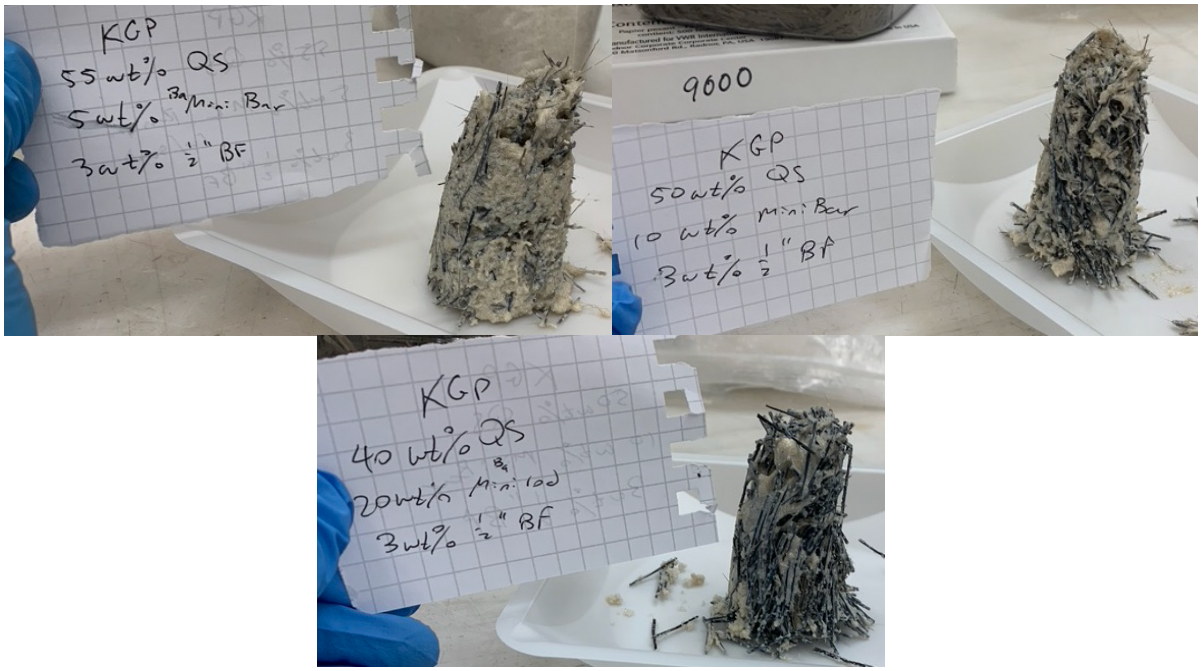

2.4.3.7 Squeeze flow

From a qualitative perspective, researchers can assess the footprint of the squeeze flow samples for how the GP may flow under the weight of subsequential layers, shown in Figure 68.

Figure 68. KGP paste sample after the squeeze flow test with 60 wt% Quikrete medium sand and 3 wt%, 1/2 in. basalt fibers.

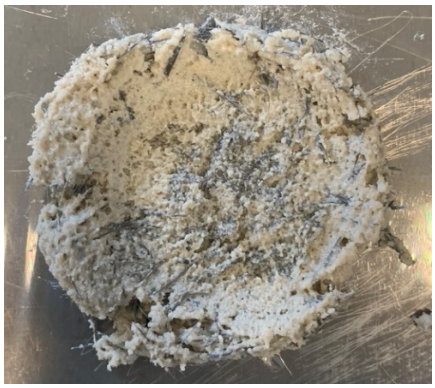

The GP paste and the Quikrete sand particles can flow, passing one another, outside the area of stress being applied to the sample. This can be seen as the edges of the sample are filled with mostly GP and sand with an upward flow shape. At the center of the sample, where the Instron head plate was compressing the sample, an excess of basalt fiber can be viewed.

Under the compression load the basalt fibers likely tangle up with one another and are unable to squeeze outwards due to excess internal friction between fibers. The fibers interlock and provide an area to trap small amounts of sand or GP composite. At lower reinforcement percentages, the resistance to deformation is less, and the footprint of the test shows greater phase separation between the GP paste and the solid reinforcements.

Quantitative stress curves of various squeeze flow tests are shown in Figure 69–Figure 72. Figure 69 specifically compares the trendlines of KGP reinforced with 60 wt% Quikrete medium sand with varying wt% of either 1/8 in. or 1/2 in. basalt fiber in steps of 1–4 weight percent at a rate of 0.1 mm/s. A sample of KGP QS60 is also included as a control to demonstrates the squeeze flow properties of a GP without fiber reinforcement. The weight reinforcement is the number directly to the right of the letters that specify reinforcement (QS for Quikrete sand as previously stated) and the underscored number after basalt fiber (BF) specifies the denominator of the fiber size (8 for 1/8 in. and 2 for 1/2 in.). A sample of 0.45 water to cement OPC with 60 wt% Quikrete fine sand is included for comparison to a cement mixture that has been 3D printed previously.

Figure 69. Squeeze flow trendlines at 0.1 mm/s of KGP with 60 wt% sand and various basalt fiber sizes and percentages.

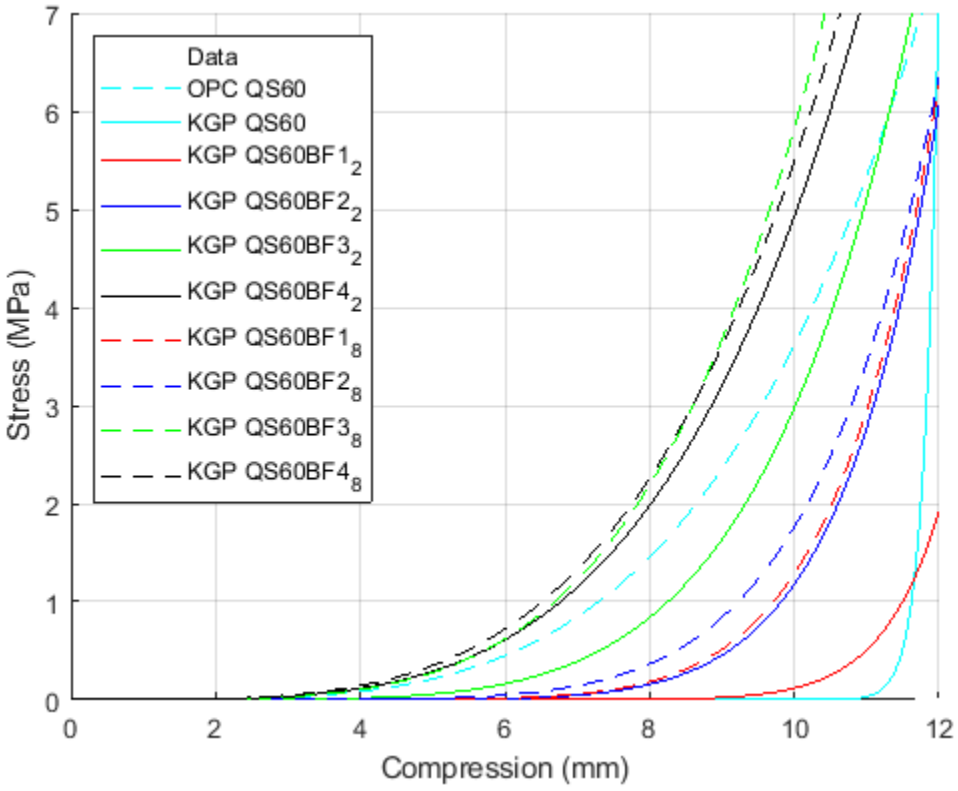

The KGP QS60 shows very little resistance to deformation during the duration of the squeeze flow. The large spike in stress at the end of the curve likely indicates the sand jamming up and interlocking to prevent further deformation very close to, if not hitting, the metal plate that the GP sample rests on. In terms of increasing the amount of basalt fiber, the more highly reinforced systems provided greater deformation resistance at lower compression distances. In terms of the physical components influencing the flow, the greater volume of basalt fiber tangled and bundled up during mixing with the sand, allowing the two different reinforcements to jam up on squeezing. Flow could also be influenced by phase separation between the solid reinforcements and the liquid geopolymeric binder. As more liquid phase is able to flow out of the composite matrix, the interparticle friction prevents further reinforcement displacement, increasing the resistance to deformation. Uniformly across all samples, the 1/8 in. basalt fiber provided greater resistance to deformation at lower compression distances for all weight percentages tested. This was likely due to the greater amount of surface area associated with the shorter fibers and increased friction, which increased tangling and jamming.

Figure 70 shows the effect of changing sand weight percentage with a constant 3 wt% of either 1/8 in. or 1/2 in. basalt fiber with a squeeze flow rate of 0.1 mm/s.

Figure 70. Squeeze flow trendlines at 0.1 mm/s of KGP with varying sand percentages and 3 wt% basalt fiber with either 1/2 in. or 1/8 in. at 0.1 mm/s.

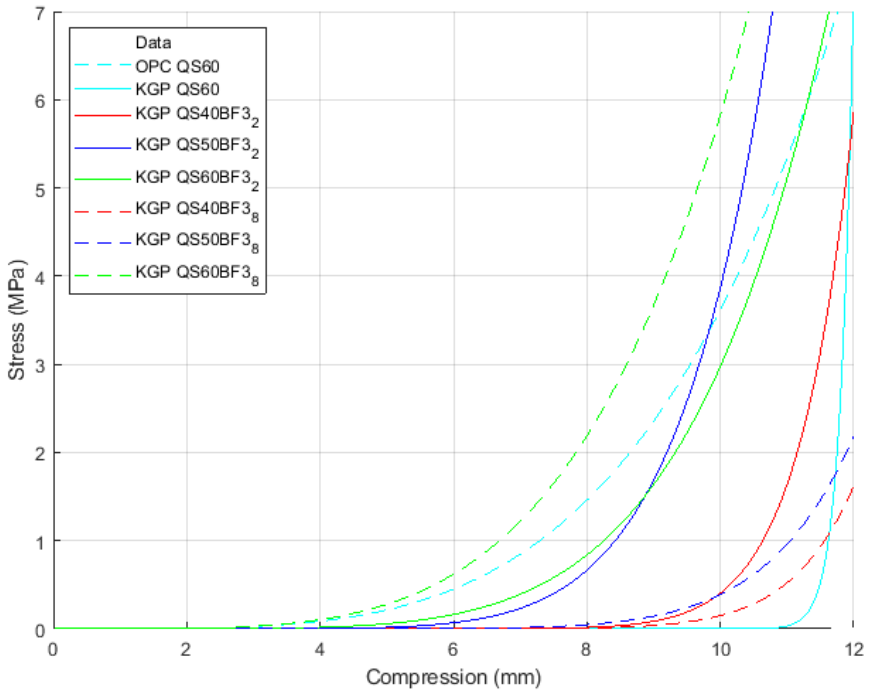

The samples containing 40 or 50 wt% sand had an opposite effect on deformation resistance when comparing the two fibers sizes than the 60 wt% sand 3 wt% basalt fiber samples. The smaller fibers in this case could be aligning in the direction of flow, which provides less resistance to deformation in the case of less heavily reinforced GPs. The larger fibers likely do not align to flow as well as the shorter fibers, increasing the amount of tangling and bundling and providing overall higher stress curves.

Figure 71 shows the squeeze flow response of varying sand percentages at different squeeze flow rates and a constant 3 wt% basalt fiber of 1/2 in.

Figure 71. Squeeze flow trendlines with varying sand percentage for both squeeze flow rates and 3 wt%, 1/2 in. basalt fiber.

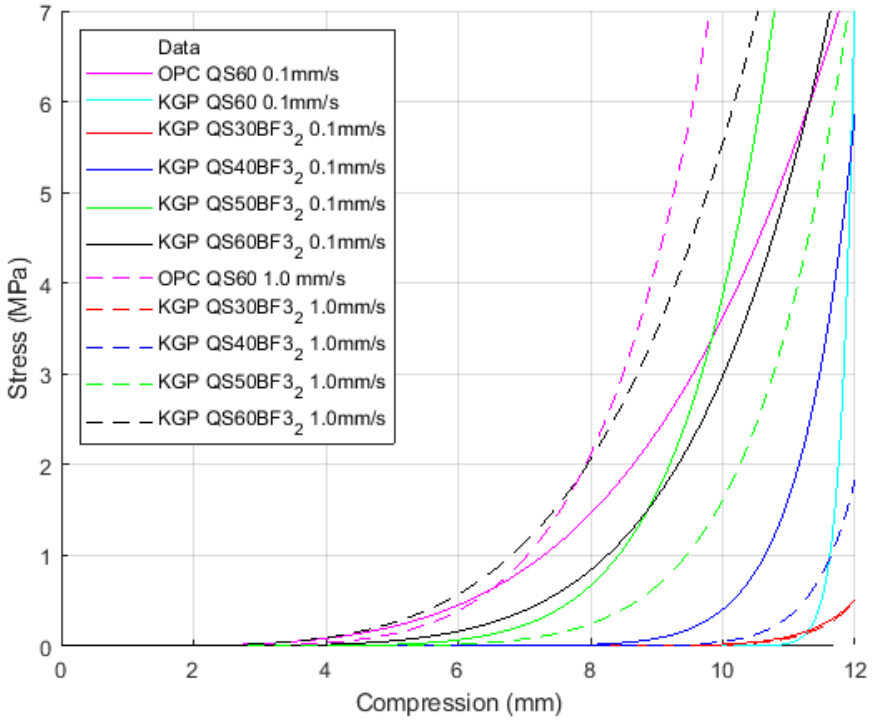

For all of compositions tested with the exception of the KGP QS60BF3_2 sample, the greater rate of squeeze reduced the amount of deformation resistance. This trend aligns with the shear thinning behavior already proven for GPs and with what is proven in literature. In addition, at lower squeeze rates, the solid and liquid phases have more time to rearrange, jam, and bundle to resist flow. At a higher deformation rate, the solid particles of both sand and fiber do not have time to interlock and jam as tightly, which allows them to flow and be displaced at lesser stresses. As expected, the higher amount of reinforcement also increased the stress required for squeeze flow to occur.

Last, Figure 72 shows the influence of fiber length with varying sand content and squeeze flow rates. The 1/8 in. fiber performed more consistently when comparing the two different squeeze flow rates.

Figure 72. Squeeze flow trendlines with varying sand percentage for both squeeze flow rates and 3 wt%, 1/8 in. basalt fiber.

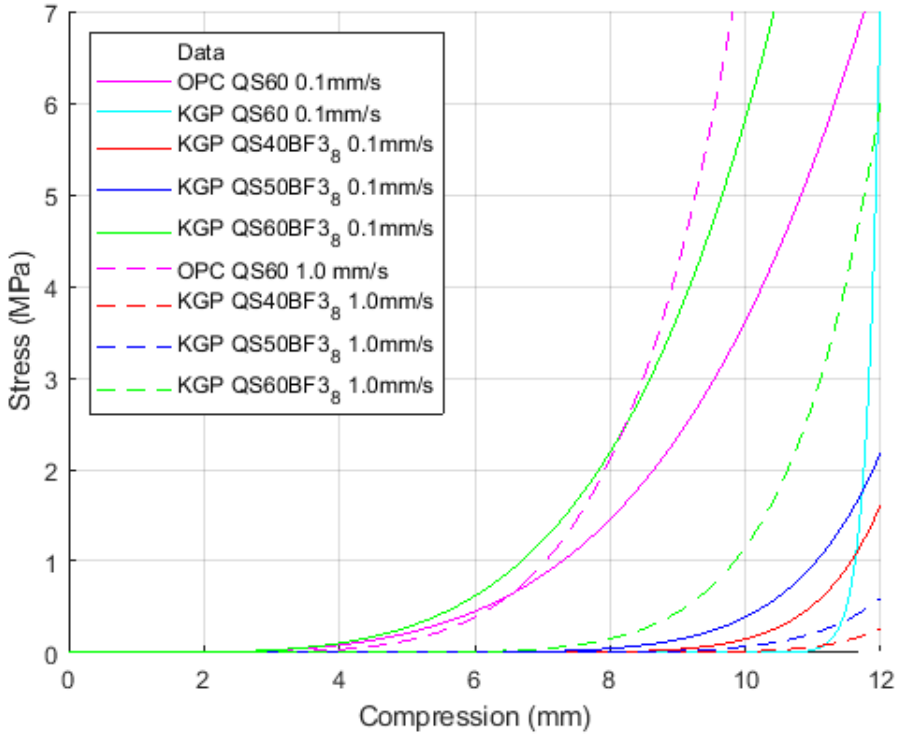

At the higher squeeze flow rate, less deformation resistance was apparent, again, as explained previously, due to the minimal time for the material to jam. Also, as the total reinforcement percentage increased, an increase in deformation was observed that aligns with the entire squeeze flow data collection.

Overall, composition of 50–60 wt% sand with 3 wt%, either 1/2 in. or 1/8 in., basalt fiber would be comparable to 60 wt% Quikrete sand in 0.45 (w/c) OPC in terms of squeeze flow properties and deformation resistance.

2.5 Ultrasonic wave reflectometry

2.5.1 Methods and materials

The GP paste and ordinary Portland cement synthesis for UWR testing was identical to that mentioned in Section 2.3.1 . The square wave pulser/receiver used was a Panametrics model 5077PR, the transducer was an Olympus panametrics–NDT V154, the signal processor was National Instruments LabVIEW 2016, and the selected buffer material was high-impact polypropylene (HIPPS). The impedance value of the HIPPS container was close in magnitude to that of the materials tested, which

allowed for optimal signal. The transducer was attached to the HIPPS container before each test with SAFC phenyl salicylate as an adhesive. Once the fresh material paste finished the high shearing and planetary mixing stage, it was immediately placed in the HIPPS container, which was placed in a plastic bag and sealed with a wet paper towel as a moisture source to imitate the ideal setting conditions. The signal source was then turned on, and data acquisition was initiated. Each test was left to run for approximately 48–72 hours to ensure the material had reached its fully solidified state.

2.5.2 Data-processing parameters

To correctly analyze the data, three tangent lines were drawn on the reflection coefficient versus time graphs after normalization of the reflection coefficient data. An example of this is shown in Figure 73, where the *blue line* represents the normalized reflection coefficient of the material (in this case a Metamax EF potassium GP), and the *red lines* are tangent lines drawn at three segments of interest in the reflection coefficient. The first intersection of tangent lines represents the onset of formation of an internal network within the cementitious material. The second intersection of the tangent lines is reflective of the final hardening or final setting of the material, where the material can resist deformation when a load is applied.

Figure 73. A UWR run of a Metamax EF potassium GP.

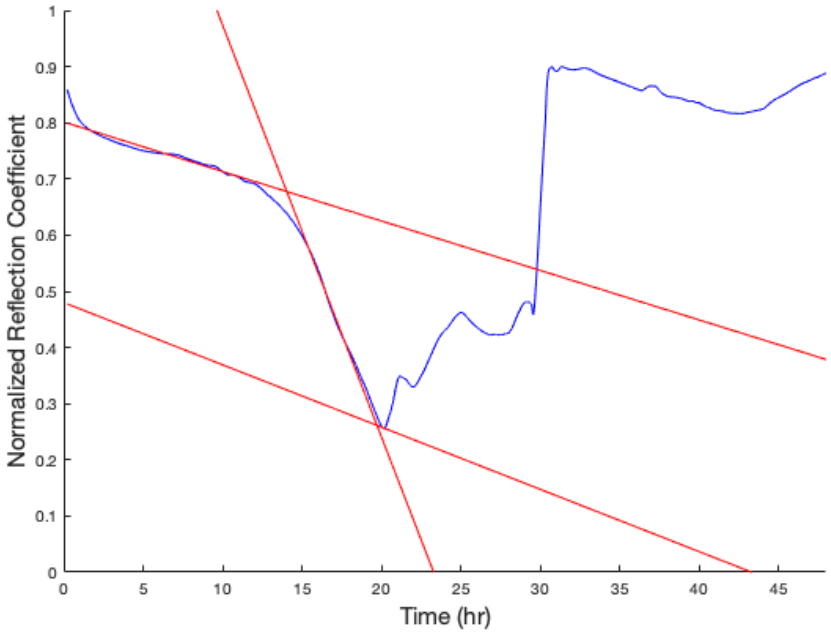

2.5.3 Ultrasonic wave reflectometry results

The results from all of the UWR testing can be found in Table 35.

Table 35. UWR data from various GP systems.

Metakaolin system	Onset time (hr)	Final set (hr) ultrasonic wave reflectometry results
Argical Trial 3	5.88	8.47
Argical Trial 2	7.24	13.54
Powerpozz Trial 1	8.95	15.19
Powerpozz Trial 2	11.08	18.12
Argical Trial 1 (NOTE: Lower pulse voltage)	11.31	15
Metamax EF 12 Molar water	13.11	19.56
Metamax EF 12 molar water	13.79	-
Metamax EF 11 molar water	14.05	19.69
Metamax EF 13 molar water	14.19	26.04
Metamax (Lot#00702G015)	15.75	25.16
Metamax EF 14 molar water	19.92	32.23
Metamax (Lot#00702G015) with 2nd Trial KASOLV	21.59	28.46
Metamax Trial 1 (Lower pulse voltage)	23.07	29.92
Metamax (Lot#00702G015) with KASOLV Trial 1	31.78	41.78

Table 35 is in ascending order of onset of set time. It was expected for the Metamax EF samples to have the quickest onset and final set times due to the extremely fine particle size; however, the Argical 1,200S metakaolin seemed to produce the fastest setting GP. This was likely due to the larger amount of specific surface area that corresponded to a greater reactivity. The specific surface areas of the metakaolins were analyzed by Samuel et al. (2020). The final set of all the material systems ranged greatly from 8.47 hr to 41.78 hr, putting great dependence of the desired set time on the type of metakaolin chosen for printing. Usage of water glass made from KASOLV powder also extended the final set of the material, ranging from approximately 28 hr to 42 hr. The effect of additional moles of water was also explored by adding 1–3 additional moles of water, which also seemed

to extend the set time of the material as expected since the GP reaction is diluted.

2.6 Mechanical properties of OPC composites versus GP composites (GPC)

2.6.1 Curing regime

Cylindrical and prismatic molds were filled with the samples, then tapped and vibrated to release entrapped air that would contribute to undesirable porosity. Samples were kept in molds for 3 days, then kept in a humid chamber for 3 days; the humid chamber was a container with a small amount of water on the bottom that was closed. Samples were kept above water to avoid any erosion. After this time, the samples were placed on a shelf and left to air dry. For GP paste, samples needed to be kept in plastic bags for additional time while drying to prevent cracking. Samples were then tested at around 28 days for strength. The weight loss from drying was monitored for all samples until negligible.

2.6.2 Materials

The following materials were used to make specimens:

- **Cement**: Quikrete Type I/II OPC powder was obtained from a local hardware store.
- **GP**: Potassium water glass was made with a potassium hydroxide solution and an amount of KASOLV beads. The KASOLV beads are hydrous potassium silicate powder and were used to make water glass in place of silica fume for large batches of samples. To make GP paste, the water glass was mixed with Metamax metakaolin.
- **Reinforcements and aggregates**: The types of sand used were fine sand and coarse sand. Large aggregates included gravel that was sifted to 3/16 in. All sand and gravel were obtained from CERL.
- **Water**: The water used was potable tap water from CERL's facility and is suitable for mixing concrete.

2.6.3 Methods

To mix concrete samples, OPC and aggregates were mixed in a bucket, and enough water was gradually added to result in a workable mixture. Each mix was conducted manually or with a handheld electric cement mixer. To release entrapped air from concrete samples, molds were tapped or

vibrated with a vibrating stick. Samples were then cast and cured in their molds for 10 days. To mix GP samples, water glass was measured into a bucket and metakaolin was added to the water glass where the ratio of water glass to metakaolin was fixed at 1.857:1. The metakaolin was mixed with a high shear mixer using high torque at 400 rpm until the mixture turned into a paste, then at high speed at 2,000 rpm; the paste was mixed for approximately 10 minutes. Each aggregate was added to the paste, and the handheld cement mixer was used to fully mix the aggregate into the paste. The samples were then vibrated on a vibrating plate for approximately 5 minutes to limit porosity. For compressive strength, plastic molds were used that were 3 in. in diameter and 6 in. tall. For flexural strength, plastic molds were used that contained six slots that measured 1 × 1 × 6 in. The sizes of the samples were made under the guidance of ASTM C39 and C78 for compressive and flexural strengths, respectively. Concerning C78, aggregates should be no larger than one-third of the depth of the sample, and therefore, gravel used in this test was sifted to 3/16 in. Additionally, the loading span must be three times the depth of the sample with at least 1 in. extra; the length of 6 in. more than accommodates this specification. When tested, compression samples were capped with neoprene Duro 70 pads to avoid any sources for cracks due to surface roughness. Flexure bars were loaded under a four-point system with the middle third of the loading span loaded by the system.

2.6.4 Test matrix

The test matrix below (Table 36) shows the designations for specimens, variables involved, and how many specimens were going to be made for compressive and flexural strength testing.

Table 36. Test matrix for OPC–GP comparison. The proposed test matrix of samples with their respective sample numbers.

	Concrete	w/c	GP	F'c	Fb
1	OPC (0.1)		KGP+MK (K.1)	3 cyl	6 bars
2	OPC+fs (0.2)		KGP+fs (K.2)	3 cyl	6 bars
3	OPC+cs (0.3)		KGP+cs (K.3)	3 cyl	6 bar
4	OPC+gravel+sand (0.4)		KGP+gravel+sand (K.4)	3 cyl	6 bars

GP with gravel as the only reinforcement is not an appropriate material because the size of the gravel is too large to be suspended in the GP matrix and will sink in the mixture, resulting in a mixture that is not reinforced or homogeneous. Therefore, when adding gravel, it is appropriate to add

sand or a fine powder reinforcement as a "filler phase." Coarse sand used in this test contained small pebbles less than 2 mm in size. OPC mortars with fine and coarse sand were made with a nominal mixture of one part cement and four parts sand. GP mortars were made with 60 wt% sand. Both concrete mixtures were made with one part cement, one part sand, and two parts gravel. For OPC composites, the w/c ratio was desired to be 0.35–0.50, but to make a workable mixture, the w/c ratios for the mortar mixtures were considerably higher.

2.6.5 Samples and weights

Table 37 and Table 38 show how much materials were used for the specimens.

Table 37. OPC sample measurements. All weights are in grams.

Sample	Water	Cement	Fine sand	Coarse sand	Gravel	w/c	c/b1(/b2)
0.1 cyl	1,202.67	3,000.01	x	x	x	0.40	x
0.1 bar	438.75	1,000.40	x	x	x	0.44	x
0.2 cyl	630.50	850.75	3,400.00	x	x	0.74	0.25
0.2 bar	251.07	300.00	1,200.00	x	x	0.60	0.25
0.3 cyl	526.98	849.95	x	3,400.88	x	0.62	0.25
0.3 bar	200.00	300.20	x	1,200.30	x	0.66	0.25
0.4 cyl	544.04	1,250.20	1,250.31	x	2,500.00	0.44	1/1/2
0.4 bar	171.30	400.06	400.00	x	800.00	0.43	1/1/2

Table 38. GP sample measurements.

Sample	Water glass	Metakaolin	Fine sand	Coarse sand	Gravel	c/b1(/b2)
K.1 cyl	1,400.50	2,597.75	x	x	x	1.00
K.1 bar	728.45	1,353.72	x	x	x	1.00
K.2 cyl	538.50	1,000.00	2,307.75	x	x	0.40
K.2 bar	192.51	357.49	750.70	x	x	0.42
K.3 cyl	861.70	1,600.00	x	3,692.40	x	0.40
K.3 bar	175.20	324.88	x	750.37	x	0.40
K.4 cyl	350.01	650.01	999.95	x	2,000.20	1/1/2
K.4 bar	210.60	391.10	600.30	x	1,200.30	1/1/2

2.6.6 Compressive strength results

The following graphs show the individual and average compressive strengths of each specimen (Figure 74–Figure 75).

Figure 74. Compressive strength of KGP versus OPC.

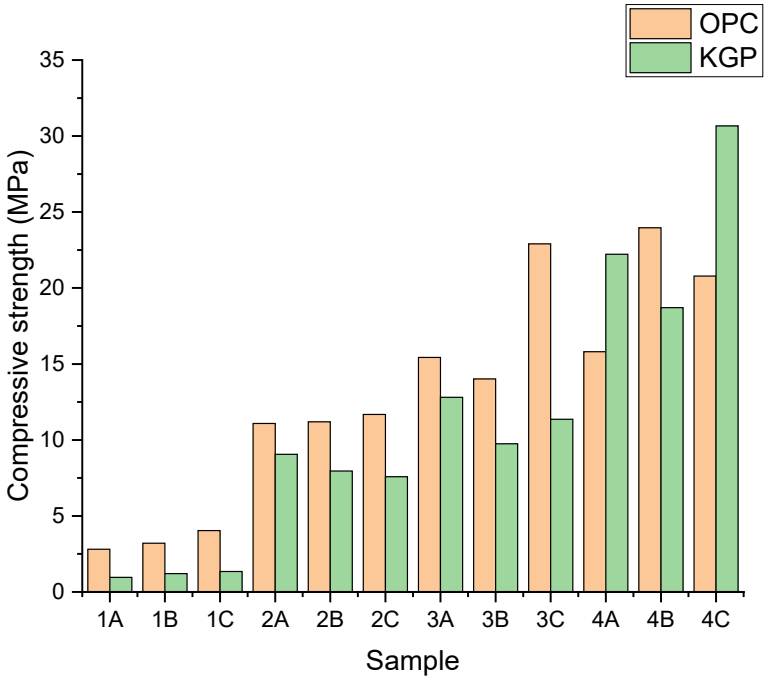

Figure 75. Average compressive strength of KGP versus OPC.

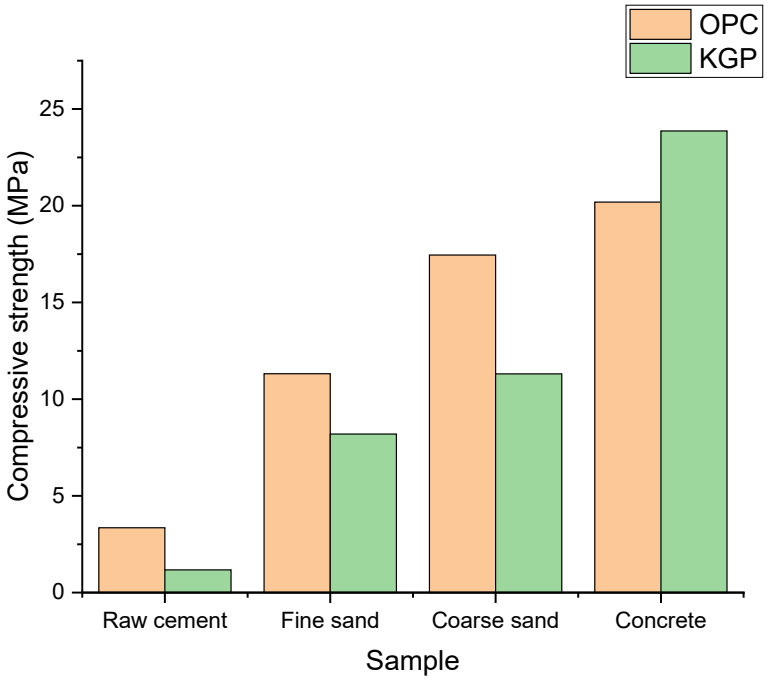

The compressive strengths of the OPC cylinders correspond with similarly sized samples found in the literature and show a considerable size effect compared to the strengths of compression cubes. GP mortars and paste

did not outperform their OPC counterparts, but GP concrete outperformed OPC concrete by nearly 10% (Figure 76–Figure 79). Cylinders failed in columns, owing to tensile failure, which is different from that of compression cubes that usually fail with two resulting cones.

Figure 76. Failure of GP and OPC paste.

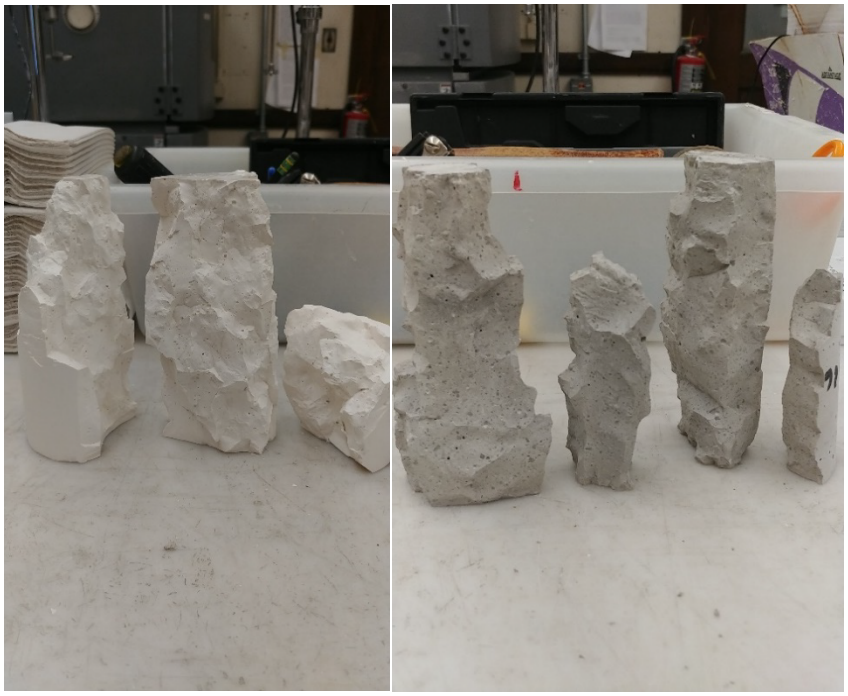

Figure 77. Failure of OPC (*top*) and GP composites with fine sand (*bottom*).

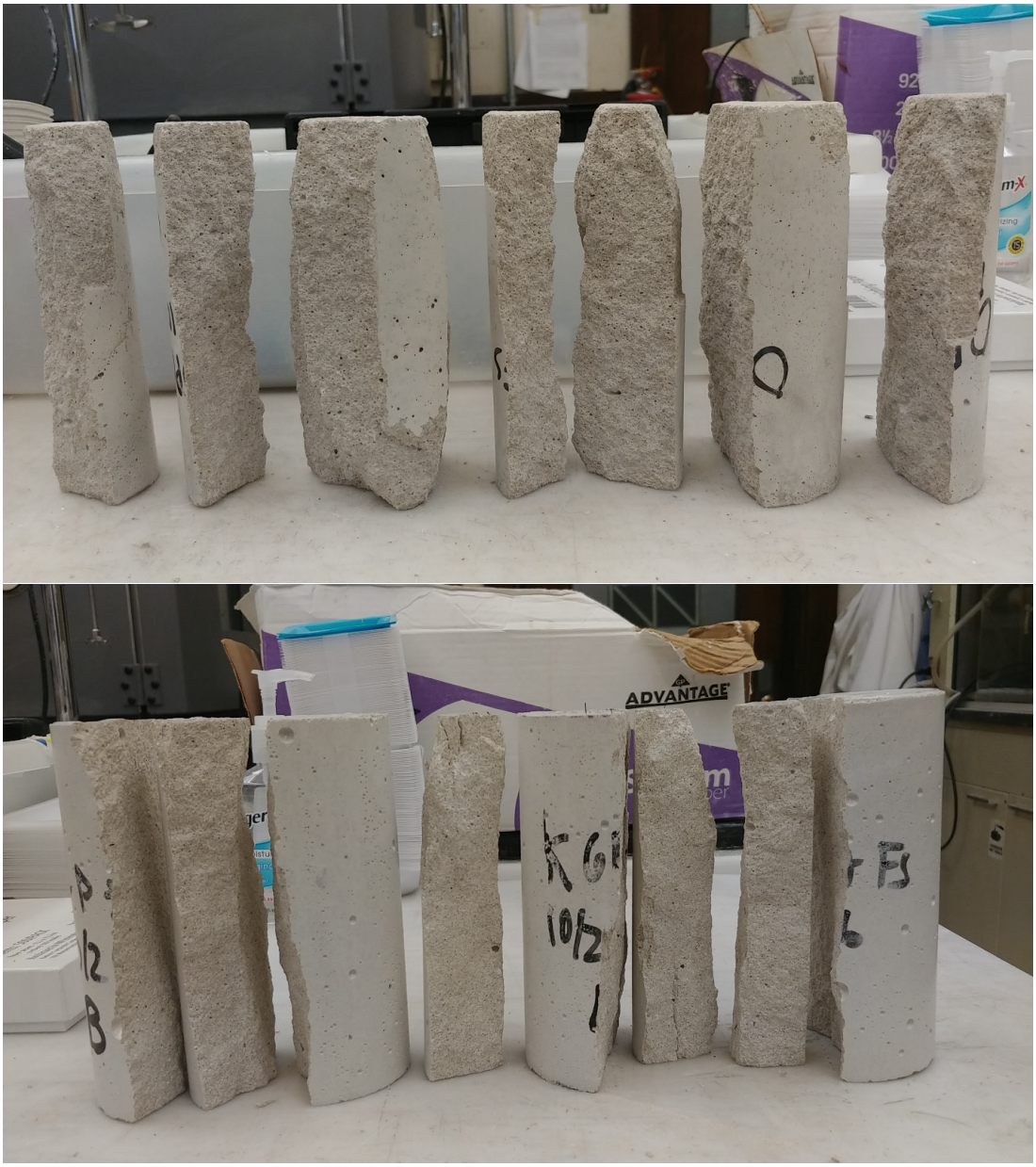

Figure 78. Failure of OPC (*top*) and GP composites with coarse sand (*bottom*).

Figure 79. Failure of OPC (*top*) and GP composites with fine sand and gravel (*bottom*).

2.6.7 Flexural strength results

The following graphs show the individual and average flexural strengths achieved by the bar specimens (Figure 80–Figure 81).

Figure 80. Flexure strength of KGP versus OPC.

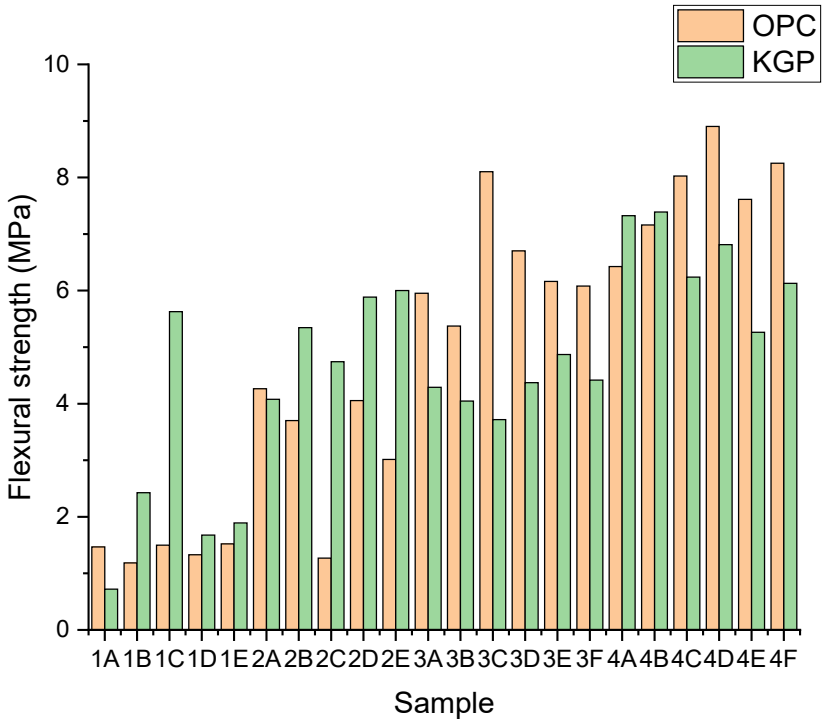

Figure 81. Average flexure strength of KGP versus OPC.

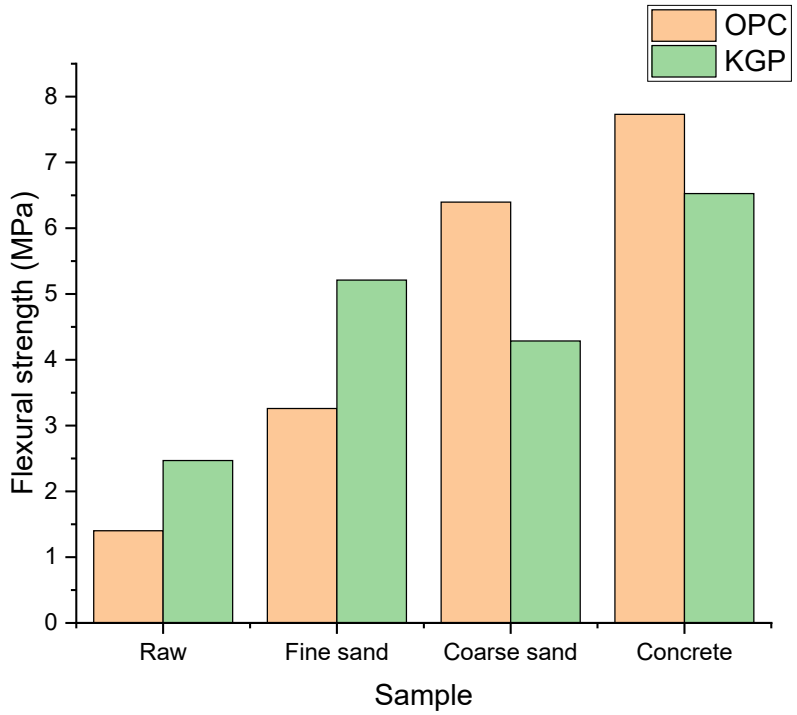

The GP coarse sand mortar and concrete bars were outperformed by OPC bars, but pure GP and fine sand mortar bars were considerably stronger than their OPC counterparts. It should be noted that the variance of the GP bars was high, possibly resulting in an artificially high average flexural strength. Despite this, the variance of strengths was relatively minimal when the samples were reinforced. Figure 82–Figure 85 show the cross sections of the failed bars.

Figure 82. Cross section of failed KGP paste and fine sand mortar bars.

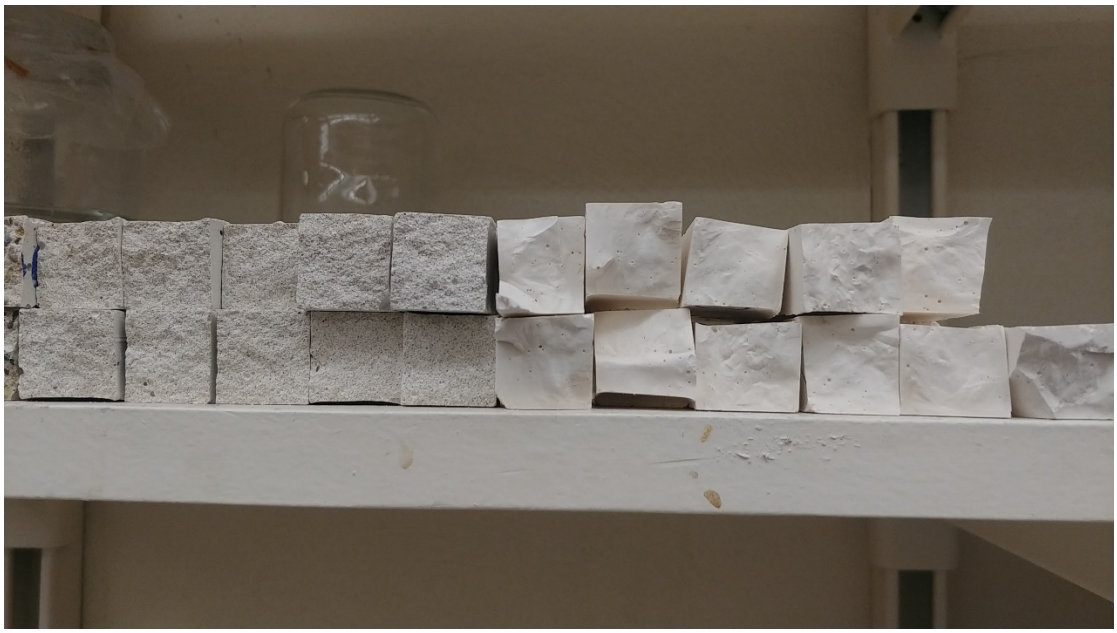

Figure 83. Cross section of failed OPC paste and fine sand mortar bars.

Figure 84. Cross section of failed KGP coarse sand mortar and concrete bars.

Figure 85. Cross section of failed OPC coarse sand mortar and concrete bars.

2.6.8 Weight loss from drying

Weight loss was seen in all samples when dried (Figure 86–Figure 91). In OPC samples, the weight loss occurred from free water that was not involved in the hydration reaction, while in GP samples, all weight loss occurred from free water escaping the geopolymeric framework. From these results, weight loss occurs at similar rates with both matrices when reinforced with the same materials. At early ages under 15 days, GP

composites lost weight at a slightly higher rate. Figure 86 shows a dramatic loss of weight in pure GP cylinders, showing that free water escapes rather quickly when the samples are not reinforced. Qualitatively, these samples were prone to cracking on drying, and numerous surface cracks were seen throughout all pure GP and OPC cylinders, shown in Figure 92. However, this cracking was not observed in the much smaller pure GP bars. Conclusively, smaller samples do not need as much care when drying in ambient conditions.

Figure 86. Water weight loss of pure cement cylinders and fine sand mortar cylinders.

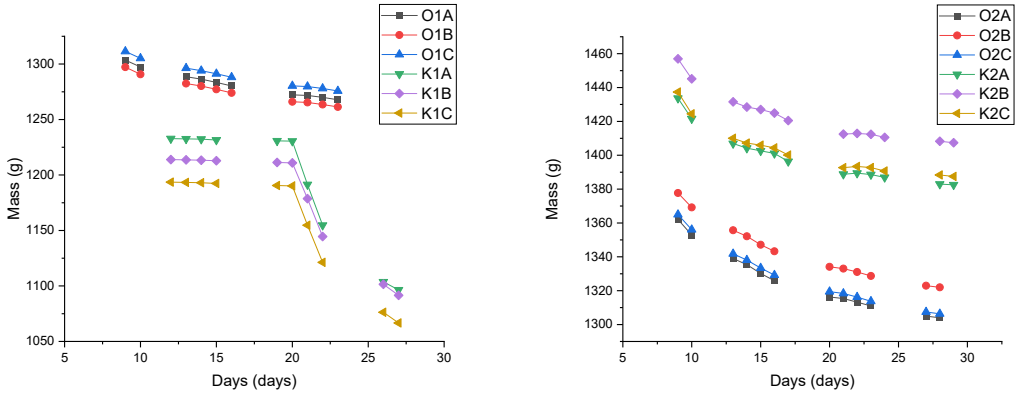

Figure 87. Water weight loss of coarse sand mortar cylinders and concrete cylinders.

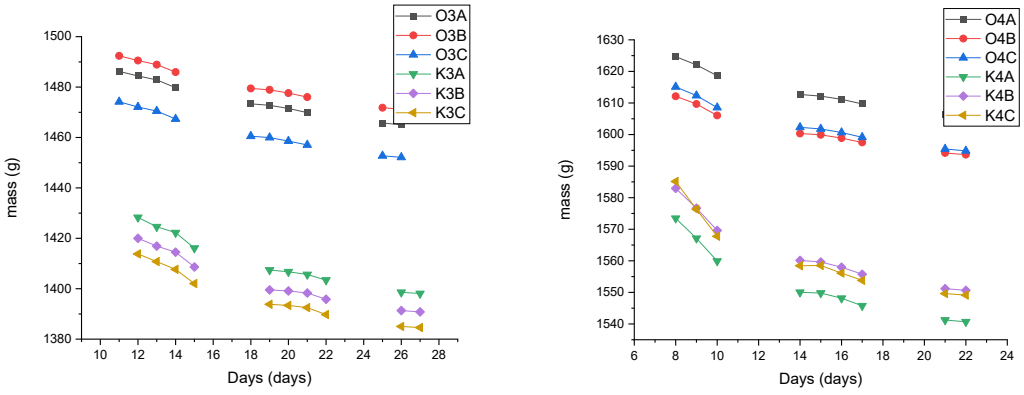

Figure 88. Water weight loss of pure cement bars.

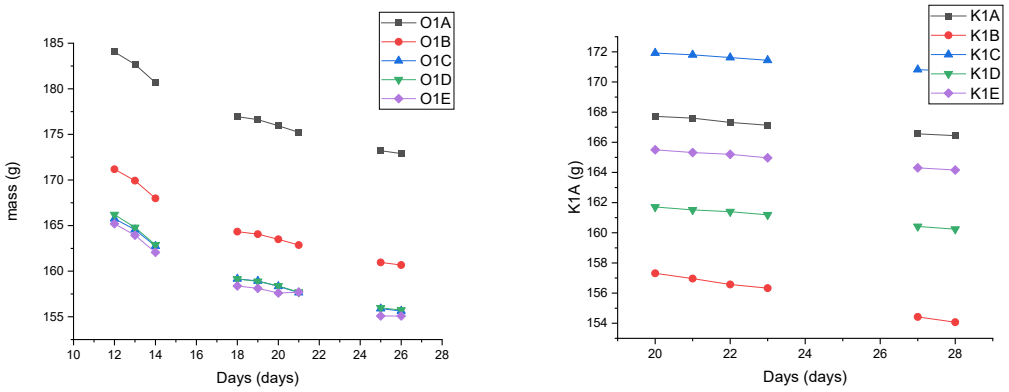

Figure 89. Water weight loss of fine sand mortar bars.

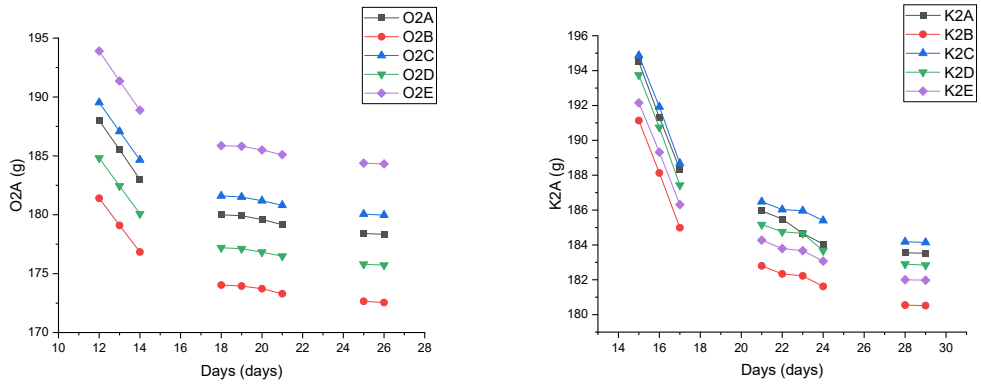

Figure 90. Water weight loss of coarse sand mortar bars.

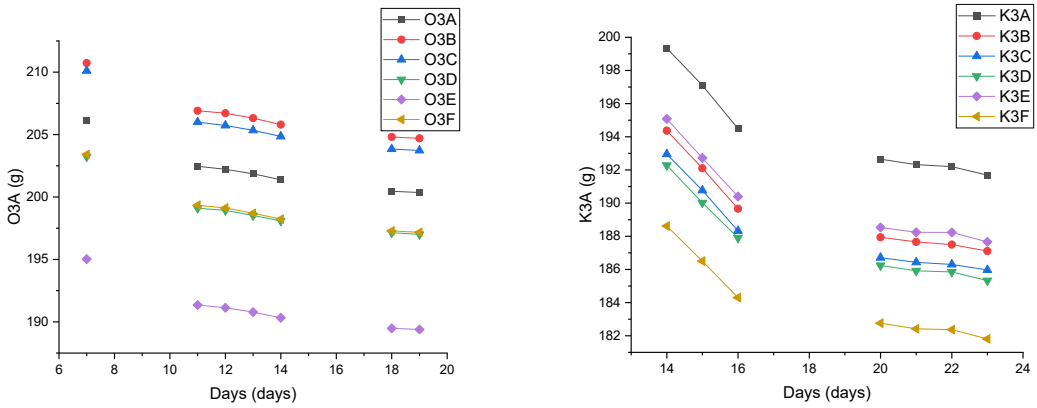

Figure 91. Water weight loss of concrete bars.

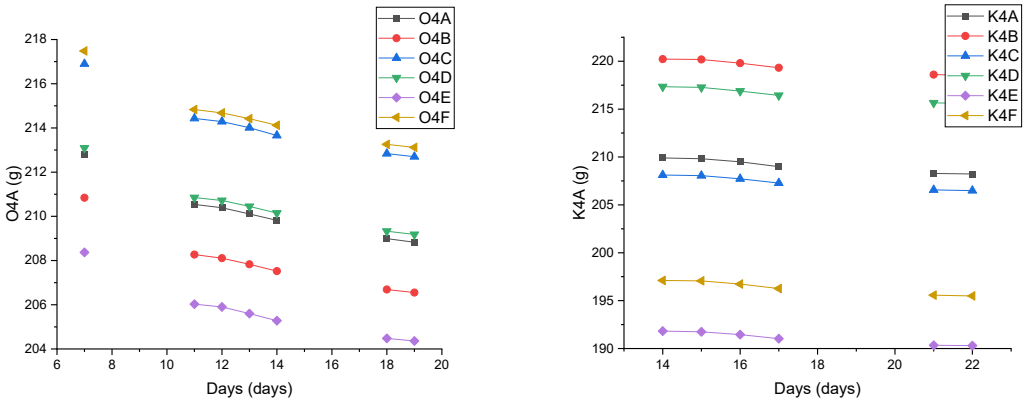

Figure 92. Surface cracks in KGP and OPC paste cylinders.

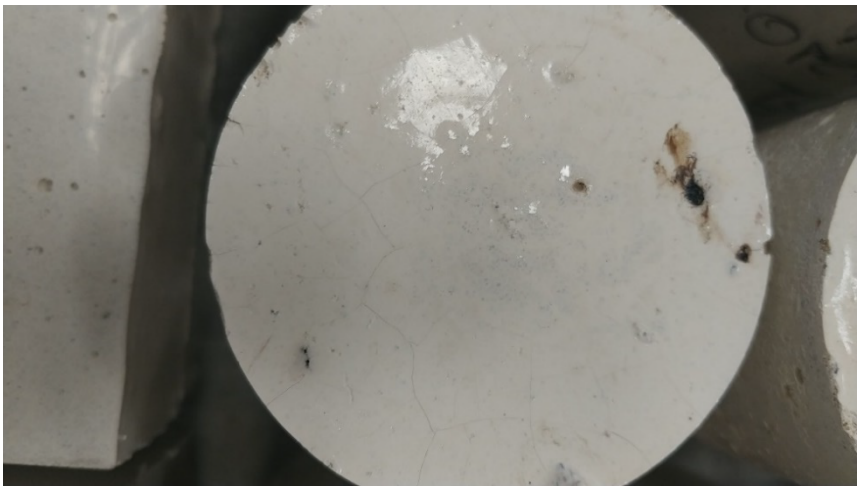

2.7 FT characteristics

Samples were made with NaGP and KGP as well as a variety of reinforcements to establish the best mix design for cold temperatures. The GP was prepared as in Sections 2.1 and 2.2. The reinforcements were added and then mixed in with a helical stand mixer. The mix was then cast into 3 × 4 × 16 in. HDPE molds, vibrated for one minute to degas, and then covered with plastic film for 9 days. After this, the samples were demolded and kept in an atmosphere of 23±2°C and 5%±10 RH until testing, which was conducted at the Cold Regions Research and Engineering Laboratory (CRREL) in New Hampshire. Samples were subdivided into categories, according to the types of additive, amount of additive, and alkali used (Table 39). The samples were tested in accordance with ASTM C666 except for specimen one, which consisted of two 2 × 3 × 16 in. bars tested together to evaluate whether decreasing the size of the sample had any effect on the freeze-thaw (FT) resistance. A "control" sample was made with Quikrete brand OPC with silica fume as an additive, then mixed, cast, and cured along with the other GP specimens.

Table 39. Compositions of varying beams tested.

			Composition (ratios by weight)					Cure time (days)
Set	Specimen	Specimen ID	CS and FS (1:1)	Other	Basalt	KGP	Gravel (<3/16 in.)	
I	1	S60.KGP.2×3 (2)	3	—	—	2	2.5	110
	2	S60.KGP.3×4	3	—	—	2	2.5	119
II	3	S50.KGP.3×4	1	—	—	1	2.5	127
	4	S40.KGP.3×4	2	—	—	3	1	102
III	5	S60.NaGP.3×4	3	—	—	2	2.5	102
	6	S50.NaGP.3×4	1	—	—	1	1	102
	7	S40.NaGP.3×4	2	—	—	3	2.5	77
IV	8	W60.KGP	-	3*	—	2	2.5	75
	9	W30.S30.KGP	1.5	1.5*	—	2	2.5	75
V	10	S30.G21.KGP	0.64	0.44†	—	1	1.04	102
	11	S35.I10.KGP	0.63	0.182‡	—	1	0.906	75
VI	12	C20.B7.KGP.3×4	-	2.86§	1	10.43	—	110
	13	I25.KGP	-	0.33‡	—	1	0.666	119

			Composition (ratios by weight)					Cure time (days)
Set	Specimen	Specimen ID	CS and FS (1:1)	Other	Basalt	KGP	Gravel (<3/16 in.)	
	14	S21.B7.KGP.3×4	0.809	—	0.123	3	—	92
	15	Control. KGP 3×4	—	—	—	1	—	119
	16	Concrete with silica 3×4	0.45 H_2O:0.55 OPC:0.0247 SF:1.54 CS:3.08 gravel					92
	17	Control. NaGP 3×4	—	—	—	1	—	119
	18	Concrete with silica and basalt 3×4	0.57 H_2O:0.55 OPC:0.0247 SF:1.54 CS:3.08 gravel:0.085 basalt fiber					92

* Wollastonite Waste Tailings (W)

† Glass Powder (Uroboros, G)

‡ Fe_2O_3 (I)

§ Chamotte (C)

The numbers in Table 39 indicate the concentration of fillers in the mortar mixes without the inclusion of gravel. For example, sample 11, S35I10 has 35 wt% sand and 10 wt% iron oxide out of the total mass of the fine additives and the GP. If gravel is taken into account, the numbers become 23 wt% sand, 6.7 wt% iron oxide, 33.3 wt% gravel, and the remainder GP.

Samples made with pure GP were cured using an extended slow drying regime. Despite this, the sample developed hairline cracks on the surface and soon disintegrated before testing could begin.

Out of all the compositions tested, only four survived past 50 cycles of freeze thaw (FT): S50.Na, S60.NaGP, S50.NaGP, Conc+SF, and S21B7.KGP (Figure 93).

Figure 93. Freeze-thaw data for 16 out of 18 compositions created.

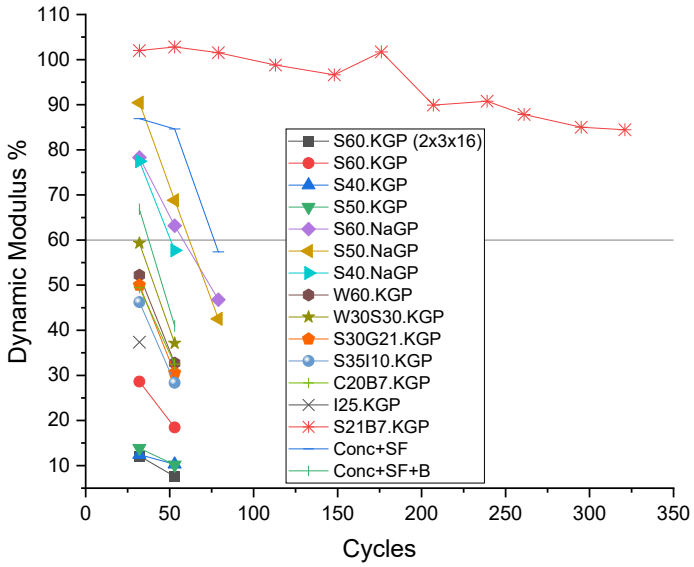

Increasing the amount of sand and gravel aggregate increased the FT resistance in the KGP samples with no clear trend in the NaGP samples. NaGP massively outperformed KGP when identical compositions containing sand and gravel were examined. Sand and gravel KGP samples were all found to absorb more water than the NaGP samples with an average of 4.65% gain in mass (SD = 0.0027) compared to 1.44% (SD = 0.0097) for the NaGP samples, using masses from before testing and after the first set of cycles. This explains why KGP is poorer in FT since more water in the pores will exert higher pressures. The root cause of KGPs increased water permeability is not known but indicates wider pore channels and more interconnected nanopores. Adding other types of nontraditional reinforcement decreases the amount of water absorbed and increases FT resistance in KGP. Samples with wollastonite tailings, sand and wollastonite tailings, and iron oxide/sand (8–11) had an average mass gain of 1.21% (SD = 0.007) and a dynamic modulus almost double the S60.KGP sample at 53 cycles. The sample made with iron oxide and gravel (13) failed by dissolving away and is the only sample that lost mass after the first set of cycles (-6.6 wt%). Mixing sand with iron oxide prevents this dissolution. The mechanism for dissolution is not known.

The calcium silicate “needles” and noncircular minerals in the wollastonite help with bonding to the matrix and crack bridging, which reduces vibrational dampening and increases the dynamic modulus. Basalt fibers

produce excellent results in KGP due to crack bridging and supersedes all the other compositions in terms of FT survivability. Iron oxide and the Uroboros glass are fine powders and inhibit water permeability by making water molecules diffuse around the particles, which explains their lower mass gain. The fine powder and fiber crack bridging effect were not observed when chamotte and basalt fiber were used as fillers. The components gained significant mass (5.5 wt%) and did not perform as well as the other basalt fiber sample due to casting defects caused by the low workability of the mixture. The concrete "control" mixture performed similar to the S60.NaGP samples, and the concrete basalt fiber sample had a lower dynamic modulus than this because the basalt fibers created large open pores on the surface and insides of the sample, which degraded FT resistance. The S60.KGP sample with the smaller 2 × 3 in. cross section (1) had one of the lowest dynamic moduli because microcrack damage has a smaller distance to traverse to induce dampening effects.

GP with traditional aggregate as well as the concrete sample (*1–7* and *16* in Figure 94) sustained spall damage, which was more concentrated at the ends of the samples, and small deep cracks ranging 1 cm long. Samples 8–10 had minor spalling at the ends and large and deep longitudinal cracks that run the length of the sample. Sample 11 was partially dissolved; 13 even more so. Sample 12 had no observable surface damage. The black lines seen in Sample *12* in Figure 94 are the surface-level casting defects. The other basalt fiber containing specimen (14, 18) showed damage in the form of an unevenly degraded and flaky surface.

Figure 94. Representative close-ups of characteristic damage for all the samples after testing had completed.

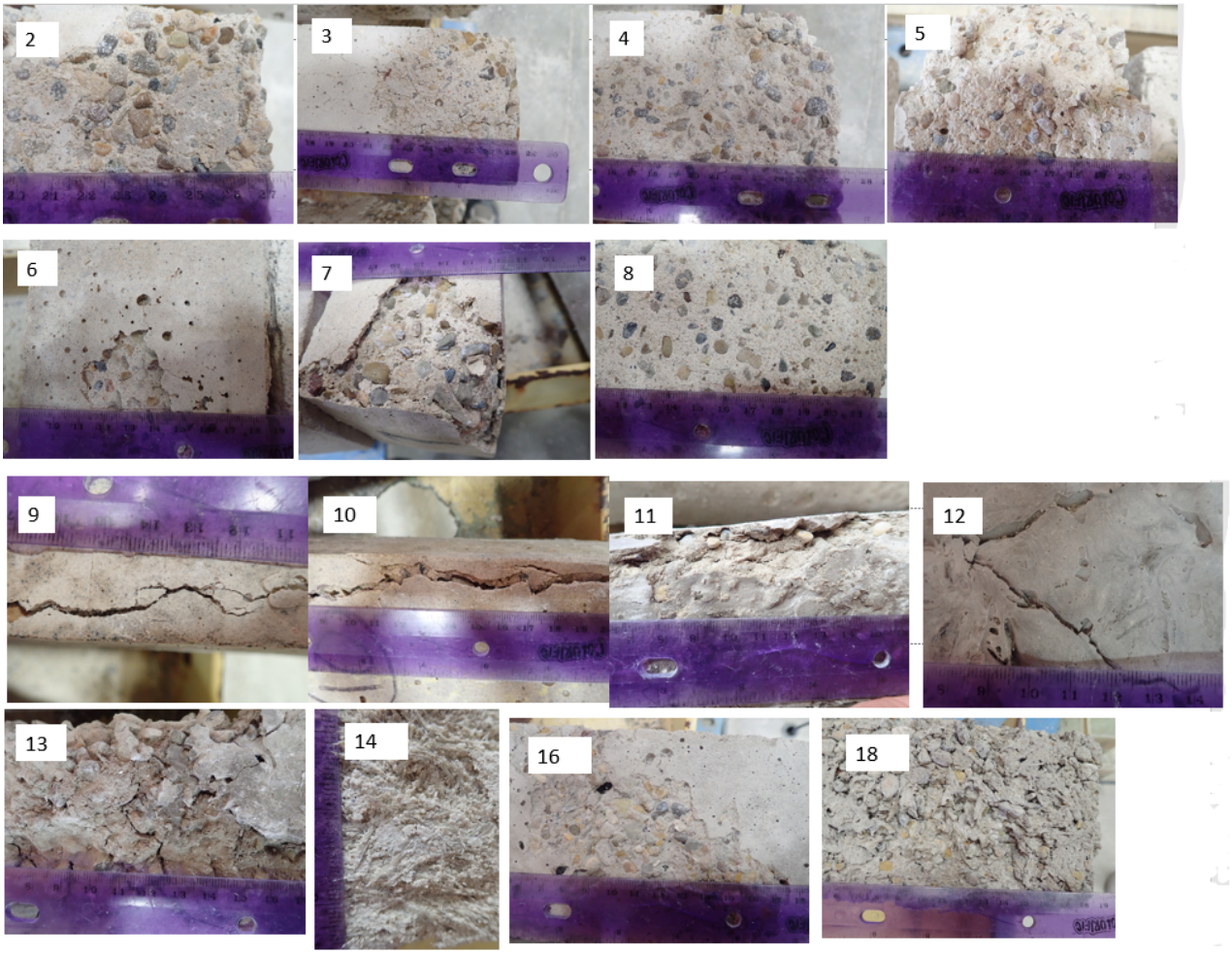

Flexure tests were completed based on ASTM C78 using a United SFM-300 mechanical testing machine with a 300 kN load cell (Table 40). The load and support span were 8 and 12 inches respectively. The loading rate was 0.127 cm/min. The sample support pads were 6 mm thick 70 dura rubber. This was done to see whether there was a correlation between FT resistance, which is based on nondestructive testing, and actual mechanical properties once testing finished.

Table 40. Loads of all the samples.

Specimen #	Load (N)
1	157
2	358.47
3	273
4	432.49
5	987.32
6	685.36
7	1,132.3
8	1,151.93
9	1,429.14
10	348.88
11	407.97
12	1,139.17
13	—
14	2,540.91
15	—
16	867
17	—
18	1,083.3

The flexure stress was calculated for each sample but was found to be low due to surface flaws and internal damage: less than 0.05 MPa for all samples. The loads of the NaGP samples (1–4) were more than twice as strong as their respective KGP samples (5–7) and comparable to the concrete specimen. The samples with wollastonite waste and basalt fiber had relatively high strengths with the sand + basalt fiber sample having the highest strength owing to crack deflection provided by the basalt as well as no considerable surface defects at or near the loading points.

Using Minitab 17 software, the *p* value was calculated to be 0.002, which indicates no statistical correlation between the two test results (Figure 95). Samples that had failed FT testing still had relatively high strengths.

Figure 95. Correlation statistics for dynamic modulus and the flexural load.

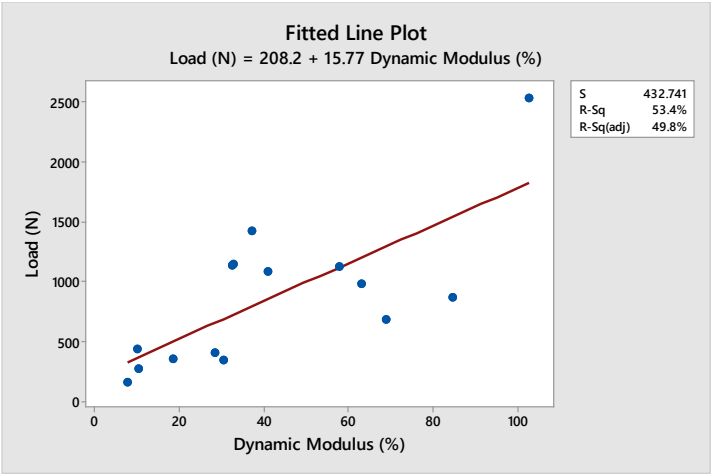

The specimens all failed by brittle failure. Specimens 1–3, 10, and 11 were more ductile than the others and survived the testing intact. The basalt fiber specimens had a nonlinear crack propagation, which explains their relatively high strength. The cracks propagated between individual fibers with minor evidence of fiber pullout. See Figure 96 for characteristic failure modes.

Figure 96. Representative pictures of the chief failure modes of the specimens. From *left* to *right*: Brittle failure (sample 7), a more ductile failure (sample 11), basalt fiber failure (sample 14).

2.8 Corrosivity measurements

Corrosivity measures how corrosive a building material is to the surroundings by measuring the electrical conductivity of a DI water and potassium chloride solution that the building material was exposed to for a given period (12 days at 71°C). A higher-measured conductivity indicates more ionic constituents got leached into solution from the sample and an

increased overall corrosivity index. ASTM D4350-16 is intended to be used for plastics and fillers but will also be used here to compare between OPC, GP, and other traditional building materials. The OPC and GP samples were mixed, cast, cured, and then dried for 28 days prior to preparing the samples.

Both sodium and potassium GP were more corrosive than the control and the thermoset composite used. There was little to no significant difference between Na and KGP corrosivities (t-test, p = 0.75), which is to say that both GPs leached roughly equal amounts of sodium and potassium hydroxide into the solution given that electrical conductivity is directly proportional to ion concentration (Table 41).

Table 41. Corrosivity results.

Samples		Specific conductance, S $ohms^{-1}$	Corrosivity index [SD] $ohms^{-1}$
Control	1	776.5	786.0 [6.67]
	2	791.7	
	3	786.8	
	4	789.2	
Derakane Vinyl Ester Thermoset	1	792.4	790.9 [5.79]
	2	786.2	
	3	798.5	
	4	786.6	
Wood OSB	1	803.4	835.0 [35.8]
	2	819.9	
	3	830.7	
	4	885.9	
Wood (Eacom Lumber 2×4, SPF (spruce/pine/fir)	1	733.7	754.1 [18.9]
	2	779.0	
	3	748.4	
	4	755.1	
Cement Paste (Quikrete OPC)	1	3,769	3,873 [87.7]
	2	3,981	
	3	3,886	
	4	3,853	
Na-based GP	1	1,086	1,069 [63.7]
	2	1,123	
	3	999	
K-based GP	1	1,104	1,086 [66.6]
	2	992.0	
	3	1,100	
	4	1,149	

The following equation is for conductivity:

$$C = kM, \quad (15)$$

where

C = the conductivity in units of siemens (S) per cm,
k = the molar conductivity in S L mol^{-1} cm^{-1}, which measures how well an ion conducts charge, and
M = the concentration in mol per liter (L).

Because of potassium's higher molar conductivity, less of it needs to be leached out to produce the same conductivity. By setting the conductivities of the NaGP and KGP samples equal to one another in Equation (10), the concentration of potassium ions in solution could be approximated as 30% less than the concentration of sodium ions. The amounts of KOH and NaOH in the bulk of the GP should be taken into consideration also since a matrix with twice as much leachable ions would have double the conductivity.

Fresh KGP contains approximately 15% potassium by mass, while NaGP contains 7.2% Na by mass. Both Na and K composites lose the same amount of water according to data in Table 16, so the relative amounts of Na and K in the cured and dried paste should both slightly increase by the same amount. Despite KGP having double the potassium content, the concentration of potassium leached out is 30% less. The inherent increased leachability of the sodium ions can be explained with sodium's higher enthalpy of solution as well as easier diffusion owing to its smaller ionic radius (Carrillo-Tripp et al. 2003).

Corrosivity of wood depends on the treatment. Treated and glued OSB has a slightly higher corrosivity than the control, while untreated pine has a lower, "negative" corrosivity, likely because it adsorbs some of the potassium ions from the initial solution (Figure 97). Most importantly, GP was found to be almost four times less corrosive than OPC paste (Quikrete). This is largely because KGP has approximately 15% potassium by mass, while OPC has approximately 60% of CaO. Residual unreacted $Ca(OH)_2$ also produces 2 mol of OH^- for every starting mol CaO. This finding is important for environmental reasons as well as engineering design; GP will not be as chemically hostile to traditional steel concrete reinforcements.

Figure 97. Example of the two specimens after 12 days in the oven.

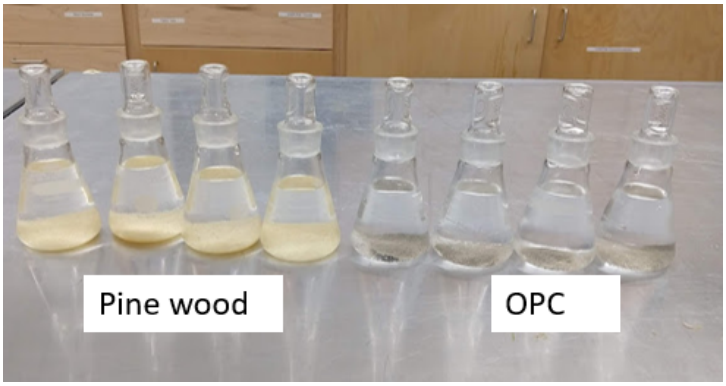

2.9 Portland cement versus GPs

Concrete is the most abundantly used construction material around the world. Concrete alone can be attributed to numerous project applications within and outside the construction industry, with varying benefits. Despite the wide use of concrete, it is energy intensive, and the environmental impact as well as economic impact are immense. Ordinary Portland cement is the number one concrete binder used in industry, and its use comes with a plethora of drawbacks. With the addition of current known additives and the emergence of GP cement technology, the economic and environmental impact of construction can be minimized. GP concrete implementation is a sustainable option for construction with its longer service life, reduced global warming potential, recycled industrial waste, life-cycle cost saving, and low carbon emissions.

The term “GP” was first introduced by Davidovits to describe a family of mineral binders with chemical composition similar to zeolites but with an amorphous microstructure. GPs have high-order molecular structures or are macromolecules, which is why they are considered polymers. Zeolites are solids with a relatively open, three-dimensional crystal structure comprised of the elements aluminum, oxygen, and silicon, with alkali metals plus water molecules. Unlike Portland cement, GPs do not form calcium silicate hydrates for matrix formation and strength but use the polycondensation of silica and alumina precursors to attain structural strength. Water is not involved in the chemical reaction of GP concrete; instead, water is expelled during curing and the subsequent drying process. This contrasts with the hydration reactions that occur when Portland cement is mixed with water, which produce the primary hydration products calcium silicate hydrate and calcium hydroxide. The source materials for GPs should be aluminosilicate based and plentiful in

silicon and aluminum. Many by-product materials, such as fly ash, silica fume, slag, rice-husk ash, red mud, etc., can be used as additive to form partial GP concrete mixes. This provides a viable use for a lot of "waste" materials that are often destined for a landfill. GPs are also unique in comparison to other aluminosilicate materials such as aluminosilicate gels, glasses, and zeolites.

Portland cements can provide adequate levels of strength, durability, and are the most popular cements used by concrete producers. However, some applications require the use of other cements to provide higher durability, fire resistance, and environmental benefits. The need for high-strength and early-strength-gaining cements in pavement repairs and the use of blended cements with aggregates susceptible to alkali-aggregate reactions are examples of such applications. Portland cement hardens by reacting with water and forms a water-resistant product. The low cost and widespread availability of the limestone, shales, and other naturally occurring materials make Portland cement one of the lowest-cost materials used over the last century throughout the world. The properties of concrete depend on the quantities and qualities of its components used in the mix design. Because cement is the most active component of concrete and usually has the greatest unit cost, its selection and proper use are important in most economically obtaining the balance of properties desired for any concrete mixture. The current world statistics on the shortage of Portland cement source materials emphasizes the necessity of GP concrete. In 2012, it was determined that every year around 2.6 trillion tons of cement are required. This quantity will increase by 25% within a span of another 10 years. Since limestone is the main source material for the ordinary Portland cement, an acute shortage of limestone may come after 25 to 50 years of constant production.

The geopolymeric materials are *polymers*; therefore, they transform, poly condense, and adopt a shape rapidly at low temperatures. Furthermore, GPs are mineral materials that are hard, resistant to weather, resistant to high temperature, and stable. GPs are used just like thermosetting organic resins but are stable up to 1,000°C–1200°C (Davidovits 1991). The trapped molecular structure of silicone dioxide yields a low-porosity, highly packed microstructure with high density. GP concretes are resistant to freeze and thaw cycling, show high chemical resistance, and can also support an insulation R-value as high as 8 per inch of cellular material (Hassan et al. 2019), which signifies the material's resistance to conductive heat flow. An

added benefit to using GP cement versus traditional cements is the ability for the operator to select dynamic and designer modulus properties for faster or slower setting times. As an environmental advantage, GPs have extremely low air and water permeability, which helps with low leaching. They can also withstand extreme heat without degradation. Additionally, the variable curing methods for ultimate strength can be adjusted to hours, days, or weeks. With curing, it was determined that an increased curing temperature in the range of 30°C–90°C increased the compressive strength of GP concrete, and longer curing times also increased the compressive strength (Abdul Aleem and Arumairaj 2012).

The ratio of alkaline liquid to fly ash by mass does not affect the compressive strength of the GP concrete. The sodium silicate to sodium hydroxide ratio by mass equal to 2 has resulted in higher compressive strength as compared to the ratio of 2.5 for the GP concrete. The compressive strength of the GP concrete increases with an increase of sodium hydroxide concentration. The compressive strength of the GP concrete increases with an increase in the curing time. However, the increase in strength beyond 24 hours is not very significant. The workability of the GP concrete mix increases with the addition of superplasticizer up to 4% of fly ash by mass. Minor reduction of compressive strength of the GP concrete is observed when the superplasticizer dosage used is greater than 2%. A one-day rest period increases the compressive strength of the GP concrete as compared to that for the concrete without the rest period. The compressive strength of the GP concrete decreases with an increase in the ratio of water to GP solids by mass (Łach et al. 2019). The workability of the GP concrete in fresh state increases with the increase of extra water added to the mix. With an increase in the curing temperature in the range of 600°C to 900°C, the compressive strength of the GP concrete also increases. Therefore, a wide variety of parameters affect the compressive strength of the GP concrete. The influencing parameters should be studied to determine the effect on the compressive strength of GP concrete before conducting additional investigations related to mechanical properties and durability of the GP concrete.

A common misnomer that a substantial portion of the GP community uses to describe GPs is alkali-activated aluminosilicates. This name is considered false because manufactures tend to use impure forms of aluminosilicate sources such as industrial waste products of slag and fly

ash that may also come from various sources. These compositions tend to lie off the stoichiometric 1:1:4:11 compositions measured by transmission electron microscopy of metakaolin-derived GPs (Kriven 2018). GPs include three classifications of inorganic polymers, which depend on the ratio of Si/Al in their structures:

- Poly (sialite) (-Si-O-AL-O-)
- Poly (sialate-siloxo) (-Si-O-Al-O-Si-O-)
- Poly (sialate-disiloxo) (-Si-O-Al-O-Si-O-Si-O-)

The distribution and relative amounts of each of the different Al and Si building blocks affect the chemical and physical properties of the final product (Thaarrini 2016). These waste products contain irreproducible impurities that cause microstructural inhomogeneities. These composites tend to have significantly more varied mechanical properties due to the fly ash sources and the presence of calcium silicate hydrate, potassium aluminosilicate hydrate, or sodium aluminosilicate hydrate binder phases, such as those that occur in cements. A key difference between alkali-activated cements and GPs is that the alkali-activated cements are hydrated, crystalline precipitates, while GPs are amorphous, inorganic polymeric nanoprecipitates that do not contain chemically bound water other than the hydrogen-bonded entrapped water. In contrast to GP cements, the structure is polymerized into a silicoaluminate, three-dimensional network of the potassium-poly(sialate-siloxo) in which the silicon unit is of the type Si(Q4) (Davidovits 2013).

The preparation process for a true GP cement follows the chemical reaction, and each step relates to a process, namely (1) mixing of K-Na silicate and metakaolin, slag, or fly ash, (2) mixing time and mixing method, (3) resting time, (4) starting to harden, and (5) hardening (Davidovits 2018).

A lot of confusion around the differences between alkali activation and geopolymerization comes from misunderstanding whether there are other activators other than basic NaOH. There is no activator for geopolymerization, only hardener or reagent. There is no “activator” because the composition of GP cement has chemically reactive ingredients and hardeners that do not require to be activated.

GP cements have been effectively introduced in the industry and are able to be implemented in many other applications. They yield synthetic mineral products with such properties as hard surfaces, thermal stability, and high surface smoothness and precise mouldability. Such products are useful for tooling; for molding art objects, ceramics, and the like; and as building materials. One of the largest issues with Portland cement and a motivating factor for the application of GP cement are the current CO_2 emissions associated with concrete. CO_2 emissions resulting from chemical reactions of concrete will continue to grow with industrial development and demand. This is specific to Portland cement manufacturing based on the resulting reaction from its formation. Portland cement results from the calcination of limestone and silico-aluminons material. The formation of CO_2 is as follows:

$$5 \cdot CaCO_3 + 2SiO_2 \rightarrow (3 \cdot CaO,SiO_2)(2 \cdot CaO,SiO_2) + 5 \cdot CO_2 \quad (16)$$

The production of 1 ton of OPC directly generates 0.55 tons of chemical CO_2 and requires the combustion of carbon fuel to yield an additional 0.40 tons of CO_2. Accordingly, 1 ton of OPC is equivalent to 1 ton of CO_2. In 1988, 1 billion metric tons of OPC produced globally accounted for one billion metric tons of CO_2, which is representative of 5% of the 1988 world CO_2 emissions, and there has been no notable change, while 1 ton of GP only liberates 0.25 t of CO_2 (a reduction of 75%). An explanation for this is that GP cements do not rely on calcium carbonate and support an emissions reduction in the range of 40% to 90%. GP concrete helps in the reduction of required energy by 36% in comparison with Portland cement. The fuel (thermal energy) usage will be reflected in the CO_2 emissions reduction (Assi et al. 2018).

Similar to zeolitic materials, GPs are able to adsorb toxic chemical wastes. They immobilize hazardous elemental wastes within the geopolymeric matrix and act as a binder to convert semisolid waste into an adhesive solid. Modern geopolymeric cements demonstrate the exceptional durability of zeolite cements and erosion resistance. Geopolymeric cements designed for waste containment provide early high-strength development, which can be enhanced with the adjunction of microwave preheating devices aimed at raising the inside temperature of the waste form to 35°C. Ambient temperature curing of GPs made from waste is used for the safe and innocuous disposal of toxic and hazardous wastes (Davidovits 1994b) Without this option for treatment, these hazardous

materials require a special landfill with double plastic-and-clay liners and leachate collection systems. These lined hazardous waste landfills are difficult and expensive to install. Also, they require long-term monitoring of at least 30 years and show high rates of failure in the first decade (Davidovits 1994). Conversely, GP monolithic structures are easier to install, are maintenance free, and a viable future initiative for hazardous waste.

Many concretes made from contaminated or wastes sources can leach, causing contaminated soils that contain both inorganic and organic toxic compounds. In situ immobilization offers simplified treatment advantages, such as speed and economy. A leaching assessment was done by Azarsa and Gupta (2020) on GP cements and Portland cement made of waste by-products to characterize the leaching potential of toxic metals. In that research, water-proof sheet membranes were used in the foundation of a section of paver blocks to prevent penetration of water to the subgrade level and allow sampling of water that had percolated through the paver blocks and had been in contact with them. Water samples that permeated through the paver blocks were collected to trace the total alkalinity, total hardness, pH, total chlorine, phosphate, copper, ammonia, iron, nitrate, and nitrite. Every 30 days, six water samples were collected from each GP cement and Portland cement collection pit. The results indicate that the pH of GP is 7.9 and the pH of Portland cement is 6.8, respectively, and these values were constant over the total age of exposure. GP cement paver blocks show higher pH values than Portland cement, which is attributable to the use of potassium hydroxide. Furthermore, as it is reported by Izquierdo et al. (2009) that heat-treatment of GP concrete improves the matrix microstructure, decreases the porosity of concrete, and decreases the leachability of the binder. So, it can be concluded that steam curing improved the microstructure of GP cement paver blocks and reduced the number of heavy metals in water samples.

Generally, water hardness concentration below 60 ppm is considered as soft; 60–120 ppm, moderately hard; 120–180 ppm, hard; and more than 180 ppm, very hard (Kozisek et al. 2020). The total hardness of GP cement and Portland cement is 120 ppm and 180 ppm, respectively, over 150 days of exposure. Iron as one of the main chemical elements of GP cement and Portland cement is 0.15 and 0.2, respectively, over the total age of exposure. For both types of concrete, other elements such as chlorine, nitrate, and nitrite were constant over 150 days, and their leachability was

below the detection limit. The results show that all the metals were immobilized effectively for both types of concretes. All the elements of K-based GPC paver blocks were constant over 150 days as the steam curing method was used to develop the paste structure, which is attributed to a full reaction of fly-ash and bottom-ash particles. This also confirms that slag-based GP cement cured at 80°C for 8 hr can effectively immobilize chemical metals when the number of chemical metals is in the range of 0.1%–0.3%. Another study done by Tome et al. (2018) looked at the encapsulation efficiency of these cements; the toxicity characteristic leaching procedure was carried out by following the USEPA method 1311. The leached metals from the GP samples were far lower than the maximum concentration of each contaminant stipulated by USEPA for toxicity characteristics. This confirms the efficiency of the developed GP to stabilize heavy metals. The concentration of cadmium released was less than the instrumental detection limit for all GP samples. This depicts high stabilization of cadmium after geopolymerization due to the very low solubility of $Cd(OH)_2$ and is in agreement with other reports.

With the innovation of GP designs, scientists can focus on components such as differentiating the concentration sodium hydroxide solutions and studying the accompanying characteristics. Likewise, the effect of different curing methods, such as hot air curing, steam curing, sun curing, and ambient curing, should also be studied. Furthermore, the molar ratios of sodium hydroxide solutions in conjunction with differing curing methods should be studied. By continually using GP cement where engineers would typically use Portland cement, researchers can study different structural elements, like concrete beam, reinforced cement concrete beam, and reinforced concrete columns. The study of concrete structures should also be studied with the above methods that include varying concentrations of sodium hydroxide solution and curing conditions (Abdul Aleem and Arumairaj 2012).

Fly-ash-based GP concrete offers several economic benefits over Portland cement concrete. The price of one ton of fly ash is only a small fraction of the price of one ton of Portland cement. Therefore, after allowing for the price of alkaline liquids needed to the make the GP concrete, the price of fly-ash-based GP concrete is estimated to be about 10%–30% cheaper than that of Portland cement concrete. In addition, the appropriate usage of one ton of fly ash earns approximately one carbon credit that has a significant redemption value. One ton of low-calcium fly ash can be used to

manufacture approximately three cubic meters of high-quality, fly-ash-based GP concrete, and hence, earn monetary benefits through carbon-credit trade. Furthermore, the very little drying shrinkage, the low creep, the excellent resistance to sulphate attack, and good acid resistance offered by the heat-cured, low-calcium, fly-ash-based GP concrete may yield additional economic benefits when it is used in infrastructure applications (Lloyd and Rangan 2010).

When performance specifications for Portland cement were written, other cements were uncommon and not considered. GP cement does not have the long-standing performance history that Portland cement has. However, with the expanding interest in GP cement, scientists should consider whether the existing cement standards provide a useful structure for continued discovery and exploration of GP cements. The implementation of new standards could make the use of GP cements accessible and challenge standard practices. GP concrete has performed very well in accelerated durability tests and leachability tests. The emergence of other nontraditional cement binders may be in the future for the concrete industry.

The demand for GP cement is driven by a market that is continuously growing in its mindfulness of carbon emissions. Considering that the scale-up from the laboratory to the real-world application is challenging, the major hurdle will be to encourage industry participation and approval of GP cement. The fact that concrete standards are established on an assumption of the use of Portland cement remains a major obstacle to the commercial acceptance of GP cement. Even when GP cement attributes are fully accepted, the foremost barrier to entry into the market is access to a suitable supply of source materials, including fly ash, granulated blast furnace slag, and alkaline activators. It is important for commercial GP concrete producers to work closely with research partners and stakeholders to develop testing methods for enhanced durability and identify feasible long-term sources for production.

3 Conclusions

3.1 Rheological conclusions

In terms of basic rheological characterization, GP pastes and OPC were proven to be shear-thinning Bingham fluids with potentially thixotropic properties. Smaller particle-sized metakaolins, such as Metamax EF, had higher viscosities than the metakaolins with larger particle sizes, such as Powerpozz. OPC paste (0.45 water to cement ratio) had the second highest viscosity range in comparison with all the potassium-based GP systems. Through stress ramp analysis, all of various metakaolin KGP systems exhibited some extent of thixotropy, but a high enough shear rate must be achieved (50 1/s) to disturb the liquid structure. The stress recovery experiments, however, allow us to estimate a recovery time of approximately 30% of the high shear time for GPs in terms of returning to initial low shear viscosity, which strengthens the argument proving the thixotropy of GPs.

The yield stress comparison showed consistently much higher yield stress values for OPC versus GP for consistent wt% of both coarse and Quikrete sand. The yield stresses for coarse sand at coordinating weight percentages were also consistently greater than the fine sand samples for both OPC and KGP. To obtain shape retentive properties, yield stresses must surpass at least 150 Pa for printability, which was not achieved by any of the KGP samples with Quikrete or coarse sand. More reinforcements or a different metakaolin must be used in addition to sand to achieve the required shape retention. When comparing the two models used for determining yield stress, the HB model was consistently higher than the stress ramp model, likely due to the interpolation necessary to calculate the yield stress.

Shape retention cones proved vital in understanding the influence of different sizes and shapes of reinforcement materials. From the shape retention testing, it was deemed that gravel, basalt minibars, and basalt minirods would likely not be useful as reinforcement material for KGP paste. Basalt fiber, however, in small weight percentages, introduces more shape retentive property to the KGP paste and is a foundational material to enhance the rheological properties of KGP reinforced with any type of sand. Of the two size of basalt fiber available, the 1/8 in. provided the best shape retention and is also least likely to cause issues in terms of clogging up the extruder head of the 3D printer.

From squeeze flow testing, the specific compositions of KGP 60 wt% Quikrete medium sand with 3 wt%, 1/2 in. basalt fiber; KGP 50 wt% Quikrete medium sand with 3 wt%, 1/2 in. basalt fiber; KGP 60 wt% Quikrete medium sand with 3 wt%, 1/8 in. basalt fiber; and KGP 60 wt% Quikrete medium sand with 3 wt%, 1/8 in. basalt fiber show exceptional potential to be used as the final composition for 4D printing. Specifically, these compositions show potential due to the amount of jamming that occurs at higher sand and fiber percentages that increases deformation resistance, which allowed the GP composite to hold its shape and support the weight of successive layers.

3.2 Mechanical properties of composites

As expected, the raw forms of OPC and GP paste had more variability in their flexural strength results than the rest of the composites. With reinforced samples, the flexural strengths were relatively precise, but some outliers resulted from inconsistent or improper sample making. For instance, improper packing of the samples may have resulted in surface segregation of sand, large pores, air bubbles, or surface cracks. Comparable flexural strengths were observed between OPC and KGP composites, but KGP realistically outperformed OPC samples as a fine sand mortar only.

Concerning compressive strength, KGP samples only outperformed OPC samples as concrete. Surface cracks were shown in both OPC and KGP paste cylinders, but these cracks showed far earlier in GP cylinders. If pure GP samples are to be tested, special care must be taken when testing larger samples. Qualitatively, porosity was kept minimal with cylinder samples, and this helped avoid the issue of crack sources appearing when the samples were loaded.

Weight loss from drying showed the loss of free water in each matrix. Because both matrices showed similar rates of drying, this may show further similarities in how KGP and OPC composites strengthen with age when reinforced with the same materials.

Smaller reinforcements gave better flexural strengths, but larger ones gave better compressive strengths. The interfacial transition zone (ITZ) is the area between the matrix and a reinforcement, and the ITZ is larger with larger reinforcements. During hydration, the ITZ diminishes with the loss of free water in OPC composites. However, the geopolymeric network

contains nanopores that may lead to a varying ITZ throughout the sample. When a sample is small, such as with the bars used in this study, the effect of the ITZ may have a drastic effect that may not be shown with a larger sample, such as the compression cylinders. These effects can be alleviated with the use of very fine filler phases, like desert sand, or through the use of a plasticizer.

3.3 Water retention and mechanical properties

The final and initial strengths of sodium and potassium GP composites containing sand and gravel vary with temperature and humidity. Both GPCs were slow to set at 10°C, 80% RH, with sodium being slower than potassium. At 20°C, 50% RH, KGP was more sensitive to the effects of humidity and gave a weaker GP than NaGP. At 40°C, 80% RH, this effect was flipped, and KGP appeared to be more stable and stronger than NaGP at 28 d, though this difference was not much. High temperature and high humidity produced the strongest GPs at 28 d than any other condition. GPs cured at low temperatures (10°C) are expected to also produce high-quality GP given enough time based on the results of the 1 × 1 × 10 cm tests. This highlights the need for a water impermeable barrier to be used when casting GPC in other environments, such as hot and dry conditions.

GPs become stronger with increasing the amount of particulate reinforcement. The addition of basalt fibers to a system of sand, glass powder, or gravel, only marginally increases the flexure strength (by a few MPa). Silica fume causes a significant increase in strength, the highest of any composite tested; however, GP composite containing SF dissolves in water, which limits its applications. The mechanism for this is still not clear. Water retention was found not to vary due to the alkali used or the metakaolin used.

3.4 Thermal considerations

Coarse aggregate and sand should be avoided in mixtures expected to withstand high temperatures in excess of 400°C for long periods of time because coarse aggregate decomposes and causes the surrounding matrix to crack and disintegrate. Adding white, recycled waste glass powder initiates self-healing beyond 800°C and increases the flexure strength.

A high weight percentage of inert mineral reinforcement and glass powder along with a GP with a low Si/Al ratio should be used for lowest thermal

shrinkage and best mechanical properties. The relative amounts of glass and inert reinforcement should be optimized based on the strength demands and tolerances of the specific application.

GP with conventional additives can tolerate high flame temperatures that are characteristic of forest fires for up to 30 seconds, after which a gradual reduction in flexural strength occurs with time. KGP is more resilient to this type of thermal treatment than NaGP, which is predicted from literature.

4 Future Work

4.1 Rheology

Future work in rheology will focus on three specific areas: the influence of using a Na-based GP for printing, oscillatory testing to further understand the rheological changes associated with the polymerization process, and the influence of printing temperature. Na-based water glass, when synthesized in-house, has a much greater viscosity than K-based water glass synthesized in-house. It is often found that additional moles of water must be added to improve the overall workability of Na-based GP paste, but little work has been done to characterize the overall flow properties. A study further focusing on the rheological properties of Na-based GPs would allow the potential use for 4D printing.

In addition, to compare to the UWR data, an in-depth study characterizing changes in storage and loss modulus of KGP paste is promising for identifying specific steps (dissolution, polymerization, formation of oligomers, etc.) in the geopolymerization. Much work has been done to explore this concept with nuclear magnetic resonance (NMR), but little has been done using the rheological properties to identify the specific time point of early polymerization mechanisms (Rouyer and Poulesquen 2015; Steins et al. 2012; Duxson, Fernández-Jiménez, et al. 2007).

Last, the influence of temperature must also be studied to gain a foundational understanding of how temperature will influence the rheological properties of the paste as it is being extruded. Studying the influence of temperature will also provide an understanding of how variations in temperature may influence flow properties and setting of GP, which is critical given the expectation of printing in both extreme hot and cold environments of GP.

4.2 Mechanical properties of composites

A better understanding of the mechanical properties of GP composites must be built on systematic studies of aggregates, aggregate size, aggregate shape, sample size, the use of additional additives, curing conditions, and microstructure. To determine the practicality of GP composites as a building material, it is useful to continue to compare these composites to OPC composites. The interface between cement and aggregates is well

studied and understood for many types of OPC composites with aggregates, including fine sand, minerals, and gravel. Additionally, aggregate size and shape have also been considered for compressive, tensile, and flexural strength to observe the correlation to overall mechanical strength. The ITZ remains a relatively difficult aspect to study but is important to porosity and fracture and crack propagation, thereby influencing the strength of composites. These effects are not well understood in GP composites, but while w/c ratio does not affect the strength of GPs due to the absence of hydration in geopolymerization, crack propagation and porosity are crucial to the mechanical strength of GP composites. Curing conditions, the use of fine "filler" phases, and additives such as fibers and plasticizers may all affect the ITZ and the mechanical strength of composites. To study these effects, backscattered electron microscopy (BSE) has been used to observe average qualitative and quantitative properties of the ITZ in OPC composites. Digital image correlation (DIC) is also a useful tool to observe crack propagation and microstructure, especially in flexural strength testing, and may be able to conjunctively observe and correlate the effect of the ITZ on mechanical strength.

Previous work on GP composites have shown compressive strengths nearing and eclipsing 100 MPa, and these findings have made GPs popular as a possible building material. However, most studies that have shown these very high strengths have been done on samples that are quite small. Studies for OPC composites have shown that cylinders that measure 6 × 12 in. generally have lower compressive strength than those that are 4 × 8 in. and smaller. More work should be done on GP composites on what seems to be a size effect in these samples. Finding the differences between the cylinder sizes will provide better insight into the feasibility of determining GP mechanical strength for building components. Combining these results with those of the ITZ may bridge the gap between ceramic and civil engineering and help advise prospective projects with specific applications of GPs.

4.3 Thermal, mechanical, and FT properties of composites

Future work in water retention and mechanical properties of GP composites could focus testing on other compositions than SG50 across a wider range of humidities. Therefore, a suitable moisture retention layer should be developed for GPCs that are laid down or printed in dry climates.

Future work for thermal properties could focus on establishing the mechanism for the strength increase of the silica fume composite as well as propane forge flame tests on a variety of different compositions.

References

Abdullahi, M. 2012. "Effect of Aggregate Type on Compressive Strength of Concrete." *International Journal of Civil and Structural Engineering* 2 (3): 791–800. https://doi.org/10.6088/ijcser.00202030008.

Abdul Aleem, M. I., and P. D. Arumairaj. 2012. "Geopolymer Concrete—A Review." *International Journal of Engineering Sciences and Emerging Technologies* 1 (2): 118–122. https://doi.org/10.7323/ijeset/v1_i2_14.

Akoz, F., N. Yuzer, and S. Koral. 1995. "The Influence of High Temperature on the Physical and Mechanical Properties of Ordinary Portland Cement and Silica Fume Mortar." *Teknik Dergi [Technical Journal of the Turkish Chamber of Civil Engineers*] 6 (26): 919–931. https://dergipark.org.tr/en/pub/tekderg/issue/12820/155481.

Alexis, M.A., C. Rumpel, H. Knicker, J. Leifeld, D. Rasse, N. Péchot, G. Bardoux, and A. Mariotti. 2010. "Thermal Alteration of Organic Matter during a Shrubland Fire: A Field Study." *Organic Geochemistry* 41 (7): 690–697. https://doi.org/10.1016/j.orggeochem.2010.03.003.

Alhozaimy, A. M. 2009. "Effect of Absorption of Limestone Aggregates on Strength and Slump Loss of Concrete." *Cement and Concrete Composites* 31 (7): 470–473. https://doi.org/10.1016/j.cemconcomp.2009.04.010.

Alonso, S., and A. Palomo. 2001. "Alkaline Activation of Metakaolin and Calcium Hydroxide Mixtures: Influence of Temperature, Activator Concentration and Solids Ratio." *Materials Letters* 47 (1–2): 55–62. https://doi.org/10.1016/S0167-577X(00)00212-3.

Anton Paar. "Amplitude Sweeps." Anton Paar Wiki. https://wiki.anton-paar.com/us-en/amplitude-sweeps/#:~:text=Amplitude%20sweeps%20are%20useful%20in,sealing%20compounds%2C%20and%20lubricating%20greases.

Anton Paar. "Basics of Thixotropy." Anton Paar Wiki. https://wiki.anton-paar.com/en/basics-of-thixotropy/#:~:text=Thixotropy%20is%20the%20property%20that,order%20to%20remain%20in%20place.

Archez, J., N. Texier-Mandoki, X. Bourbon, J. F. Caron, and S. Rossignol. 2021. "Shaping of Geopolymer Composites by 3D Printing." *Journal of Building Engineering* 34:101894. https://doi.org/10.1016/j.jobe.2020.101894.

Assi, L., K. Carter, E. Deaver, R. Anay, and P. Ziehl. 2018. "Sustainable Concrete: Building a Greener Future." *Journal of Cleaner Production* 198:1641–1651. https://doi.org/10.1016/j.jclepro.2018.07.123.

Austin, S. A., P. J. Robins, and C. I. Goodier. 1999. "The Rheological Performance of Wet-Process Sprayed Mortars." *Magazine of Concrete Research* 51 (5): 341–352. https://doi.org/10.1680/macr.1999.51.5.341.

Aygörmez, Y., O. Canpolat, M. M. Al-mashhadani, and M. Uysal. 2020. "Elevated Temperature, Freezing-Thawing and Wetting-Drying Effects on Polypropylene Fiber Reinforced Metakaolin Based Geopolymer Composites." *Construction and Building Materials* 235: 117502. https://doi.org/10.1016/j.conbuildmat.2019.117502.

Azarsa, P., and R. Gupta. 2020a. "Durability and Leach-Ability Evaluation of K-Based GP Concrete in Real Environmental Conditions." *Case Studies in Construction Materials* 13:e00366. https://doi.org/10.1016/j.cscm.2020.e00366.

Azarsa, P., and R. Gupta. 2020b. "Freeze-Thaw Performance Characterization and Leachability of Potassium-Based Geopolymer Concrete." *Journal of Composites Science* 4 (45). https://doi.org/10.3390/jcs4020045.

Bakharev. T. 2005. "Resistance of Geopolymer Materials to Acid Attack." Cement and Concrete Research 35 (4): 658–670. https://doi.org/10.1016/j.cemconres.2004.06.005.

Barbero, R., J. T. Abatzoglou, S. Larkin, C. A. Kolden, and B. Stocks. 2015. "Climate Change Presents Increased Potential for Very Large Fires in the Contiguous United States." *International Journal of Wildland Fire* 24 (7): 892–899. https://www.fs.usda.gov/treesearch/pubs/53089.

Barnes, H. A., and J. O. Carnali. 1990. "The Vane-In-Cup as a Novel Rheometer Geometry for Shear Thinning and Thixotropic Materials." *Journal of Rheology* 34 (6): 841–866. https://doi.org/10.1122/1.550103.

Barnes, H. A. 1999. "The Yield Stress—a Review or 'Παντα Ρει'—Everything Flows?" *Journal of Non-Newtonian Fluid Mechanics* 81 (1–2): 133–178. https://doi.org/10.1016/S0377-0257(98)00094-9.

Barnes, H. A., and Q. D. Nguyen. 2001. "Rotating Vane Rheometry—a Review." *Journal of Non-Newtonian Fluid Mechanics* 98 (1): 1–14. https://doi.org/10.1016/S0377-0257(01)00095-7.

Bentz, D. P., S. Z. Jones, P. E. Stutzman, J. Arnold, M. Boisclair, P. Rothfeld, J. Tanesi, H. Kim, J. Munoz, and M. Beyene. 2017. *Influence of Aggregate Characteristics on Concrete Performance*. Gaithersburg, MD: National Institute of Standards and Technology. https://doi.org/10.6028/NIST.TN.1963.

Berker, A. 2002. "Rheology for Adhesion Science and Technology." In *Adhesion Science and Engineering*, edited by A. V. Pocius, D. A. Dillard and M. Chaudhury, 443–498. Amsterdam, Netherlands: Elsevier.

Boer, M. M., V. R. de Dios, and R. A. Bradstock. 2020. "Unprecedented Burn Area of Australian Mega Forest Fires." *Nature Climate Change* 10: 171–172. https://doi.org/10.1038/s41558-020-0716-1.

Bong, S. H., B. Nematollahi, A. Nazari, M. Xia, and J. Sanjayan. 2019. "Method of Optimisation for Ambient Temperature Cured Sustainable Geopolymers for 3D Printing Construction Applications." *Materials* 12 (6): 902. https://doi.org/10.3390/ma12060902.

Bos, F. P., Z. Ahmed, R. Wolfs, and T. Salet. 2018. "3D Printing Concrete with Reinforcement." In *High Tech Concrete: Where Technology and Engineering Meet*, edited by D.A. Hordijk and M. Luković, 2484–2493. Cham, Switzerland: Springer International Publishing. https://doi.org/10.1007/978-3-319-59471-2_283.

Carpinteri, A., B. Chiaia, and G. Ferro. 1997. "A New Explanation for Size Effects on the Flexural Strength of Concrete." *Magazine of Concrete Research* 49 (178): 45–53. https://doi.org/10.1680/macr.1997.49.178.45.

Carrillo-Tripp, M., H. Saint-Martin, and I. Ortega-Blake. 2003. "A Comparative Study of the Hydration of Na+ and K+ with Refined Polarizable Model Potentials." *The Journal of Chemical Physics* 118 (15): 7062–7073. https://doi.org/10.1063/1.1559673.

Center for Geopolymer Research and Applications. n. d. "Educational Videos." The Grainger College of Engineering, University of Illinois at Urbana Champaign. https://cegra.engineering.illinois.edu/educational-videos/.

Davidovits, J. 1991. "Geopolymers: Inorganic Polymeric New Materials." *Journal of Thermal Analysis and Calorimetry* 37 (8): 1633–1656.

Davidovits, J. 1994a. "Geopolymers: Man-Made Rock Geosynthesis and the Resulting Development of Very Early High Strength Cement." *J. Materials Edu*cation 16 (2 and 3): 91–137.

Davidovits, J. 1994b. "Properties of Geopolymer Cements." In *First International Conference on Alkaline Cements and Concretes*, 131–149. Kiev, Ukraine: Scientific Research Institute on Binders and Materials.

Davidovits, J. 2002. "Environmentally Driven Geopolymer Cement Applications." Paper presented at Geopolymer 2002 Conference, Melbourne, Australia. 28–29 October 2002. https://www.geopolymer.org/wp-content/uploads/ENVIRONMENT.pdf.

Davidovits, J. 2013. "Geopolymer Cement a Review." *Geopolymer Science and Technics*, Technical Paper #21, Geopolymer Institute Library. https://www.geopolymer.org/wp-content/uploads/GPCement2013.pdf.

Davidovits, J. 2015. *Geopolymer Chemistry and Applications*. 4th ed. Saint-Quentin, France: Geopolymer Institute.

Duxson, P., A. Fernández-Jiménez, J.L. Provis, G C Lukey, A Palomo, and J. S. J. van Deventer. 2007. "Geopolymer Technology: The Current State of the Art." *Journal of Materials Science*. 42:2917–2933. https://doi.org/10.1007/s10853-006-0637-z.

Duxson, P., G. C. Lukey, and J. S. J. van Deventer. 2006. "Thermal Evolution of Metakaolin Geopolymers: Part 1—Physical Evolution." *Journal of Non-Crystalline Solids* 352 (52–54): 5541–5555. https://doi.org/10.1016/j.jnoncrysol.2006.09.019.

Duxson, P., G. C. Lukey, and J. S. J. van Deventer. 2007. "The Thermal Evolution of Metakaolin Geopolymers: Part 2—Phase Stability and Structural Development." *Journal of Non-Crystalline Solids* 353 (22–23): 2186–2200. https://doi.org/10.1016/j.jnoncrysol.2007.02.050.

Duxson, P., S. W. Mallicoat, G. C. Lukey, W. M. Kriven, and J. S. J. van Deventer. 2007. "The Effect of Alkali and Si/Al Ratio on the Development of Mechanical Properties of Metakaolin-Based Geopolymers." *Colloids and Surfaces A: Physicochemical and Engineering Aspects* 292 (1): 8–20. https://doi.org/10.1016/j.colsurfa.2006.05.044.

The Engineering ToolBox. 2009. "Concrete Mixtures." Material Properties. https://www.engineeringtoolbox.com/concrete-sand-cement-gravel-mixtures-d_1547.html.

Garside, M. 2021. "U.S. and World Cement Production 2020." Statista.com.

Geopolymer Institute. 2012. "What is a Geopolymer? Introduction." https://www.geopolymer.org/science/introduction/#:~:text=Geopolymers%20are%20chains%20or%20networks,at%20temperatures%20%3E%20500%C2%B0C.

Gibbons, G., R. Williams, P. Purnell, and E. Farahi. 2010. "3D Printing of Cement Composites." *Advances in Applied Ceramics* 109 (5): 287–290. https://doi.org/10.1179/174367509X12472364600878.

Gordon, M., J. L. Bell, and W. M. Kriven. 2005. "Comparison of Naturally and Synthetically-Derived, Potassium-Based Geopolymers." In. *Advances in Ceramic Matrix Composites X: Proceedings of the 106th Annual Meeting of The American Ceramic Society, Indianapolis, Indiana, 2004,* edited by J. P. Singh, N. P. Bansal, W. M. Kriven, 95–106. Westerville, OH: The American Ceramic Society. https://doi.org/10.1002/9781118408353.ch9.

Goss, M., D. L. Swain, J. T. Abatzoglou, A. Sarhadi, C. A. Kolden, A. P. Williams, and N. S. Diffenbaugh. 2020. "Climate Change is Increasing the Likelihood of Extreme Autumn Wildfire Conditions across California." *Environmental Research Letters* 15 (9): 094016. https://iopscience.iop.org/article/10.1088/1748-9326/ab83a7/meta.

Grandes, F. A., V. K. Sakano, A. C. A. Rego, M. S. Rebmann, F. A. Cardoso, and R. G. Pileggi. 2021. "Rheological Behavior and Flow Induced Microstructural Changes of Cement-Based Mortars Assessed by Pressure Mapped Squeeze Flow." *Powder Technology* 393:519–538. https://doi.org/10.1016/j.powtec.2021.07.082.

Grandes, F.A., V. K. Sakano, A. C. A. Rego, F. A. Cardoso, and R. G. Pileggi. 2018. "Squeeze Flow Coupled with Dynamic Pressure Mapping for the Rheological Evaluation of Cement-Based Mortars." *Cement and Concrete Composites* 92:18–35. https://doi.org/10.1016/j.cemconcomp.2018.05.016.

Grim, Ralph E. 1962. "Clay Mineralogy: The Clay Mineral Composition of Soils and Clays is Providing an Understanding of Their Properties." *Science* 135 (3507): 890–898. https://doi.org/10.1126/science.135.3507.890.

Grimshaw, Rex. 1971. *The Chemistry and Physics of Clay and Allied Ceramic Materials*. London: Ernest Benn.

Hager, I. 2013. "Behaviour of Cement Concrete at High Temperature." B*ulletin of the Polish Academy of Sciences: Technical Sciences* 61 (1): 145–154. https://doi.org/10.2478/bpasts-2013-0013.

Hassan, A., M. Arif, and M. Shariq. 2019. "Use of Geopolymer Concrete for a Cleaner and Sustainable Environment—A Review of Mechanical Properties and Microstructure." *Journal of Cleaner Production* 223:704-728. https://doi.org/10.1016/j.jclepro.2019.03.051.

He, R., N. Dai, and Z. Wang. 2020. "Thermal and Mechanical Properties of Geopolymers Exposed to High Temperature: A Literature Review." *Advances in Civil Engineering* 2020: 1–17. https://doi.org/10.1155/2020/7532703.

Heah, C. Y., H. Kamarudin, A. M. Mustafa Al Bakri, M. Binhussain, M. Luqman, I. Khairul Nizar, C. M. Ruzaidi, and Y. M. Liew. 2011. "Effect of Curing Profile on Kaolin-Based Geopolymers." *Physics Procedia* 22:305–311. https://doi.org/10.1016/j.phpro.2011.11.048.

Huat, O. C. 2006. "Performance of Concrete Containing Metakaolin as Cement Replacement Material." Master's Thesis, University Technology Malaysia. http://eprints.utm.my/id/eprint/2198/1/OngCheeHuatMFKA2006.pdf.

Husem, M. 2006. "The Effects of High Temperature on Compressive and Flexural Strengths of Ordinary and High-Performance Concrete." *Fire Safety Journal* 41 (2): 155–163. https://doi.org/10.1016/j.firesaf.2005.12.002.

Izquierdo, M., X. Querol, J. Davidovits, D. Antenucci, H. Nugteren, and C. Fernández-Pereira. 2009. "Coal Fly Ash-Slag-Based Geopolymers: Microstructure and Metal Leaching." *Journal of Hazardous Materials* 166 (1): 561-566. https://doi.org/10.1016/j.jhazmat.2008.11.063.

Keane, P. F., J. S. Foltz, V. Chadha, C. P. Marsh, and W. M. Kriven. 2020. "Amorphous Self-Healed, Chopped Basalt Fiber-Reinforced, Geopolymer Composites." *Journal of the American Ceramic Society* 104 (7): 3443–3451. https://doi.org/10.1111/jace.17648.

Khoshnevis, B. 2004. "Automated Construction by Contour Crafting—Related Robotics and Information Technologies." *Automation in Construction* 13 (1): 5–19. https://doi.org/10.1016/j.autcon.2003.08.012.

Kirchmeier-Young, M. C., N. P. Gillett, F. W. Zwiers, A. J. Cannon, and F. S. Anslow. 2018. "Attribution of the Influence of Human-Induced Climate Change on an Extreme Fire Season." *Earth's Future* 7 (1): 2–10. https://doi.org/10.1029/2018EF001050.

Komljenović, M., Z. Baščarević, and V. Bradić. 2010. "Mechanical and Microstructural Properties of Alkali-Activated Fly Ash Geopolymers." *Journal of Hazardous Materials* 181 (1–3): 35–42. https://doi.org/10.1016/j.jhazmat.2010.04.064.

Kong, D. L. Y., J. G. Sanjayan, and K. Sagoe-Crentsil. 2007. "Comparative Performance of Geopolymers Made with Metakaolin and Fly Ash after Exposure to Elevated Temperatures." *Cement and Concrete Research* 37 (12): 1583–1589. https://doi.org/10.1016/j.cemconres.2007.08.021.

Korniejenko, K. E. Frączek, E. Pytlak, and M.Adamski. 2016. "Mechanical Properties of Geopolymer Composites Reinforced with Natural Fibers." *Procedia Engineering* 151: 388–393. https://doi.org/10.1016/j.proeng.2016.07.395.

Kozisek, F. 2020. Regulations for Calcium, Magnesium or Hardness in Drinking Water in the European Union Member States. *Regulatory Toxicology and Pharmacology* 112:104589. https://doi.org/10.1016/j.yrtph.2020.104589.

Kriven, W. M. 2018. "5.9 Geopolymer-Based Composites." In *Comprehensive Composite Materials II*, edited by P.W.R. Beaumont and C. H. Zweben, 269–280. Amsterdam, Netherlands: Elsevier. https://doi.org/10.1016/B978-0-12-803581-8.09995-1.

Kriven, W. M. 2021. "Geopolymers and Geopolymer-Derived Composites." In *Encyclopedia of Materials: Technical Ceramics and Glasses*, edited by M. Pomeroy, 424–438. Amsterdam, Netherlands: Elsevier.

Kuenzel, C., L. J.Vandeperre, S.Donatello, A. R. Boccaccini, and C. Cheeseman. 2012. "Ambient Temperature Drying Shrinkage and Cracking in Metakaolin-Based Geopolymers." *Journal of the American Ceramic Society* 95 (10): 3270–3277. https://doi.org/10.1111/j.1551-2916.2012.05380.x.

Kukko, H., and R. Mannonen. 1982."Chemical and Mechanical Properties of Alkali-Activated Blast Furnace Slag (F-Concrete)." *Nordic Concrete Research* 1. https://trid.trb.org/view/196484.

Łach, M., M. Hebdowska-Krupa, and N. Komar. 2019. "Strength and Leachability of Geopolymers with the Addition of Municipal Solid Waste Ashes." *IOP Conference Series: Materials Science and Engineering* 706 (1): 012010. https://iopscience.iop.org/article/10.1088/1757-899X/706/1/012010.

Lahoti, M., K. K. Wong, K. H. Tan, and E.-H. Yang. 2018. "Effect of Alkali Cation Type on Strength Endurance of Fly Ash Geopolymers Subject to High Temperature Exposure." *Materials & Design* 154: 8–19. https://doi.org/10.1016/j.matdes.2018.05.023.

Larson, R. G. 1999. *The Structure and Rheology of Complex Fluids*. New York: Oxford University Press. *Engineering Pro Collection*.

Le, T. T., S. A. Lim, S. Lim, R. A. Buswell, A. G. G. Gibb, and T. Thorpe. 2012. "Mix Design and Fresh Properties for High-Performance Printing Concrete." *Materials and Structures* 45: 1221–1232. https://link.springer.com/article/10.1617/s11527-012-9828-z.

Lehne, J., and F. Preston. 2018. *Making Concrete Change: Innovation in Low-Carbon Cement and Concrete*. Great Britain: Chantham House.

Li, Ning, C. Shi, Q. Wang, Z. Zhang, and Z. Ou. 2017. "Composition Design and Performance of Alkali-Activated Cements." *Materials and Structures* 50 (178). https://doi.org/10.1617/s11527-017-1048-0.

Lim, S. R. A. Buswell, T. T. Le, S. A. Austin, A. G. F. Gibb, and T. Thorpe. 2012. "Developments in Construction-Scale Additive Manufacturing Processes." *Automation in Construction* 21: 262–268. https://doi.org/10.1016/j.autcon.2011.06.010.

Lloyd, N., and B. V. Rangan. 2010. "Geopolymer Concrete: A Review of Development and Opportunities." In *Proceedings of the 35th Conference on Our World in Concrete & Structures: The Challenge of a Low Carbon Age*, 25–27 August 2010, Singapore, edited by C. Tam, K. Ong, and S. Teng, and M. Zhang, 307–314. Singapore: CI-Premier Pte Ltd.

Lootens, D., P. Jousset, L. Martinie, N. Roussel, and R. J. Flatt. 2009. "Yield Stress during Setting of Cement Pastes from Penetration Tests." *Cement and Concrete Research* 39 (5): 401–408. https://doi.org/10.1016/j.cemconres.2009.01.012.

Manjunatha, G. S., Radhakrishna, K. Venugopal, and S. V. Maruthi. 2014. "Strength Characteristics of Open Air Cured Geopolymer Concrete." *Transactions of the Indian Ceramic Society* 73 (2): 149–156. https://doi.org/10.1080/0371750X.2014.923330.

Marchment, T., and J. Sanjayan. 2020. "Mesh Reinforcing Method for 3D Concrete Printing." *Automation in Construction* 109:102992. https://doi.org/10.1016/j.autcon.2019.102992.

Masi, G., W. D. A. Rickard, M. C. Bignozzi, A. van Riessen. 2015. "The Effect of Organic and Inorganic Fibres on the Mechanical and Thermal Properties of Aluminate Activated Geopolymers." *Composites Part B: Engineering* 76:218–228. https://doi.org/10.1016/j.compositesb.2015.02.023.

Mermerdaş, K., S. İpek, and Z. Mahmood. 2021. "Visual Inspection and Mechanical Testing of Fly Ash-Based Fibrous Geopolymer Composites under Freeze-Thaw Cycles." *Construction and Building Materials* 283:122756. https://doi.org/10.1016/j.conbuildmat.2021.122756.

Mewis, J., and N. J. Wagner. 2009. "Thixotropy." *Advances in Colloid and Interface Science* 147–148:214–227. https://doi.org/10.1016/j.cis.2008.09.005.

Møller, P., J. Mewis, and D. Bonn. 2006. "Yield Stress and Thixotropy: On the Difficulty of Measuring Yield Stresses in Practice." *Soft Matter* 2:274–283. https://doi.org/10.1039/B517840A.

Morrison, F. A. 2001. *Understanding Rheology*. New York: Oxford University Press.

Mullineux, G. 2008. "Non-Linear Least Squares Fitting of Coefficients in the Herschel–Bulkley Model." *Applied Mathematical Modelling* 32 (12): 2538–2551. https://doi.org/10.1016/j.apm.2007.09.010.

Ndalila, M. N., G. J. Williamson, and D. M. J. S. Bowman. 2018. "Geographic Patterns of Fire Severity Following an Extreme Eucalyptus Forest Fire in Southern Australia: 2013 Forcett-Dunalley Fire." *Fire* 1 (3): 40. https://doi.org/10.3390/fire1030040.

Nematollahi, B, V. Praful, J. Sanjayan, M. Xia, V. Nerella, and V. Mechtcherine. 2018. "Systematic Approach to Develop Geopolymers for 3D Concrete Printing Applications." *Archives of Civil and Mechanical Eng*ineering.

Nerella, V. N.,S. Hempel, and V. Mechtcherine. 2019. "Effects of Layer-Interface Properties on Mechanical Performance of Concrete Elements Produced by Extrusion-Based 3D-Printing." *Construction and Building Materials* 205:586–601. https://doi.org/10.1016/j.conbuildmat.2019.01.235.

Nguyen, Q. D., and D. V. Boger. 1992. "Measuring the Flow Properties of Yield Stress Fluids." *Annual Review of Fluid Mechanics*, 24:47–88. https://doi.org/10.1146/annurev.fl.24.010192.000403.

Okoye, F.N. 2016. "Strength Characteristics of Green Concrete." PhD diss., Sharda University.

Owens, C. E., A. J. Hart, and G. H. McKinley. 2020. "Improved Rheometry of Yield Stress Fluids Using Bespoke Fractal 3D Printed Vanes." *Journal of Rheology* 64:643–662. https://doi.org/10.1122/1.5132340.

Panda, B., S. C. Paul, N. A. N. Mohamed, Y. W. D. Tay, and M. J. Tan. 2018. "Measurement of Tensile Bond Strength of 3D Printed Geopolymer Mortar." *Measurement* 113:108–116. https://doi.org/10.1016/j.measurement.2017.08.051.

Pegna, J. 1997. "Exploratory Investigation of Solid Freeform Construction." *Automation in Construction* 5 (5): 427–437. https://doi.org/10.1016/S0926-5805(96)00166-5.

Peijiang, S. 2005. "Fly Ash Based Inorganic Polymeric Building Materia." Phd diss., Wayne State University.

Perera, D. S., O. Uchida, E. R. Vance, and K. S. Finnie. 2007. "Influence of Curing Schedule on The Integrity of Geopolymers." *Journal of Materials Science* 42 (9): 3099–3106. https://doi.org/10.1007/s10853-006-0533-6.

Perrot, A., A. Pierre, S. Vitaloni, and V. Picandet. 2015. "Prediction of Lateral Form Pressure Exerted by Concrete at Low Casting Rates." *Materials and Structures* 48 (7): 2315–2322. https://doi.org/10.1617/s11527-014-0313-8.

Potgieter-Vermaak, S.S., and J.H. Potgieter. 2006. "Metakaolin as an Extender in South African Cement." *Journal of Materials in Civil Engineering* 18 (4): 619–623. https://doi.org/10.1061/(ASCE)0899-1561(2006)18:4(619).

Powers, T. C. 1954. "Void Space as a Basis for Producing Air-Entrained Concrete." *ACI Journal Proceedings* 50 (5): 741–760.

Powers, T. C., and R.A Helmuth. 1953. "Theory of Volume Changes in Hardened Portland Cement Paste during Freezing." In *Proceedings of the Thirty-Second Annual Meeting of the Highway Research Board*, 13–16 January 1953, Washington, DC, 285–297. Highway Research Board. https://onlinepubs.trb.org/Onlinepubs/hrbproceedings/32/32-019.pdf.

Prasad, M. S., K. J. Reid, and H. H. Murray. 1991. "Kaolin: Processing, Properties and Applications." *Applied Clay Science* 6 (2): 87–119. https://doi.org/10.1016/0169-1317(91)90001-P.

Provis, J. L., and J. S. J. van Deventer. 2007a. "Geopolymerisation Kinetics. 1. In Situ Energy-Dispersive X-Ray Diffractometry." *Chemical Engineering Science* 62 (9): 2309–2317. https://doi.org/10.1016/j.ces.2007.01.027.

Provis, J. L., and J. S. J. van Deventer. 2007b. "Geopolymerisation Kinetics. 2. Reaction Kinetic Modelling." *Chemical Engineering Science* 62 (9): 2318–2329. https://doi.org/10.1016/j.ces.2007.01.028.

Rahier, H., W. Simons, B. Van Mele, and M. Biesemans. 1997. "Low-Temperature Synthesized Aluminosilicate Glasses: Part III Influence of the Composition of the Silicate Solution on Production, Structure and Properties." *Journal of Materials Science* 32 (9): 2237–2247. https://doi.org/10.1023/A:1018563914630.

Rajamane, N.P., M. C. Nataraja, and N. Lakshmanan. 2011. "An Introduction to Geopolymer Concrete." *The Indian Concrete Journal* 85 (11): 25–28.

Ramujee, K., and M. PothaRaju. 2017. "Mechanical Properties of Geopolymer Concrete Composites." *Materials Today: Proceedings* 4 (2): 2937–2945. https://doi.org/10.1016/j.matpr.2017.02.175.

Rehman, A. U., and V. M. Sglavo. 2020. "3D Printing of Geopolymer-Based Concrete for Building Applications." *Rapid Prototyping Journal* 26 (10): 1783–1788. https://doi.org/10.1108/RPJ-09-2019-0244.

Rickard, W. D. A., A. van Riessen, and P. Walls. 2010. "Thermal Character of Geopolymers Synthesized from Class F Fly Ash Containing High Concentrations of Iron and α-Quartz." *International Journal of Applied Ceramic Technology* 7 (1): 81–88. https://doi.org/10.1111/j.1744-7402.2008.02328.x.

Roussel, N., and P. Coussot. 2005. "'Fifty-Cent Rheometer' for Yield Stress Measurements: From Slump to Spreading Flow." *Journal of Rheology* 49 (3): 705–718. https://doi.org/10.1122/1.1879041. .

Roussel, N. 2006 "A Thixotropy Model for Fresh Fluid Concretes: Theory, Validation and Applications." *Cement and Concrete Research* 36 (10): 1797–1806. https://doi.org/10.1016/j.cemconres.2006.05.025.

Rouyer, J., and A. Poulesquen. 2015. "Evidence of a Fractal Percolating Network During Geopolymerization." *Journal of the American Ceramic Society* 98 (5): 1580–1587. https://doi.org/10.1111/jace.13480.

Rovnaník, P. 2010. "Effect of Curing Temperature on the Development of Hard Structure of Metakaolin-Based Geopolymer." *Construction and Building Materials* 24 (7): 1176–1183. https://doi.org/10.1016/j.conbuildmat.2009.12.023.

Roy, D. M. 1999. "Alkali-Activated Cements Opportunities and Challenges." *Cement and Concrete Research* 29 (2): 249–254. https://doi.org/10.1016/S0008-8846(98)00093-3.

Saikia, N., D. J. Bharali, P. Sengupta, D. Bordoloi, R. Goswamee, P. C. Saikia, and P. C. Borthakur. 2003. "Characterization, Beneficiation and Utilization of a Kaolinite Clay from Assam, India." *Applied Clay Science* 24 (1–2): 93–103. https://doi.org/10.1016/S0169-1317(03)00151-0.

Samuel, D. M., A. Sutrisno, and W. M. Kriven. 2020. "Relative Importance of Al(V) and Reinforcement to the Flexural Strength of Geopolymer Composites." *Journal of the American Ceramic Society* 104 (7):3452–3460. https://doi.org/10.1111/jace.17656.

Sanjayan, J.G., B. Nematollahi, M. Xia, and T. Marchment. 2018. "Effect of Surface Moisture on Inter-Layer Strength of 3D Printed Concrete." *Construction and Building Materials* 172:468–475. https://doi.org/10.1016/j.conbuildmat.2018.03.232.

Sankar, K., P. Stynoski, and W. M. Kriven. 2018. "Sodium Silicate Activated Slag-Fly Ash Binders: Part III—Composition of Soft Gel and Calorimetry." *Journal of the American Ceramic Society* 102 (6): 3175–3190. https://doi.org/10.1111/jace.16219.

Sankar, K., A. Sutrisno, and W. M. Kriven. 2018. "Slag-Fly Ash and Slag-Metakaolin Binders: Part II—Properties of Precursors and NMR Study of Poorly Ordered Phases." *Journal of the American Ceramic Society* 102 (6): 3204–3227. https://doi.org/10.1111/jace.16224.

Santín, C., S. Doerr, A. Merino, R. Bryant, and Neil J. Loader. 2016. "Forest Floor Chemical Transformations in a Boreal Forest Fire and Their Correlations with Temperature and Heating Duration." *Geoderma* 264 (Part A): 71–80. https://doi.org/10.1016/j.geoderma.2015.09.021.

Sanz, J., A. Madani, J. M. Serratosa, J. S. Moya, and S. Aza. 1988. "Aluminum-27 and Silicon-29 Magic-Angle Spinning Nuclear Magnetic Resonance Study of the Kaolinite-Mullite Transformation." *Journal of the American Ceramic Society* 71 (10): C418-C421. https://doi.org/10.1111/j.1151-2916.1988.tb07513.x.

Sarker, P. K., S. Kelly, and Z. Yao. 2014. "Effect of Fire Exposure on Cracking, Spalling and Residual Strength of Fly Ash Geopolymer Concrete." *Materials & Design* 63:584–592. https://doi.org/10.1016/j.matdes.2014.06.059.

Shi, C., D. Roy, and P. Krivenko. 2006. Alkali-Activated Cements and Concretes. London: CRC Press. https://doi.org/10.1201/9781482266900.

Singh, N. B. 2018. "Fly Ash-Based Geopolymer Binder: A Future Construction Material." *Minerals* 8 (7): 299. https://doi.org/10.3390/min8070299.

Steins, P., A. Poulesquen, O. Diat, and F. Frizon. 2012. "Structural Evolution during Geopolymerization from an Early Age to Consolidated Material." *Langmuir* 28 (22): 8502–8510. https://doi.org/10.1021/la300868v.

Stutzman, P., and S. Leigh. 2022. *Phase Composition Analysis of the NIST Reference Clinkers by Optical Microscopy and X-Ray Powder Diffraction*. Washington, DC: National Institute of Standards and Technology. https://www.govinfo.gov/content/pkg/GOVPUB-C13-eec6527a1895562f25c5cbfe652bb02d/pdf/GOVPUB-C13-eec6527a1895562f25c5cbfe652bb02d.pdf.

Subramaniam, K. V., and J. Lee. 2007. "Ultrasonic Assessment of Early-Age Changes in the Material Properties of Cementitious Materials." *Materials and Structures* 40:301–309. https://doi.org/10.1617/s11527-006-9107-y.

Swamy, V., S. K. Saxena, B. Sundman, and J. Zhang. 1994. "A Thermodynamic Assessment of Silica Phase Diagram." *Journal of Geophysical Research: Solid Earth* 99 (B6): 11787–11794. https://doi.org/10.1029/93JB02968.

Tanesi, J., and R. Meininger. 2007. "Freeze-Thaw Resistance of Concrete with Marginal Air Content." *Transportation Research Record: Journal of the Transportation Research Board* 2020 (1): 61–66. https://doi.org/10.3141/2020-08.

Temuujin, J., A. Minjigmaa, W. Rickard, M. Lee. I. Williams, and A. van Riessen. 2010. "Fly Ash Based Geopolymer Thin Coatings on Metal Substrates and Its Thermal Evaluation." *Journal of Hazardous Materials* 180 (1–3): 748–752. https://doi.org/10.1016/j.jhazmat.2010.04.121.

Thaarrini, J., and S. Dhivya. 2016. "Comparative Study on the Production Cost of Geopolymer and Conventional Concretes." *International Journal of Civil Engineering Research* 7 (2): 117–124. https://www.ripublication.com/ijcer16/ijcerv7n2_03.pdf.

Tome, S., M.-A. Etoh, J. Etame, and K. Sanjay. 2018. "Characterization and Leachability Behaviour of Geopolymer Cement Synthesised from Municipal Solid Waste Incinerator Fly Ash and Volcanic Ash Blends." *Recycling* 3 (4): 50. https://doi.org/10.3390/recycling3040050.

Toutou, Z., N. Roussel, and C. Lanos. 2005. "The Squeezing Test: A Tool to Identify Firm Cement-Based Material's Rheological Behaviour and Evaluate Their Extrusion Ability." *Cement and Concrete Research* 35 (10): 1891–1899. https://doi.org/10.1016/j.cemconres.2004.09.007.

Turco, M., J. von Hardenberg, A. AghaKouchak, M. C. Llasat, A. Provenzale, and R. M. Trigo. 2017. "On the Key Role of Droughts in the Dynamics of Summer Fires in Mediterranean Europe." *Scientific Reports* 7 (1): 81. https://doi.org/10.1038/s41598-017-00116-9.

Vu, C.-C., O. Plé, J. Weiss, and D. Amitrano. 2020. "Revisiting the Concept of Characteristic Compressive Strength of Concrete." *Construction and Building Materials* 263:120126. https://doi.org/10.1016/j.conbuildmat.2020.120126.

Wang, A., Y. Zheng, Z. Zhang, K. Liu, Y. Li, L. Shi, and D. Sun. 2020. "The Durability of Alkali-Activated Materials in Comparison with Ordinary Portland Cements and Concretes: A Review." *Engineering* 6 (6): 695–706. https://doi.org/10.1016/j.eng.2019.08.019.

Wang, H., H. Li, and F. Yan. 2005. "Synthesis and Mechanical Properties of Metakaolinite-Based Geopolymer." *Colloids and Surfaces A: Physicochemical and Engineering Aspects* 268 (1–3): 1–6. https://doi.org/10.1016/j.colsurfa.2005.01.016.

Wang, H., Z. Peng, and S. Zhang. 2011. "Characterization and Thermal Behavior of Kaolin." *Journal of Thermal Analysis and Calorimetry* 105:157–160. https://doi.org/10.1007/s10973-011-1385-0.

Wang, S.-D., X.-C. Pu, K. L. Scrivener, and P. L. Pratt. 1995. "Alkali-Activated Slag Cement and Concrete: A Review of Properties and Problems." *Advances in Cement Research* 7 (27): 93–102. https://doi.org/10.1680/adcr.1995.7.27.93.

Wang, X., D. Jiang, and X. Lang. 2017. "Future Extreme Climate Changes Linked to Global Warming Intensity." *Science Bulletin* 62 (24): 1673–1680. https://doi.org/10.1016/j.scib.2017.11.004.

Wangler, T., E. Lloret, L. Reiter, N. Hack, F. Gramazio, M. Kohler, M. Bernhard, B. Dillenburger, J. Buchli, N. Roussel, and R. Flatt. 2016. "Digital Concrete: Opportunities and Challenges." *RILEM Technical Letters* 1:67–75. https://doi.org/10.21809/rilemtechlett.2016.16.

Weber, K., R. Yadev, J. Davis, K. Blair, J. Schnase, M. Carroll, and R. Gill. "Geography of Wildfires Across the West." Slide presentation, GIS Training and Research Center, Idaho State University. https://giscenter.isu.edu/research/Techpg/nasa_RECOVER/pdf/GeographyWildfires.pdf.

World Wide Travel Organization. n. d. "Worldwide Weather Forecasts and Climate Information." https://weather-and-climate.com/.

Wright, P. J. F., and F. Garwood. 1952. "The Effect of the Method of Test on the Flexural Strength of Concrete." *Magazine of Concrete Research* 4 (11): 67–76. https://doi.org/10.1680/macr.1952.4.11.67.

Xiao, J., H. Liu, and T. Ding. 2021. "Finite Element Analysis on the Anisotropic Behavior of 3D Printed Concrete under Compression and Flexure." *Additive Manufacturing* 39:101712. https://doi.org/10.1016/j.addma.2020.101712.

Yan, D., L. Xie, X. Qian, S. Ruan, and Q. Zeng.2020. "Compositional Dependence of Pore Structure, Strength and Freezing-Thawing Resistance of Metakaolin-Based Geopolymers." *Materials* 13 (13): 2973. https://doi.org/10.3390/ma13132973.

Yousefi Oderji, S., B. Chen, M. R. Ahmad, and S. F. A. Shah. 2019. "Fresh and Hardened Properties of One-Part Fly Ash-Based Geopolymer Binders Cured at RT: Effect of Slag and Alkali Activators." *Journal of Cleaner Production* 225:1–10. https://doi.org/10.1016/j.jclepro.2019.03.290.

Yuan, Q., Z. Li, D. Zhou, T. Huang, H. Huang, D. Jiao, and C. Shi. 2019. "A Feasible Method for Measuring the Buildability of Fresh 3D Printing Mortar." *Construction and Building Materials* 227: 116600. https://doi.org/10.1016/j.conbuildmat.2019.07.326.

Zhao, M., G. Zhang, K. W. Htet, M. Kwon, C. Liu, Y. Xu, and M. Tao. 2019. "Freeze-Thaw Durability of Red Mud Slurry-Class F Fly Ash-Based Geopolymer: Effect of Curing Conditions." *Construction and Building Materials* 215: 381–390. https://doi.org/10.1016/j.conbuildmat.2019.04.235.

Zibouche, F., H. Kerdjoudj, J.-B. d'Espinose de Lacaillerie, and H. Van Damme.2009. "Geopolymers from Algerian Metakaolin. Influence of Secondary Minerals." *Applied Clay Science* 43 (3–4): 453–458. https://doi.org/10.1016/j.clay.2008.11.001.

Żołek-Tryznowska, Z. 2016. "Rheology of Printing Inks." In *Printing on Polymers: Fundamentals and Applications*, 87–99. Amsterdam, Netherlands: Elsevier. https://doi.org/10.1016/B978-0-323-37468-2.00006-3.

Abbreviations

AAC	Alkali-activated cements
BF	Basalt fiber
BJP	Binder jet printing
BSE	Backscattered electron microscopy
C	Chamotte
CERL	Construction Engineering Research Laboratory
CI	Confidence interval
CMC	Sodium carboxymethyl cellulose
CMS	Sodium carboxymethyl starch
CS	Coarse sand
DI	Deionized
DIC	Digital image correlation
ERDC	Engineer Research and Development Center
FS	Fine sand
GBFS	Granulated blast furnace slag
GFRP	Glass fiber-reinforced polymer
GP	Geopolymer
GPC	Geopolymer composite
HB	Herschel-Bulkley
HRM	Highly reactive metakaolin
ITZ	Interfacial transition zone
KGP	Potassium-based geopolymer
LVER	Linear viscoelastic region
MB	Minibar
MG	Medium glass
MK	Metakaolin
MR	Minirod
MRL	Materials Research Laboratory

NMR	Nuclear magnetic resonance
OPC	Ordinary Portland cement
Q	Quikrete medium sand
QS	Quikrete medium sand
RDM	Relative dynamic modulus
RH	Relative humidity
RT	Room temperature
SEM	Scanning electron microscope
SF	Silica Fume
SH	Specific humidity
SLS	Elective laser sintering
UWR	Ultrasonic wave reflectometry
W	Wollastonite tailings
XFS	X-ray florescence spectroscopy
XRD	X-ray diffraction spectroscopy

Appendix A: Water Retention and Mechanical Properties

The initial round of water retention coating testing was done with weigh boats, then moved to slices of PVC for a more standardized and repeatable test. A picture of some weigh boat samples is below (Figure A-1).

Figure A-1. Pictures of discs of pure KGP with their respective coatings: (*a*) paper; (*b*) cornstarch; (*c*) sand; (*d*) talc; (*e*) silicone mold release spray; and (*f*) 55 wt% sand (<425 µm) composite after 9 days of drying at ambient conditions.

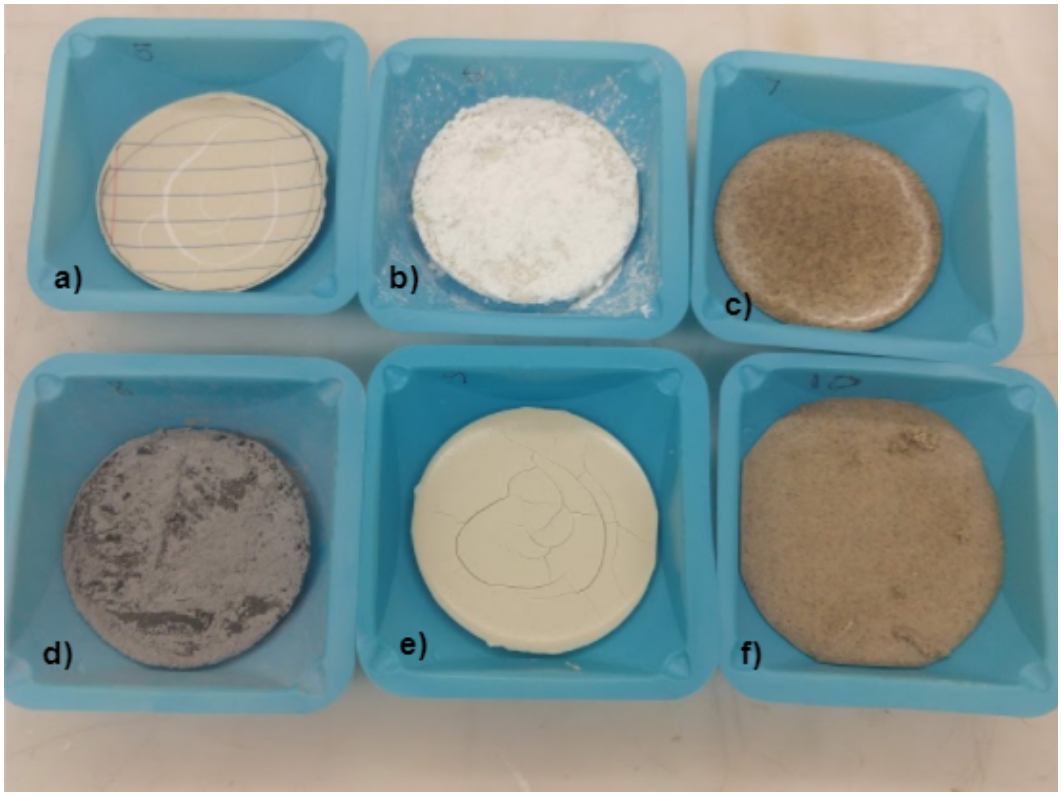

Note in Figure A-1 the shrinkage around the edges of all the samples except the composite.

Figure A-2. Percent mass retention of pure KGP with various coatings, dried under ambient conditions (20°C, 50%±10 RH) for 206 hours, a control specimen dried under 95% RH, and a 55 wt% sand composite.

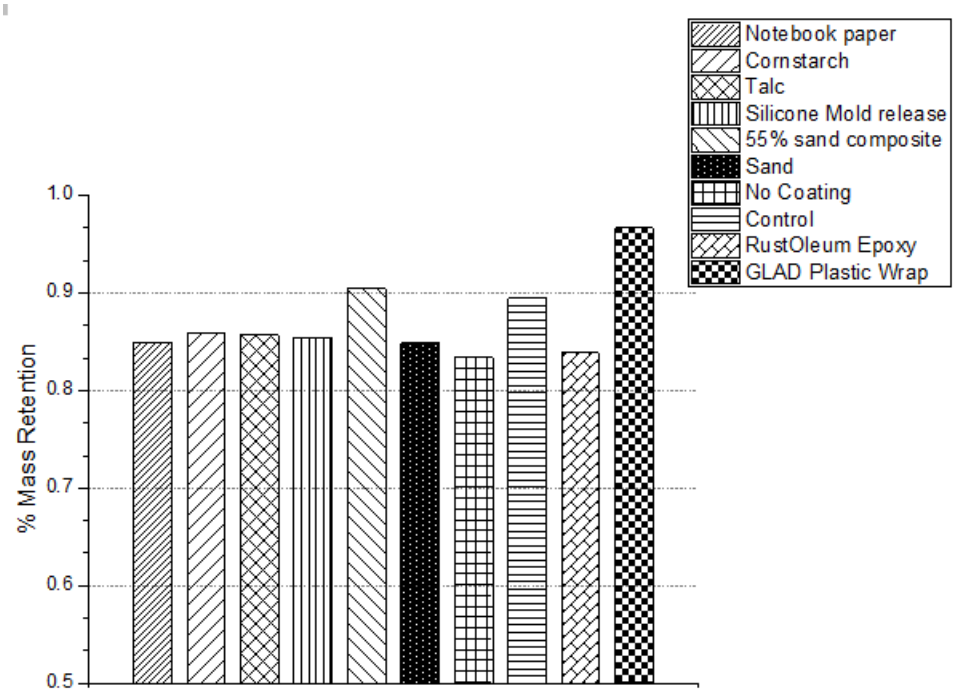

The Saran wrap had a 96.7% mass retention. When the wrap was removed, the GP lost additional mass. The "Control" sample featured GP that had cured completely under high humidity and then lost about 10% of residual water after exposure to 50%±10 RH.

The other coatings are not suitable for water retention.

Additional water retention tests were made with a more uniform geometry by cutting slices of 3 in. PVC pipe and attaching them to a plastic weigh boat with hot glue and using whole composites and composites and coatings.

A composite consisting of 55 wt% sand made with potassium water glass and Metamax metakaolin was cast into the puck molds and then spray coated with two compositions: a diluted solution of metsobead water glass (1 wg:3 water by vol), and a 5% Sikafilm solution. Sikafilm is a commercial moisture retardant for use in concrete and, as such, was used here.

Figure A-3. Mass retention of the S55 control sample with no coating and the two coatings.

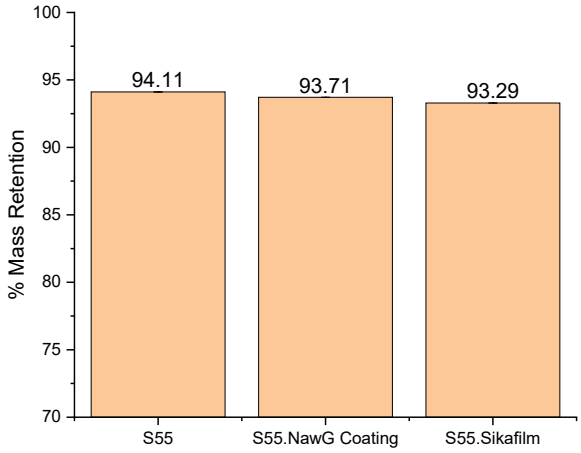

A.1 Silica fume X-Ray Diffraction (XRD)

Figure A-4. Raw curve and peak fitting and identification for silica fume.

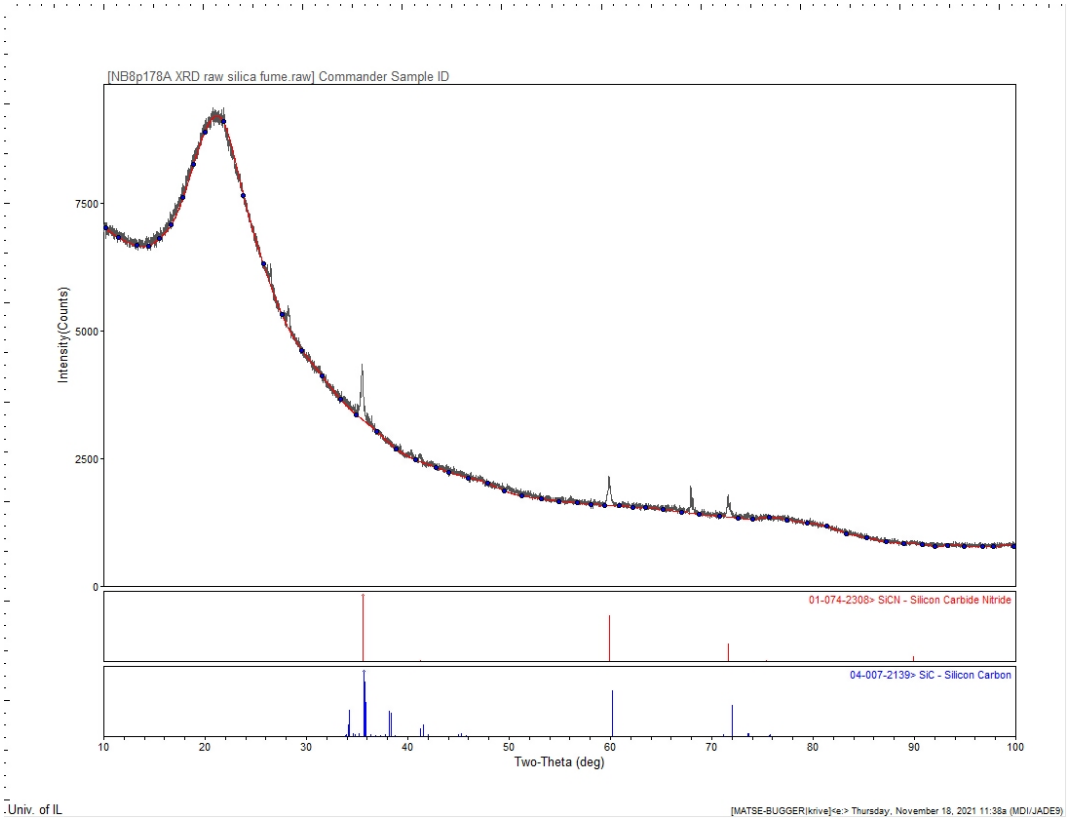

A.2 Water glass aging

Figure A-5. Sodium water glass after 7 d in freezer (*left*). Potassium water glass after 7 d in freezer (*right*).

Figure A-6. Lateral views of the tested water glass age and control samples. A single representative bar was chosen. Bars were grouped by water glass age time and control type. The two bars in each group—(*a*), (*b*), etc.—are sodium (*top*) and potassium (*bottom*) GPs. The groups are (*a*) freezer, (*b*) 7 d age, (*c*) 14 d age, (*d*) control, and (*e*) control.9d.

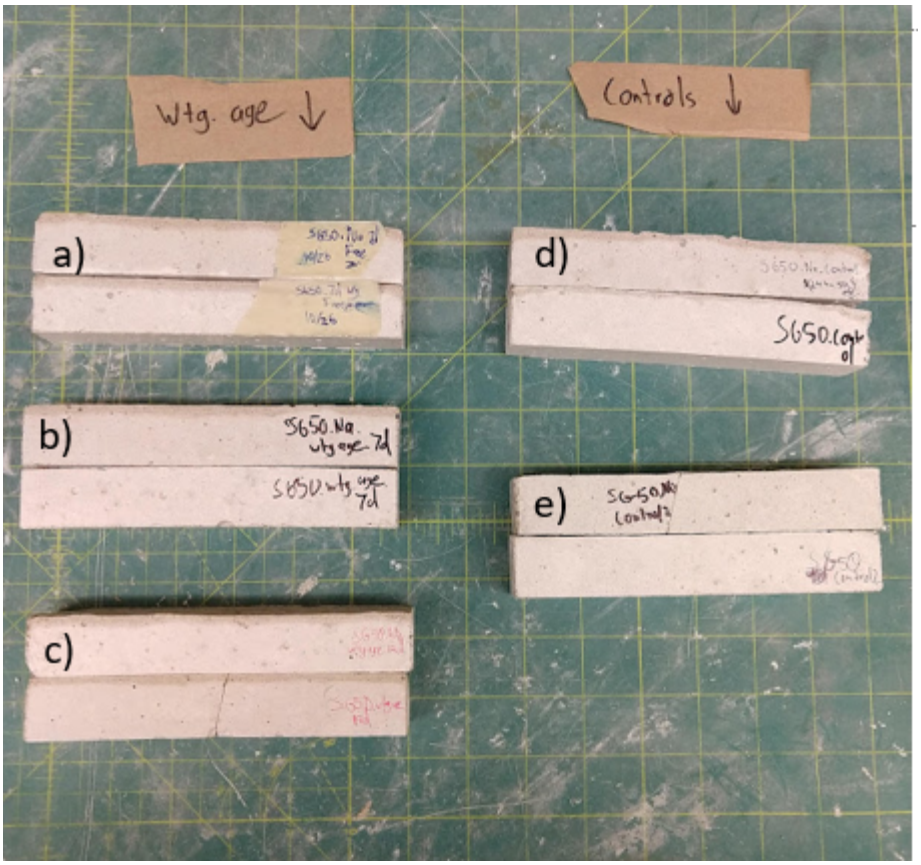

Figure A-7. Lateral views of control.2d samples: (*a*) SG50, (*b*) SG50.Na.

A.3 Flexure strength of GPC after simulated fire conditions

Figure A-8. Images of the torched surfaces after testing. SG50 samples in the *left* picture and SG50.Na samples in the *right*. Samples heated at the same temperature are in columns, and samples heated for the same time periods are in rows.

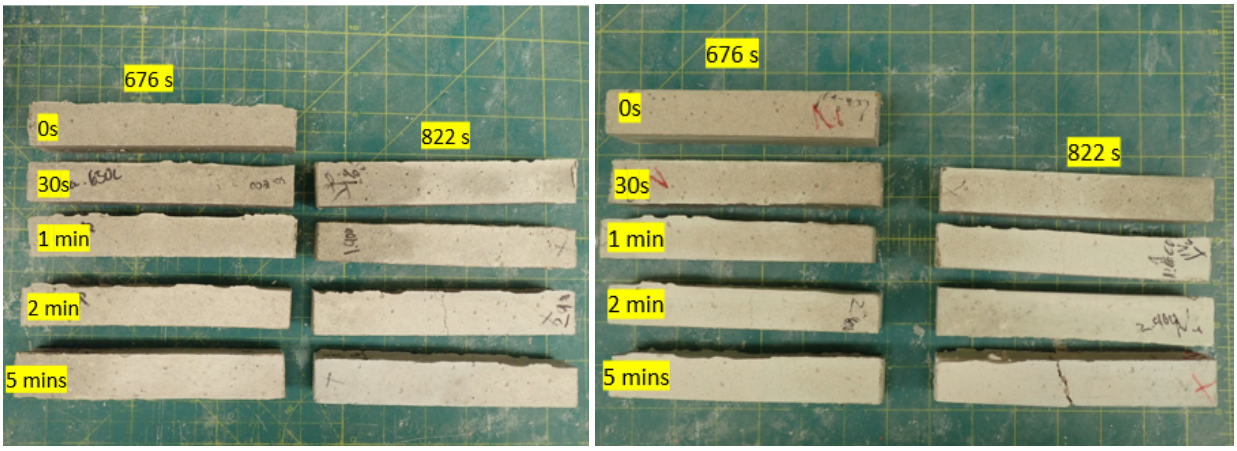

Figure A-9. Flexure testing setup for the flame test samples. Pictured is the SG50.Na, 2 minute, 676°C sample after failure has occurred.

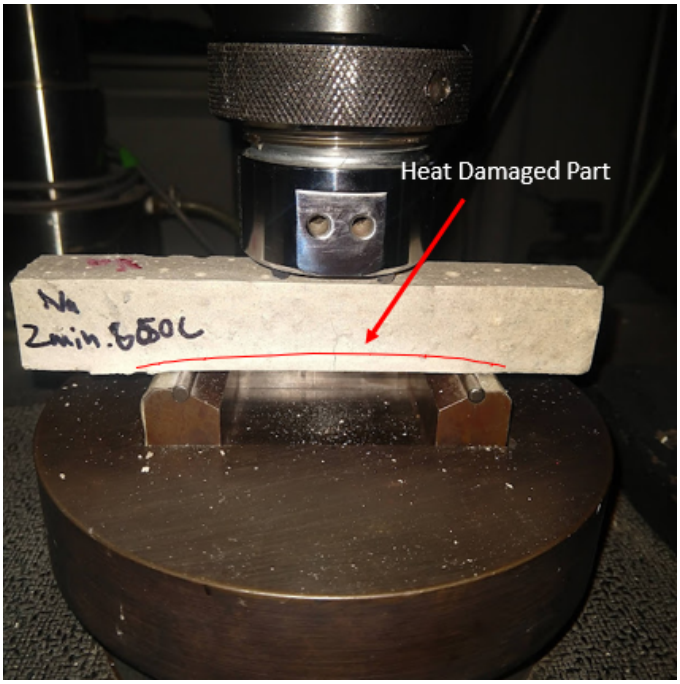

Appendix B: Rheology Values

Appendix B consists of all excess data points gathered from rheological testing.

B.1 Shear sweep rheology values

Table B-1. Compiled list of calculated values from the power law model.

System	Segment	K constant (Pa × s²)	Lower bound	Upper bound	Rate index *(n)*	Lower bound	Upper Bound
KGP 25 wt% Chamotte	Ramp 1	134.3	-22.75	291.3	0.7498	0.5372	0.96231
KGP 25 wt% Chamotte	Down 1	18.51	15.26	21.76	0.2486	0.2214	0.2758
KGP 25 wt% Chamotte	Ramp 2	57.91	25.14	90.68	0.3808	0.2918	0.4698
KGP 25 wt% Chamotte	Down 2	32.57	23.84	41.3	0.4131	0.3703	0.4559
KGP 25 wt% sand	Ramp 1	56.18	6.351	106	0.7727	0.6081	0.93735
KGP 25 wt% sand	Down 1	24.38	15.4	33.36	0.5722	0.5101	0.6342
KGP 25 wt% sand	Ramp 2	68.07	16.08	120.1	0.6334	0.5044	0.7625
KGP 25 wt% sand	Down 2	24.32	15.59	33.06	0.6521	0.5906	0.7135
KGP 20 wt% sand/20 wt% chamotte	Ramp 1	220	-14.75	454.7	0.7603	0.5646	0.95606
KGP 20 wt% sand/20 wt% chamotte	Down 1	27.58	22.23	32.93	0.1376	0.1082	0.167
KGP 20 wt% sand/20 wt% chamotte	Ramp 2	87.37	50.39	124.4	0.2978	0.2321	0.3635
KGP 20 wt% sand/20 wt% chamotte	Down 2	38.08	30.06	46.1	0.2051	0.1733	0.237
KGP 50 wt% sand	Ramp 1	108.2	-0.9707	217.3	0.7273	0.5472	0.9074
KGP 50 wt% sand	Down 1	17.63	14.51	20.75	0.3345	0.3083	0.3607
KGP 50 wt% sand	Ramp 2	82.61	25.27	140	0.5207	0.4081	0.6333
KGP 50 wt% sand	Down 2	29.12	18	40.23	0.4945	0.4319	0.557
KGP 60 wt% sand	Ramp 1	196.8	-3.595	397.2	0.72	0.5392	0.90078
KGP 60 wt% sand	Down 1	21.97	18.21	25.72	0.2884	0.2614	0.3153
KGP 60 wt% sand	Ramp 2	90.8	30.04	151.6	0.4533	0.3466	0.56
KGP 60 wt% sand	Down 2	27.86	19.88	35.84	0.3928	0.3466	0.4391
Plain KGP	Ramp 1	35.86	3.982	67.74	0.7867	0.6194	0.95404
Plain KGP	Down 1	14.26	10.06	18.46	0.5919	0.5214	0.7859
Plain KGP	Ramp 2	44.25	9.943	78.56	0.6536	0.5214	0.7859
Plain KGP	Down 2	14.5	9.253	19.76	0.7039	0.6397	0.768
KGP 60 wt% sand with Superplasticizer	Ramp 1	95.37	4.903	185.8	0.7	0.5325	0.8645

System	Segment	K constant (Pa × s²)	Lower bound	Upper bound	Rate index *(n)*	Lower bound	Upper Bound
KGP 60 wt% sand with Superplasticizer	Down 1	20.76	13.26	28.25	0.37	0.303	0.4188
KGP 60 wt% sand with Superplasticizer	Ramp 2	72.24	24.45	120	0.5	0.3885	0.6016
KGP 60 wt% sand with Superplasticizer	Down 2	26.47	19.21	33.73	0.451	0.4071	0.4944
KGP 25wt% Silica fume	Ramp 1	920.3	74.67	1766	0.633	0.2035	0.7881
KGP 25wt% Silica fume	Down 1	101.3	62.69	139.9	0.1427	0.083	0.2024
KGP 25wt% Silica fume	Ramp 2	277	177.5	376.6	0.2917	0.236	0.3473
KGP 25wt% Silica fume	Down 2	449.6	288.4	610.7	0.5028	0.4465	0.5595
Argical KGP	Ramp 1	77.27	-0.3276	154.9	0.7701	0.5842	0.2425
Argical KGP	Down 1	21.54	16.7	26.37	0.5363	0.6724	0.5716
Argical KGP	Ramp 2	86.38	14.71	158.1	0.6526	0.5114	0.7941
Argical KGP	Down 2	12.23	5.901	18.55	0.672	0.39	0.7444
Powerpozz KGP	Ramp 1	8.682	1.591	15.77	0.7599	0.6101	0.90962
Powerpozz KGP	Down 1	0.615	0.49	0.74	0.2123	0.1849	0.2397
Powerpozz KGP	Ramp 2	9.274	3.142	15.41	0.5641	0.4554	0.6727
Powerpozz KGP	Down 2	1.488	1.102	1.793	0.4614	0.4225	0.5002
Metamax EF KGP	Ramp 1	729.2	-52.42	1511	0.7886	0.5865	0.99077
Metamax EF KGP	Down 1	59.63	47.4	71.86	0.0578	0.027	0.0887
Metamax EF KGP	Ramp 2	144.4	86.12	202.7	0.1775	0.1158	0.2393
Metamax EF KGP	Down 2	121	86.39	155.6	0.1847	0.1408	0.2285
Metastar 501 HP KGP	Ramp 1	79.45	10.43	148.5	0.7642	0.6042	0.9241
Metastar 501 HP KGP	Down 1	21.62	16.55	26.69	0.3414	0.304	0.3788
Metastar 501 HP KGP	Ramp 2	47.85	20.85	74.84	0.4171	0.3278	0.5064
Metastar 501 HP KGP	Down 2	21	18.33	23.67	0.3532	0.334	0.3724
Quikrete OPC	Ramp 1	34.25	26.46	42.04	0.0863	0.0518	0.1209
Quikrete OPC	Down 1	4.982	4.09	5.875	-0.212	-0.239	-0.184
Quikrete OPC	Ramp 2	29.24	25.75	32.73	0.0371	0.019	0.0552
Quikrete OPC	Down 2	4.651	3.593	5.71	-0.234	-0.269	-0.199
KGP 10 wt% Q	Ramp 1	124.9	-7.746	257.6	0.7528	0.3194	0.4343
KGP 10 wt% Q	Down 1	37.23	8.356	66.1	0.3194	0.1964	0.4424
KGP 10 wt% Q	Ramp 2	81.96	17.04	146.9	0.4343	0.3085	0.5602
KGP 10 wt% Q	Down 2	45.06	31.79	58.32	0.3383	0.2975	0.3792
KGP 20 wt%Q	Ramp 1	151.7	-12.79	316.3	0.7357	0.5408	0.93048
KGP 20 wt% Q	Down 1	58.68	22.46	94.89	0.3674	0.2692	0.4657
KGP 20 wt%Q	Ramp 2	111.4	29.27	193.4	0.4543	0.3368	0.5719

System	Segment	K constant (Pa × s²)	Lower bound	Upper bound	Rate index *(n)*	Lower bound	Upper Bound
KGP 20 wt% Q	Down 2	53.36	39.39	67.32	0.3325	0.2977	0.3674
KGP 10 wt% CS	Ramp 1	134.5	-4.808	273.9	0.7466	0.5588	0.93534
KGP 10 wt% CS	Down 1	64.38	18.49	110.3	0.4364	0.3228	0.55
KGP 10 wt% CS	Ramp 2	118.1	20.41	215.7	0.5206	0.3864	0.6547
KGP 10 wt% CS	Down 2	98.29	43.89	153.1	0.5195	0.4323	0.6078
KGP 20 wt% CS	Ramp 1	177.4	-9.686	364.5	0.7242	0.5363	0.91205
KGP 20 wt% CS	Down 1	51.87	37.19	66.54	0.3242	0.2845	0.3639
KGP 20 wt% CS	Ramp 2	121.4	32.33	210.4	0.4624	0.3452	0.5796
KGP 20 wt% CS	Down 2	83.98	17.77	150.2	0.4184	0.2902	0.5467
KGP 30 wt% Q	Ramp 1	170.8	-25.46	367.1	0.7204	0.5163	0.9245
KGP 30 wt% Q	Down 1	29.41	16.49	42.32	0.2047	0.1366	0.2727
KGP 30 wt% Q	Ramp 2	66.72	25.37	108.1	0.322	0.2255	0.4186
KGP 30 wt% Q	Down 2	26.34	9.047	43.63	0.1806	0.0766	0.2845
KGP 10wt% CS + 10 wt% Q	Ramp 1	147	-11.89	305.8	0.7276	0.5346	0.92063
KGP 10wt% CS + 10 wt% Q	Down 1	30.93	13.5	48.37	0.2575	0.1712	0.3437
KGP 10wt% CS + 10 wt% Q	Ramp 2	72.92	19.71	126.1	0.3877	0.2728	0.5026
KGP 10wt% CS + 10 wt% Q	Down 2	28.67	7.14	50.2	0.2439	0.125	0.3628
KGP 30 wt% CS	Ramp 1	201.9	-23.42	427.3	0.7014	0.5057	0.897
KGP 30 wt% CS	Down 1	22.15	18.18	26.12	0.1294	0.1053	0.1534
KGP 30 wt% CS	Ramp 2	57.32	24.03	90.61	0.2757	0.1858	0.3656
KGP 30 wt% CS	Down 2	27.27	20.26	34.29	0.1623	0.1251	0.1994
KGP 15wt% CS + 15 wt% Q	Ramp 1	182.2	-22.82	387.4	0.71136	0.5146	0.91249
KGP 15wt% CS + 15 wt% Q	Down 1	23.2	9.036	37.37	0.161	0.0649	0.2572
KGP 15wt% CS+ 15 wt% Q	Ramp 2	69.55	25.95	113.1	0.3253	0.2276	0.423
KGP 15wt% CS+ 15 wt% Q	Down 2	25.55	8.672	42.42	0.1696	0.066	0.2733
OPC 10 wt% Q	Ramp 1	118	32.12	204	0.2794	0.1669	0.3919
OPC 10 wt% Q	Down 1	14.81	13.73	15.88	-0.078	-0.088	-0.069
OPC 10 wt% Q	Ramp 2	31.28	27.1	35.46	0.0079	-0.012	0.0281
OPC 10 wt% Q	Down 2	8.616	6.643	10.59	-0.174	-0.209	-0.139
OPC 20 wt% Q	Ramp 1	317.6	-69.56	704.7	0.4556	0.2616	0.6496
OPC 20 wt% Q	Down 1	11.98	9.417	14.55	-0.135	-0.168	-0.102

System	Segment	K constant (Pa × s²)	Lower bound	Upper bound	Rate index *(n)*	Lower bound	Upper Bound
OPC 20 wt% Q	Ramp 2	30.53	26.5	34.55	-0.01	-0.029	0.0104
OPC 20 wt% Q	Down 2	20.51	11.16	29.87	-0.056	-0.27	0.0141
OPC 10 wt% CS	Ramp 1	265	-52.9	582.8	0.4452	0.2546	0.6357
OPC 10 wt% CS	Down 1	10.5	8.047	12.96	-0.116	-0.152	-0.079
OPC 10 wt% CS	Ramp 2	23.94	21.31	26.57	-0.006	-0.0023	0.0105
OPC 10 wt% CS	Down 2	14.63	13.92	15.32	-0.066	-0.072	-0.059
OPC 20 wt% CS	Ramp 1	265	-52.9	582.8	0.4452	0.2546	0.6357
OPC 20 wt% CS	Down 1	10.5	8.047	12.96	-0.116	-0.152	-0.079
OPC 20 wt% CS	Ramp 2	23.94	21.31	26.57	-0.006	-0.023	0.0105
OPC 20 wt% CS	Down 2	14.63	13.92	15.34	-0.066	-0.072	-0.059
OPC 30 wt% Q	Ramp 1	443.1	-149.8	1036	0.506	0.2904	0.7217
OPC 30 wt% Q	Down 1	24.74	23.81	25.67	-0.055	-0.059	-0.05
OPC 30 wt% Q	Ramp 2	35.23	30.33	40.12	-0.023	-0.044	-0.002
OPC 30 wt% Q	Down 2	25.73	25.75	26.7	-0.065	-0.07	-0.06
OPC 30 wt% CS	Ramp 1	732.5	-242.8	1708	0.5323	0.3162	0.7484
OPC 30 wt% CS	Down 1	22.09	18.69	25.5	-0.12	-0.144	-0.096
OPC 30 wt% CS	Ramp 2	59.79	49.2	25.5	0.0132	-0.013	0.04
OPC 30 wt% CS	Down 2	33.93	32.87	35	-0.054	-0.058	-0.05
OPC 40 wt% Q	Ramp 1	679.7	-216.2	1576	0.5425	0.3279	0.7571
OPC 40 wt% Q	Down 1	21.83	19.52	24.13	-0.106	-0.122	-0.09
OPC 40 wt% Q	Ramp 2	39.16	33.94	44.39	-0.033	-0.053	-0.012
OPC 40 wt% Q	Down 2	32.29	31.02	33.56	-0.067	-0.073	-0.061
OPC 40wt% CS	Ramp 1	1150	-362.9	2662	0.55637	0.3483	0.7792
OPC 40wt% CS	Down 1	35.15	32.54	37.75	-0.119	-0.13	-0.107
OPC 40wt% CS	Ramp 2	87.16	71.46	102.9	0.006	-0.021	0.9331
OPC 40wt% CS	Down 2	67.16	64.54	69.72	-0.04	-0.045	-0.035
OPC 50 wt% Q	Ramp 1	987.3	-354.2	2329	0.5614	0.3391	0.7838
OPC 50 wt% Q	Down 1	38.48	32.78	44.18	-0.079	-0.102	-0.055
OPC 50 wt% Q	Ramp 2	54.29	46.08	62.49	-0.038	-0.061	-0.016
OPC 50 wt% Q	Down 2	45.87	36.58	55.16	-0.089	-0.121	-0.058
OPC 50 wt% CS	Ramp 1	2650	-445.6	5746	0.5992	0.4059	0.7924
OPC 50 wt% CS	Down 1	106.1	96.53	115.7	-0.057	-0.07	-0.044
OPC 50 wt% CS	Ramp 2	267.8	210.5	325.1	0.0815	0.0533	0.1126
OPC 50 wt% CS	Down 2	128.2	122.2	134.2	-0.052	-0.058	-0.046
KGP 40 wt% Q	Ramp 1	236	-45.27	517.3	0.7132	0.5026	0.9238
KGP 40 wt% Q	Down 1	46.6	35.88	57.32	0.2557	0.223	0.2884

System	Segment	K constant (Pa × s²)	Lower bound	Upper bound	Rate index *(n)*	Lower bound	Upper Bound
KGP 40 wt% Q	Ramp 2	151.3	49.62	253	0.4413	0.3344	0.5482
KGP 40 wt% Q	Down 2	64.77	14.32	115.2	0.3357	0.2106	0.4607
OPC 60 wt% Q	Ramp 1	2499	-765.8	5765	0.5944	0.3788	0.81
OPC 60 wt% Q	Down 1	87.45	64.43	110.5	-0.093	-0.134	-0.053
OPC 60 wt% Q	Ramp 2	350.9	233.8	468.1	0.125	0.0765	0.1734
OPC 60 wt% Q	Down 2	181.3	172.5	190.1	-0.033	-0.039	-0.028
KGP 40 wt% CS	Ramp 1	243.5	-38.48	525.5	0.6868	0.4857	0.888
KGP 40 wt% CS	Down 1	20.42	17.08	23.75	0.0828	0.0603	0.1054
KGP 40 wt% CS	Ramp 2	52.08	23.81	80.35	0.2205	0.137	0.304
KGP 40 wt% CS	Down 2	22.13	13.73	30.53	0.085	0.0258	0.1441
KGP 50 wt% Q	Ramp 1	262.7	-41.34	566.7	0.7506	0.5401	0.96102
KGP 50 wt% Q	Down 1	69.23	27.06	111.4	0.3413	0.2447	0.4379
KGP 50 wt% Q	Ramp 2	165.6	68.91	262.3	0.4955	0.4015	0.5896
KGP 50 wt% Q	Down 2	77.18	24.45	129.9	0.3551	0.2454	0.5896
OPC 60 wt% CS	Ramp 1	5793	-937.8	12520	0.6516	0.4561	0.8472
OPC 60 wt% CS	Down 1	266.5	201.3	331.8	-0.047	-0.085	-0.008
OPC 60 wt% CS	Ramp 2	6101	-2448	14650	0.5231	0.3087	-0.008
OPC 60 wt% CS	Down 2	167.1	158	176.2	-0.063	-0.071	-0.054
KGP 50 wt% CS	Ramp 1	354.7	-77.85	787.2	0.676	0.4655	0.8864
KGP 50 wt% CS	Down 1	10.68	9.517	11.84	-0.098	-0.115	-0.081
KGP 50 wt% CS	Ramp 2	39.74	25.56	53.92	0.0864	0.0322	0.1407
KGP 50 wt% CS	Down 2	22.52	19.93	25.1	-0.004	-0.019	0.0117
KGP 60 wt%Q	Ramp 1	424.6	-61.7	910.9	0.7131	0.5107	0.91549
KGP 60 wt% Q	Down 1	35.37	18.56	52.17	0.0896	0.0152	0.164
KGP 60 wt% Q	Ramp 2	169	85.26	253.9	0.3518	0.274	0.4296
KGP 60 wt% Q	Down 2	38.32	24.72	51.91	0.0585	0.003	0.1141
KGP 60 wt% CS	Ramp 1	562.3	-111.9	1236	0.6595	0.4545	0.8645
KGP 60 wt% CS	Down 1	9.953	8.333	11.57	-0.261	-0.286	-0.236
KGP 60 wt% CS	Ramp 2	133.9	59.81	207.9	0.1343	0.0505	0.2181
KGP 60 wt% CS	Down 2	23.71	21.93	25.5	-0.128	-0.139	-0.116
OPC 10wt% CS + 10 wt% Q	Ramp 1	328.9	-54.54	712.3	0.4481	0.2629	0.6333
OPC 10wt% CS + 10 wt% Q	Down 1	13.27	12.27	14.27	-0.13	-0.141	-0.119
OPC 10wt% CS + 10 wt% Q	Ramp 2	30.78	26.39	35.17	-0.021	-0.042	0.0008

System	Segment	K constant (Pa × s²)	Lower bound	Upper bound	Rate index *(n)*	Lower bound	Upper Bound
OPC 10wt% CS + 10 wt% Q	Down 2	11.69	10.34	13.05	-0.174	-0.191	-0.156

B.2 Stress ramp rheological values

Table B-2. Compiled list of values calculated from the Hershel Bulkley model.

System	Segment	Yield stress (Pa)	Lower YS bound	Upper YS bound	HB index(*p*)	Lower HB index bound	Upper HB index bound
KGP 25 wt% Chamotte	Ramp 1	6.693	5.236	8.147	1.257	1.225	1.29
KGP 25 wt% Chamotte	Down 1	7.209	5.802	8.616	1.413	1.373	1.454
KGP 25 wt% Chamotte	Ramp 2	8.078	6.611	9.544	1.17	1.143	1.196
KGP 25 wt% Chamotte	Down 2	7.482	5.591	9.372	1.374	1.326	1.422
KGP 25 wt% sand	Ramp 1	4.012	3.104	4.921	1.252	1.214	1.29
KGP 25 wt% sand	Down 1	3.688	2.653	4.723	1.27	1.225	1.316
KGP 25 wt% sand	Ramp 2	4.646	3.839	5.453	1.195	1.167	1.223
KGP 25 wt% sand	Down 2	3.678	2.486	4.87	1.242	1.197	1.288
KGP 20 wt% sand/20 wt% chamotte	Ramp 1	9.291	5.372	13.21	1.118	1.089	1.146
KGP 20 wt% sand/20 wt% chamotte	Down 1	15.18	12.34	18.02	1.393	1.361	1.426
KGP 20 wt% sand/20 wt% chamotte	Ramp 2	14.8	12.04	17.55	1.111	1.09	1.132
KGP 20 wt% sand/20 wt% chamotte	Down 2	15.64	12.93	18.35	1.347	1.316	1.378
KGP 50 wt% sand	Ramp 1	5.542	3.104	4.921	1.099	1.214	1.29
KGP 50 wt% sand	Down 1	6.221	4.584	7.857	1.216	1.188	1.53
KGP 50 wt% sand	Ramp 2	6.852	5.895	7.81	1.063	1.051	1.076
KGP 50 wt% sand	Down 2	5.907	4.118	7.697	1.188	1.158	1.218
KGP 60 wt% sand	Ramp 1	6.121	-1.194	13.44	0.8712	0.827	0.9155
KGP 60 wt% sand	Down 1	9.102	3.279	11.93	1.117	1.088	1.145
KGP 60 wt% sand	Ramp 2	10.56	7.648	13.47	0.9715	0.9488	0.9942
KGP 60 wt% sand	Down 2	9.197	6.228	12.17	1.115	1.086	1.144
Metamax KGP	Ramp 1	2.863	2.113	3.613	1.417	1.349	1.484
Metamax KGP	Down 1	2.475	1.698	3.251	1.415	1.345	1.48
Metamax KGP	Ramp 2	3.313	2.571	4.054	1.358	1.301	1.405
Metamax KGP	Down 2	2.456	2.571	4.054	1.362	1.301	1.415
KGP 60 wt% sand with Superplasticizer	Ramp 1	4.434	2.591	6.277	1.073	1.053	1.093

System	Segment	Yield stress (Pa)	Lower YS bound	Upper YS bound	HB index(p)	Lower HB index bound	Upper HB index bound
KGP 60 wt% sand with Superplasticizer	Down 1	6.195	4.525	7.865	1.229	1.205	1.254
KGP 60 wt% sand with Superplasticizer	Ramp 2	6.53	5.576	7.484	1.067	1.055	1.078
KGP 60 wt% sand with Superplasticizer	Down 2	5.944	4.199	7.689	1.195	1.168	1.221
KGP 25wt% Silica Fume	Ramp 1	42.41	35.51	49.3	0.8253	0.757	0.8936
KGP 25wt% Silica Fume	Down 1	41.65	39.43	43.86	1.091	1.053	1.13
KGP 25wt% Silica Fume	Ramp 2	50	46.28	53.72	0.7564	0.7146	0.7983
KGP 25wt% Silica Fume	Down 2	43.71	38.05	49.37	0.9662	0.8608	1.072
Argical KGP	Ramp 1	4.622	3.601	5.643	1.246	1.189	1.303
Argical KGP	Down 1	3.659	2.654	4.664	1.247	1.19	1.304
Argical KGP	Ramp 2	5.472	4.431	6.413	1.164	1.118	1.209
Argical KGP	Down 2	3.496	2.137	4.854	1.181	1.12	1.242
Powerpozz KGP	Ramp 1	0.9009	0.606	1.196	1.63	1.573	1.68
Powerpozz KGP	Down 1	0.7479	0.4659	1.03	1.626	1.571	1.681
Powerpozz KGP	Ramp 2	1.053	0.7529	1.353	1.625	1.568	1.682
Powerpozz KGP	Down 2	0.6803	0.3778	0.9828	1.613	1.556	1.67
Metamax EF KGP	Ramp 1	38.82	30.52	47.13	1.087	0.0736	2.101
Metamax EF KGP	Down 1	41.94	39.87	44.02	1.468	1.399	1.538
Metamax EF KGP	Ramp 2	50.69	48.19	53.18	1.202	1.154	1.25
Metamax EF KGP	Down 2	46.25	43.21	49.26	1.403	1.322	1.483
Metastar 501 HP KGP	Ramp 1	5.402	4.214	5.59	1.341	1.25	1.432
Metastar 501 HP KGP	Down 1	5.491	4.561	6.421	1.357	1.284	1.43
Metastar 501 HP KGP	Ramp 2	6.546	5.639	7.453	1.297	1.237	1.357
Metastar 501 HP KGP	Down 2	5.559	4.506	6.612	1.315	1.244	1.387
Quikrete OPC	Ramp 1	18.65	17.33	19.97	0.7968	0.7183	0.8753
Quikrete OPC	Down 1	16.17	14.31	18.04	0.6874	0.5949	0.78
Quikrete OPC	Ramp 2	20.01	18.15	21.87	0.9067	0.7846	1.029
Quikrete OPC	Down 2	16.76	14.86	18.65	0.6768	0.5843	0.7693
KGP 10 wt% Q	Ramp 1	6.409	5.148	7.67	1.525	1.376	1.671
KGP 10 wt% Q	Down 1	6.557	6.007	7.107	1.592	1.524	1.66
KGP 10 wt% Q	Ramp 2	7.895	7.045	8.745	1.507	1.411	1.604
KGP 10 wt% Q	Down 2	7.223	6.584	7.862	1.57	1.493	1.647
KGP 20 wt%Q	Ramp 1	7.163	5.853	8.474	1.405	1.292	1.518
KGP 20 wt% Q	Down 1	8.035	7.377	8.692	1.504	1.441	1.568

System	Segment	Yield stress (Pa)	Lower YS bound	Upper YS bound	HB index(p)	Lower HB index bound	Upper HB index bound
KGP 20 wt%Q	Ramp 2	9.47	8.479	10.46	1.368	1.285	1.45
KGP 20 wt% Q	Down 2	9.104	8.284	9.925	1.477	1.4	1.554
KGP 10 wt% CS	Ramp 1	6.772	5.491	8.054	1.473	1.338	1.608
KGP 10 wt% CS	Down 1	6.858	6.193	7.523	1.535	1.46	1.61
KGP 10 wt% CS	Ramp 2	8.347	7.42	9.275	1.47	1.373	1.567
KGP 10 wt% CS	Down 2	7.788	6.906	8.67	1.493	1.397	1.588
KGP 20 wt% CS	Ramp 1	7.962	6.601	9.324	1.382	1.285	1.478
KGP 20 wt% CS	Down 1	8.52	7.894	9.146	1.466	1.416	1.516
KGP 20 wt% CS	Ramp 2	10.02	9.087	10.95	1.342	1.279	1.406
KGP 20 wt% CS	Down 2	9.761	8.923	10.6	1.43	1.366	1.495
KGP 30 wt% Q	Ramp 1	7.327	6.078	8.576	1.309	1.246	1.372
KGP 30 wt% Q	Down 1	8.421	7.875	8.967	1.41	1.378	1.442
KGP 30 wt% Q	Ramp 2	9.402	7.875	8.967	1.28	1.239	1.321
KGP 30 wt% Q	Down 2	8.822	8.245	9.399	1.4	1.367	1.432
KGP 10wt% CS + 10 wt% Q	Ramp 1	6.693	5.535	7.851	1.379	1.301	1.458
KGP 10wt% CS + 10 wt% Q	Down 1	6.99	6.509	7.471	1.456	1.419	1.492
KGP 10wt% CS + 10 wt% Q	Ramp 2	8.056	7.351	8.761	1.351	1.305	1.396
KGP 10wt% CS + 10 wt% Q	Down 2	7.357	6.847	7.867	1.438	1.401	1.474
KGP 30 wt% CS	Ramp 1	8.197	6.794	9.6	1.311	1.258	1.364
KGP 30 wt% CS	Down 1	9.192	8.66	9.723	1.422	1.398	1.446
KGP 30 wt% CS	Ramp 2	9.864	9.029	10.7	1.242	1.213	1.27
KGP 30 wt% CS	Down 2	9.546	9.001	10.09	1.412	1.388	1.435
KGP 15wt% CS + 15 wt% Q	Ramp 1	7.75	6.465	9.034	1.321	1.26	1.382
KGP 15wt% CS + 15 wt% Q	Down 1	8.637	8.133	9.141	1.41	1.383	1.438
KGP 15wt% CS+ 15 wt% Q	Ramp 2	9.61	8.803	10.42	1.279	1.243	1.315
KGP 15wt% CS+ 15 wt% Q	Down 2	9.057	8.523	9.59	1.279	1.243	1.315
OPC 10 wt% Q	Ramp 1	20.97	13.39	22.55	0.8133	0.7356	0.891
OPC 10 wt% Q	Down 1	20.97	19.26	22.69	0.688	0.617	0.7591
OPC 10 wt% Q	Ramp 2	22.79	19.78	25.8	0.906	0.7582	1.054
OPC 10 wt% Q	Down 2	22.14	20.47	23.8	0.6535	0.5966	0.7104

System	Segment	Yield stress (Pa)	Lower YS bound	Upper YS bound	HB index(p)	Lower HB index bound	Upper HB index bound
OPC 20 wt% Q	Ramp 1	23.34	21.03	25.66	0.787	0.6949	0.8791
OPC 20 wt% Q	Down 1	24.93	23.35	26.5	0.6354	0.5846	0.6862
OPC 20 wt% Q	Ramp 2	24.5	21.34	27.66	1.002	0.841	1.163
OPC 20 wt% Q	Down 2	27.54	25.97	29.11	0.6095	0.5653	0.6538
OPC 10 wt% CS	Ramp 1	20.52	18.6	22.43	0.992	0.8711	1.113
OPC 10 wt% CS	Down 1	19.58	18.18	20.98	0.6653	0.6124	0.7182
OPC 10 wt% CS	Ramp 2	18.79	16.94	20.64	1.01	0.8972	1.123
OPC 10 wt% CS	Down 2	20.7	19.19	22.21	0.6245	0.5747	0.6744
OPC 20 wt% CS	Ramp 1	25.6	22.53	28.66	1.038	0.877	1.199
OPC 20 wt% CS	Down 1	27.49	25.98	29	0.6788	0.6321	0.7255
OPC 20 wt% CS	Ramp 2	25.11	22.12	28.11	1.119	0.9484	1.29
OPC 20 wt% CS	Down 2	31.45	29.6	33.1	0.6504	0.596	0.7048
OPC 30 wt% Q	Ramp 1	25.97	23.14	28.8	0.8369	0.7287	0.9451
OPC 30 wt% Q	Down 1	31.95	30.33	33.58	0.6992	0.6442	0.7543
OPC 30 wt% Q	Ramp 2	29.98	26.37	33.59	1.016	0.8351	1.196
OPC 30 wt% Q	Down 2	35.77	34.06	37.47	0.6672	0.6142	0.7201
OPC 30 wt% CS	Ramp 1	33.98	28.92	39.04	1.094	0.8803	1.308
OPC 30 wt% CS	Down 1	40.33	38.03	42.62	0.7392	0.6764	0.802
OPC 30 wt% CS	Ramp 2	36.45	30.89	42.01	1.151	0.886	1.416
OPC 30 wt% CS	Down 2	43.13	41.02	45.24	0.7122	0.6546	0.7697
OPC 40 wt% Q	Ramp 1	33.63	29.26	38	0.9057	0.7537	1.058
OPC 40 wt% Q	Down 1	39.73	38.05	41.41	0.7738	0.7211	0.8266
OPC 40 wt% Q	Ramp 2	33.83	29.19	38.47	1.099	0.8771	1.32
OPC 40 wt% Q	Down 2	47.42	45.83	29.02	0.7495	0.7003	0.7988
OPC 40wt% CS	Ramp 1	46.88	39.05	54.71	1.127	0.8416	1.413
OPC 40wt% CS	Down 1	62.07	58.39	65.74	0.8373	0.7413	0.9331
OPC 40wt% CS	Ramp 2	51.77	42.45	61.1	1.234	0.8424	1.625
OPC 40wt% CS	Down 2	73.65	69.68	77.62	0.8412	0.7306	0.9517
OPC 50 wt% Q	Ramp 1	42.13	35.19	49.07	0.8614	0.6902	1.033
OPC 50 wt% Q	Down 1	59.33	57.3	61.35	0.9176	0.8532	0.9819
OPC 50 wt% Q	Ramp 2	46.32	38.82	53.83	1.193	0.8664	1.519
OPC 50 wt% Q	Down 2	73.09	70.92	75.25	0.9213	0.8503	0.9924
OPC 50 wt% CS	Ramp 1	93.17	73.84	112.5	1.184	0.5636	1.804
OPC 50 wt% CS	Down 1	116.7	106.6	126.8	1.11	0.7945	1.42
OPC 50 wt% CS	Ramp 2	100.6	58.7	142.5	-0.5676	-2.177	1.04

System	Segment	Yield stress (Pa)	Lower YS bound	Upper YS bound	HB index(p)	Lower HB index bound	Upper HB index bound
OPC 50 wt% CS	Down 2	143.7	133.6	153.7	1.142	0.6994	1.58
KGP 40 wt% Q	Ramp 1	8.995	7.42	10.57	1.19	1.137	1.242
KGP 40 wt% Q	Down 1	10.55	9.78	11.32	1.323	1.291	1.354
KGP 40 wt% Q	Ramp 2	12.2	10.64	13.77	1.147	1.093	1.201
KGP 40 wt% Q	Down 2	11	10.09	11.92	1.305	1.266	1.344
OPC 60 wt% Q	Ramp 1	81.98	61.87	102.1	0.9229	0.3007	1.545
OPC 60 wt% Q	Down 1	134.2	126.6	141.8	0.8049	0.5598	1.05
OPC 60 wt% Q	Ramp 2	101.6	80.37	122.9	0.8738	0.4067	1.341
OPC 60 wt% Q	Down 2	174.1	158.6	189.5	0.9524	0.3741	1.531
KGP 40 wt% CS	Ramp 1	9.415	7.864	10.97	1.241	1.208	1.275
KGP 40 wt% CS	Down 1	11.24	10.36	12.13	1.4	1.376	1.425
KGP 40 wt% CS	Ramp 2	11.62	10.51	12.53	1.168	1.148	1.189
KGP 40 wt% CS	Down 2	12.05	11.13	12.97	1.395	1.369	1.421
KGP 50 wt% Q	Ramp 1	10.28	8.165	12.39	1.167	1.11	1.224
KGP 50 wt% Q	Down 1	10.71	9.882	11.55	1.257	1.231	1.282
KGP 50 wt% Q	Ramp 2	12.39	10.45	14.34	1.105	1.055	1.154
KGP 50 wt% Q	Down 2	11.38	10.46	12.3	1.251	1.222	1.28
OPC 60 wt% CS	Ramp 1	169.9	124.8	215	1.357	-0.01846	2.732
OPC 60 wt% CS	Down 1	228.5	178	279	-0.7193	-2074	0.6358
OPC 60 wt% CS	Ramp 2	194.1	147.8	240.4	1857	-0.5989	4.313
OPC 60 wt% CS	Down 2	196.3	179.2	213.4	1.036	0.6731	1.398
KGP 50 wt% CS	Ramp 1	12.89	10.75	15.02	1.144	1.121	1.167
KGP 50 wt% CS	Down 1	18.37	16.15	20.59	1.357	1.324	1.39
KGP 50 wt% CS	Ramp 2	19.59	16.3	22.87	1.092	1.054	1.13
KGP 50 wt% CS	Down 2	20.47	18.24	22.71	1.359	1.322	1.296
KGP 60 wt%Q	Ramp 1	15.19	11.64	18.74	1.047	1.003	1.092
KGP 60 wt% Q	Down 1	18.27	16.39	20.14	1.202	1.171	1.232
KGP 60 wt% Q	Ramp 2	20.88	17.09	24.66	1.037	0.9872	1.088
KGP 60 wt% Q	Down 2	23.14	21.06	25.22	1.082	1.052	1.11
KGP 60 wt% CS	Ramp 1	19.05	13.71	24.29	0.948	0.9165	0.9795
KGP 60 wt% CS	Down 1	39.2	31.3	47.01	1.213	1.133	1.293
KGP 60 wt% CS	Ramp 2	39.9	31.16	48.63	0.9378	0.8748	1.001
KGP 60 wt% CS	Down 2	40.77	35.2	46.34	1.206	1.147	1.266
OPC 10wt% CS + 10 wt% Q	Ramp 1	24.27	21.89	26.65	0.8999	0.665	2.308

System	Segment	Yield stress (Pa)	Lower YS bound	Upper YS bound	HB index(p)	Lower HB index bound	Upper HB index bound
OPC 10wt% CS + 10 wt% Q	Down 1	25.69	23.93	27.44	0.6572	0.5989	0.7155
OPC 10wt% CS + 10 wt% Q	Ramp 2	23.79	20.48	27.1	1.055	0.8582	1.251
OPC 10wt% CS + 10 wt% Q	Down 2	29.61	27.68	31.55	0.6433	0.5787	0.7079

REPORT DOCUMENTATION PAGE

Form Approved
OMB No. 0704-0188

Public reporting burden for this collection of information is estimated to average 1 hour per response, including the time for reviewing instructions, searching existing data sources, gathering and maintaining the data needed, and completing and reviewing this collection of information. Send comments regarding this burden estimate or any other aspect of this collection of information, including suggestions for reducing this burden to Department of Defense, Washington Headquarters Services, Directorate for Information Operations and Reports (0704-0188), 1215 Jefferson Davis Highway, Suite 1204, Arlington, VA 22202-4302. Respondents should be aware that notwithstanding any other provision of law, no person shall be subject to any penalty for failing to comply with a collection of information if it does not display a currently valid OMB control number. PLEASE DO NOT RETURN YOUR FORM TO THE ABOVE ADDRESS.

1. REPORT DATE (DD-MM-YYYY)	2. REPORT TYPE	3. DATES COVERED (From - To)
April 2023	Final	FY20–FY22

4. TITLE AND SUBTITLE
4D Printing Structures for Extreme Temperatures Using Metakaolin Based Geopolymers

5a. CONTRACT NUMBER

5b. GRANT NUMBER

5c. PROGRAM ELEMENT
0603119A

6. AUTHOR(S)
Ghassan Al-Chaar, Allison Brandvold, Andrij Kozych, and William Mendoza

5d. PROJECT NUMBER
BO3

5e. TASK NUMBER
17

5f. WORK UNIT NUMBER

7. PERFORMING ORGANIZATION NAME(S) AND ADDRESS(ES)
US Army Engineer Research and Development Center (ERDC)
Construction Engineering Research Laboratory (CERL)
2902 Newmark Drive
Champaign, IL 61822

8. PERFORMING ORGANIZATION REPORT NUMBER
ERDC/CERL TR-23-7

9. SPONSORING / MONITORING AGENCY NAME(S) AND ADDRESS(ES)
Office of Senator Dick Durbin
711 Hart Building
Washington, DC 20510

Army Futures Command
Austin, TX 78701

10. SPONSOR/MONITOR'S ACRONYM(S)

11. SPONSOR/MONITOR'S REPORT NUMBER(S)

12. DISTRIBUTION / AVAILABILITY STATEMENT
Distribution Statement A. Approved for public release: distribution is unlimited.

13. SUPPLEMENTARY NOTES

14. ABSTRACT

Geopolymers (GPs) are a class of amorphous, aluminosilicate-based ceramics that cure at room temperature. GPs are formed by mixing an aluminosilicate source, which is metakaolin in this case, with an alkali activator solution, which can be either sodium or potassium water glass. GPs have attracted interest for use in structural applications over the past few decades because they have superior mechanical properties to ordinary Portland cement (OPC). Additionally, they can tolerate much higher temperatures and produce a fraction of the CO2 compared to OPC. This project aims to develop geopolymer composites for 4D printing (the fourth dimension being time) and test their mechanical properties. GP rheology and ambient conditions curing effect will be evaluated for fresh GP. Freeze-thaw resistance will be evaluated on potentially printable composites for extreme temperature resistance, etc.

15. SUBJECT TERMS
Ceramic-matrix composites, Kaolin, Composite materials, Three-dimensional printing, Portland cement

16. SECURITY CLASSIFICATION OF:			17. LIMITATION OF ABSTRACT	18. NUMBER OF PAGES	19a. NAME OF RESPONSIBLE PERSON
a. REPORT	b. ABSTRACT	c. THIS PAGE			Ghassan Al-Chaar
Unclassified	Unclassified	Unclassified	SAR	202	19b. TELEPHONE NUMBER (include area code) (217) 373-7247